Transactions of the ASME®

Journal of Fluids Engineering

Published Quarterly by The American Society of Mechanical Engineers

VOLUME 111 • NUMBER 3 • SEPTEMBER 1989

Technical Briefs

Announcements and Special Notices

(Contents continued on page 262)

FLUIDS ENGINEERING DIVISION
Technical Editor
FRANK M. WHITE (1989)
Executive Secretary
L. T. BROWN (1989)
Calendar Editor
M. F. ACKERSON

Associate Editors
Fluid Machinery
WIDEN TABAKOFF (1991)
UPENDRA S. ROHATGI (1990)
Fluid Measurements
JOHN F. FOSS (1990)
Fluid Mechanics
J. CRAIG DUTTON (1990)
DANIEL C. REDA (1990)
DEMETRI P. TELIONIS (1989)
Fluid Transients
FREDERICK J. MOODY (1989)
Numerical Methods
DAVID G. LILLEY (1991)
Multiphase Flow
EFSTATHIOS E. MICHAELIDES (1991)
GEORGES L. CHAHINE (1990)
Review Articles
K. N. GHIA (1989)

BOARD ON COMMUNICATIONS
Chairman and Vice President
R. NICKELL

Members-at-Large
W. BEGELL
T. F. CONRY
M. FRANKE
R. L. KASTOR
M. KUTZ
R. MATES
T. C. MIN
E. M. PATTON
R. E. REDER
R. D. ROCKE
F. W. SCHMIDT
W. O. WINER
A. J. WENNERSTROM
B. ZIELS

President, **C. O. VELZY**
Executive Director
D. L. BELDEN
Treasurer,
ROBERT A. BENNETT

PUBLISHING STAFF
Mng. Dir., Publ.,
CHARLES W. BEARDSLEY
Managing Editor,
CORNELIA MONAHAN
Editorial Production Assistant,
MARISOL ANDINO

Transactions of the ASME, Journal of Fluids Engineering (ISSN 0098-2202) is published quarterly (Mar., June, Sept., Dec.) for $100 per year by The American Society of Mechanical Engineers, 345 East 47th Street, New York, NY 10017. Second class postage paid at New York, NY and additional mailing offices. POSTMASTER: Send address changes to Transactions of the ASME, Journal of Fluids Engineering, c/o THE AMERICAN SOCIETY OF MECHANICAL ENGINEERS, 22 Law Drive, Box 2300, Fairfield, NJ 07007-2300. **CHANGES OF ADDRESS** must be received at Society headquarters seven weeks before they are to be effective. Please send old label and new address. **PRICES:** To members, $29.00, annually: to nonmembers, $100. Add $15.00 for postage to countries outside the United States and Canada.

STATEMENT from By-Laws. The Society shall not be responsible for statements or opinions advanced in papers or . . . printed in its publications (B7.1, Par. 3). **COPYRIGHT © 1989** by The American Society of Mechanical Engineers. Reprints from this publication may be made on condition that full credit be given the TRANSACTIONS OF THE ASME, JOURNAL OF FLUIDS ENGINEERING and the author, and date of publication be stated.

INDEXED by Applied Mechanics Reviews and Engineering Information, Inc.

Downloaded 03 Jun 2010 to 171.66.16.159. Redistribution subject to ASME license or copyright; see http://www.asme.org/terms/Terms_Use.cfm

Contents (continued)

Y. T. Fung
Mechanical Engineer,
Laboratory for Computational Physics
and Fluid Dynamics,
Naval Research Laboratory,
Washington, DC 20375

Unstable Waves of Jet Flows With Density Inhomogeneity

Instability of axisymmetric jet flows of a fluid having a radius-dependent density is investigated. The necessary condition for the existence of unstable waves depends not only on the velocity profile but also on the density gradient as well. Large density gradients, positive or negative, have stabilizing effects. The semicircle theorem for amplified waves is valid in this case. It is shown by considering the top-hat type velocity profile that the velocity-dependent semicircle bound is the best possible.

Introduction

The problem to be considered concerns linear unstable waves of axisymmetric jet flows in the presence of density inhomogeneities. Such flow phenomena occur when a jet is discharged into a stratified medium, e.g., pollutants and industrial waste discharged into the environment, cooling water discharged from power plants into rivers and lakes, and flow patterns generated by vehicles moving in the ocean. Investigating the instability characteristics of such jet flows is necessary to fully understand the overall behavior of the flow patterns and their corresponding effects on the environment. Changing the instability characteristics of the flow can mean controlling the flow patterns, for example, produced by vehicles moving in the ocean. As in the case of two-dimensional shear flows, axisymmetric jet flows may possess amplified waves due to the Kelvin-Helmholtz mechamism except that the formulation for jet flows is complicated by the absence of the Squire transformation and the consideration of cylindrical geometry.

In a well-known paper concerning unbounded parallel flows of the jet-wake type, Batchelor and Gill (1962) presented a general mathematical analysis of the stability characteristics of axisymmetric flows of homogeneous fluids. A necessary condition for instability and a semi-circle theorem for possible unstable waves were derived. By discussing the governing equation near the jet axis, they were able to reach some general conclusions on the characteristic difference between the axisymmetric and nonaxisymmetric modes. Meanwhile Reynolds (1962) conducted an experimental study and observed axisymmetric condensations and puffs in a water tank. The axisymmetric mode of a jet column was also examined by Gill (1962) with a slightly viscous jet flow model and later by Mattingly and Chang (1974) with a coordinated theoretical and experimental investigation. The latter found that the dominant disturbance in the jet was an axisymmetric one. It is expected that initial disturbances will follow the direction of mean flows and the axisymmetric waves will in general first amplify for the onset of instability.

In this theoretical study, the effect of radial density variations on the stability of incompressible axisymmetric jet flows will be investigated. Both the necessary condition for instability and the semicircle bound on amplified waves will be obtained through a unified integral representation. The results obtained here show that the necessary condition for the existence of amplified waves depends not only on the velocity profile, but also on the effect of density inhomogeneities. Both positive and negative density gradients have stabilizing effects. The semi-circle theorem for unstable waves can be extended to flows with radius-dependent density. For top-hat profiles of jet or wake type, the semicircle bound is found to be the best possible.

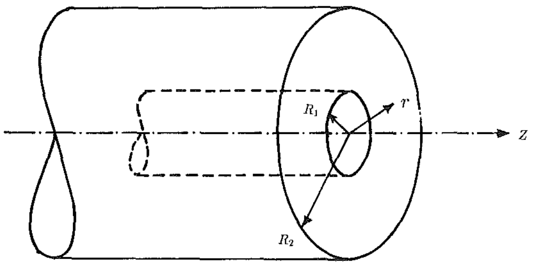

Fig. 1 Geometry of the flow domain

Governing Equations and Instability Characteristics

The jet flow to be considered consists of a radius-dependent axial velocity $W(r)$ in a fluid with density $\rho(r)$, and is confined within the annular region between two concentric cylinders located at $r=R_1$ and $r=R_2$ as shown in Fig. 1. Applying the linear perturbations analysis to the governing equations for the present flow and using the normal mode approach such that

$$\hat{\phi}(r,\theta,z;t)=\phi(r)\exp\{i(kz+m\theta-kct)\}$$

where $\hat{\phi}$ represents the perturbations in the velocity, density, and pressure fields, one finds, after neglecting the gravitational effects, that the sinusoidal waves of the present flow are governed by two ordinary differential equations

$$\left(k^2+\frac{m^2}{r^2}\right)p=i\rho k\left[DW-(W-c)\left(Du+\frac{u}{r}\right)\right], \qquad (1)$$

$$Dp=-i\rho k(W-c)u \qquad (2)$$

with $D=d/dr$.

Contributed by the Fluids Engineering Division for publication in the JOURNAL OF FLUIDS ENGINEERING. Manuscript received by the Fluids Engineering Division September 5, 1988.

Here u and p are perturbations in radial velocity and pressure, respectively. To consider only temporal instabilities, the azimuthal wave number m is an integer, the axial wave number k is real, while the phase velocity $c = c_r + ic_i$ is in general complex. Since the equations are invariant under complex conjugation, a nonzero c_i implies instability.

Combining equations (1) and (2) and eliminating the variable p, one finds a single differential equation governing instability as follows:

$$(W-c)\left\{D\left[\rho q\left(Du+\frac{u}{r}\right)\right]-\rho u\right\}-D_*(\rho q D W)u=0 \tag{3}$$

where $D_* = D - 1/r$ and $q = r^2/(m^2+k^2r^2)$. Equation (3) and boundary conditions $u(R_1) = u(R_2) = 0$ represent an eigenvalue problem for inviscid unstable waves of axisymmetric jet flows in a stratified medium. Reminiscent of the Rayleigh equation encountered in the stability of two-dimensional shear flow, equation (3) possesses a first-order singularity for neutral disturbances and analytical solutions in terms of well-known functions are in general not possible except for some special flow profiles. We will emphasize the effect of density inhomogeneities and seek solutions to those flow profiles which admit exact solutions in terms of modified Bessel functions. To do this, one must avoid the first-order singularity in the equation as c_i vanishes.

Before obtaining exact solutions to equation (3) we will briefly re-examine the inviscid instability characteristics of the flow via an integral representation. The analysis in the present case is particularly simple and the principal steps of deriving these characteristics are reproduced here for the sake of completeness. To perform the analysis, we look for unstable waves with $c_i > 0$ and make the transformation $u = (W-c)^n\psi$. Here n is an arbitrary real constant. Multiplying the resultant equation by the complex conjugate $r\bar{\psi}$, integrating it over the flow domain, and applying the boundary conditions that ψ vanishes at the solid boundaries of the inner and outer cylinders, one obtains

$$\begin{aligned}\int_{R_1}^{R_2}\Big\{&(W-c)^{2n}\rho[q\,|D^*\psi|^2+|\psi|^2]\\&-(W-c)^{2n-1}[(n-1)D(\rho Q)]r\,|\psi|^2\\&-(W-c)^{2n-2}[n(n-1)\rho q(DW)^2]\,|\psi|^2\Big\}rdr=0\end{aligned} \tag{4}$$

where $Q = rDW/(m^2+k^2r^2)$ and $D^* = D + 1/r$. Letting $n = 0$ one finds, from the imaginary part of the resultant integral.

$$c_i\int_{R_1}^{R_2} D(\rho Q)\frac{|r\psi|^2}{|W-c|^2}\,dr=0 \tag{5}$$

For instability, the expression $D(\rho Q)$ must vanish at least at one interior point within the flow domain, i.e.,

$$\frac{DQ}{Q}+\frac{D\rho}{\rho}=0 \tag{6}$$

The first term of the above equation is reminiscent of the inflexion point theory encountered in plane parallel flows, and has been discussed in detail in the study of homogeneous jet flows (Batchelor and Gill, 1962). The second term depends solely on density inhomogeneities and will have significant contributions when the condition for instability of the otherwise homogeneous flow field is satisfied. It is shown from equation (6) and later via the exact solution for a special flow profile, that the necessary condition for amplified waves established for homogeneous fluids is not sufficient if density inhomogeneities are present. Cylindrical vortex sheets can be stable if large density gradients are present in the flow.

The refinement of condition (6) can be obtained by equation (5) and the real part of equation (4) for $n = 0$. One can easily show a strong necessary condition for instability is

$$D\left(\frac{\rho r D W}{m^2+k^2r^2}\right)(W-W_s)\le 0 \tag{7}$$

where W_s is the mean velocity evaluated at a certain point inside the flow field where condition (6) is satisfied.

The semicircle bound can easily be derived by combining the real imaginary parts of integral (4) for $n = 1$. Imposing the upper and lower limits a and b for the mean axial velocity, one obtains

$$\begin{aligned}0\ge\int_{R_1}^{R_1}&(W-a)(W-b)\rho[q|D^*\psi|^2+|\psi|^2]rdr\\&=\left\{[c_r-\frac{1}{2}(a+b)]^2+c_i^2\right.\\&\left.-\left[\frac{1}{2}(a-b)\right]^2\right\}\int_{R_1}^{R_2}\rho[q\,|D^*\psi|^2+|\psi|^2]rdr\end{aligned} \tag{8a}$$

$$\left[c_r-\frac{1}{2}(a+b)\right]^2+c_i^2\le\left[\frac{1}{2}(a-b)\right]^2 \tag{8b}$$

Thus the semicircle theorem is valid in the presence of density inhomogeneities, saying that the complex wave velocity must lie inside a semicircle with the diameter equal to the range of the velocity. The subsequent section will show that this semicircle bound provides an exact solution for some particular flow profiles.

Two Exact Solutions and Their Semicircle Bounds

To examine the validity of the earlier obtained instability characteristics and to gain some information on instability growth rates as a function of velocity, density, and wave numbers, one must seek explicit solutions to equation (3) for some special flow configurations. We will consider those profiles for which solutions in terms of modified Bessel functions are possible. One of such profiles to investigate is

$$\begin{aligned}&W=W_1,\ \rho=\rho_1\left(\frac{r}{R}\right)^{\sigma_1}\quad \text{for } R_1\le r<R\\&W=W_2,\ \rho=\rho_2\left(\frac{r}{R}\right)^{\sigma_2}\quad \text{for } R\le r\le R_2\end{aligned} \tag{9}$$

where W_1, W_2, ρ_1, ρ_2, σ_1, and σ_2 are constants. This flow represents a top-hat jet core with radius-dependent density surrounded by a fluid column with different density. Because

Nomenclature

$c = c_r + ic_i$ = complex phase velocity
D = d/dr
I_v = modified Bessel function of the first kind of order v
k = axial wave number
K_v = modified bessel function of the second kind of order v
m = azimuthal wave number
p = pressure perturbation
r = radius
R = position of the interface
R_1, R_2 = positions of solid boundaries
u = velocity perturbation in the radial direction
W = axial velocity
κ = kR
κ_1, κ_2 = kR_1, kR_2
ψ = transformation of u
ρ = density
$\sigma, \sigma_1, \sigma_2$ = parameters for density variations

the discontinuity in the velocity at the interface $r=R$ satisfies instability condition (6) for homogeneous fluids, this velocity profile will generally be unstable for all modes in uniform media via the Kelvin-Helmholtz mechanism. However, it will be demonstrated later that these unstable waves can be stabilized if large density gradients are considered.

The perturbations in radial velocity and pressure for the flow profile in equation (9) are given by

$$u_j=r^{-\frac{\sigma_j}{2}-1}\left\{A_j\left[\frac{\sigma_j}{2}+\frac{krI'_{v_j}(kr)}{I_{v_j}(kr)}\right]I_{v_j}(kr)\right.$$

$$\left.+B_j\left[\frac{\sigma_j}{2}+\frac{krK'_{v_j}(kr)}{K_{v_j}(kr)}\right]K_{v_j}(kr)\right\}$$

$$p_j=-i\rho_jR^{-\sigma_j}k(W_j-c)r^{\frac{\sigma_j}{2}}\{A_jI_{v_j}(kr)+B_jK_{v_j}(kr)\}\qquad(10)$$

with $v_j=\sqrt{m^2+(\sigma_j/2)^2}$ for $j=1,2$. Here $I_{v_j}(kr)$ and $K_{v_j}(kr)$ are the modified Bessel functions of the first and second kind of order v_j, and a prime denotes the total derivative with respect to the quantity shown.

By integrating equations (1) and (2) across the interface at $r=R$, both the kinematical and dynamical interfacial conditions are obtained as follows:

$$\left\langle\frac{u}{W-c}\right\rangle=0$$

$$\langle p\rangle=0\qquad(11)$$

where

$$\langle f\rangle=f(R_{+0})-f(R_{-0}).$$

Making use of the boundary conditions at $r=R_1$, R_2 and applying the matching conditions (11) yield the secular relation for instability

$$\frac{(W_1-c)[I_{v_1}(\kappa)-H_1K_{v_1}(\kappa)]}{\left[\frac{\sigma_1}{2}+\frac{\kappa I'_{v_1}(\kappa)}{I_{v_1}(\kappa)}\right]I_{v_1}(\kappa)-H_1\left[\frac{\sigma_1}{2}+\frac{\kappa K'_{v_1}(\kappa)}{K_{v_1}(\kappa)}\right]K_{v_1}(\kappa)}$$

$$-\alpha\frac{(W_2-c)[K_{v_2}(\kappa)-H_2I_{v_2}(\kappa)]}{\left[\frac{\sigma_2}{2}+\frac{\kappa K'_{v_2}(\kappa)}{K_{v_2}(\kappa)}\right]K_{v_2}(\kappa)-H_2\left[\frac{\sigma_2}{2}+\frac{\kappa I'_{v_2}(\kappa)}{I_{v_2}(\kappa)}\right]I_{v_2}(\kappa)}=0\qquad(12)$$

Here

$$H_1=\frac{\left[\frac{\sigma_1}{2}+\frac{\kappa_1I'_{v_1}(\kappa_1)}{I_{v_1}(\kappa_1)}\right]I_{v_1}(\kappa_1)}{\left[\frac{\sigma_1}{2}+\frac{\kappa_1K'_{v_1}(\kappa_1)}{K_{v_1}(\kappa_1)}\right]K_{v_1}(\kappa_1)}$$

$$H_2=\frac{\left[\frac{\sigma_2}{2}+\frac{\kappa_2K'_{v_2}(\kappa_2)}{K_{v_2}(\kappa_2)}\right]K_{v_1}(\kappa_1)}{\left[\frac{\sigma_2}{2}+\frac{\kappa_2I'_{v_2}(\kappa_2)}{I_{v_2}(\kappa_2)}\right]I_{v_2}(\kappa_2)}$$

where $\alpha=\rho_2/\rho_1$, $\kappa=kR$, $\kappa_1=kR_1$, and $\kappa_2=kR_2$. The expression H_1 vanishes as $R_1\rightarrow0$ and so does H_2 as $R_2\rightarrow\infty$ to represent solutions for unbounded flows. Solving equation (12) for the wave velocity yields

$$c=\frac{E_1W_1-\alpha E_2W_2\pm(W_1-W_2)(\alpha E_1E_2)^{1/2}}{E_1-\alpha E_2}\qquad(13)$$

Here

$$E_1=\frac{[I_{v_1}(\kappa)-H_1K_{v_1}(\kappa)]}{\left[\frac{\sigma_1}{2}+\frac{\kappa I'_{v_1}(\kappa)}{I_{v_1}(\kappa)}\right]I_{v1}(\kappa)-H_1\left[\frac{\sigma_1}{2}+\frac{\kappa K'_{v_1}(\kappa)}{K_{v_1}(\kappa)}\right]K_{v_1}(\kappa)}$$

$$E_2=\frac{[K_{v_2}(\kappa)-H_2I_{v_2}(\kappa)]}{\left[\frac{\sigma_2}{2}+\frac{\kappa K'_{v_2}(\kappa)}{K_{v_2}(\kappa)}\right]K_{v_2}(\kappa)-H_2\left[\frac{\sigma_2}{2}+\frac{\kappa I'_{v_2}(\kappa)}{I_{v_2}(\kappa)}\right]I_{v_1}(\kappa)}$$

It can be shown that $E_1\geq0$ and $E_2\leq0$ for all the values of $\kappa_1\leq\kappa\leq\kappa_2$. Nonzero c_i is therefore expected for all modes except for very small or large density ratios. A liquid jet impinging into the atmosphere is of course stable for all modes even in the presence of the strong Kelvin-Helmholtz effects arising from the cylindrical vortex sheets. This stabilization phenomenon stems from the fact that instability condition (6) is violated by large density gradients even though DQ vanishes inside the flow field. One other interesting feature we like to point out is that all amplified waves marked by equation (13), in spite of the density variations, wave numbers and locations of the solid boundaries, lie exactly on the boundary described by equation (8b) with the stable solutions corresponding to $\alpha\rightarrow0$ and $\alpha\rightarrow\infty$ at both ends of the semi-circle. This exactness may be explained by examining integral (8*a*) for the flow under consideration. The velocity profile for the two-region flow can be written as

$$W=W_1+(W_2-W_1)H(r-R)\quad\text{for}\quad R_1\leq r\leq R_2\qquad(14)$$

where $H(r-R)$ is the Heaviside function. The quality of equation (8*b*) is obtained through the substitution of equation (14) for W in integral (8*a*). Note that the instability growth rate for fixed k first increases with increasing α, reaches a maximum at an intermediate value and then decreases with still larger α, with the maximum growth rate ($|W_2-W_1|/2$) governed by

$$\frac{I_{v_1}(\kappa)-H_1K_{v_1}(\kappa)}{\left[\frac{\sigma_1}{2}+\frac{\kappa I'_{v_1}(\kappa)}{I_{v_1}(\kappa)}\right]I_{v_1}(\kappa)-H_1\left[\frac{\sigma_1}{2}+\frac{\kappa K'_{v_1}(\kappa)}{K_{v_1}(\kappa)}\right]K_{v_1}(\kappa)}$$

$$+\alpha\frac{K_{v_2}(\kappa)-H_2I_{v_2}(\kappa)}{\left[\frac{\sigma_2}{2}+\frac{\kappa K'_{v_2}(\kappa)}{K_{v_2}(\kappa)}\right]K_{v_2}(\kappa)-H_2\left[\frac{\sigma_2}{2}+\frac{\kappa I'_{v_2}(\kappa)}{I_{v_2}(\kappa)}\right]I_{v_2}(\kappa)}=0.\qquad(15)$$

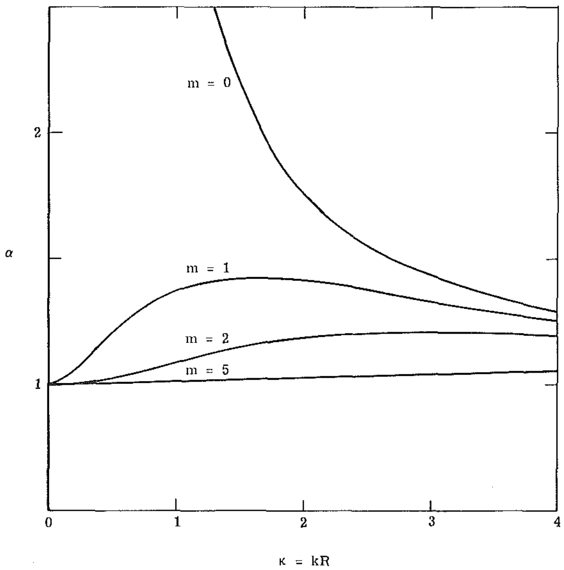

Fig. 2 Curves of maximum growth rates ($|W_2-W_1|/2$) for $\sigma_1=\sigma_2=0$

The special case of $\sigma_1 = \sigma_2 = 0$ in equation (15) for unbounded flows is plotted in Fig. 2 which shows the characteristic difference between the axisymmetric mode and the asymmetric ones.

The second example whose instability characteristics we wish to study for axisymmetric perturbations is a three-region flow with the profile given as:

$$\begin{aligned} W &= W_1 & \rho &= \rho_1 & & 0 \le r \le R_1 \\ W &= \frac{R_2^{2-\sigma} - r^{2-\sigma}}{R_2^{2-\sigma} - R_1^{2-\sigma}}\, W_1 + \frac{r^{2-\sigma} - R_1^{2-\sigma}}{R_2^{2-\sigma} - R_1^{2-\sigma}}\, W_2 & \rho &= \rho_2 \left(\frac{r}{R_2}\right)^{\sigma} & & R_1 \le r \le R_2 \quad (16) \\ W &= \mathrm{W}_2 & \rho &= \rho_3 & & R_2 \le r < \infty \end{aligned}$$

Here ρ_1, ρ_2, ρ_3, and σ are arbitrary constants. This profile can be used to model a jet exhausting into an environment of different density and velocity with the middle region representing the shear layer to allow transitions of the physical quantities of the jet to its surroundings. One can examine such flow instabilities by adjusting the parameters W_j, R_j, ρ_j, and σ. The perturbation radial velocities and pressures for the flow in the inner and outer regions can be reduced from equation (10) by setting $m = 0$ and $\sigma_j = 0$, while the solutions in the middle region are given by

$$u_2 = r^{\mu-1}[AI_\mu(kr) + BK_\mu(kr)]$$

$$p_2 = i\rho_2 \left(\frac{r}{R_2}\right)^{2(1-\mu)} r^{\mu-2} \frac{1}{k} \left\{ \frac{2\mu(W_2 - W_1)}{R_2^{2\mu} - R_1^{2\mu}}\, r^{2\mu}[AI_\mu(kr) + BK_\mu(kr)] \right.$$
$$\left. - \left[\frac{R_2^{2\mu} - r^{2\mu}}{R_2^{2\mu} - R_1^{2\mu}}\, W_1 + \frac{r^{2\mu} - R_1^{2\mu}}{R_2^{2\mu} - R_1^{2\mu}}\, W_2 - c\right] \left\{ A\left[\mu + \frac{krI_\mu'(kr)}{I_\mu(kr)}\right] I_\mu(kr) + \mathrm{B}\left[\mu + \frac{krK_\mu'(kr)}{K_\mu(kr)}\right] K_\mu(kr) \right\} \right\} \quad (17)$$

where $\mu = 1 - \sigma/2$. Applying the matching conditions (11) at both interfaces $r = R_1$ and $r = R_2$ gives the secular relation

$$\begin{vmatrix} \left[F_1(W_1 - c) + \dfrac{2\mu\delta^{2\mu}(W_2 - W_1)}{1 - \delta^{2\mu}}\right] I_\mu(\kappa_1) & \left[G_1(W_1 - c) + \dfrac{2\mu\delta^{2}(W_2 - W_1)}{1 - \delta^{2\mu}}\right] K_\mu(\kappa_1) \\ \left[F_2(W_2 - c) + \dfrac{2\mu(W_2 - W_1)}{1 - \delta^{2\mu}}\right] I_\mu(\kappa_2) & \left[G_2(W_2 - c) + \dfrac{2\mu(W_2 - W_1)}{1 - \delta^{2\mu}}\right] K_\mu(\kappa_2) \end{vmatrix} = 0 \quad (18)$$

where

$$F_1 = -\mu + \frac{\kappa_1 I_0(\kappa_1)}{\alpha_1 I_0'(\kappa_1)} - \frac{\kappa_1 I_\mu'(\kappa_1)}{I_\mu(\kappa_1)}$$

$$F_2 = -\mu + \frac{\kappa_2 K_0(\kappa_2)}{\alpha_2 K_0'(\kappa_2)} - \frac{\kappa_2 I_\mu'(\kappa_2)}{I_\mu(\kappa_2)}$$

$$G_1 = -\mu + \frac{\kappa_1 I_0(\kappa_1)}{\alpha_1 I_0'(\kappa_1)} - \frac{\kappa_1 K_\mu'(\kappa_1)}{K_\mu(\kappa_1)}$$

$$G_2 = -\mu + \frac{\kappa_2 K_0(\kappa_2)}{\alpha_2 K_0'(\kappa_2)} - \frac{\kappa_2 K_\mu'(\kappa_2)}{K_\mu(\kappa_2)}$$

$$\delta = \frac{R_1}{R_2},\ \alpha_1 = \frac{\rho_2}{\rho_1}\left(\frac{R_1}{R_2}\right)^{\sigma},\ \alpha_2 = \frac{\rho_2}{\rho_3}.$$

Rearranging determinant (18) by using the identity

$$I_\mu'(z)K_\mu(z) - I_\mu(z)K_\mu'(z) = \frac{1}{z},$$

one finds the solution for the wave velocity

$$c_r = \frac{W_1 + W_2}{2} + \frac{\mu(W_2 - W_1)}{1 - \delta^{2\mu}} \frac{(F_1 + G_2\delta^{2\mu})I_\mu(\kappa_1)K_\mu(\kappa_2) - (G_1 + F_2\delta^{2\mu})K_\mu(\kappa_1)I_\mu(\kappa_2)}{F_1G_2I_\mu(\kappa_1)K_\mu(\kappa_2) - G_1F_2K_\mu(\kappa_1)I_\mu(\kappa_2)} \quad (19a)$$

$$c_i = \frac{\mu(W_2 - W_1)}{1 - \delta^{2\mu}} \frac{\sqrt{\Delta}}{F_1G_2I_\mu(\kappa_1)K_\mu(\kappa_2) - G_1F_2K_\mu(\kappa_1)I_\mu(\kappa_2)} \quad (19b)$$

and

$$\Delta = 4\delta^{2\mu} - \left[\left(\frac{1 - \delta^{2\mu}}{2\mu} + \frac{1}{G_2} - \frac{\delta^{2\mu}}{F_1}\right) F_1G_2I_\mu(\kappa_1)K_\mu(\kappa_2) \right.$$
$$\left. - \left(\frac{1 - \delta^{2\mu}}{2\mu} + \frac{1}{F_2} - \frac{\delta^{2\mu}}{G_1}\right) G_1F_2K_\mu(\kappa_1)I_\mu(\kappa_2)\right]^2 \quad (19c)$$

Thus amplified waves exist whenever $\Delta > 0$. Equations (19) for the particular case $W_2 = 0$, $\rho_1 = \rho_2 = \rho_3$ and $\sigma = 0$ reduce to the result investigated earlier by Michalke and Schade (1963) in their study of shear flow instability in uniform fluids except that β^4 should be dropped from their equations (91) and (94). It should be pointed out that the complex wave speed in their limiting case as R_1 approaches R_2 appears to be incorrect. The solution for unbounded cylindrical vortex sheets should have been recovered if the proper limiting process had been taken. The flow in that limiting case was certainly unstable for all axial wave numbers with the real wave velocity approaching the velocity of the center of the jet as $k \to 0$. The limiting process as $R_1 \to R_2$ reduces equtions (19) to

$$c_r = \frac{W_1 + W_2}{2} + \frac{(W_1 - W_2)}{2} \frac{[I_0(\kappa)K_1(\kappa) - \alpha K_0(\kappa)I_1(\kappa)]}{[I_0(\kappa)K_1(\kappa) + \alpha K_0(\kappa)I_1(\kappa)]} \quad (20a)$$

$$c_i = \pm(W_1 - W_2) \frac{\sqrt{\alpha I_0(\kappa)K_0(\kappa)I_1(\kappa)K_1(\kappa)}}{I_0(\kappa)K_1(\kappa) + \alpha K_0(\kappa)I_1(\kappa)} \quad (20b)$$

with α representing the density ratio between the outer and inner regions. Equations (20) can of course be reduced from equation (13) for the special case of $\sigma_1 = \sigma_2 = 0$ and $m = 0$ for unbounded axisymmetric waves. It in fact can be shown that the general expression (19a) for c_r possesses a limiting value W_1 for long axial wavelengths. This acts as a support to Bat-

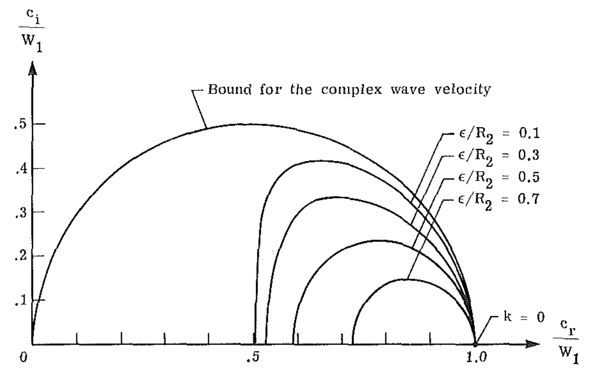

Fig. 3 Instability growth rate versus the shear layer thickness for the special case $\alpha_1 = \alpha_2 = \sigma = 1$ and $W_2 = 0$

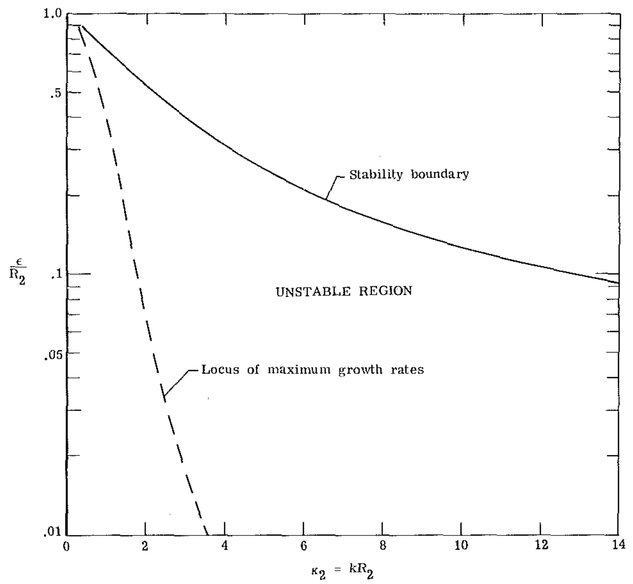

Fig. 4 Variations of the stability boundary and the maximum growth rates for the special case $\alpha_1 = \alpha_2 = \sigma = 1$ and $W_2 = 0$

chelor and Gill's finding that long waves with axisymmetry travel with the speed of the center of the jet. The corresponding instability discriminant reduced from (19*c*) takes the form

$$\Delta = -\frac{2}{\alpha_1 \alpha_2 \mu^2}[\alpha_1 \mu(1-\delta^{2\mu}) + (1-\delta^{2\mu})^2]\kappa_2^2 \log \kappa_2 > 0 \qquad (21)$$

Thus long waves are always unstable except for $k = 0$. For sufficiently large wave numbers, the asymptotic form of the modified Bessel functions reduces equation (19*c*) to

$$\Delta = -\left[\frac{G_1 F_2 + 2\mu(G_1 - F_2 \delta^{2\mu})}{1-\delta^{2\mu}}\right]^2 < 0 \qquad (22)$$

Therefore amplified waves cannot exist in their short wavelength range except for the limiting case $R_1 = R_2$ in which the maximum growth rates for uniform fluids occurs in the limit $k \to \infty$. These instability behaviors are plotted out in Figs. 3 and 4 for the special case of $\alpha_1 = \alpha_2 = \sigma = 1$ and $W_2 = 0$, with $\epsilon = R_2 - R_1$ representing the shear layer thickness. Both the velocity and density in this case vary linearly across the shear layer. Figure 3 shows the instability growth rates in comparison with the eigenvalue bound in their complex velocity domain. The amplified rate for fixed shear layer thickness ϵ first increases with increasing k, reaches a maximum value at an intermediate value of wave number, and decreases to zero at the relatively large value of k given by equation (19*c*) when the discriminant vanishes. These instability growth rates approach the semicircle bound as the shear layer thickness diminishes and the maximum growth rate $|W_2 - W_1|/2$ for cylindrical vortex sheets is reached when $\epsilon = 0$. Note that the complex wave velocity expands to the left portion inside the semicircle as the density ratio between the jet core and the surroundings decreases. For sufficiently small or large density ratios, the flow is stable against all disturbances. The neutral stability boundary and the maximum growth rates are shown in Fig. 4 as a function of the wave number and the shear layer thickness. The figure suggests that, for nonzero shear layer thickness, disturbances for which $\epsilon > 2/k$ are stable, and the maximum growth rate occurs when $k\epsilon$ is of the order of one-tenth. It is also shown through this particular flow configuration that amplified waves with axisymmetry may exist for some slowly varying profiles in the long axial wavelength range.

Concluding Remarks

The instability characteristics of axisymmetric jet flows in inhomogeneous fluids were discussed. The exact solutions to the governing stability equation confirm these characteristics; in particular, the semicircle theorem provides the best possible bound on all amplified waves of the top-hat type velocity profiles. The discharge of a jet into a stratified medium may produce some organized flow patterns which do not exist in a homogeneous environment. An understanding of the instability characteristics is of practical interest, because changing those characteristics of the flow can mean controlling the flow patterns, for example, produced by vehicles moving in the ocean.

References

Batchelor, G. K., and Gill, A. E., 1962, *Journal of Fluid Mechanics*, Vol. 14, p. 529.

Gill, A. E., 1962, *Journal of Fluid Mechanics*, Vol. 14, p. 567.

Mattingly, G. E., and Chang, C. C., 1974, *Journal of Fluid Mechanics*, Vol. 65, p. 541.

Michalke, A., and Schade, H., 1963, *Ingenieur-Archiv*, Vol. XXXIII, p. 1.

Reynolds, A. J., 1962, *Journal of Fluid Mechanics*, Vol. 14, p. 552.

Extension of the Circle Theorems by Surface Source Distribution

O. Rand
Faculty of Aerospace Engineering,
Technion—Israel Institute of Technology,
Haifa 32000, Israel

The paper presents a closed-form analytical solution for the source strength distribution along the circumference of a two-dimensional circular cylinder that is required for producing an arbitrary distribution of normal velocity. Being suitable to be used with flows having arbitrary vorticity distribution, the present formulation can be considered as an alternative and extensive form of the circle theorems. Using the conformal transformation technique, the formulation also serves as a closed-form solution of Laplace's equation in any two-dimensional flow domain that is reducible to the outer or inner region of a circular cylinder having arbitrary prescribed normal velocity over its boundary.

1 Introduction

The first and second circle theorems (see for example reference [1]) constitute well-known closed-form analytic procedures that enable the calculation of the flow disturbance resulting from the introduction of a circular cylinder to a given two-dimensional flow field.

The first circle theorem applies to incompressible, inviscid, and irrotational two-dimensional motion and assumes known complex potential in the absence of the circular cylinder, which is free from singularities in the region that should be occupied by the cylinder. The procedure is based on introducing an "image" singularity inside the circular boundary for each original singularity, such that the flow due to the singularity and its images together have the circle as a streamline. In a similar way, it is possible to introduce a circular around known singularities by additional image singularities outside the cylinder.

The second circle theorem applies to two-dimensional motion having constant vorticity distribution and is based on the ability to express the stream function of general two-dimensional flow with constant vorticity as a superposition of irrotational flow and a term that is proportional to the vorticity strength and keeps the circle as a streamline (see reference [1]).

The following derivation presents a closed-form explicit and exact solution for the source strength distribution over a circular cylinder that is required for obtaining a prescribed normal velocity distribution along its circumference. Thus, the present derivation constitutes an alternative formulation to the circle theorems. Its specific advantages will be discussed in what follows.

2 Theoretical Derivation

Following Green's second identity (see for example reference [2]), it is possible to show that any irrotational flow field can be associated by various types of surface distributions over its boundaries, one of which is a surface source distribution. Consequently, the disturbance due to the introduction of a boundary to an existing flow field can also be represented by distributing source singularities over the boundary surface and determining their strength by applying the nonpenetration condition at each point on the surface (Neumann problem). Using this procedure which is similar to the well-known panel methods, the solution of Laplace's equation is reduced to solving an integral equation for the source strength distribution over the boundary. Once the latter has been determined, the resulting flow field throughout the domain is easily obtained. Detailed description of the various two and three-dimensional panel methods along with the various involved numerical techniques can be found in reference [3].

The following formulation can be viewed as a closed-form panel method solution for a two-dimensional problem. The derivation is based on a special property of the circular cylinder that will be discussed first.

Consider a two-dimensional point source of a unit strength located on a circular cylinder circumference at the point S (Fig. 1). The induced velocity due to this source at a point P on the cylinder is given by:

$$V = \frac{1}{2\pi d} \tag{1}$$

Following the notation of Fig. 1, it is clear that

$$d = 2R\cos\theta \tag{2}$$

$$V_n = V\cos\theta \tag{3}$$

where R is the cylinder radius, d is the distance between S and P, and V_n is the component of V normal to the cylinder surface. θ is defined in Fig. 1. Substituting equations (1) and (2) into equation (3) yields:

$$V_n = \frac{1}{4\pi R} \tag{4}$$

Thus, *the normal induced velocity of any source on a circular cylinder is constant over all its circumference.* This result is valid as long as $\theta \neq \pm\pi/2$. For that case, which represents the self-induced velocities of a source element, a curved panel (of angle ϕ) having constant source distribution per unit length (k) is considered (Fig. 2). Careful integration of its influence

---

Contributed by the Fluids Engineering Division for publication in the JOURNAL OF FLUIDS ENGINEERING. Manuscript received by the Fluids Engineering Division April 4, 1988.

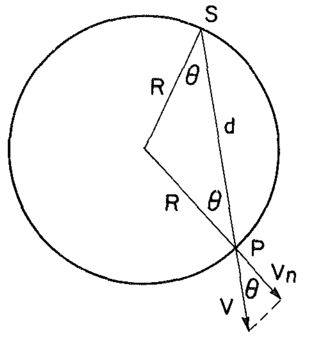

Fig. 1 The induced velocity of a source on a circular cylinder over other points along the circumference

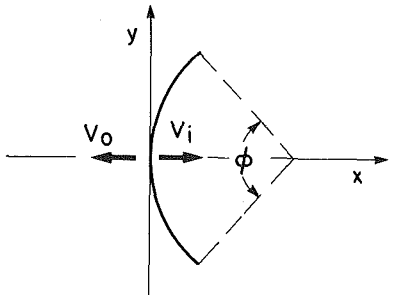

Fig. 2 Curved panel of constant source distribution

shows that the normal outward velocities for small values of x are:

$$V_0 = \frac{k}{2}\left(1 + \frac{\phi}{2\pi}\right) \quad (\text{for } x = -\epsilon^2,\ \epsilon \to 0) \tag{5}$$

$$V_i = \frac{k}{2}\left(1 - \frac{\phi}{2\pi}\right) \quad (\text{for } x = \epsilon^2,\ \epsilon \to 0) \tag{6}$$

In these equations the quantity $k\phi/4\pi$ represents the regular contribution already obtained by equation (4), while the quantity $k/2$ represents the well-known self-induced contribution. The latter is in fact the limit value of the outward velocity induced by a straight source line at a point which is infinitely close to it (see reference [4]). For the sake of convenience, two cases will be considered separately at this stage.

2.1 Case a: Flow Outside a Circular Cylinder. In this section, the circumferential source distribution ($k(\gamma)$) that is required for obtaining prescribed normal velocity distribution ($V_n(\gamma)$) outside a circular cylinder (see Fig. 3) is determined. Based on equations (4,5), the above requirement is satisfied by the following relation:

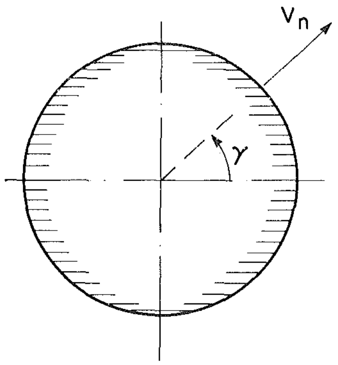

Fig. 3 Notation for flow outside a circular cylinder

$$V_n(\gamma) = \int_0^{2\pi} \frac{k(\gamma')}{4\pi}\, d\gamma' + \frac{k(\gamma)}{2} \tag{7}$$

Integrating equation (7) yields:

$$\int_0^{2\pi} V_n(\gamma)d\gamma = \int_0^{2\pi} k(\gamma)d\gamma \tag{8}$$

Substitution of equation (8) into equation (7) yields:

$$k(\gamma) = 2V_n(\gamma) - \frac{1}{2\pi}\int_0^{2\pi} V_n(\gamma')d\gamma' \tag{9}$$

Thus, equation (9) constitutes a closed-form expression for the desired source distribution.

Clearly, if equation (9) is used for determining the required source distribution for normal velocity distribution of zero mean value, the only remaining contribution is the self-induced one. For example, suppose that the circular cylinder of Fig. 3 is introduced to a uniform free-stream velocity U (flows from left to right). The normal velocity required for satisfying the nonpenetration condition is $V_n = -U\cos\gamma$, and according to equation (9) $k = -2U\cos\gamma$. The numerical solution of this elementary problem, using a panel method and solving a set of algebraic equations, can be found in reference [4].

2.2 Case b: Flow Inside a Circular Cylinder. Due to the difference between equation (5) and equation (6), equation (9) is not suitable if one wishes to prescribe the normal velocity $V_n(\gamma)$ over the inside surface of a circular cylinder circumference as shown in Fig. 4 (note that the positive direction of V_n is directed toward the cylinder center). Using equations (4,6) the appropriate condition in this case takes the form:

$$V_n(\gamma) = -\int_0^{2\pi} \frac{k(\gamma')}{4\pi}\, d\gamma' + \frac{k(\gamma)}{2} \tag{10}$$

Integrating equation (10) yields:

Nomenclature

d = distance between points on the circular cylinder (see Fig. 1)
f = conformal transformation function
i = $\sqrt{-1}$
k = source strength per unit length
l = the noncircular cylinder circumference
R = the circular cylinder radius
s = coordinate along the noncircular cylinder circumference
u_0, v_0 = velocities at z_0
V = source induced velocity
V_n = the normal components of the velocity of over the cylinder surface
V_i, V_0 = surface normal velocities defined by Fig. 2
x, y = coordinate normal and tangent to the curved panel, respectively (see Fig. 2)
z = complex coordinate in the plane in which the noncircular cylinder is given
γ = angle defined in Figs. 3 and 4
ζ = complex coordinate in the plane to which the noncircular cylinder is transformed as a unit circle
θ = angle defined in Fig. 1
ϕ = curved panel angle (see Fig. 2)
$(\ )_0$ = values associated with the point z_0
$(\ )_{(\gamma)}$ = values associated with the point $z = f(e^{i\gamma})$

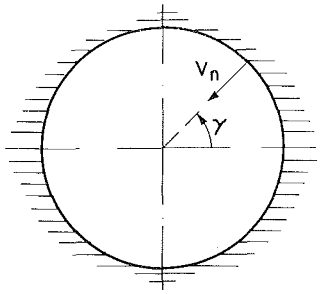

Fig. 4 Notation for flow inside a circular cylinder

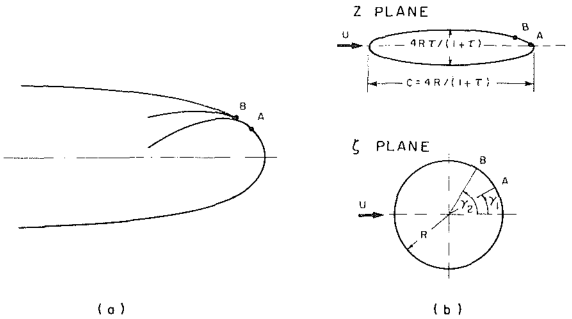

Fig. 6 Circulation control airfoil (section 4.2): (*a*) training edge geometry; (*b*) notation

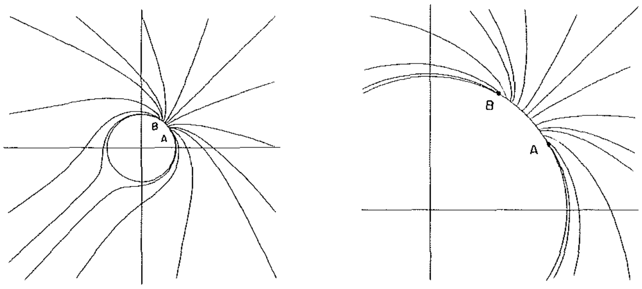

Fig. 5 Flow field around a circular cylinder having prescribed normal velocity (section 4.1)

$$\int_0^{2\pi} V_n(\gamma)d\gamma=0 \tag{11}$$

which implies that the total source strength in a closed two-dimensional domain should vanish. However, the value of the integral term in equation (10) remains arbitrary. Consequently, equation (10) is reduced to:

$$k(\gamma)=2V_n(\gamma)+\bar{k} \tag{12}$$

where $\bar{k}$ is arbitrary (in contrast with equation (9)). Different values of $\bar{k}$ will cause no change in the inner flow field (but will cause of course additional flow from the cylinder surface to the outer region or vice versa).

It should be noted that a similar derivation can be carried out by replacing the source distribution by vortices distribution and the normal velocity by tangential velocity. Such formulation is suitable for cases where the potential derivative in the tangential direction is prescribed. However, cases of prescribed normal velocity seem to be much more useful.

3 Noncircular Cylinder

The application of the present formulation to noncircular cylinders using the conformal transformation technique is discussed in this section.

Consider a flow domain in the z plane which has known transformation function $z=f(\zeta)$ to the inside or outside region of a circular cylinder of unit radius in the ζ plane. In addition, it is desired to determine the surface source distribution that will produce a known distribution of velocity component, V_n, normal to the domain boundary. Since relative angles are not changed by the conformed transformation, the normal velocity components in the ζ plane are $V_n\,|dz/d\zeta|$. Consequently, it is possible to determine the surface source distribution in the ζ plane (equations 9,12). The velocity components (u_0,v_0) at the point $z_0=f(\zeta_0)$ are therefore:

$$u_0-iv_0=\frac{1}{(dz/d\zeta)_0}\,\frac{1}{2\pi}\int_0^{2\pi}\frac{2V_n(\gamma)\left|\frac{dz}{d\zeta}(\gamma)\right|-k_a}{\zeta_0-e^{i\gamma}}\,d\gamma \tag{13}$$

where $(\ )_0$ represents values of the point z_0, $V_n(\gamma)$ is the normal velocity at the boundary points $z=f(e^{i\gamma})$ and $(dz/d\zeta)\,(\gamma)$ is the values of $dz/d\zeta$ at these points. In the case of a flow outside a closed domain, k_a is the averaged normal velocity in the ζ plane, namely:

$$k_a=\frac{1}{2\pi}\int_0^{2\pi}V_n(\gamma)\left|\frac{dz}{d\zeta}(\gamma)\right|$$
$$=\frac{1}{2\pi R}\,d\gamma\oint_l V_n(s)ds \tag{14}$$

In the case of a flow inside a closed domain $-k_a$ is arbitrary.

Note that in light of the ability to transform any noncircular cylinder in the z plane to a circular cylinder in the ζ plane, equations (9), (12) constitute a general closed-form solution of Laplace equation with Neumann boundary conditions.

4 Illustrative Applications

4.1 Blowing From a Circular Cylinder Surface. A simple application of the present formulation is given in this section. In this example equation (9) is used to find the source distribution based on the requirement that the normal (outward) velocity around a circular cylinder will vanish except for the interval 30 deg $<\gamma<$ 60 deg where the normal velocity is unit. Equation (9) shows that this flow is created by a source distribution of strength 23/12 for 30 deg $<\gamma<$ 60 deg and $-1/12$ elsewhere. The associated streamlines are shown in Fig. 5 where the interval of nonvanishing normal velocity is denoted by A-B.

4.2 Circulation-Control Airfoil. The next example deals with circulation-control airfoil. This kind of airfoil has a blunt trailing edge (usually elliptic contour). An air jet is issuing from a slot on the upper surface near the trailing edge. It is then possible to control the circulation around the airfoil by changing the blowing intensity, and to delay separation by energizing the boundary layer. The trailing edge geometry of elliptic circulation control airfoil is shown in Fig. 6(*a*). The ability to obtain high lift coefficients and to control it without changing the geometric angle of attack, makes the circulation control airfoil very attractive to both rotorcraft and fixed wing applications.

In the following example, an elliptic airfoil of chord C and thickness ratio τ subjected to a free-stream velocity U at zero angle of attack (see Fig. 6(*b*)) is discussed. The airfoil is placed in the z complex plane into which it is transformed from a circle radius R in the ζ plane (see Fig. 6(*b*)) by the conformal transformation:

$$z=\zeta+\frac{1-\tau}{1+\tau}\cdot\frac{R^2}{\zeta} \tag{15}$$

Blowing occurs between points A and B (determined by the angles γ_1 and γ_2 in the ζ plane) and is assumed to be given in the ζ plane by:

$$\begin{cases} \tilde{V}_n = \tilde{W} \sin\left(\dfrac{\gamma-\gamma_1}{\gamma_2-\gamma_1} \bullet \pi\right) & (\gamma_1 < \gamma < \gamma_2) \\ \tilde{V}_n = 0 & (\gamma < \gamma_1, \gamma > \gamma_2) \end{cases} \tag{16}$$

where W determines the blowing intensity and ($\tilde{}$) represents nondimensional values with respect to the free-stream velocity. According to equation (9), the above-mentioned normal velocity can be obtained by the following source distribution per unit length:

$$\begin{cases} \tilde{k} = 2\tilde{W} \sin\left(\dfrac{\gamma-\gamma_1}{\gamma_2-\gamma_1} \bullet \pi\right) - \tilde{W}\dfrac{\gamma_2-\gamma_1}{\pi^2} & (\gamma_1 < \gamma < \gamma_2) \\ \tilde{k} = -\tilde{W}\dfrac{\gamma_2-\gamma_1}{\pi^2} & (\gamma < \gamma_1, \gamma > \gamma_2) \end{cases} \tag{17}$$

In order to simulate tangential blowing as imposed by the geometric structure of the blowing slot (see Fig. 6(*a*)), a stagnation point should be forced at the upper end of the blowing slot (point B). This would give an approximation to the circulation associated with the specific blowing intensity. Since the normal velocity vanishes at that point, one must insure that, the tangential velocity vanishes as well. The tangential velocity induced by the blowing is determined by integrating the sources influence along the entire circular cylinder:

$$\tilde{V}_T(\gamma_2) = \frac{1}{4\pi}\int_0^{2\pi} \tilde{k}(\gamma) tg\left(\frac{\pi-\gamma+\gamma_2}{2}\right) d\gamma \tag{18}$$

Substituting equations (17) in equation (18) and taking advantage of the fact that constant source distribution does not contribute to the tangential velocity along the contour, equation (18) is reduced to:

$$V_T(\gamma_2) = \tilde{W} I_1 \tag{19a}$$

$$I_1 = \frac{1}{2\pi}\int_{\gamma_1}^{\gamma_2} \sin\left(\frac{\gamma-\gamma_1}{\gamma_2-\gamma_1}\pi\right) tg\left(\frac{\pi-\gamma+\gamma_2}{2}\right) d\gamma \tag{19b}$$

Consequently, the required circulation is given by:

$$\frac{\Gamma}{2\pi UR} = -\tilde{W} I_1 \tag{20}$$

and the corresponding lift coefficient is:

$$C_L \equiv \frac{\rho U\Gamma}{\dfrac{1}{2}\rho U^2 C} = -\tilde{W}\pi(1+\tau)I_1 \tag{21}$$

Equation (21) gives the desired expression for the lift coefficient as a function of the blowing velocity. However, in order to compare it with experimental results, it should be formulated as a function of the blowing momentum which can be directly measured. Clearly, the normal velocity distribution in the z plan is $V_n / |dz/d\zeta|$ and therefore the blowing momentum is given by:

$$J \equiv \rho \int_A^B \frac{V_n^2}{|dz/d\zeta|^2} d\zeta = \rho R \int_{\gamma_1}^{\gamma_2} \frac{V_n^2}{|dz/d\zeta|} d\gamma \tag{22}$$

Thus, the blowing momentum coefficient is:

$$C_\mu \equiv \frac{J}{\dfrac{1}{2}\rho U^2 C} = \frac{1+\tau}{2}\tilde{W}^2 I_2 \tag{23a}$$

$$I_2 = \int_{\gamma_1}^{\gamma_2} \frac{\sin^2\left(\dfrac{\gamma-\gamma_1}{\gamma_2-\gamma_1}\pi\right)}{|dz/d\zeta|} d\gamma \tag{23b}$$

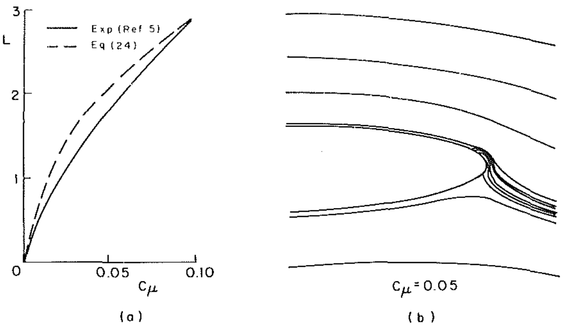

Fig. 7 Circulation control airfoil (section 4.2 $\tau = 0.2$, $\gamma_1 = 15°$, $\gamma_2 = 22°$): (*a*) Lift coefficient versus blowing coefficient; (*b*) streamlines around the trailing edge

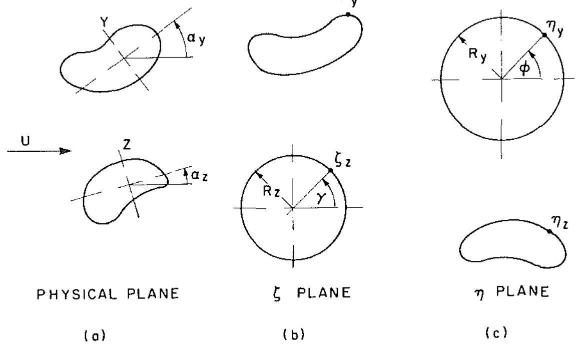

Fig. 8 Nonpenetration problem notation (section 4.3): (*a*) Physical plane; (*b*) ζ plane; (*c*) η plane

Substituting $\tilde{W}$ from equation (23*a*) into equations (21) enables us to write:

$$C_L = -\pi I_1 \sqrt{\frac{2(1+\tau)}{I_2}} \sqrt{C_\mu} \tag{24}$$

The above relation is shown in Fig. 7(*a*) and compared with measurements carried out for low values of C_μ and reported in reference [5]. The corresponding flow field for $C_\mu = 0.05$ is shown in Fig. 7(*b*).

The above example shows the ability of the present formulation to provide a simple analytical solution for the potential flow around an arbitrary cylinder. In the specific case, the solution can provide analytical approximation to the influence of certain parameters of the problem and a basis for more elaborate exploration of the boundary layer and wake effects.

4.3 Nonpenetration Problems. The purpose of the following example is to demonstrate the application of the present formulation for solutoin of flow fields with one or more surfaces where the nonpenetration condition should be applied. For the sake of simplicity, a flow field with two closed surfaces (bodies) subjected to a uniform free-stream velocity U is considered. Figure 8(*a*) shows the problem geometry with two local complex planes Y and Z. It is assumed that the function $Z(\zeta)$ that transforms the Z body to a circle of radius R_z in the ζ plane and the function $Y(\eta)$ that transforms the Y body to a circle of radius R_y in the η plane are known. Thus, the problem is concentrated on finding the source per unit length $k_z(\gamma)$ and $k_y(\phi)$ that should be distributed along the circle's circumference (in the ζ and η planes, respectively), that will assure, together with the free-stream velocity, the nonpenetration condition along the bodies' boundaries. The normal velocity induced by the free-stream velocity and the k_z sources over the Y body's surface in the η plan is:

$$V_{y(\phi)} = R_z \int_0^{2\pi} k_{z(\gamma)} W_{(\gamma,\phi)} d\gamma + U_{y(\phi)} \tag{25a}$$

Similarly, the normal velocity over the Z body is:

$$V_{z(\gamma)} = R_y \int_0^{2\pi} k_{y(\phi)} V_{(\phi,\gamma)} d\phi + U_{z(\gamma)} \tag{25b}$$

where $W_{(\gamma,\phi)}$ and $V_{(\phi,\gamma)}$ are influence functions given by:

$$W_{(\gamma,\phi)} = \text{Real}\left[\frac{e^{(\alpha_y - \alpha_z)}}{2\pi(\zeta_y - \zeta_z)} \, \frac{\left(\dfrac{dY}{d\eta}\right)_{\eta_y}}{\left(\dfrac{dz}{d\zeta}\right)_{\zeta_y}} \, \frac{\eta_y}{R_y} \right] \tag{26a}$$

$$V_{(\phi,\gamma)} = \text{Real}\left[\frac{e^{(\alpha_z - \alpha_y)}}{2\pi(\eta_z - \eta_y)} \, \frac{\left(\dfrac{dz}{d\zeta}\right)_{\zeta_z}}{\left(\dfrac{dY}{d\eta}\right)_{\eta_z}} \, \frac{\zeta_z}{R_z} \right] \tag{26b}$$

and $U_{y(\phi)}$, $U_{z(\gamma)}$ are the free-stream velocity (normal) components. In these equations, ζ_z is a point on the circle in the ζ plane and η_z is its image in the η plane while η_y is a point on the circle in the η plane and ζ_y is its image in the ζ plane (see Figs. 8(*b,c*)). The reader may verify that singular points of the transformations cause no difficulties in calculating W and V.

Now, according to equation (9), the source distribution required to satisfy the nonpenetration condition is equal to minus twice the normal velocity (the averaged normal velocity is zero since a closed body is represented by zero net sources strength), and therefore:

$$k_{y(\phi)} = -2R_z \int_0^{2\pi} k_{z(\gamma)} W_{(\gamma,\phi)} d\gamma - 2U_{y(\phi)} \tag{27a}$$

$$k_{z(\gamma)} = -2R_y \int_0^{2\pi} k_{y(\phi)} V_{(\phi,\gamma)} d\gamma - 2U_{z(\gamma)} \tag{27b}$$

Note that if only one of the bodies exists, its source distribution is directly obtained with no further derivation. However, substituting equation (27*a*) into equation (27*b*) enables one to write:

$$k_{z(\gamma)} = \int_0^{2\pi} k_{z(\gamma')} P_{(\gamma'\gamma)} d\gamma' + Q_{(\gamma)} \tag{28}$$

where:

$$P_{(\gamma'\gamma)} = 4\, R_y R_z \int_0^{2\pi} W_{(\gamma',\phi)} \cdot V_{(\phi,\gamma)} d\phi \tag{29}$$

$$Q_{(\gamma)} = 4\, R_y \int_0^{2\pi} U_{y(\phi)} V_{(\phi,\gamma)} d\phi - 2U_{z(\gamma)} \tag{30}$$

By resubstituting equation (28) in itself it is possible to express k_z by the following series:

$$k_{z(\gamma)} = k_{1(\gamma)} + k_{2(\gamma)} + \;.\;.\;.\;.\;. \tag{31}$$

where:

$$k_{1(\gamma)} = Q_{(\gamma)} \tag{32a}$$

$$k_{i+1(\gamma)} = \int_0^{2\pi} k_{i(\gamma')} P_{(\gamma',\gamma)} d\gamma' \quad (i = 1,2,3,\ldots) \tag{32b}$$

Unless the bodies are extremely close, only two terms are needed in equation (31). At this stage two important facts should be noted. First, although the flow field contains two bodies, equation (28) is an equation for k_z only (after the calculation of which k_y can be directly obtained from equation (27*a*)). Secondly, although it has similar structure, equation (28) is different from the kind of equations obtained in the standard panel method schemes. The difference is essentially the regular nature of the influence function $P_{(\gamma',\gamma)}$ which has a finite and regular value for any combination of γ' and γ. This characteristic is due to the fact that $P_{(\gamma',\gamma)}$ is a result of influence functions of sources of one body on the other body's surface (see equation (29)), in contrast with the standard panelling schemes where the influence functions also includes the influence of sources on points of their own surface. Consequently, infinite discretization of k_z is possible and equation (31) provides a straightforward solution which contains no matrix inversion. The extension of the present formulation for multi-bodies' flow fields is clear.

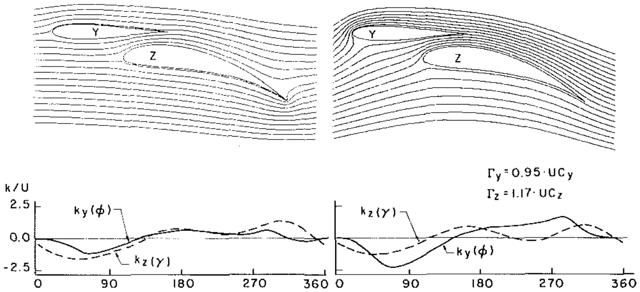

Fig. 9 Two airfoils interaction (section 4.3): (*a*) Sources only; (*b*) Sources and circulations

An example of a flow field which was calculated according to the above mentioned procedure is shown in Fig. 9(*a*), where the interaction of two airfoils is simulated. In Fig. 9(*b*) circulations were added to each one of the bodies to satisfy the conditions at the trailing edges. The resulted source distributions are also shown.

5 Conclusions

Closed-form explicit analytical expressions for the surface source distribution required for obtaining a prescribed normal velocity distribution over a two-dimensional circular cylinder were derived. The formulation can be considered as an alternative as well as an extension of the circle theorems. The main features of the present formulation are:

(*a*) The potential flow (source distribution) velocity components which are determined by the present derivation can be superposed on existing flow field velocity components in order to match certain boundary conditions. Thus, the latter field may include general distribution of vorticity.

(*b*) Unlike the circle theorems, the present formulation contains no restriction of having no singularities inside the cylinder (in the case of outer flow - see section 2.1) or outside the cylinder (in the case of inner flow - see section 2.2).

(*c*) The existence of singularities at the circular cylinder center or its immediate vicinity (for the case of inner flow), is somewhat problematic if one wishes to use the circle theorems, since it requires the location of the image singularities at very large (or infinite) distances. The present formulation contains no similar constraint.

Finally, the present derivation constitutes a closed-form solution of Laplace equation with Neumann boundary conditions in any domain (provided that it can be transformed to the inside or outside of a circular cylinder) having arbitrary prescribed normal velocity.

References

1 Milane-Thomson, L. M., *Theoretical Aerodynamics*, MacMillan & Co. Ltd., London, 1968.

2 Lamb, L., *Hydrodynamics*, Dover Publications, New York, 1945.

3 Hess, J. L., "Review of Integral-Equation Techniques for Solving Potential Flow Problems with Emphasis on the Surface-Source Method," *Computer Methods in Applied Mechanics and Engineering*, Vol. 5, 1975, pp. 145-196.

4 Bertin, J. J., and Smith, M. L., *Aerodynamics for Engineers*, Prentice-Hall, Inc., New Jersey, 1979, pp. 63-68.

5 Kind, R. J., and Maull, D., "An Experimental Investigation of a Low-Speed Circulation Controlled Airfoil," *Aeronautical Quarterly*, Vol. 19, May 1968, pp. 170-182.

W. P. Jones
Reader.

A. Pascau
Research Student.

Department of Chemical Engineering
and Chemical Technology,
Imperial College,
London SW7 2AZ, England

Calculation of Confined Swirling Flows With a Second Moment Closure

A Reynolds stress transport equation model and the $k-\epsilon$ *turbulence model have been applied to the calculation of a confined, strongly swirling flow. A comparison of the results with measurement shows clearly the superiority of the transport equation model. It reproduces the major features of the flow including the strong stabilizing effects of the swirl on the shear stresses and the calculated axial and circumferential components of mean velocity are in reasonable agreement with measured profiles. The corresponding normal stresses are, however, overpredicted but previously suggested modifications to the* ϵ*-equation to account for rotation did not bring any improvement. The* $k-\epsilon$ *model does not contain any mechanism to describe the stabilizing effects of swirling motion and as a consequence it performs poorly; large discrepancies exist between the measured and calculated mean velocity field.*

Introduction

Swirling flows [1] form a constituent part of many types of combustion system and, for example in gas turbine combustors, swirl is often used as a means of providing an aerodynamic blockage which aids in stabilizing the flame and creates a region of strong shear where fuel and air intimately mix. As a consequence, swirl is likely to exert a significant influence on combustion efficiency, the temperature pattern at the combustor exit and the emission levels of any combustion generated pollutants. The ability to predict the properties of confined swirling flows is therefore of some importance and a model for achieving this would form an essential component of a calculation method for predicting the performance of practical combustion systems. The problems of devising a prediction method for turbulent reacting swirling flows can perhaps best be approached by considering first the isothermal case so that attention can be focused on the modelling of turbulent transport. Providing an adequate model can be devised, then it should form the basis for reacting flow applications for which, in addition, a combustion model is required. An ability to accurately calculate the properties of isothermal swirling flows is obviously, however, a necessary prerequisite for a successful application to the reacting case. So far, only eddy viscosity models of turbulence appear to have been used in simulating the mixing of confined swirling jets; an excellent review is given in reference [12]. This extensive computational work [2–12] has highlighted various shortcomings of such models, prominent amongst which are the poor prediction of the size and strength of the recirculation zone in strong-swirling flows [3, 5, 10, 12] and the inability of two-equation $k-\epsilon$ type models to predict the observed combined forced-free vortex motion [2, 3, 12]. The poor predictive capability of the $k-\epsilon$ model in these cases is likely to be due in part to the scalar eddy viscosity hypothesis and Lilley and Chigier [14] have shown that the eddy viscosity is, in fact, highly anisotropic in swirling flows. Ad hoc modifications to the $k-\epsilon$ model to account for this anisotropy have generally resulted in much improvement in the accuracy of predictions [15, 16], although they are of necessity not of general applicability. Further attempts to improve the accuracy of the predictions, through the use of multiple scale models [13] or algebraic Reynolds stress models [11] appear not to have led to any significant improvement.

One obvious choice of method for overcoming some of the limitations inherent in the $k-\epsilon$ and eddy viscosity models is provided by Reynolds stress transport (RST) equation turbulence models in which the components of the stress are obtained from solution of their respective, modelled partial differential conservation equations. In this context, it is to be noted that algebraic stress models, which have been used with considerable success in thin shear layers, do not provide unique solutions [3, 6] in flows involving complex strain fields and are thus not, in general, suitable alternatives. So far only a small number of applications of RST turbulence models to swirling flows have been reported and the majority of these have been concerned with free swirling jets [17, 18] in which some problems have been identified. An assessment of the performance of transport equation models in confined swirling flows is thus needed.

The present paper is concerned with the prediction of the experiment of So, Ahmed, and Mongia [19], in which a central jet of 8.7 mm and an annular swirling jet issue into a chamber of I.D. 125 mm in which they then mix. The swirling motion is created by a 15-blade swirler with a 60-degree vane angle, giving a ratio between the angular and axial velocities of 2.25. Two reasons contributed to the selection of this experiment as a test case:

Contributed by the Fluids Engineering Division for publication in the JOURNAL OF FLUIDS ENGINEERING. Manuscript received by the Fluids Engineering Division May 13, 1987.

1 The measurements show that the circumferential velocity profiles correspond to a combined forced/free vortex flow and it is known in these circumstances that $k-\epsilon$ model predictions tend too rapidly towards a solid body rotation. Reynolds stress transport equation models appear to offer a means of overcoming this deficiency and the flow provides a means of establishing whether or not this is so.

2 The flow is one where stability forces exerted a strong influence on the turbulence structure. The Rayleigh criterion for stability $(\partial/\partial r(\rho W^2 r^2)>0)$ is satisfied over 80 percent of the radius and this feature conditions the flow development. The capacity of a Reynolds stress transport model to mimic the effect of stabilization on the flow can then be assessed. It is important to note here that the standard $k-\epsilon$ model contains no mechanism to account for the stabilizing effect of the swirling motion.

Mathematical Predictions

The analysis in this paper is based upon the solution of the ensemble-averaged Navier-Stokes equations using either the $k-\epsilon$ model or the RST model. For solution the equations were written in cylindrical polar coordinates in a form appropriate to axisymmetric flows but, for reasons of brevity, are given below in cartesian tensor form.

Governing Equations. The ensemble-averaged Navier-Stokes equations for an incompressible flow are:

Continuity

$$\frac{\partial U_j}{\partial x_j}=0 \tag{1}$$

Momentum

$$\frac{\partial U_i}{\partial t}+\frac{\partial U_i U_j}{\partial x_j}=-\frac{1}{\rho}\frac{\partial P}{\partial x_i}+\frac{\partial}{\partial x_j}(\tau_{ij}-\overline{u_i u_j}) \tag{2}$$

where

$$\tau_{ij}=\nu\left(\frac{\partial U_i}{\partial x_j}+\frac{\partial U_j}{\partial x_i}\right)$$

$k-\epsilon$ Model. In the $k-\epsilon$ model the Reynolds stresses are linearly related to the mean rate of strain by a scalar eddy viscosity

$$-\overline{u_i u_j}=\frac{-2}{3}\delta_{ij}k+\nu_t\left(\frac{\partial U_i}{\partial x_j}+\frac{\partial U_j}{\partial x_i}\right) \tag{3}$$

where $k=\overline{u_i u_i}/2$ is the turbulent kinetic energy, $\nu_t=C_\mu(k^2/\epsilon)$ is the turbulent eddy viscosity and ϵ is the dissipation rate of turbulence kinetic energy.

k and ϵ are obtained from their modelled transport equations

$$\frac{dk}{dt}=\frac{\partial}{\partial x_i}\left(\frac{\nu_t}{\sigma_k}\frac{\partial k}{\partial x_i}\right)+P-\epsilon \tag{4a}$$

$$\frac{d\epsilon}{dt}=\frac{\partial}{\partial x_j}\left(\frac{\nu_t}{\sigma_\epsilon}\frac{\partial \epsilon}{\partial x_j}\right)+\frac{\epsilon}{k}(C_{\epsilon_1}P-C_{\epsilon_2}\epsilon) \tag{4b}$$

where

$$P=\nu_t\frac{\partial U_i}{\partial x_j}\left(\frac{\partial U_i}{\partial x_j}+\frac{\partial U_j}{\partial x_i}\right)$$

The values of the constants used in this model are given in Table 1.

Table 1

C_μ	σ_k	σ_ϵ	C_{ϵ_1}	C_{ϵ_2}
0.09	1.	1.3	1.44	1.92

Reynolds Stress Transport Equation Model. The modelled Reynolds stress transport equation used in this paper is written as [20]

$$\frac{d\overline{u_i u_j}}{dt}+\overline{u_i u_l}\frac{\partial U_j}{\partial x_l}+\overline{u_j u_l}\frac{\partial U_i}{\partial x_l}=\frac{\partial}{\partial x_l}\left(C_s\frac{k}{\epsilon}\overline{u_l u_m}\frac{\partial \overline{u_i u_j}}{\partial x_m}\right)+A_{ij}-\frac{2}{3}\delta_{ij}\epsilon \tag{5}$$

where A_{ij}, the pressure-strain term, is given by

$$\begin{aligned}A_{ij}=&-C_1\frac{\epsilon}{k}\left(\overline{u_i u_j}-\frac{2}{3}\delta_{ij}k\right)+C_2\delta_{ij}\overline{u_l u_m}\frac{\partial U_l}{\partial x_m}\\&+C_3\left(\overline{u_l u_j}\frac{\partial U_i}{\partial x_l}+\overline{u_l u_i}\frac{\partial U_j}{\partial x_l}\right)+C_4 k\left(\frac{\partial U_i}{\partial x_j}+\frac{\partial U_j}{\partial x_i}\right)\\&-\left(\frac{3}{2}C_2+C_3\right)\left(\overline{u_l u_j}\frac{\partial U_l}{\partial x_i}+\overline{u_l u_i}\frac{\partial U_l}{\partial x_j}\right)\end{aligned} \tag{6}$$

The ϵ equation adopted is [20]

$$\frac{d\epsilon}{dt}=\frac{\partial}{\partial x_l}\left(C_\epsilon\frac{k}{\epsilon}\overline{u_l u_m}\frac{\partial \epsilon}{\partial x_m}\right)-C_{\epsilon_1}\frac{\epsilon}{k}\overline{u_l u_m}\frac{\partial U_l}{\partial x_m}-C_{\epsilon_2}\frac{\epsilon^2}{k} \tag{7}$$

The values of the constants used in this model are given in Table 2.

Table 2

C_s	C_1	C_2	C_3	C_4	C_ϵ	C_{ϵ_1}	C_{ϵ_2}
0.22	1.5	−0.53	0.67	−0.12	0.18	1.4	1.9

Nomenclature

A_{ij} = modelled pressure-strain tensor

D = diameter of the test duct

D_j = jet diameter

k = ½$(\bar{u}^2+\bar{v}^2+\bar{w}^2)$; turbulent kinetic energy

R = radius of duct

R_i = inner radius of swirler

u,v,w = fluctuating velocity components

$\bar{u}v$ = shear status

$\bar{u}^2,\bar{v}^2,\bar{w}^2$ = normal stresses

$\overline{u_i u_j}$ = Reynolds stress tensor

U,V,W = mean velocity components

U_0 = mean area averaged velocity

δ_{ij} = Kronecker delta

$|\Omega|$ = rotation rate

ϵ = dissipation rate

The Influence of Rotation. Previous experience in the use of the $k-\epsilon$ model in the prediction of swirling flows has made evident the need to include modifications to account for the effect of rotation on the turbulence. It is generally accepted [24], at least in flows without mean strain, that rotating motion inhibits the transfer of energy from the large to the small scales where it is dissipated via the action of the molecular viscosity. This being true, the dissipation rate equation should contain some explicit dependence on swirl level in a manner so as to reduce the dissipation rate as swirl is increased. For thin shear layers a simple and effective way of accomplishing this is that adopted by Launder et al. [22] and Rodi [23], in which a coefficient in the ϵ equation is made a function of an appropriate Richardson number. However a major drawback of this approach for recirculating flows is that the Richardson number is not invariant under rotation of the coordinate system and hence the approach is invalid for flows in which the boundary layer approximation is not appropriate.

In addition the use of an eddy viscosity implies that the principal axes of $\overline{u_i u_j}$ and the mean strain are aligned. This is hardly ever satisfied in any turbulent flow but in simple shear flows with a single nonzero component of the mean rate of strain, has little consequence beyond an incorrect prediction of the normal stresses. However, in flows with complex mean strain fields the consequences are often severe; in strongly swirling flows appreciable errors in the predicted mean velocity field can result. For example Kobayashi and Yoda [15] show that the values of eddy viscosity calculated from their measured values of shear stress and mean strain rate differ by up to two orders of magnitude depending upon which components were used.

A Reynolds stress transport equation turbulence model, such as the one used here, clearly provides a natural method of overcoming the latter limitation of scalar eddy viscosity models without need for any modifications. However, for the influence of rotation on energy transfer the modifications suggested by the numerical simulations of Bardina, Ferziger, and Rogallo [24] (hereafter BFR) and the LES computations of Aupoix, Cousteix, and Liandrat [25] (hereafter ACL) of rotating, quasi-isotropic turbulence in the absence of mean strain have been investigated. An additional term

$$-C_{\epsilon_3}\,|\Omega|\,\epsilon \tag{8}$$

is introduced into the ϵ-equation. C_{ϵ_3} is in general a function of the dimensionless rotation rate, $|\Omega|k/\epsilon$, where the rotation rate is defined as:

$$|\Omega| = \left(\frac{\Omega_{ij}\ \Omega_{ij}}{2}\right)^{1/2}$$

with

$$\Omega_{ij} = \frac{1}{2}\left(\frac{\partial U_i}{\partial x_j} - \frac{\partial U_j}{\partial x_i}\right) \tag{9}$$

The two different models used are the BFR model in which $C_3 = 0.15$ and that of ACL where C_{ϵ_3} is a function, given in graphical form, of $|\Omega|k/\epsilon$.

In order to ensure that the resulting model is consistent with local equilibrium flow measurements, modification to the constant C_{ϵ_1} is also necessary; for both models the value required was $C_{\epsilon_1} = 1.65$.

Numerical Procedure. The computations were performed using the computer program described in reference [25]. A staggered grid was used, in which U and V velocities were stored midway between grid nodes. For the Reynolds stress calculation, the volumes used for $\overline{uw}$ and $\overline{vw}$ were the same as those for U and V and $\overline{uv}$ was stored in the middle of the control volume with surfaces corresponding to the grid lines. The procedure utilizes a conservative, linearized discretization in which hybrid differencing is used for the convective terms, though, in practice, for the RST model computation this reduces effectively to upwind differences. The time dependent forms of the equations are solved and steady-state solution are obtained by integrating forward in time until steady conditions prevail. The updating of the velocities at every time step to satisfy continuity is described in Marquis [27] and no special stabilization procedures such as described by Huang et al. [28] were needed. The solution domain corresponded to the region between the first measuring station at $x/D = 0.07$, and the exit plane at $x/D = 2.8$. The estimation of inlet profiles generated by practical vaned swirlers is subject to some uncertainty [29] and as has been stressed by Abujelala et al. [4] and Sturgess et al. [5], boundary conditions exert an important influence on predictions of swirling flows. The location of the inlet plane at $x/D = 0.07$ allowed measured profiles to be used as boundary conditions and these limit any uncertainties present in the inlet conditions. For boundary conditions at $x/D = 0.07$, measured profiles of the mean velocity components, U and W and the stresses $\overline{u^2}$ and $\overline{w^2}$ were used. The continuity equation was used to evaluate the mean component of radial velocity, V and $\overline{v^2}$ was estimated as a function of $\overline{u^2}$ and $\overline{w^2}$. For the Reynolds stress transport equation computations, and in the absence of other information, all shear stresses were set to zero. The dissipation rate at the inlet was obtained from

$$\epsilon = \frac{k^{3/2}}{l}$$

where

$$\begin{array}{ll} l = \dfrac{D_j}{2} & 0 < r \le \dfrac{D_j}{2} \\ l = 0.027D & D < r \le R_i \\ l = (R - R_i) & R_i < r \le R \end{array}$$

At the exit plane the measured profile was imposed as a boundary condition for the mean axial component of velocity, U and zero-gradient conditions adopted for all other variables. In this flow the downstream (exit) U-velocity profile exerts a determining influence on the flowfield. Due to the strong swirl the flow is close to subcriticality [30, 31] and in these circumstances a zero-gradient condition for the axial mean velocity is clearly inappropriate and measured profiles must be used if the flow is to be uniquely specified. At both inlet and exit planes the measured U velocity profiles have been corrected slightly by about 5 percent in total so that they both correspond to the measured mass-flow rate.

To establish that the results were free of significant numerical error two finite difference grids were used. First a grid of 50×33 nodes in the x and r directions were utilized and subsequently the computations were repeated using 100×66 nodes obtained by halving the mesh spacings in both directions. With both the $k-\epsilon$ and RST turbulence models there were only very small differences between the two results obtained with the two grids. The largest change with grid refinement was evident in the profile of axial mean velocity at the second measuring station using the RST model and as can be seen in Fig. 1(*a*) difference of about 4 percent of the maximum occurs around a localized region at $r/R \simeq 0.4$. However the changes with grid refinement in the profiles of all other quantities including the other components of mean velocity and the Reynolds stress components at this and subsequent downstream stations were everywhere less than 1 percent. As a consequence, it can be concluded with a reasonable degree of confidence that solutions essentially free of numerical error have to be obtained.

Discussion

Mean Velocities. Figure 2 shows the decay of centerline velocity for the RST equation model with and without ϵ-equation rotation terms and the $k-\epsilon$ model along with experimental results. As the measured profile for the U-velocity was used as a boundary condition at the exit, the two predictions and the measurements coincide at the last station. However, in the initial region the calculated decay with the $k-\epsilon$ model is much more rapid than either the RST model or the measurements indicate and is so rapid that the core jet is predicted to disappear by $x/D_j=6$. Furthermore the $k-\epsilon$ model incorrectly predicts the center-line velocity to increase in the region $6 \leq x/D_j \leq 24$ and then to decrease toward the fixed value at the exit. This anomalous behavior of the $k-\epsilon$ model arises because it seriously overestimates the levels of shear stress throughout the domain, particularly in the vicinity of the center-line which consequently results in the core jet disappearing much too quickly. Regarding the Reynolds stress model, the BFR modification to the ϵ equation gives rise to the slowest decay in the center-line velocity, whereas the standard unmodified ϵ-equation yields the fastest decay and is in closest agreement with the measured values.

With the RST model and for the mean velocity components, the main influence of the rotation modifications to the ϵ-equation is confined to the vicinity of the center-line and elsewhere the results are practically identical. For this reason only the results of the RST model calculations with the standard ϵ-equation, which produces closest agreement, are shown in comparison with the $k-\epsilon$ results and measured profiles in Figs. 3 and 4. For the axial component of velocity, Fig. 3, both the $k-\epsilon$ and RST models are in reasonable agreement with measured profiles in the outer region, $r/R>0.5$. However in the inner half of the flow the $k-\epsilon$ results, in contrast to the RST model calculations are in poor agreement with the measured profiles. The $k-\epsilon$ model predicts that the core jet and wake between the swirler and annular jet disappear by $x/D=0.35$ whereas the RST model and measurements show that they persist beyond $x/D=1$. The evolution of the azimuthal velocity component, W, is shown in Fig. 4 where as expected the $k-\epsilon$ results tend incorrectly and rapidly towards a solid body rotation over an appreciable region of the flow. In contrast the RST equation model is able to reproduce the essential features of the measured W-profiles including the local maximum which appears in the initial part of the flow. This occurs because a radial velocity is induced near the inner edge of the swirler by the jet decay, and angular momentum conservation results in a decrease in W as fluid elements rotate at a larger radius and vice versa. Further downstream this effect disappears and the radial gradient of W predicted by the RST model at and close to the center-line appears to be too small compared with that measured. However experimental uncertainty may be to blame in part for this discrepancy for

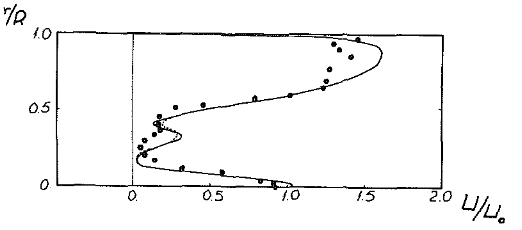

Fig. 1 The effect of grid refinement: the radial profile of axial mean velocity at $x/D=0.07$
——— 50 × 33, grid; ——— 100 × 66 grid

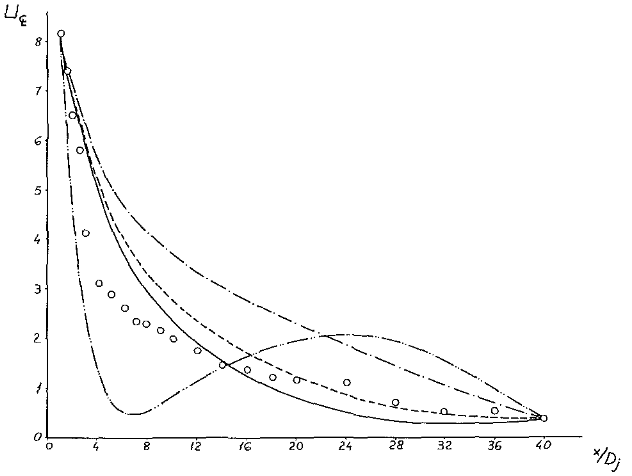

Fig. 2 Center-line axial velocity. Normalized by $U_0=7$m/s
—— Reynolds stress model with no rotation term
——— Reynolds stress + ACK ϵ-equation modification
—.— Reynolds stress + BFR ϵ-equation modification
—..— $k-\epsilon$ model
o Measurements

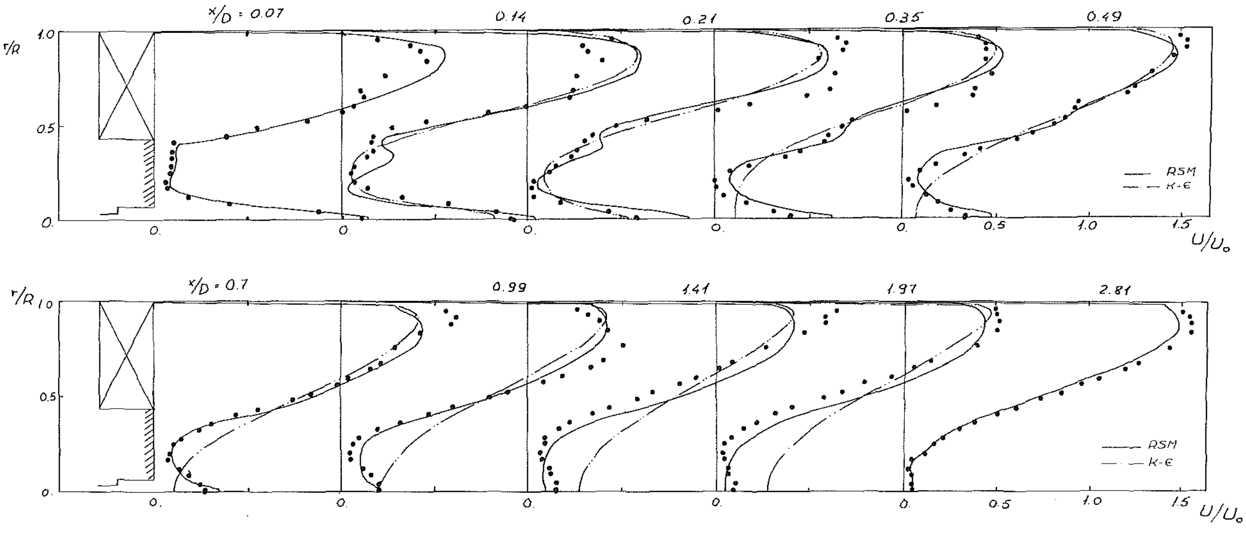

Fig. 3 Radial profiles of axial velocity normalized by $U_0=7$m/s
Measurements
——— Reynolds stress model with no rotation term
—··— k—ϵ model

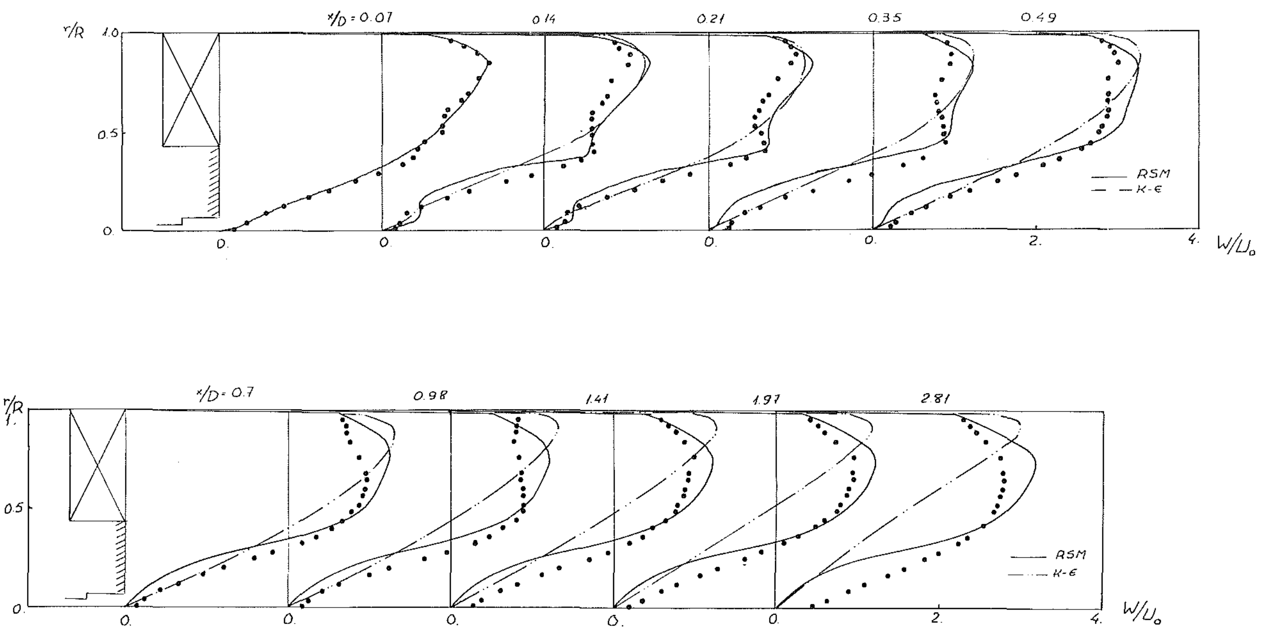

Fig. 4 Radial profiles of swirl velocity normalized by $U_0 = 7\text{m/s}$. Same legend as Fig. 3.

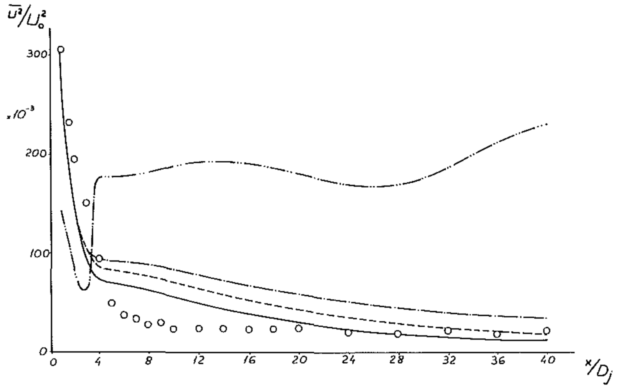

Fig. 5 $\bar{u}^2$ Normal stress at the centerline. Normalized by $U_0^2 = 49\text{m}^2/\text{s}^2$. Same legend as Fig. 2.

finite values of W are measured at $r = 0$. In the outer part of the flow values of W are somewhat overpredicted but again this may be associated with asymmetry in the measured flow.

Turbulence Quantities. Figures 5 and 6 show the measured and predicted variation of the two normal stresses $\bar{u}^2$ and $\bar{w}^2$ along the center-line. As was the case with the mean velocity the $k-\epsilon$ results are in extremely poor agreement with measured levels, and $\bar{u}^2$ and $\bar{w}^2$ are overpredicted practically everywhere by a factor of 5 or more. The RST equation results with and without ϵ-equation rotation modifications are all somewhat similar and are closer to the measurements; close to the jet inlet the predicted center-line decay is slightly too rapid and downstream in the region $4 \leq x/D \leq 20$ the levels of both $\bar{u}^2$ and $\bar{w}^2$ are overpredicted by an appreciable amount. A more detailed view of this behavior is provided by the radial profiles of $\bar{u}^2$ and $\bar{w}^2$ at various axial locations through the flow, shown in Figs. 7 and 8. Because of the poor $k-\epsilon$ model performance only the RST equation results are plotted. As is evident from the profiles the measurements show that the low values of $\bar{u}^2$ and $\bar{w}^2$ present in the inlet profiles in the region $0.2 \leq r/R \leq 0.4$ persist with largely unchanged magnitude over an appreciable axial distance to about $x/D \simeq 0.2$. In the calculations both $\bar{u}^2$ and $\bar{w}^2$ appear to diffuse from the two maxima located on the center-line and in the outer part of the flow with the consequences that the predicted center-line values decay too rapidly and that the values in the region $0.2 \leq r/R \leq 0.4$ increase significantly. A probable reason for this is that the stabilizing influence of the swirling mean motion is to significantly suppress the triple velocity correlations, $u_iu_ju_k$, responsible for the turbulent transport of Reynolds stress. The simple gradient model used in the present computations involves only turbulence quantities and as a result does not include a mechanism to account for any direct stabilizing effects of the mean swirling motion on the turbulent transport of u_iu_j.

Further downstream, beyond $x/D \approx 0.4$ the levels of the two normal stresses are overpredicted compared with measured levels by a factor of up to two over much of the flow. As the production terms in the normal stress equations are generally small in this flow the results suggest that the ϵ-equation may be the cause of the discrepancy in this downstream region and that predicted dissipation rate levels may be too low. This effect is, however, the opposite of that implied by the two ϵ-equation rotation modifications which is to reduce dissipation rates and thus give even larger values of the normal stresses. This outcome is clearly shown in Figs. 7 and 8 where the BFR model produces the largest effect and as a consequence neither the BFR nor ACL modifications leads to improved predictions except perhaps in the vicinity of the exit plane. Finally Figs. 9 and 10 shows the variation of $\bar{v}^2$ and $\overline{uv}$ through the flow. Though no measurements are available for comparison Fig. 10 shows clearly the strong stabilizing effects of the swirl whereby shear stresses are suppressed to quite small values everywhere except near the outer wall where the flow is either neutral or unstable.

Conclusion

The $k-\epsilon$ model and a Reynolds stress transport equation turbulence model have been used to predict a strongly swirling confined flow. The transport equation model in conjunction with the standard ϵ-equation reproduces the major features of the flow including the strong stabilizing effects of the swirl on the turbulence. This has the effect of suppressing the shear stresses and as a result the mean velocity field evolves only

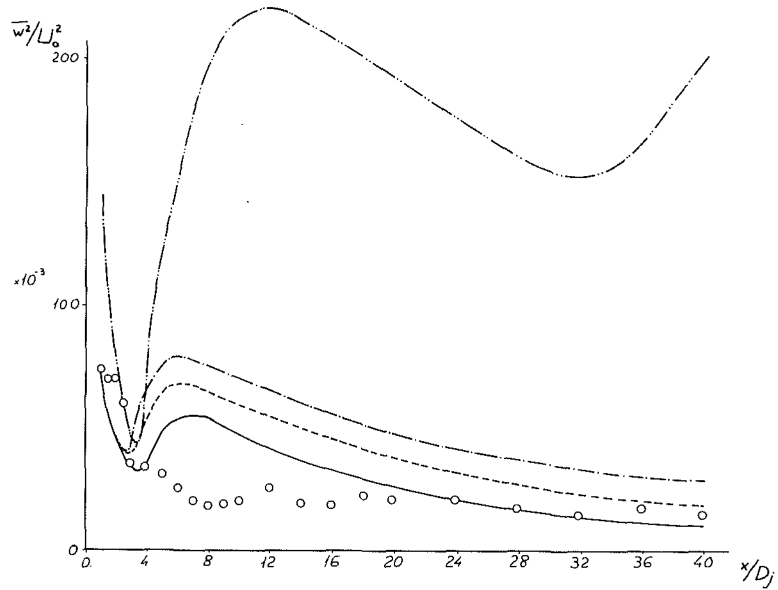

Fig. 6 $\bar{w}^2$ normal stress at the centerline. Normalized by $U_0^2 = 49\text{m}^2/\text{s}^2$. Same legend as Fig. 2.

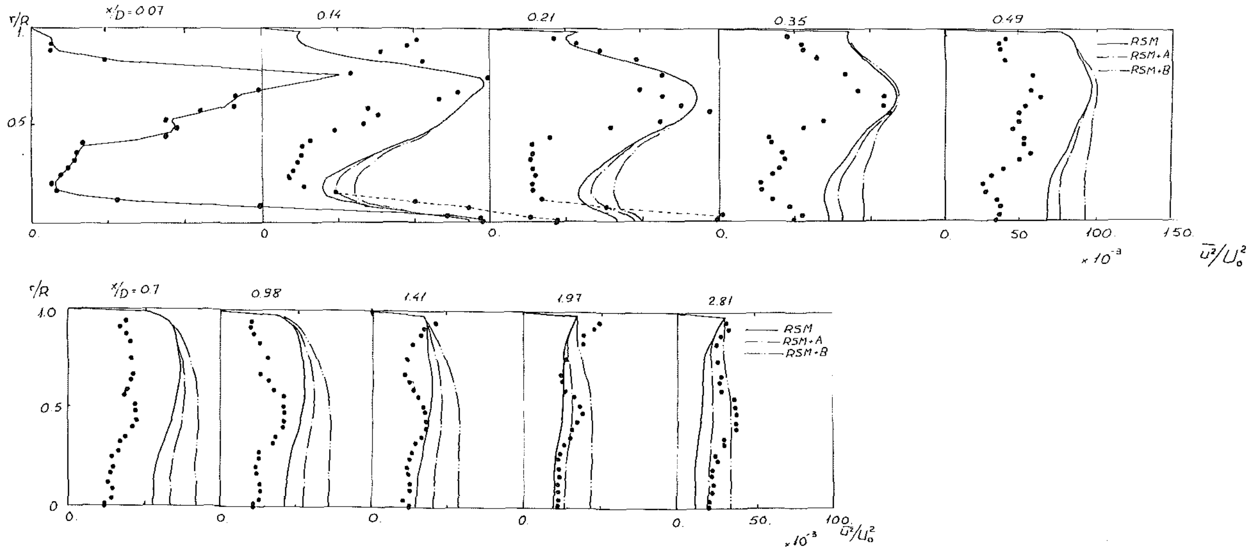

Fig. 7 Radial profiles of $\bar{u}^2$ normal stress. Normalized by $U_0^2 = 49\text{m}^2/\text{s}^2$. Same legend as Fig. 3.

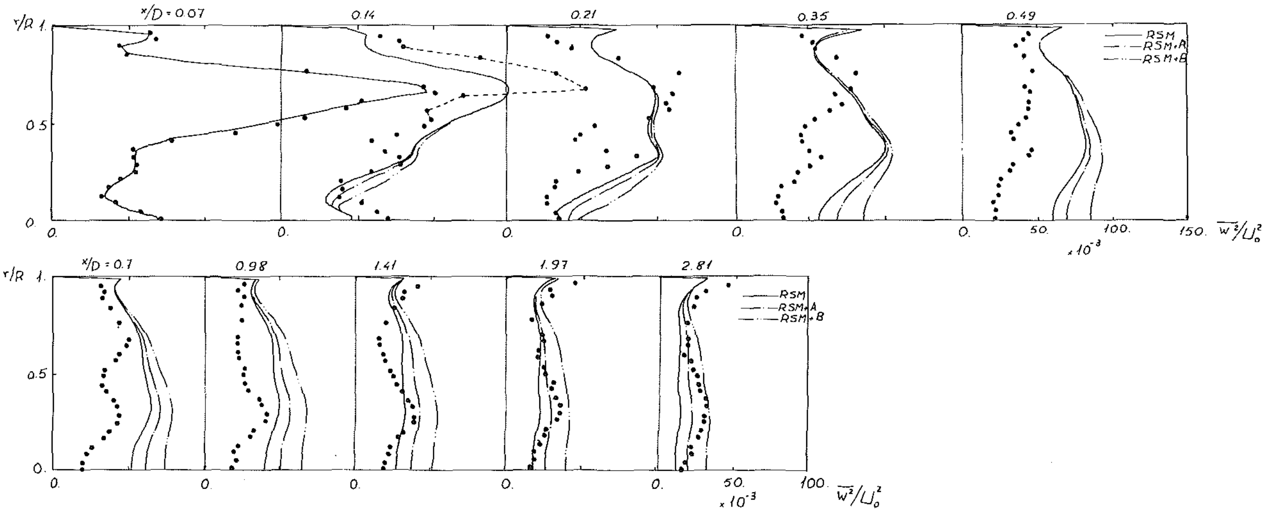

Fig. 8 Radial profiles of $\bar{w}^2$ normal stress. Normalized by $U_0^2 = 49\text{m}^2/\text{s}^2$. Same legend as Fig. 3.

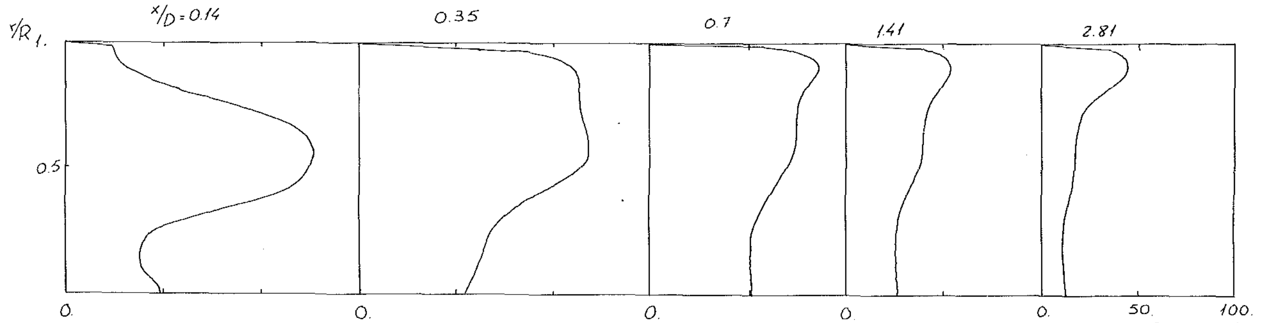

Fig. 9 Radial profiles of $\bar{v}^2$ normal stress. Normalized by $U_0^2 = 49 m^2/s^2$. Calculated results with no rotation term are plotted.

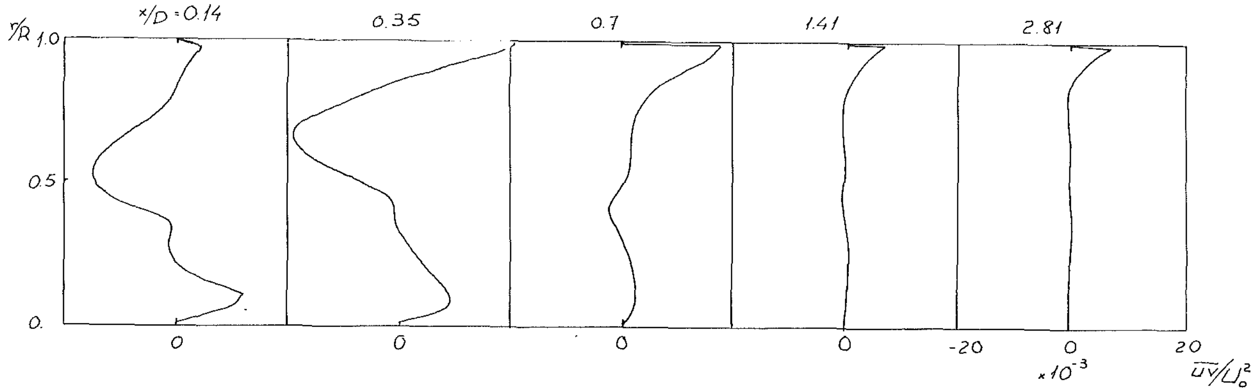

Fig. 10 Radial profiles of $\overline{uw}$ shear stress. Normalized by $U_0^2 = 49 m^2/s^2$. Calculated results with no rotation term are plotted.

slowly with axial distance particularly in the downstream region of the flow. This effect appears to be correctly described by the transport equation model and the resulting calculated profiles of both axial and swirl components of mean velocity are in reasonable agreement with those measured. With regard to the axial and circumferential components of the normal stresses the situation is less satisfactory and the levels are overpredicted by up to 100 percent in parts of the flow. In the region near the inlet the source of this discrepancy is felt to be the simple gradient model used to represent turbulent (diffusive) transport of the Reynolds stress. The influence of the swirling mean motion seems to be to suppress turbulent transport of the normal stresses but the gradient model used does not contain any mechanism to reproduce this effect.

The addition of modifications to the ϵ-equation in an attempt to account for influences of rotation, when used in conjunction with the transport equation model had little beneficial effect. The effects on the mean field were confined to the core jet region and brought a small (probably insignificant) deterioration in model performance. For the normal stresses the effects were also not too large but over most of the flow the changes were in the opposite direction of that required to produce improved agreement with measured values. Purely on the basis of the present results there seems little to warrant the inclusion of ϵ-equation rotation modifications of the type investigated and the present comparisons suggest that further amendments may be needed if the ϵ-equation is to reproduce the combined effects of rotation rate and mean rate of strain.

In spite of the limitations of the transport equation model results it is clear that the $k-\epsilon$ model does not provide a viable alternative method of calculating accurately, confined strongly swirling flows. The model contains no mechanism to account for the stabilizing (or otherwise) effect of swirl and as a consequence leads to results which are in very poor agreement with those measured. Since the mechanism which accounts for any of the stabilizing effects of swirling motion appears naturally in Reynolds stress transport equation models such models appear to offer the best choice for predicting the characteristics of swirling turbulent flows.

Acknowledgment

Financial support for the work reported in this paper was provided by the Procurement Executive of the Ministry of Defence and this the authors are grateful to acknowledge.

References

1 Gupta, A. K., Lilley, D. G., and Syred, N., *Swirl Flows*, Abacus Press, Tunbridge Wells, England, 1984.

2 Brondum, D. C., Bennett, J. C., Weinberg, B. C., and McDonald, H., "Numerical and Experimental Investigation of Non-Swirling and Swirling Jets," AIAA Paper 86-0040, 1986.

3 Sturgess, G. J., and Syed, S. A., "Calculation of Confined Swirling Flows," AIAA Paper 85-0060, 1985.

4 Abujelala, M. T., and Lilley, D. G., "Confined Swirling Flow Predictions," AIAA Paper 83-0316, 1983.

5 Sturgess, G. J., Syed, S. A., and McManus, K. R., "Importance of Inlet Boundary Conditions for Numerical Simulation of Combustor Flows," AIAA paper 83-1263, 1983.

6 Hendricks, C. J., and Brighton, J. A., "The Prediction of Swirl and Inlet Turbulence Kinetic Energy Effects on Confined Jet Mixing," ASME Journal of Fluids Engineering, Vol. 97, Mar. 1975, pp. 51-59.

7 Kubo, I., and Gouldin, F. C., "Numerical Calculations of Turbulent Swirling Flow," ASME Journal of Fluids Engineering, Vol. 97, Sept. 1975, pp. 310-315.

8 Rhode, D. L., Lilley, D. C., and McLaughlin, D. K., "On the Prediction of Swirling Flowfields Found in Axisymetric Combustor Geometries," ASME Journal of Fluids Engineering, Vol. 104, Sept. 1982, pp. 378-384.

9 Ramos, J. I., "Turbulent Non-reacting Swirling Flows," *AIAA Journal*, Vol. 22, No. 6, June 1984, pp. 846-847.

10 Srinivasan, R., and Mongia, H. C., "Numerical Computations of Swirling Recirculating Flow; Final Report," NASA CR-165196, Sept. 1980.

11 Rhode, D. L., and Stowers, S. T., "Turbulence Model Assessment for Confined Mixing of Coswirling Concentric Jets," AIAA paper 85-1269, 1985.

12 Sloan, D. G., Smith, P. J., and Smoot, L. D., "Modelling of Swirl in Turbulent Flow Systems," *Progress in Energy and Combustion Science*, Vol. 12, 1986, pp. 163-250.

13 Chen, C. P., "Confined Swirling Jet Predictions Using a Multiple Scale Turbulence Model," NASA CR-178484, Aug. 1985.

14 Lilley, D. G., and Chigier, N. A., "Nonisotropic Turbulent Stress Distribution in Swirling Flows from Mean Value Distributions," *International Journal of Heat and Mass Transfer*, Vol. 14, 1971, pp. 573-585.

15 Kobayashi, T., and Yoda, M., "Modified $k-\epsilon$ Model for Turbulent Swirling Flow in a Straight Pipe," *JSME International Journal*, Vol. 30, No. 259, 1987, pp. 66-71.

16 Sander, G. F., and Lilley, D. G., "The Performance of an Annular Vane Swirler," AIAA-83-1326, Seattle, Washington, June 27-29, 1983.

17 Launder, B. E., and Morse, A. P., "Numerical Prediction of Axisymmetric Free Shear Flows with a Reynolds Stress Closure," *Turbulent Shear Flows I*, Springer-Verlag, Berlin, 1979, pp. 279-294.

18 Gibson, M. M., and Younis, B. A., "Calculation of Swirling Jets with a Reynolds Stress Closure," *Physics of Fluids*, Vol. 29, No. 1, Jan. 1986, pp. 38-48.

19 So, R. M. C., Ahmed, S. A., and Mongia, H. C., "An Experimental Investigation of Gas Jets in Confined Swirling Air Flow," NASA CR-3832, 1984.

20 Jones, W. P., and Musonge, P., "Closure of the Reynolds Stress and Scalar Flux Equations," *Physics of Fluids*, Vol. 31, 1988, pp. 3589-3604.

21 Launder, B. E., Reece, G. J., and Rodi, W., "Progress in the Development of a Reynolds Stress Turbulence Closure," *Journal of Fluid Mechanics*, Vol. 68, Part 3, 1975, pp. 537-566.

22 Launder, B. E., Priddin, C. H., and Sharma, B. J., "The Calculation of Turbulent Boundary Layers on Spinning and Curved Surfaces," ASME JOURNAL OF FLUIDS ENGINEERING, Vol. 99, 1977, pp. 231-239.

23 Rodi, W., "Influence of Buoyancy and Rotation on Equations for the Turbulent Length Scale," *Proceedings 2nd Symposium on Turbulent Shear Flows*, Imperial College, London. 10.37.10.42. 1979.

24 Bardina, J., Ferziger, J. H., and Rogallo, R. S., "Effect of Rotation on Isotropic Turbulence. Computation and Modelling," *Journal of Fluid Mechanics*, Vol. 154, 1985, pp. 321-336.

25 Aupoix, B., Cousteix, J., and Liandrat, J., "Effects of Rotation on Isotropic Turbulence," *Proceedings 4th Symposium on Turbulent Shear Flows*, Karlsruhe, 1983, pp. 9.7-9.12.

26 Jones, W. P., and Marquis, A. J., "Calculation of Axisymetric Recirculating Flows with a Second Order Turbulence Model," *Proceedings 5th Symposium on Turbulent Shear Flows*, Cornell University, 1985, pp. 20.1-20.6.

27 Marquis, A. J., "The Application of High-Order Convection Approximations and Second Order Turbulence Closures to Recirculating Flows," Ph.D. thesis University of London, 1986.

28 Huang, P. G,. and Leschziner, M. A., "Stabilization of Recirculating-Flow Computations Performed with Second-Moment Closures and Third Order Discretization," *Proceedings 5th Symposium on Turbulent Shear Flows*, Cornell University, 1985, pp. 20.7-20.12.

29 Abujelala, M. T., and Lilley, D. G., "Limitations and Empirical Extensions of the $k-\epsilon$ Model as Applied to Turbulent Confined Swirling Flows," AIAA-84-0441, Reno, Nevada, Jan. 9-12, 1984.

30 Benjamin, T. B., "Theory of the Vortex Breakdown Phenomenon," *J. Fluid Mech.*, Vol. 14, 1962, pp. 593-629.

31 Escudier, M. P., and Keller, J. J., "Recirculation in Swirling Flow: A Manifestation of Vortex Breakdown," *AIAA Journal*, Vol. 23, pp. 111-116.

The Effect of Pitch Location on Dynamic Stall

E. J. Jumper[1]
Professor,
Department of Aeronautics and Astronautics,
Air Force Institute of Technology,
Wright-Patterson AFB, Ohio

R. L. Dimmick
Aeronautical Engineer,
Wright-Patterson AFB, Ohio

A. J. S. Allaire
Aeronautical Engineer,
Major, Canadian Armed Forces

This paper reports the results of theoretical and wind-tunnel studies of the effect of pitch location on dynamic stall for an airfoil pitching at constant rate. A modified momentum-integral method was used to predict the effect of pitch location and rate on the delay in quarter-chord separation. The wind-tunnel study involved the collection of time-varying pressure readings from 16 locations on an NACA 0015 airfoil that were subsequently used to determine lift, pressure-drag, and moment coefficients as functions of angle of attack for 140 test cases, covering 28 dynamic airspeed/pitch-rate/pitch-location combinations. Dynamic-stall effects of change (from steady flow) in the angle of attack at which separation occurs at the quarter chord (for comparison with the momentum-integral results), and change in the angle of attack at which stall occurs were extracted from these data and found to collapse best onto a non-dimensional pitch rate given by the chord times the pitch rate divided by two times the free-stream velocity. An adjusted non-dimensional rate formed by replacing one half the chord with the fraction of the chord corresponding to the pitch location was also examined and found not to be the proper non-dimensional variable for collapsing the data. The quarter-chord separation data compared favorably with the theoretical predictions.

Introduction

Experimental studies of dynamic stall have been reported in the literature since the work of Kramer [1] in 1932, and have appeared with increasing frequency until the present. Reference [2] is especially helpful in reviewing the experimental work that has been reported. Unlike the majority of such experiments which studied periodic motions, we have concentrated exclusively on the constant-pitch-rate (constant-$\dot{\alpha}$) problem. More importantly, our experiments have been tailored to address specific issues that have surfaced from our concurrent theoretical studies of the constant-$\dot{\alpha}$ dynamic-stall problem. As reported in two earlier papers [3, 4], constant-pitch-rate experiments for an airfoil pitching about the midchord were performed to obtain (*a*) the angle of attack at which the flow separates from the upper surface of the airfoil at the quarter-chord location [3, 4], (*b*) the lift, pressure-drag and moment coefficients as functions of angle of attack [4], and (*c*) the angle at which dynamic stall occurred [4]. The data of reference [3] were collected specifically for a comparison with a concurrent theoretical study [5, 6] that, because the study was a boundary-layer analysis, required information concerning the effect of pitch on the angle of attack at which the flow separated at the quarter chord. Reference [4] extended the goals of the constant-$\dot{\alpha}$ experiments to include stall angle, thereby necessitating the collection of a more detailed description of the time-varying pressure field about the airfoil.

The work mentioned so far dealt exclusively with midchord pitch location, yet it is clear that the effect of changing the pitch location is of fundmental importance in the understanding and ability to predict dynamic-stall events. At the most elementary level, one notes that attempts to correlate dynamic-stall data obtained by different researchers are hampered by the lack of common pitch locations. Reference [7], for example, reports on constant-$\dot{\alpha}$ experiments, but the pitch locations are for 31 percent and 37.5 percent chord locations. Although not for constant-$\dot{\alpha}$ motions, references [8 and 9] report on experiments that pitched about the quarter chord. Even more dramatic pitch location differences are to be found in references [1 and 10] where, in the former case, the airstream was made to change its angle with respect to a fixed airfoil, and in the latter an entire aircraft configuration was made to pitch about its equivalent CG location. With the advent of new aircraft that are being designed to pitch at high angular rates, it is now more important than ever before to understand how to interpret the likely effects of pitch location.

Theoretical Treatment

Experimental results reported in reference [3] demonstrate that quarter-chord separation is delayed to a higher angle of attack for the pitching airfoil (dynamic separation) than for the static case (static separation). Further, the experimental results reported in reference [4] show that there is a systematic link between dynamic separation at the quarter chord and dynamic stall. Flow visualization studies [11] have shown that in the dynamic cases separation begins at the trailing edge and progresses forward on the airfoil; prior to quarter-chord

---

[1] Present position: Chief, Laser Devices Division, Advanced Radiation Technology Office, Air Force Weapons Laboratory, Kirtland AFB, New Mexico.

Contributed by the Fluids Engineering Division for publication in the JOURNAL OF FLUIDS ENGINEERING. Manuscript received by the Fluids Engineering Division July 14, 1987.

separation, though the flow is separated, the general flow pattern is along the contours of the airfoil (after quarter-chord separation, the flow may no longer follow the contours). Such experimental evidence suggests that an understanding of, and ability to predict the onset of dynamic (quarter-chord) separation is of fundamental importance to the understanding of dynamic stall. Further, because the flow generally follows the contour of the airfoil up to quarter-chord separation, boundary-layer methods rather than Navier-Stokes solvers could be employed to study separation up to quarter-chord separation. Based on such information, a modified momentum-integral boundary-layer method for unsteady flows was developed and applied to the dynamic-stall problem for an airfoil pitching about the midchord [5, 6]. As is the case with all boundary-layer methods, a description of the pressure/velocity field at the edge of the boundary layer was needed.

Such a pressure/velocity field was modelled in a way that allowed the effect of each of the contributing influences on quarter-chord separation to be assessed separately. As described in references [5 and 6], the effect of the unsteadiness of the flow (neglecting the wake), the motion of the airfoil tangent to the surface (i.e., in the direction of the flow), and the motion of the airfoil perpendicular to the surface (i.e., into the flow) were estimated using the momentum-integral method. The effect of the perpendicular motion was assessed using a perturbation method which required estimating a "mass-ingestion" parameter (the perturbation method is extensively discussed in reference [6]). It was noted in references [5 and 6] that this parameter should have an average value of less than 10δ (premultiplier of δ was referred to as a relaxation coefficient); an argument was presented that it should be approximatey 4δ at the quarter chord, but that it should also be larger closer to the leading edge [5, 6]. The prediction of the effect of pitch (about the midchord) on quarter-chord separation for a mass-ingestion parameter assumed to be constant at the quarter-chord value of 4δ is shown in Fig. 1, by the curve labeled 4δ. The nondimensional pitch rate of the abscissa of Fig. 1 is given by

$$\dot{\alpha}_{ND} = \frac{1/2c\dot{\alpha}}{U_\infty} \tag{1}$$

where c is the chord, $\dot{\alpha}$ is the rate of change of angle of attack and U_∞ is the freestream velocity. Also shown in Fig. 1 are the experimentally obtained quarter-chord separation data from reference [3]. As pointed out in reference [5], while the extent of the effect was not explained by those contributing influences examined, the asymptotic slope appeared to have been nearly matched with a mass-ingestion parameter of 4δ. Since the intent of reference [5] was to address these influences only approximately, no attempt was made to further refine the mass-ingestion parameter. In this paper, however, we have further refined the mass-ingestion parameter to match the slope more closely; a mass-ingestion parameter of 7δ seems to better match the slope and is given and so indicated in Fig. 1. It was conjectured in Reference [5] that the additional quarter-chord delay required to match the data could be due to the wake. To investigate the effect of the unsteady wake requires a more complete description of the pressure/velocity field.

A method for obtaining a more complete description of the pressure/velocity field was developed that used conformal-mapping techniques to model the unsteady, inviscid (i.e., external) flow field for a Joukowski airfoil pitching about approximately the midchord and shedding vortices into the wake [12]. This treatment of the flow allowed for a complete, inviscid (and noninteractive) description of the pressure distribution on the airfoil surface as a function of time (assuming that the flow remained attached to the airfoil). The gross effects on the lift-coefficient versus angle-of-attack curve may be summarized as follows: the modelling predicted that the airfoil should experience a sudden jump in lift coefficient at rotation onset and the lift-curve slope should be depressed (see Fig. 2)

These effects have been characterized as functions of the non-dimensional pitch of equation (1). The predicted C_L jump was determined to be [12, 13]

$$\Delta C_L\left(\dot{\alpha}_{ND}, \frac{t}{c}\right) = 3.14\ \dot{\alpha}_{ND}\left[1 + \frac{2}{3}\left(\frac{t}{c}\right)\right] \tag{2}$$

where t/c is the thickness ratio. The predicted effect of $\dot{\alpha}_{ND}$ on the lift-curve slope, C_{L_α}, for a zero thickness airfoil (flat plate) is shown in Fig. 3. The curve in Fig. 3 can be approximated by

$$C_{L_\alpha}(\dot{\alpha}_{ND}) \simeq 3.6 + 2.68 \exp\left(-\dot{\alpha}_{ND} \times 10^3/4.216\right) \tag{3}$$

Equation (3) is only slightly modified by the inclusion of thickness ratio. It can be shown that the effect described by equation (2) is due to the rotation of the airfoil [13], and is referred to in aeroelasticity as an apparent camber effect [14]. The effect described by equation (3) is due to the vortices shed into the wake causing a "time lag" which results in a different lift coefficient for a given angle of attack in the dynamic case than that for the steady case at the same angle of attack, similar to the "starting-vortex" time lag of the Wagner problem [15]. As discussed in reference [4], the NACA 0015 airfoil used in the midchord-pitch-location experiments exhibited lift-curve characteristics (while the flow was "fully" attached) that were similar to the unsteady airfoil characteristics of a Joukoski airfoil pitching at constant rate as described by equations (2) and (3).

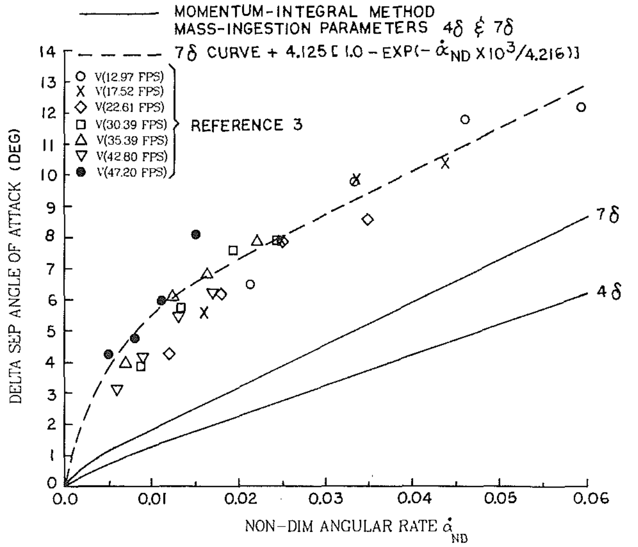

Fig. 1 Measured and predicted dynamic delay in quarter-chord separation for an airfoil pitching about the midchord, from references [3 and 5]

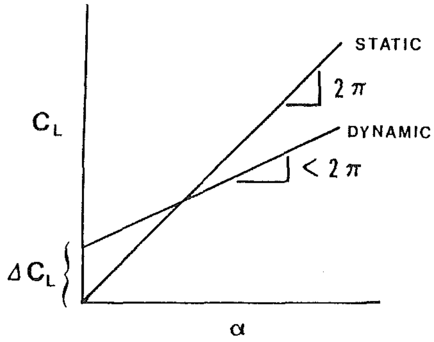

Fig. 2 Lift-curve effects due to airfoil rotation about the midchord, from reference [12]

Returning to the momentum-integral method of modelling the quarter-chord separation delay for the pitching airfoil, references [5 and 6] modelled the influence of the "apparent camber" only [i.e., equation (2) effect only], and did not include the effect of the shed-vortex wake (c.f., above). With the aid of the wake dependence given by equation (3), the suggestion of reference 5, that the additional delay in quarter-chord separation might be due to the effect of the wake, may now be inferred. Figure 1 indicates the need for an additional influence beyond the "7δ" prediction that is large at small $\dot{\alpha}_{ND}$ (≤ 0.01), and saturates at around $\dot{\alpha}_{ND} \simeq 0.01$; such behavior is clearly exhibited by the wake effect, as indicated from equation (3), and depicted in Fig. 3.

Further for the purposes of this discussion, let us assume that the two effects (i.e., the "apparent-camber" effect and the wake effect) are "additive." In line with the "additive" assumption (c.f., above), and further assuming that we may attribute the additional delay in quarter-chord separation to the wake, the mathematical form of the correction should be consistent with that of Fig. 3. This leads to the following additional quarter-chord separation delay

$$[\Delta\alpha_{SEP}(\dot{\alpha}_{ND})]_W = 4.125[1.0 - \exp(-\dot{\alpha}_{ND} \times 10^3/4.216)] \qquad (4)$$

The conformity in functional form to that of Fig. 3 can be noted by comparing equation (4) with equation (3). The curve given by the dashed line in Fig. 1 gives the result of adding the additional quarter-chord separation delay to the momentum-integral prediction with a mass-ingestion parameter of 7δ. While the size of the coefficient of equation (4) (i.e., 4.125) was obtained by determining the magnitude of the required adjustment in order for the 7δ curve to match the data at an $\dot{\alpha}_{ND}$ of 0.04, the close conformity of the subsequent prediction to the functional form of the data in Fig. 1 gives corroborative support to the notion that the additional delay may be attributed to the wake.

From the method of modelling the pitching Joukowski airfoil [12, 13], it is clear that the wake effect does not depend on pitch location; however, the "apparent camber" effect can be shown to be affected by pitch location [13]. While the conformal-mapping technique allows for pitching about approximately the the midchord only, the momentum-integral method [5, 6] allows the exploration of the effect on separation of pitch locations other than the midchord. Fig. 4 gives the effect of pitch location on separation delay as predicted by the momentim-integral method of references [5 and 6]. These results include the "correction" for wake effect given by equation (4). It has been suggested that a more appropriate nondimensional rate would be to replace 1/2 c with the fraction of the chord, measured from the leading edge, corresponding to the pitch location. Such an adjusted nondimensional rate would be given by

$$(\dot{\alpha}_{ND})_A = \frac{L_R \dot{\alpha}}{U_\infty} \qquad (5)$$

where L_R is the fraction of c corresponding to the pitch location. The modified angular rate of equation (5) was used to recollapse the theoretical predictions given in Fig. 4, the result is given in Fig. 5. It should be noted that the use of this adjusted nondimensional angular rate reverses the relative positions of the curves and spreads them out. From this behavior it may be inferred that, if the theoretical method is correct, then the parameter of equation (5) is not the proper variable for further collapsing the effect of pitch location.

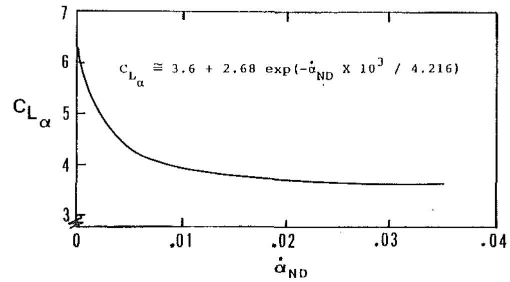

Fig. 3 **Lift-curve slope depression due to airfoil rotation about the midchord, from references [4 and 12]**

Experimental Approach

The same basic setup described in reference [4] was used for this series of tests. A 1.02 ft chord NACA 0015 airfoil instrumented with 16 ENDEVCO 8507-2, 2-psi (full-range) pressure transducers at the locations indicated in Fig. 6, was made to rotate about a rotation shaft at 0.08 c, 0.25 c (quarter chord), and 0.5 c (midchord). The face diameter of the 8507-2 transducers is 0.09 inches and they were surface mounted in the airfoil. The rated frequency response of the transducers is approximately 9,000 Hz (20 percent of the resonant frequency), far exceeding the dynamic requirements of the experiment. The airfoil assembly was mounted via the rotation shaft at approximately the center of the 5 ft × 3 ft × 0.25 ft test section of the wind tunnel such that it spanned the width of the tunnel. A high-torque, constant-speed motor was attached to

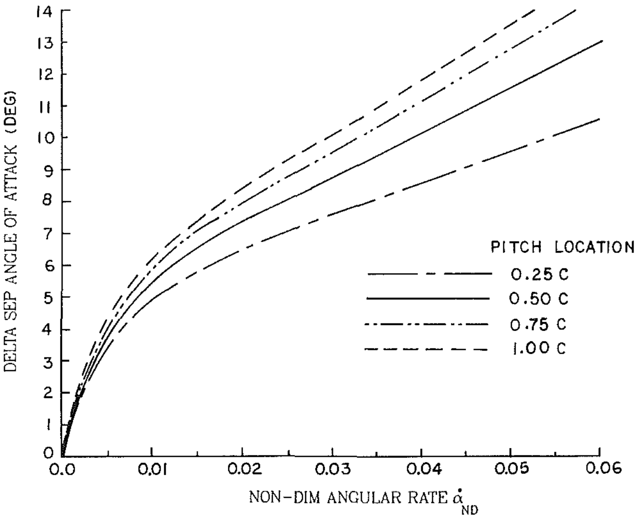

Fig. 4 **Predicted pitch-location effect on dynamic delay in quarter-chord separation**

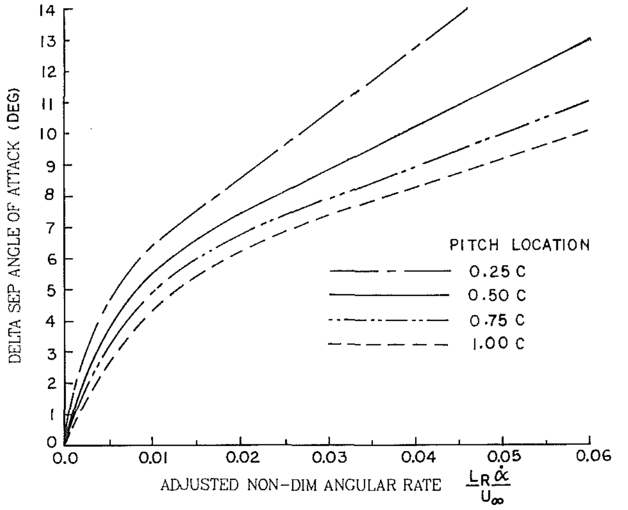

Fig. 5 **Predicted dynamic quarter-chord separation delay plotted versus adjusted non-dimensional rate**

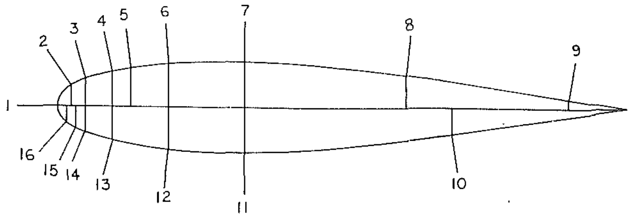

X/C(1) = 0.000
X/C(2) = 0.025
X/C(3) = 0.049
X/C(4) = 0.098
X/C(5) = 0.131
X/C(6) = 0.197
X/C(7) = 0.328
X/C(8) = 0.615
X/C(9) = 0.902
X/C(10) = 0.697
X/C(11) = 0.328
X/C(12) = 0.197
X/C(13) = 0.098
X/C(14) = 0.049
X/C(15) = 0.033
X/C(16) = 0.016

Fig. 6 Pressure-transducer locations

the rotation shaft, via a gear train, to provide constant-$\dot{\alpha}$ pitching rates from approximately 45-180 deg/s, depending on the voltage applied and rotation location. Angular position information was provided by sensing the wiper voltage on a ten-turn potentiometer attached via a separate gear train to the rotation shaft.

Pressure and position data were obtained using the same microcomputer-based data acquisition system described in reference [4]. It consisted of an S-100 bus, Z-80A-based microcomputer. Of particular interest here was the analog-to-digital (A-to-D) conversion modules. Two Dual Systems Control Corporation AIM-12 multiplexed A-to-D modules (each on an S-100 bus compatible card) were used. These modules were software and hardware configured to sequentially read the pressure-transducer output voltages in differential mode. The AIM-12 in differential mode has a 114 db common-mode rejection when configured to read ±50 millivolts. The use of the ENDEVCO transducers and Dual A-to-D board combination obviated the need for signal conditioners.

The transducers measured the pressure difference between their particular airfoil-surface location and ambient (i.e., room) pressure. The tunnel was a draw-down type, and owing to pressure drops through the inlet screens, all pressures were biased toward negative readings, including the stagnation pressure. Under the conditions of the experiment, the maximum (absolute) voltage was approximately 1/3 full scale of the transducer design range.

Sources of Error. The AIM-12 module can resolve to one part in 4096 (12 bit) over the full range of ± 50 millivolts. Combined with the pressure transducers the resolution over the range of the experiment was such that the A-to-D conversion could resolve to approxiamtely 1×10^{-4} psig, so that the error introduced in a single measurement could be expected to be accurate to better than 1 percent. These pressure measurements were then used to compute pressure coefficients, and these pressure coefficients to compute chord-normal and chord-tangent coefficents (c.f., below) by computing the exact integral between polygonal curves. Thus the error introduced by the measurement was of the linear-sum type and can be divided into error in the expected value, and variance. The error in expected value in turn has two parts, the first being simple randomness error (noise) and systematic error. Based on our experience in previous experiments [4], the expected value of the computed integral between polygonal lines should be that of the "exact" value. Further an attempt was made to minimize systematic error by, (*a*) using our own calibration to obtain transducer sensitivities, and (*b*) by calibrating each transducer before and after each set of runs. The later showed that the maximum change in sensitivity in any transducer, over the entire study was less than 2 percent, and there was far less change from one calibration to the next. The variance can be shown to be small, though not as small as in previous studies [4]. In order to minimize the impact of the variance, duplicated runs (c.f., below) for a given dynamic $\dot{\alpha}/U_\infty$/rotation-point combination were averaged, unlike previous studies [4] that presented every data point. As in the previous study [4], some error can be expected to have been introduced due to the fact that the data were collected sequentially rather than simultaneously (c.f., below); however, this error is clearly small for two reasons: a) the pressure changes were small over the time between successive samples of the same transducer, and b) the changes in pressure were smooth (c.f., reduced data curves below).

The data collection was accomplished by software-directed sampling of the 16 pressure transducer voltages and the position voltage via the A-to-D boards, along with one internal time-clock sample per pass. The sample rate was 4250 samples/s. The readings were stored in memory, and then written to disk at the completion of an experiment. The same microcomputer system was then used to reduce the data into the various appropriate forms needed to interpret the results. For more details see reference [16].

Results

A total of 140 usable dynamic-stall data runs were made at tunnel speeds ranging in flow velocity from approximately 25-45 ft/s (Reynolds number range, 1.47×10^5 to 2.67×10^5). Each tunnel-speed and pitch-rate/pitch-location combination was repeated five times, giving a total of 28 dynamic combinations. Each dynamic run was started at approximately 0 deg angle of attack. Additionally a static C_L versus α run was made at each tunnel speed of interest.

Since a time signal, a location signal, and 16 pressure signals were sampled in a serial fashion, a picture of the pressure distribution at a particualr instant in time was approximated by linearly interpolating the signals closest to the time of interest. This yielded consistent pressure distributions from one run to the next of the duplicated runs. Examples of the results of a dynamic data run for $\dot{\alpha}_{ND} = 0.036$ are given in Fig. 7, representing distributions ranging from prior to stall to beyond dynamic stall. It should be noted that the point at $(x/c) = 1.0$ was estimated following McAlister et. al. [9], using the readings from transducer 8 and 9 (c.f., Fig. 6).

The first information extracted from the data was quarter-chord separation angle for the 0.25 c and 0.50 c pitch-location runs. The method of reference [3] was used to determine when separation occurred. This involved tracking the pressure coefficient from transducer 6 (c.f., Fig. 6) and identifying the angle at which the normalized local maximum occurred. As discussed in reference [3], this normalized maximum coincides with quarter-chord separation. The quarter-chord separation data are shown in Fig. 8, along with the theoretical prediction for 0.25 c and 0.50 c pitch locations from Fig. 4.

The chord-normal aerodynamic coefficient, C_Y, was obtained by numerical integration that found the area between polygonal curves of the pressure coefficients of the Fig. 7 type as follows

$$C_Y = -\oint c_p d\left(\frac{x}{c}\right) \tag{6}$$

where c_p is the pressure coefficient and (x/c) is the ratio of the distance from the leading edge divided by the chord. In a similar way the chord-tanget aerodynamic coefficient, C_X, was numerically determined by intergrating with respect to (y/c). The lift coefficient and pressure-drag coefficient were then determined by

$$C_L = C_Y \cos\alpha - C_X \sin\alpha \tag{7}$$

and

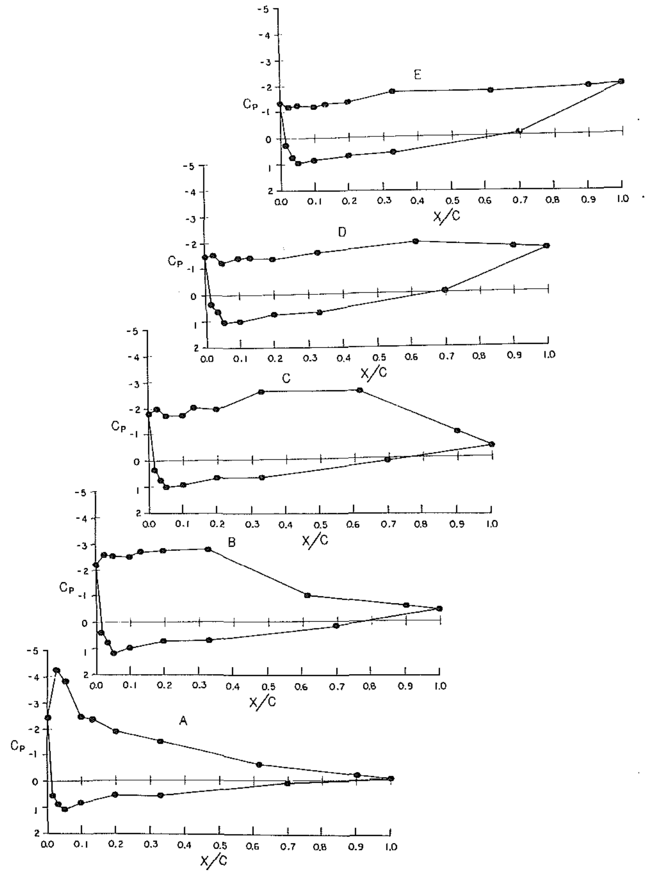

Fig. 7 Series of C_p distributions for $\dot{\alpha}_{ND} = 0.036$ case, where dynamic stall was at 32.2°: A. $\alpha = 22.1°$; B. $\alpha = 27.5°$; C. $\alpha = 30.8°$; D. $\alpha = 37.0°$; and E. $\alpha = 38.8°$.

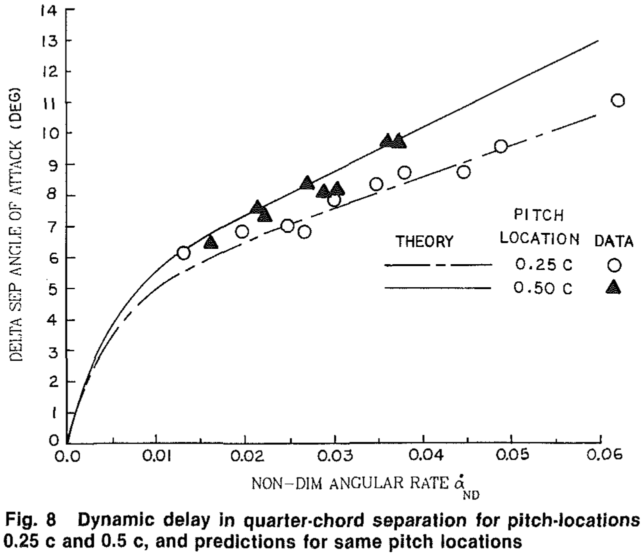

Fig. 8 Dynamic delay in quarter-chord separation for pitch-locations 0.25 c and 0.5 c, and predictions for same pitch locations

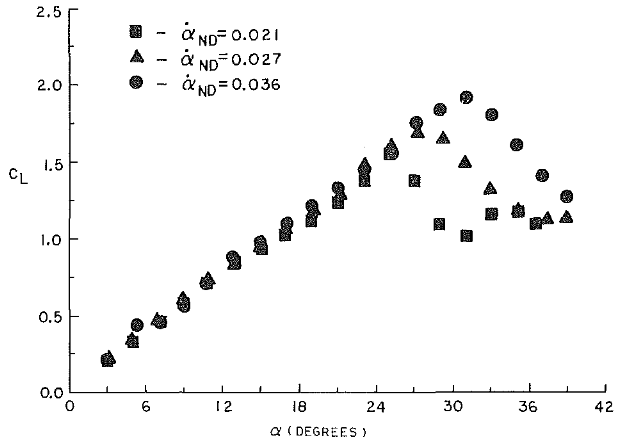

Fig. 9 Overlay of lift coefficient versus angle of attack for 3 dynamic data sets at a tunnel speed of approximately 29.1 ft/s, pitching about the midchord, for $\dot{\alpha}_{ND}$'s of 0.021, 0.027 and 0.036.

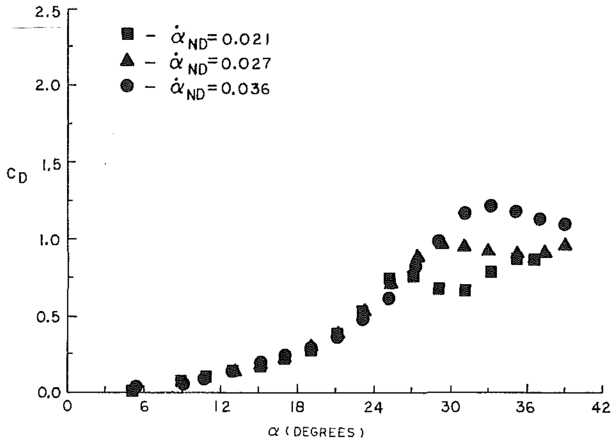

Fig. 10 Overlay of (pressure) drag coefficient versus angle of attack for 3 dynamic data sets at a tunnel speed of approximately 29.1 ft/s, pitching about the midchord, for $\dot{\alpha}_{ND}$'s of 0.021, 0.027 and 0.036.

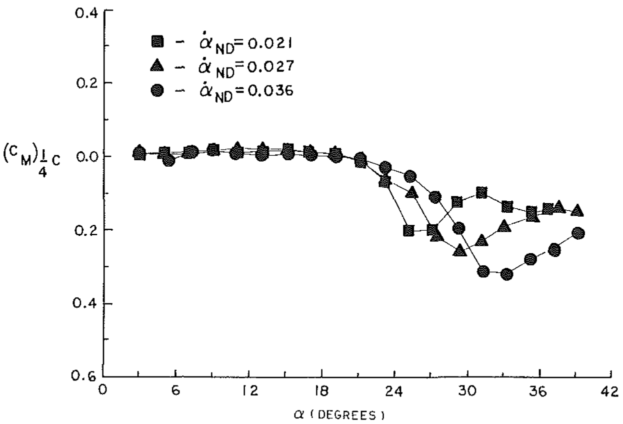

Fig. 11 Overlay of quarter-chord moment coefficient versus angle of attack for 3 dynamic data sets at a tunnel speed of approximately 29.1 ft/s, pitching about the midchord, for $\dot{\alpha}_{ND}$'s of 0.021, 0.027 and 0.036.

$$C_D = C_Y \sin\alpha + C_X \cos\alpha \tag{8}$$

Finally, the quarter-chord moment coefficient was found by numerical integration of

$$(C_M)_{1/4c} = \oint c_p\left(\frac{x}{c} - 0.25\right) d\left(\frac{x}{c}\right) \tag{9}$$

The results of these reduced data are summarized in Fig. 9, 10, and 11. These figures include C_L versus α, C_D versus α, and C_M versus α overlaid for $\dot{\alpha}_{ND}$'s of 0.021, 0.027, and 0.036 at a tunnel speed of approximately 29 ft/s, for a pitch location of 0.5c (i.e., midchord). Similar curves for each tunnel speed, pitch location and angular rate can be found in, reference [16].

From curves similar to those in Fig. 9, the dynamic change in stall angle from that in steady flow can be extracted. Figure 12 gives the result of this exercise.

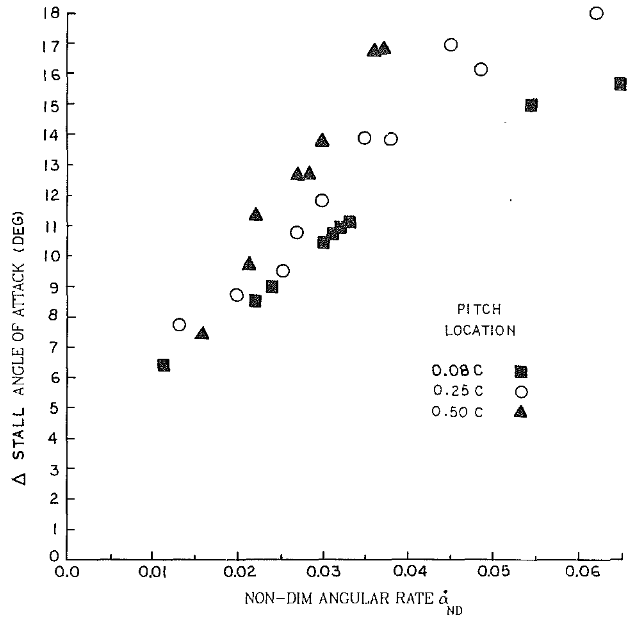

Fig. 12 Dynamic change (from steady flow) in stall angle of attack for pitch locations of 0.08 c, 0.25 c and 0.5 c

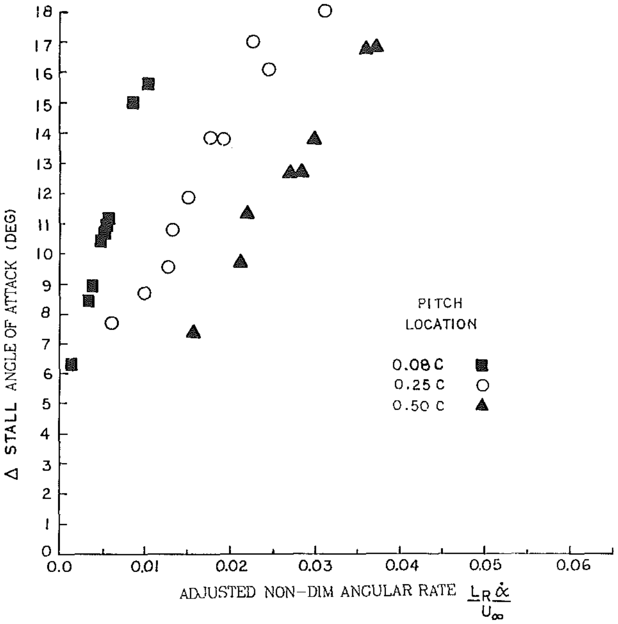

Fig. 14 Dyanamic change (from steady flow) in stall angle of attack for pitch locations of 0.08 c, 0.25 c and 0.5 c, plotted versus adjusted non-dimensional rate

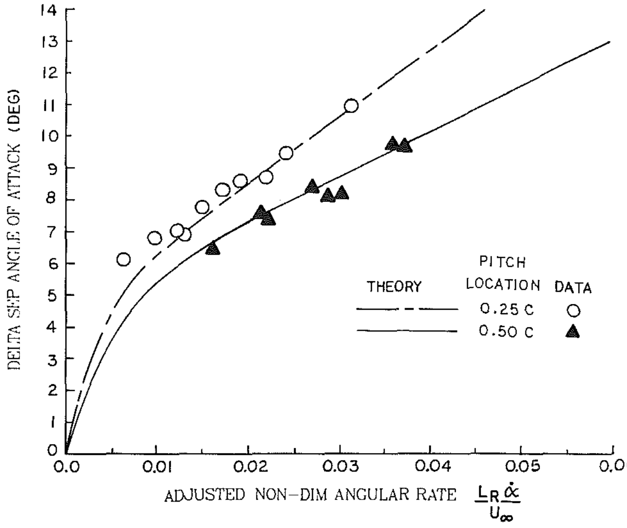

Fig. 13 Dynamic change (from steady flow) in quarter-chord separation for pitch-locations 0.25 c and 0.5 c, plotted versus adjusted non-dimensional rate

Discussion

Quarter-Chord Separation Delay. Although there is some scatter in the quarter-chord separation data shown in Fig. 8, it appears that the trend in dynamic delay is consistent with the theoretical method, as can be seen by the overlay of the predicted delay (c.f., Fig. 4). It is clear that using the adjusted non-dimensional rate of equation (5) does not further collapse the data, as can be seen in Fig. 13. The trends are reversed and the data is spread out in identically the same way as the theoretical prediction.

Stall Delay. There are a number of observations that can be drawn from the dynamic-stall delay given in Fig. 12. First, as in the case of the separation delay, use of the adjusted non-dimensional rate of equation (5) does not improve the collapse of the data as can be seen in Fig. 14. Secondly, cross correlation between Figs. 8 and 12 show that the splitting of the observed stall-angle delay data for the different pitch-locations follows the same trend as the quarter-chord separation delay, and the spacing of the splitting is similar in extent. Using the same arguments used in reference [4], it is possible to demonstrate that the additional delay in angle of attack between quarter-chord separation and stall is consistent with the detachment of the flow just after quarter-chord separation, the formation of a vortex, and the convection of the vortex over the airfoil. First, let us assume that the catastrophic detachment of the flow and formation of the vortex is nearly coincident with quarter-chord separation. Once the vortex has detached it becomes a free vortex subject to motion based on the flow velocity. Robinson, et al. [17] have shown that this convection speed is on the order of 0.4 U_∞, and following Chow and Chiu [18] the vortex influences the lift spike over a distance of roughly half to 75 percent the chord length, c; then the convection time of this influence is

$$t_c \simeq 3.5 \frac{1/2c}{U_\infty} \tag{10}$$

where the 1/2 is introduced for convenience. In this time the angle of attack will change by

$$\Delta\alpha = \dot{\alpha} t_c \simeq 200 \frac{(1/2\ c\dot{\alpha})}{U_\infty} \tag{11}$$

where $\dot{\alpha}$ is in radians/s, and the predicted delay is in degrees, so that the difference between the separation angle of attack and the stall angle of attack should scale as

$$\Delta\alpha_s - \Delta\alpha_{SEP} \simeq 200\dot{\alpha}_{ND} \tag{12}$$

Thus, such a treatment would indicate that the difference between the two should widen, approximately linearly, with increasing $\dot{\alpha}_{ND}$. In fact, the data of reference 4 did widen linearly and by nearly the amount given by equation (12). It can be shown that application of equation (12) to the predicted (or actual, since they appear to agree) quarter-chord separation delay leads to delayed stall predictions of approximately those observed and given in Fig. 12.

We may thus conclude that the differences in dynamic stall delay when the pitch location is changed appear to be due primarily to the effect of pitch location on the delay in dynamic quarter-chord separation. This conclusion is consistent with the findings of Helin and Walker [19], who noted from flow-visualization studies of constraint-$\dot{\alpha}$ experiments that the detachment of the flow from the airfoil, and subsequent formation of the vortex was delayed to higher angles of attack as pitch location was moved aft (from leading toward trailing edge) on the airfoil; however, once the vortex was formed, it seemed to convect over the airfoil at the same rate as would be expected of a midchord-pitching airfoil. This seems to imply that no special "vortex-trapping advantage" is realized by movement of the pitch location along the chord line.

Conclusion

The results given in this paper demonstrate that pitch location does affect dynamic stall. The extent of the effect, although relatively small for $\dot{\alpha}_{ND}$ up to 0.04, is clearly evident. The fact that this effect is relatively small, is itself of interest; because most schemes devised for attempting to exploit dynamic stall for lift-augmentation favor pitching about the quarter chord. It also seems clear that the pitch-location dynamic-stall effects can be inferred from the theoretical prediction of the effect on delay in dynamic quarter-chord separation, at least for the constant $\dot{\alpha}$ case. Finally, for constant-$\dot{\alpha}$ motions, the nondimensional pitch rate of equation (1) appears to be the best nondimensional parameter for data collapse of pitch-location effect.

References

1 Karmer, von M., "Die Zunahume des Maximalauftriesbes von Tragflugeln bei plotzlicher Anstellwinkelvergro Berung (Boeneffekt)," *Zietschrift fur Flugtechnik und Motorluftschiffahrt*, Vol. 7, 14 Apr. 1932, pp. 185–189.

2 Ericsson, L. E., and Reding, J. P., "Unsteady Airfoil Stall, Review and Extension," *Journal of Aircraft*, Vol. 8, Aug. 1971, pp. 609–616.

3 Daley, D. C., and Jumper, E. J., "Experimental Investigation of Dynamic Stall for a Pitching Airfoil," *Journal of Aircraft*, Vol. 21, Oct. 1984, pp. 831–832.

4 Jumper, E. J., Schreck, S. J., and Dimmick, R. L., "Lift-Curve Characteristics for an Airfoil Pitching at Constant Rate," *Journal of Aircraft*, Vol. 25, Oct. 1987, pp. 680–687.

5 Jumper, E. J., Hitchcock, J. E., Lawrence, T. S., and Docken, R. G., Jr., "Investigating Dynamic Stall Using a Modified Momentum-Integral Method," AIAA paper number AIAA-87-0431, Jan. 1987.

6 Jumper, E. J., "Mass Ingestion: A Perturbation Method Useful in Analyzing Some Boundary-Layer Problems," ASME preprint number 86-WA/FE-10, Dec. 1986.

7 Francis, M. S., Keesee, J. E., and Rettelle, J. P., Jr., "An Investigation of Airfoil Dynamic Stall with Large Amplitude Motion," Technical Report FJSRL-TR-83-0010, Oct. 1983, F. J. Seiler Research Laboratory.

8 Carta, F. O., and Carlson, R. G., "Determination of Airfoil and Rotor Blade Dynamic Stall Response," *Journal of the American Helicopter Society*, Apr. 1973, pp. 31–99.

9 McAllister, K. W., Carr, L. W., and McCroskey, W. J., "Dynamic Stall Experiments on the NACA 0012 Airfoil," NASA Technical Paper 1100, 1978.

10 Silverstein, A., Katzoff, S., and Hootman, J. A., "Comparative Flight and Full-Scale Wind-Tunnel Measurements of the Maximum Lift of an Airplane," NACA Report No. 618, 1938.

11 Walker, J. M., Helin, H. E., and Strickland, J. H., "An Experimental Investigation of an Airfoil Undergoing Large Amplitude Pitching Motions," AIAA paper Number AIAA-85-0039, Jan. 1985.

12 Tupper, K. W., "The Effect of Trailing Vortices on the Production of Lift on an Airfoil Undergoing a Constant Rate of Change of Angle of Attack," Thesis, AFIT/GAE/AA/83D-24, Dec. 1983, Air force Institute of Technology.

13 Allaire, A. J. S., "Investigation of Potential and Viscous Flow Effects Contributing to Dynamic Stall," Thesis, AFIT/GAE/AA/84S-1, Sept. 1984, Air Force Institute of Technology.

14 Bisplinghoff, R. L., and Ashley, H., *Principles of Aeroelasticity*, Dover Publications, New York, 1975.

15 von Wagner, H., "Dynamischer Auftrieb von Tragflugeln," *Zeitchrift fuer Angewandte Mathematik und Mecdhanik*, Vol. 5, Feb. 1925, p. 17.

16 Dimmick, R. L., "Pitch-Location Effects on Dynamic Stall," Thesis, AFIT/GAE/AA/85D-4, Dec. 1985, Air Force Institute of Technology.

17 Robinson, M., Helin, H., Gilliam, F., Russell, J., and Walker, J., "Visualization of Three-Dimensional Forced Unsteady Separated Flow," AIAA Paper AIAA-86-1066. May 1986.

18 Chow, C. Y., and Chiu, C. S., "Unsteady Loading on an Airfoil Due To Vortices Released Intermittently from its Surface," *Journal of Aircraft*, Vol. 23, Oct. 1986, pp. 750–755.

19 Helin, H. E., and Walker, J. M., "Interrelated Effects of Pitch Rate and Pivot Point on Airfoil Dynamic Stall," AIAA Paper AIAA-85-0130, Jan. 1985.

A. Ihara
Associate Professor.

H. Watanabe
Research Associate.

Institute of Fluid Science,
Tohoku University,
Sendai, Japan

S. Shizukuishi
Graduate Student,
Tohoku University,
Sendai, Japan

Experimental Research of the Effects of Sweep on Unsteady Hydrofoil Loadings in Cavitation

An experiment was conducted to investigate the effects of sweep angle on hydrofoil loadings in cavitation. Tests were carried out in a water tunnel on constant-chord full-span hydrofoils at four angles of attack for sweep angle 0, 15, 30, and 45 deg, respectively. The results obtained were that the strong, periodic oscillations which appeared under some conditions of partial cavitation decreased their amplitudes with an increase in sweep angle. Moreover, the lift-drag ratio showed the higher value for the highly swept hydrofoil and remained higher down to some lower cavitation numbers than those for the slightly swept model.

Introduction

It has been well-known for some decades that cavitation causes a severe oscillation on the hydrofoil under some conditions of partial cavitation. These oscillatory phenomena, which are the main obstacle to speeding up the hydraulic machinery, have interested several investigators [1-5], and have been investigated by them to elucidate the details. In these days, however, to suppress such an oscillation seems to be an important problem for the engineering of hydraulic machinery.

One of the ideas for suppressing such an oscillation is to give a sweep angle to the test model, because the sweep angle will cause secondary flow around it and make inhomogeneous cavity break-off from its surface, weakening the change of circulation around it. From the above-mentioned viewpoint, Ihara [6] has carried out the experiments of measuring unsteady hydraulic forces for the nonlifting body by using a circular cylinder as a test model and has obtained a result that the sweep angle has remarkably reduced the amplitude of oscillation induced by cavitation. It is an interesting problem to know whether the sweep angle given to the lifting body such as a hydrofoil weakens the oscillation caused by cavitation as well as that given to the nonlifting body. Experimental studies on the effects of sweep angle on the performance of a cavitating hydrofoil are not new. Crimi [7] has made a report on the effects of a sweep angle on the cavitation performance of four constant-chord semi-span hydrofoils with the NACA 16-309 foil section. However, Crimi's experiment has not clarified the unsteady characteristic of loadings. Moreover, none has reported on the cavitation performance of full-span hydrofoil as far as the authors know.

The main object of this study is to clarify experimentally the effects of a sweep angle on the steady and unsteady loadings of cavitating hydrofoils with the constant-chord and full-span configuration, for the purpose of applying it to the internal machine such as a water turbine or pump. The test models have the Clark Y. 11.7 foil section and sweep angles 0, 15, 30, and 45 deg, respectively.

Experimental Methods

Test Hydrofoils. A series of constant-chord, full-span hydrofoils with sweep angles were tested. They were divided into four classes of sweep angles $\tau=0$, 15, 30, and 45 deg. Each class had the angles of attack $\alpha=0$, 5, 10, and 15 deg, respectively. All models had the same chord length and foil section in the vertical plane normal to the foil axis. The basic nonswept model had the span of about 100 mm and the chord length of 60 mm, giving the aspect ratio of 1.7 which is probably corresponding to the ordinary ones in an axial flow pump. As indicated in Fig. 1, the foil section in the vertical plane normal to the foil axis had the Clark Y. 11.7 profile. This foil section in spite of the classical one was selected because the foil characteristics were well-known [8, 9]. Each hydrofoil was arranged at the test section so that the base plate connected to the force measuring device would stand downstream. As the cross-section of the swept foil in the vertical plane parallel to the freestream differs with the angle of attack, the hydrofoil integrated with the base plate was individually manufactured corresponding to the angle of attack for the sweep angle given. Each model had the parallel alignment of the foil axis to the upper and lower wall of the test section and the full span for the flow width. In case of a zero sweep angle, only one test model was made because the angle of attack could be controlled by rotating it around the center of the hydrofoil. To construct the test models, the following method was employed: (i) At first, the base plate and the hydrofoil were made of brass independently of each other. The hydrofoil was finished by hand to get the accuracy within ±0.05 mm for the prescribed value after it was machined by a numerically controlled milling machine. (ii) The hole with the cross-sectional shape of the foil section in the vertical plane

---

Contributed by the Fluids Engineering Division for publication in the JOURNAL OF FLUIDS ENGINEERING. Manuscript received by the Fluids Engineering Division October 6, 1987.

Table 1 Sweep angle and angle of attack for each test model

Sweep Angle		Angle of Attack	
nominal value	real value	nominal value	real value
15°	16.3°	0°	2.0°
15°	14.2°	5°	4.5°
15°	14.8°	10°	11.0°
15°	16.8°	15°	14.8°
30°	30.0°	0°	0.4°
30°	29.6°	5°	3.7°
30°	29.4°	10°	8.0°
30°	28.1°	15°	13.8°
45°	44.4°	0°	1.6°
45°	44.6°	5°	6.2°
45°	44.5°	10°	11.1°
45°	44.6°	15°	15.8°

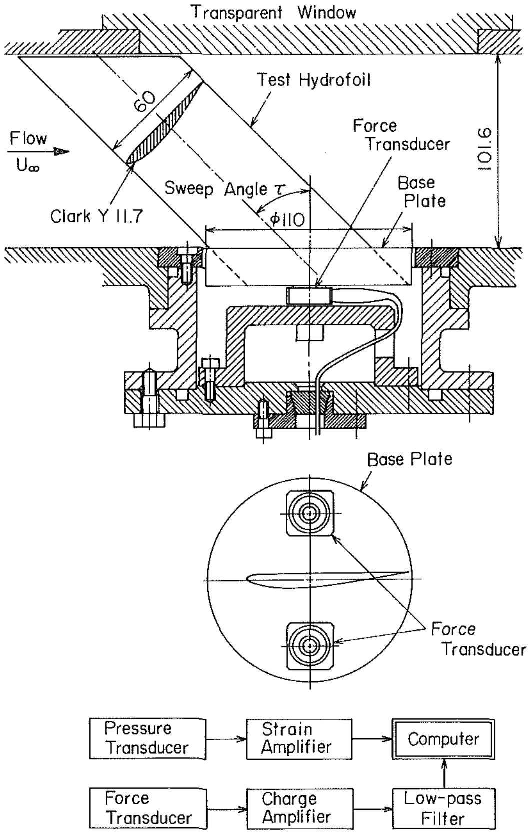

Fig. 1 Arrangement of the test hydrofoil and the force measuring system at the test section

parallel to the free stream and the axis parallel to the foil axis was made in the base plate by using a spark erosion machine. (iii) The hydrofoil was inserted in this hole and then connected to the base plate by brazing. (iv) Finally, the corner between the base plate and the hydrofoil was finished by hand and then the length of the hydrofoil was adjusted by cutting the edge to fit into the test section. As it was difficult to combine the hydrofoil with the base plate accurately to the prescribed angle of attack for the prescribed sweep angle, the models accomplished had some differences both in sweep and incident angles from the nominal values. These differences are shown in Table 1. The gap between the model end and the facing wall of the test section was within 0.1 mm.

Force Balance. As indicated by Murai et al. [9], the loading acting on the swept-back hydrofoil placed within parallel side walls is not distributed uniformly along the spanwise direction. Therefore, the balance based on the measurement of bending moment could not be employed. Furthermore, the balance for measuring unsteady forces was required to have a high eigenfrequency above the frequency of interest. Therefore, the loadings were measured by using the piezoelectric load washer (Type 9251A, Kistler Instrument) which can decompose a shearing force acting in any direction into components perpendicular to one another. As illustrated in Fig. 1, the balance was made of two load washers. With the aid of elastic bolts and the base plate, two load washers were pressed to the vertical wall of the balance box, so that the shear forces on the load washers could be transmitted into the quartz by friction. The maximum force could be 2.5kN where the threshold for dynamic measurements was 0.1N. Interference between the drag D and the lift L and vice versa was lower than 5 percent and linear, so that the correction of this leak could easily be made by the computer after A-D sampling. Because of the high rigidity of the quartz elements themselves, the natural frequency of the force measuring system was determined by the foil stiffness. The eigenfrequency of this force measuring system was, in any case, more than twice that of the

Nomenclature

A = plane area of test hydrofoil $= cl$
c = chord length normal to foil axis
c' = chord length parallel to freestream
C_D = drag coefficient $= 2D/\rho U_\infty^2 A$
$C_{D\mathrm{mean}}$ = time mean of drag coefficient
$C_{D\mathrm{rms}}$ = root mean square of drag coefficient fluctuations
C_L = lift coefficient $= 2L/\rho U_\infty^2 A$
$C_{L\mathrm{mean}}$ = time mean of lift coefficient
$C_{L\mathrm{rms}}$ = root mean square of lift coefficient fluctuations
D = drag force on model
D' = skin friction acting on base plate
f = frequency of oscillation
H = height of flow passage at test section
l = span
L = lift force on model
P_∞ = tunnel static pressure
P_v = vapor pressure of water
Re = Reynolds number $= U_\infty c/\nu$
U = freestream velocity
U_∞ = mean freestream velocity $= \int_0^W U(X)dX/W$
W = width of flow passage at test section
X = distance from side wall at test section
α = angle of attack in vertical plane normal to foil axis, degrees
α' = angle of attack in vertical plane parallel to freestream, degrees
ν = kinematic viscosity of water
ρ = density of water
σ = cavitation number $= 2(P_\infty - P_v)/\rho U_\infty^2$
τ = sweep angle, degrees

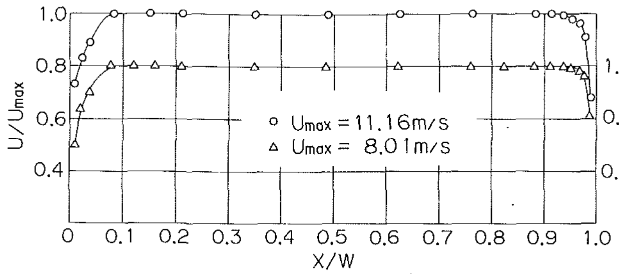

Fig. 2 Velocity distributions at the center of the test section

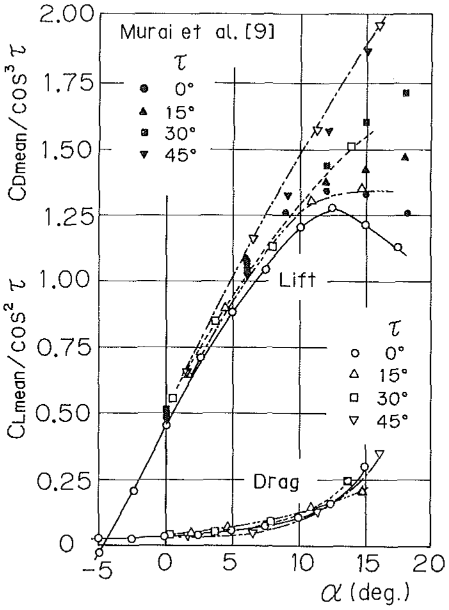

Fig. 3 Lift and drag coefficients versus the angle of attack at the fully wetted condition

third harmonics of the resonant frequency induced by cavitation. The evaluation of the signal was performed by using a digital computer equipped with an analog-to-digital converter. The mean force coefficients $C_{L\text{mean}}$, $C_{D\text{mean}}$, temporary maximum and minimum force coefficients $C_{L\max}$, $C_{L\min}$, $C_{D\max}$, $C_{D\min}$, root mean square of fluctuating force coefficients $C_{L\text{rms}}$, $C_{D\text{rms}}$ and power spectrum of the force fluctuations were calculated from the sampled data. The sampling of data was carried out at the rate of 500 Hz for 30 seconds. All of these data were used for calculation. Power spectra were calculated by using F.F.T. algorithm. In these measurements, the measured data included the skin friction force acting on the base plate. Furthermore, no corrections were made for tunnel interference effects such as wall blockage, wake blockage and longitudinal pressure gradient.

Cavitation Test

The test model was mounted on the measuring section 101.6 mm in width and 260 mm in height of the cavitation tunnel in the Institute of Fluid Science, Tohoku University. Details of this facility can be seen in reference [1]. As the velocity distribution is important for the force measurement for the model extended over the full flow-width, it was measured at the middle height of the test section by using laser Doppler velocimeter (55X system, DISA). The result is shown in Fig. 2. The thickness of the turbulent boundary-layer adjacent to the side wall was about 8 percent of the flow width. The average velocity U_∞ for full flow-width was employed for calculating force coefficients and cavitation numbers. The longitudinal freestream turbulence level at this test section was 0.73 percent at the tunnel speed 9.04m/s. The air-content of the tunnel water was measured with the Van Slyke type air-content meter which had been designed by Numachi [10] and was found to be between 31 and 34 PPM for the test run and was always oversaturated. Cavitation number was calculated from the following equation:

$$\sigma = 2(P_\infty - P_v)/\rho U_\infty^2 \qquad (1)$$

where P_∞, P_v, and U_∞ are the static pressure of the freestream, the vapor pressure corresponding to the working-water temperature and the mean freestream velocity, respectively. Force measurements were conducted at the tunnel speed 10.0m/s, and the tunnel water temperature was between 10.8, and 14.9°C. Reynolds number based on the chord length c and the tunnel speed U_∞ was about 5.0×10^5.

Experimental Results

Force Coefficients at Fully Wetted Condition. The mean lift and drag coefficients at the fully wetted condition are shown in Fig. 3 against the angle of attack α which is measured in the vertical plane normal to the foil axis. The lift coefficients are divided by $\cos^2\tau$ and the drag coefficients by $\cos^3\tau$ to confirm the realization of the law of cross flow [11]. It can be noticed from this figure that the stall angle increases with an increase in sweep angle. Each curve for the drag coefficient is almost coincident. However, a good quantitative coincidence cannot be obtained for the lift coefficients. $C_L/\cos^2\tau$ corresponding to the high sweep angle shows somewhat high value. This tendency is probably caused by the wall blockage because the pitch-chord ratio (H/c', where H is the height of the flow passage at the test section, and c' is the chord length measured in the freestream direction) of the test system decreases with an increase in sweep angle because c' increases with an increase in sweep angle. To confirm the validity of our measurements, the lift data obtained by Murai et al. [9] for Clark Y. 11.7 foil section by integrating the pressure distribution measured around the model surface are plotted on the same figure. Our results coincide approximately with the data obtained by Murai et al., though a somewhat mild increase in the slope of the lift coefficient is obtained in our case. These differences of gradient are probably caused by the difference of the pitch-chord ratio (H/c') of the test equipment.

Cavitation Appearance. The cavitation aspects at the angle of attack $\alpha = 10$ deg are shown in Figs. 4 (*a*, *b*, *c*, *d*) for each sweep angle in some different cavitation numbers. A good qualitative indication of the effects of the sweep on cavitation can be obtained from these figures. The cavity length is almost the same in the spanwise direction when the unswept foil is partially cavitating. The highly swept foil, on the other hand, can be seen to undergo much cavitation over the root, and a good deal of the foil surface near the tip is wetted. On the 45 deg swept foil, the cavity break-off as has been seen on the unswept foil, can scarcely be found. The difference in this cavitation occurrence might cause the difference in the unsteady characteristics of loading. Details will be described later.

Force Coefficients at Cavitating Conditions. The force coefficients measured at cavitating conditions are shown in Figs. 5(*a*, *b*), 6(*a*, *b*), 7(*a*, *b*), and 8(*a*, *b*). In these figures, the mean lift and drag coefficients, $C_{L\text{mean}}$, $C_{D\text{mean}}$, the root mean square of the lift and drag coefficient fluctuations, $C_{L\text{rms}}$, $C_{D\text{rms}}$, the fluctuating range of C_L and C_D are plotted against the cavitation number for $\alpha = 0$, 5, 10, and 15 deg, each graph being for a different sweep angle. The remarkable phenomenon which can be seen from these figures is that fluctuations included in the lift and drag coefficients decrease with an increase in sweep angle.

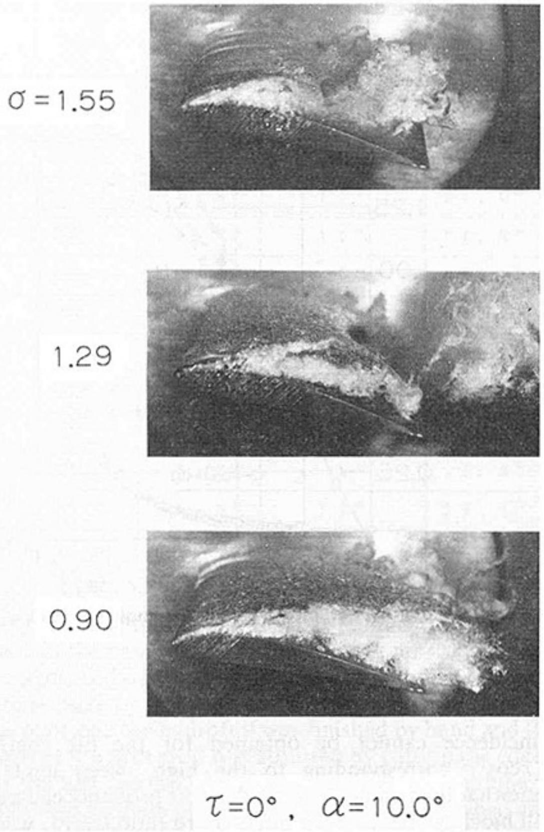

Fig. 4(*a*) Cavitation occurring on the test model at $\alpha = 10$ and $\tau = 0$ deg

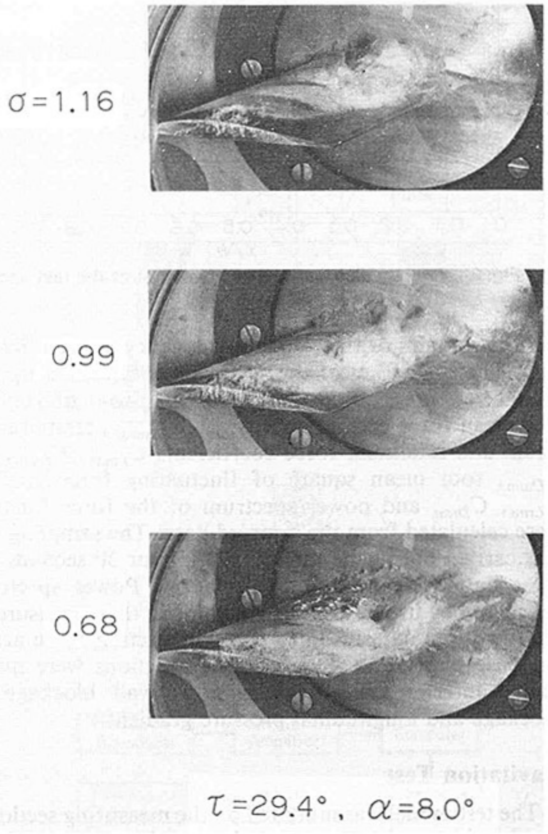

Fig. 4(*c*) Cavitation occurring on the test model at $\alpha = 8.0$ and $\tau = 29.4$ deg

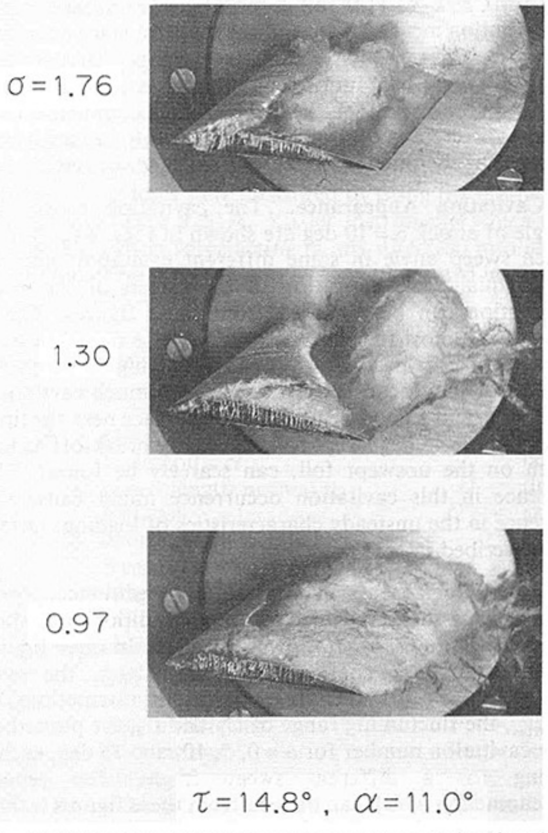

Fig. 4(*b*) Cavitation occurring on the test model at $\alpha = 11.0$ and $\tau = 14.8$ deg

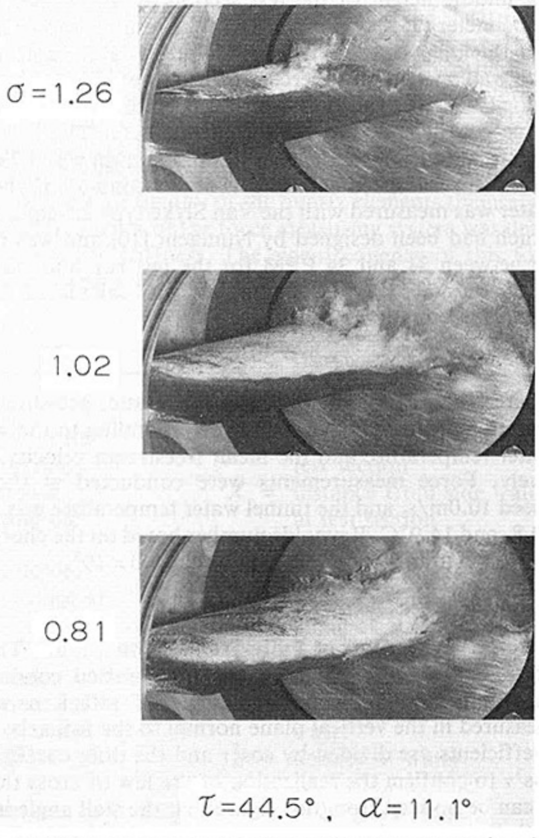

Fig. 4(*d*) Cavitation occurring on the test model at $\alpha = 11.1$ and $\tau = 44.5$ deg

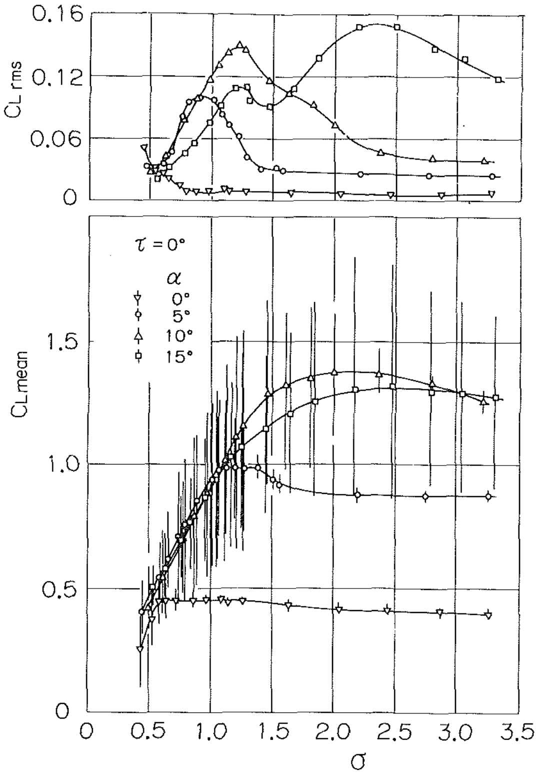

Fig. 5(*a*) **Mean lift coefficients versus cavitation number at $\tau = 0$ deg. Bar is the range of the lift coefficient fluctuation**

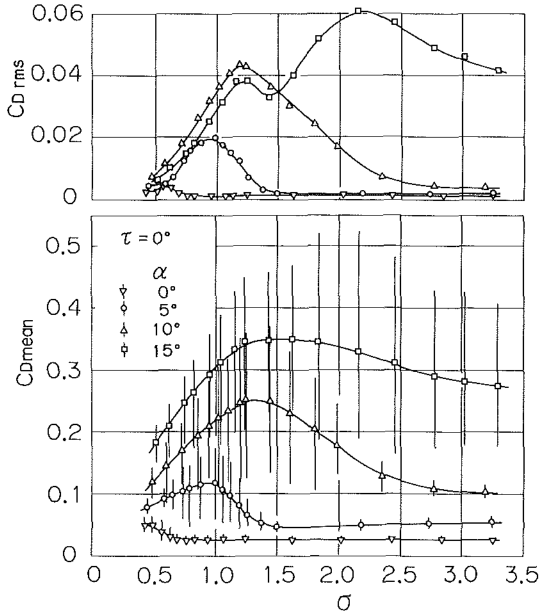

Fig. 5(*b*) **Mean drag coefficients versus cavitation number at $\tau = 0$ deg. Bar is the range of the drag coefficient fluctuation**

Discussion of Results

Amplitude of Strong Oscillations. As previously mentioned, the amplitude of the strong oscillations decreases with an increase in sweep angle. To show this fact more quantitatively, the root mean square value of the lift coefficient fluctuations at $\alpha = 10$ deg divided by the mean value is plotted in Fig. 9 against the cavitation number. The data plotted were obtained by interpolation from the measured data because the measurements were carried out at the slightly different angles from nominal values. The effects due to a slight difference in sweep angle from nominal values are not removed because it can be thought to be small. We can see from this figure that $C_{L\mathrm{rms}}$ which amounts to about 13 percent of the mean value on the unswept foil in maximum decreases with an increase in sweep angle, and that at last on the 45 deg swept foil it takes a value of only a few percent, which is slightly higher than that at the fully wetted conditions. This fact tells us that to give a large sweep angle to the model is an excellent method for suppressing an oscillation induced by cavitation.

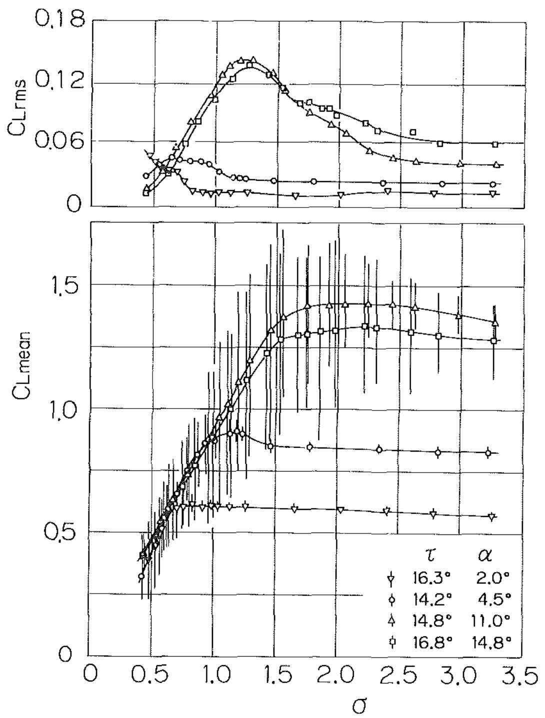

Fig. 6(*a*) **Mean lift coefficients versus cavitation number at $\tau \simeq 15$ deg. Bar is the range of the lift coefficient fluctuation**

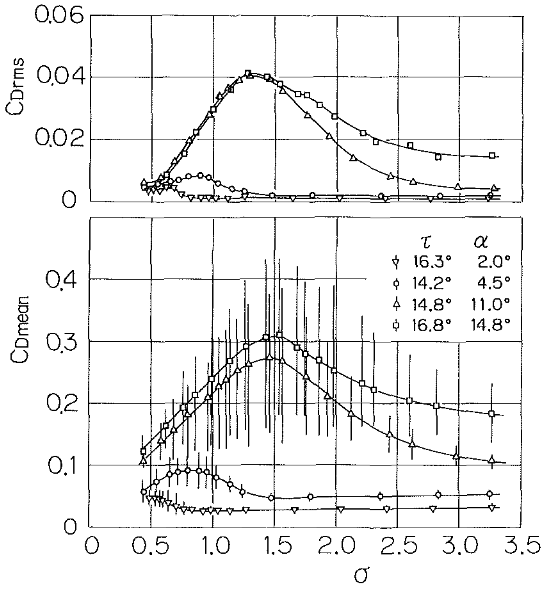

Fig. 6(*b*) **Mean drag coefficients versus cavitation number at $\tau \simeq 15$ deg. Bar is the range of the drag coefficient fluctuation**

Force Similarity at the Cavitating Conditions. To investigate the force similarity at the cavitating conditions, the data obtained were arranged by the velocity component normal to the foil axis. The results obtained at $\alpha = 10$ deg by the interpolation of the data are shown in Fig. 10. As can be seen

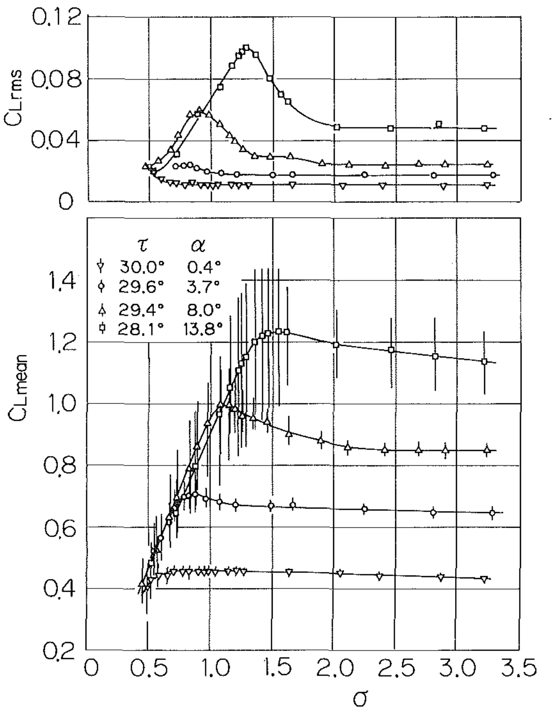

Fig. 7(a) Mean lift coefficients versus cavitation number at $\tau \simeq 30$ deg. Bar is the range of the lift coefficient fluctuation

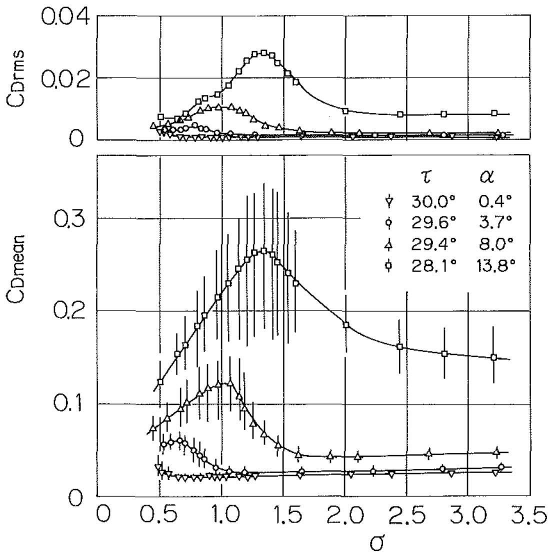

Fig. 7(b) Mean drag coefficients versus cavitation number at $\tau \simeq 30$ deg. Bar is the range of the drag coefficient fluctuation

from this figure, a good coincidence in $C_{D\mathrm{mean}}/\cos^3\tau$ is obtained in the strong oscillatory range though it is not in $C_{L\mathrm{mean}}/\cos^2\tau$. Moreover, we can notice that the range of the strong oscillation can approximately be expressed by $\sigma/\cos^2\tau = 0.7 \sim 2.0$ in spite of the difference in sweep angle except the case on the 45 deg swept foil. This fact tell us that the range of the cavitation number where strong oscillation occurs for the swept foil can be deduced from the data of the unswept foil.

Lift-Drag Ratios. It is important to know a lift-drag ratio for designing a hydraulic machine. The lift-drag ratios at $\alpha = 5$ and 10 deg are plotted in Figs. 11(*a*, *b*) against the cavitation number. These figures were also obtained by interpolation from the measured data. At a glance, we can notice that the lift-drag ratios on the highly swept foil are superior to those on with smaller sweep at both angles of attack in the full range of cavitation number, particularly in the range of low cavitation number, though the data on the unswept foil are superior to those on the 15 deg swept foil at some cavitation numbers. This fact tells us that there is a possibility to speed up the hydraulic machine considerably by employing a highly swept hydrofil with high efficiency.

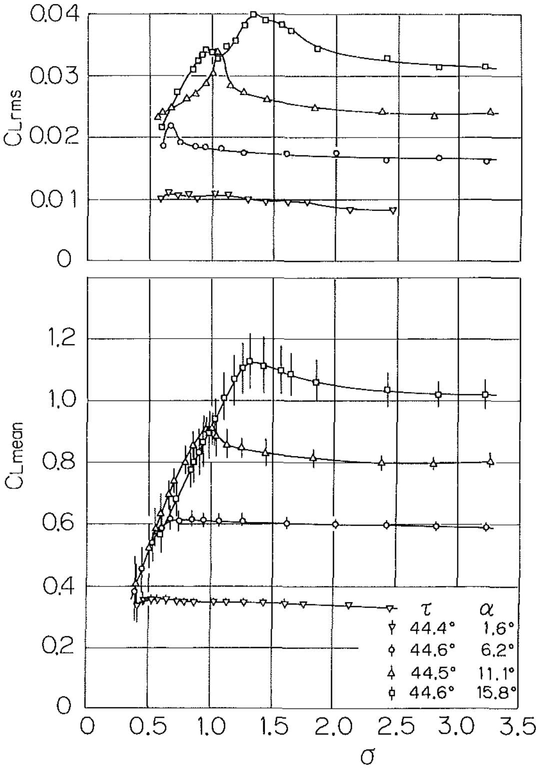

Fig. 8(a) Mean lift coefficients versus cavitation number at $\tau \simeq 45$ deg. Bar is the range of the lift coefficient fluctuation

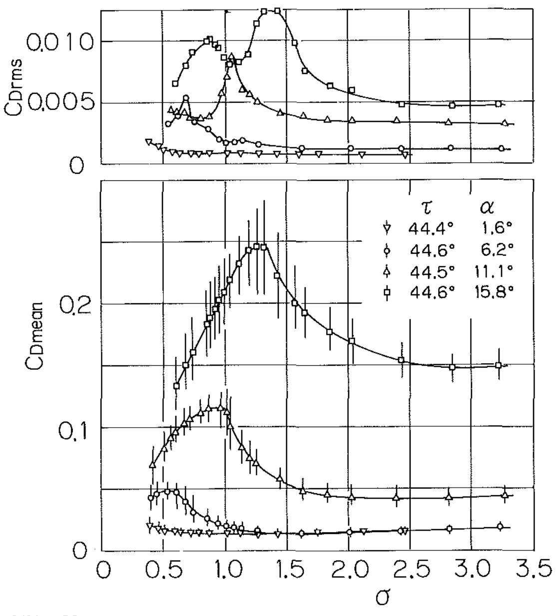

Fig. 8(b) Mean drag coefficients versus cavitation number at $\tau \simeq 45$ deg. Bar is the range of the drag coefficient fluctuation

Oscillating Characteristics. The power spectra of lift force fluctuations at $\alpha \simeq 10$ deg are shown in Fig. 12 for each sweep angle and the cavitation number at which the oscillation was severest. It can be seen from this figure that the height of reso-

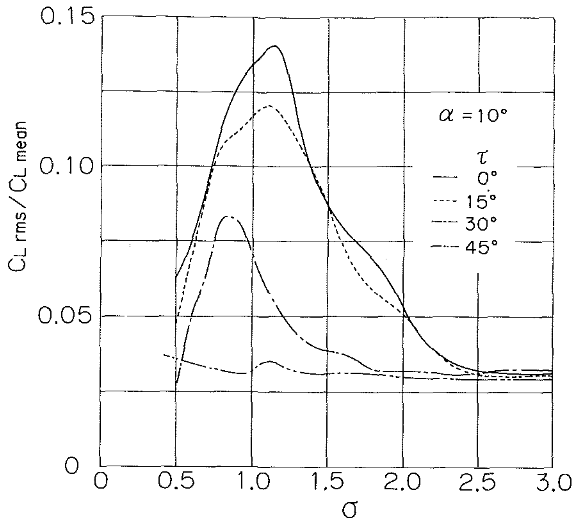

Fig. 9 C_{Lrms}/C_{Lmean} versus cavitation number at $\alpha = 10$ deg for various sweep angles. (These diagrams were obtained by interpolation from measured data.)

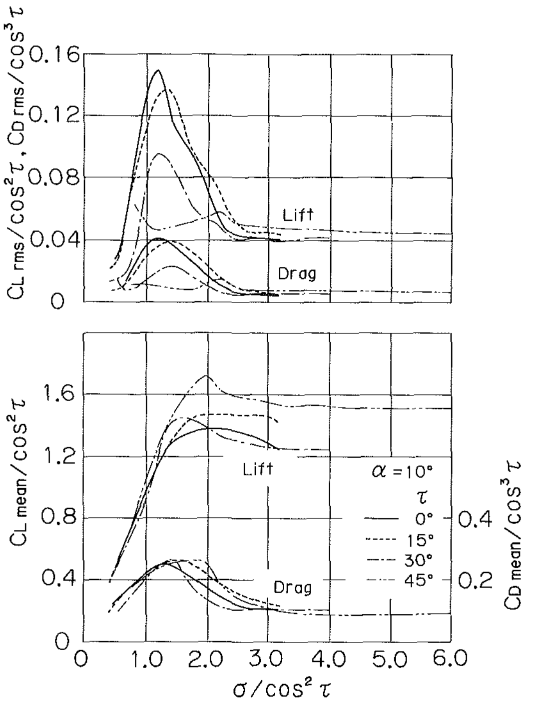

Fig. 10 Lift and drag coefficients versus cavitation number based on the velocity component normal to the foil axis at $\alpha = 10$ deg. (These diagrams were obtained by interpolation from measured data.)

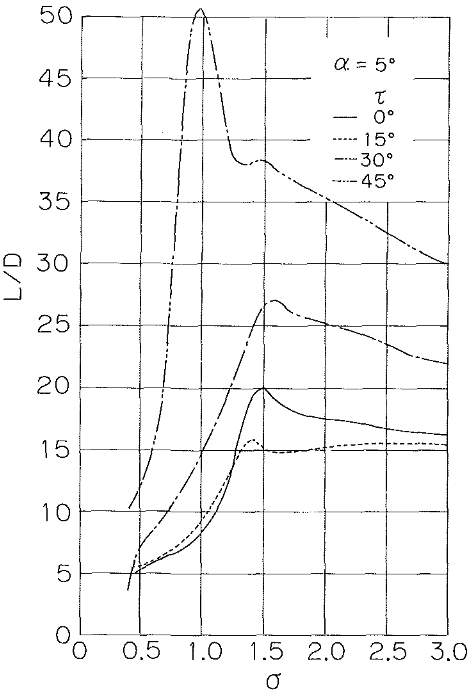

Fig. 11(*a*) Mean lift-drag ratios versus cavitation number at $\alpha = 5$ deg. (These diagrams were obtained by interpolation from measured data.)

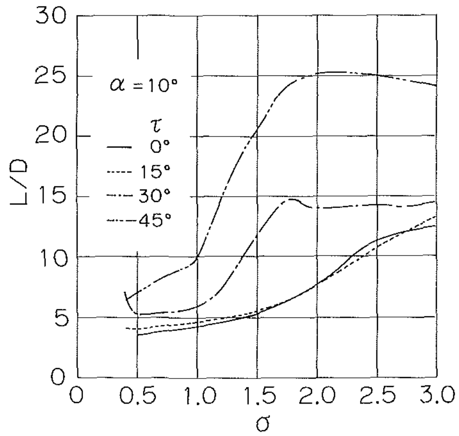

Fig. 11(*b*) Mean lift-drag ratios versus cavitation number at $\alpha = 10$ deg. (These diagrams were obtained by interpolation from measured data.)

nant peak about 25 Hz decreases with an increase in sweep angle until it disappears for the 45 deg swept foil. This result can be supposed to correspond to the fact that the large regular break-off of cavities observed for the lower sweep angle (Fig. 4(*a*, *b*, *c*)) did not occur at 45 deg (Fig. 4(*d*)). It is interesting to note that the disappearance of the periodic cavity shedding reported by Ihara [6] on the nonlifting body at a large yaw angle also occurs on the lifting body such as a hydrofoil. The power spectra of the lift fluctuation were used to measure the frequency of the strong oscillation of cavitation. The results obtained are shown as Strouhal number against $\sigma/\cos^2\tau$ in Fig. 13. As a velocity scale, the velocity component normal to the foil axis was employed to calculate the Strouhal number. The reason is to confirm whether the constant Strouhal number for the cavity shedding is obtained in spite of the difference of sweep angle as well as for the vortex shedding from yawed circular cylinders as has been reported by Smith et al. [13]. In comparison, data obtained by other investigators are also plotted on the same figure: a plano-convex section by Wade and Acosta [3], an elliptic-parabolic section by Alexander [4] and an NACA 4412 section by Nishiyama et al. [5]. Results for the 45 deg swept foils are not presented because no peak appeared in the power spectrum. As can be seen from this figure, the range of $fc/U_\infty \cos\tau$ for the unswept and swept foils as well almost coincides with the results obtained by other investigators, though our data have a tendency to increase somewhat with an increase in sweep angle.

Experimental Uncertainty

The lift data shown in Figs. 5(*a*), 6(*a*), 7(*a*) and 8(*a*) have a maximum uncertainty of about 3 percent except the dispersion shown in the figures. This maximum uncertainty is primarily due to the zero drift of the force transducer of the piezoelectric type. The drag data shown in Figs. 5(*b*), 6(*b*), 7(*b*), and 8(*b*)

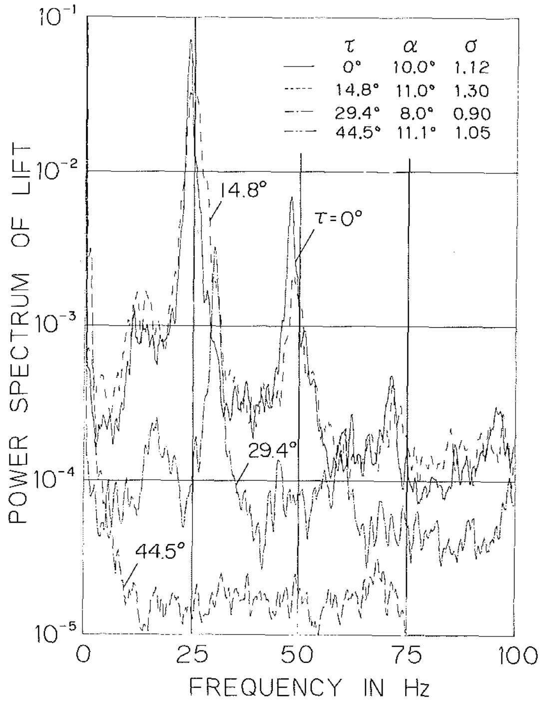

Fig. 12 Power spectrum of lift force fluctuations at $\alpha = 10$ deg for various sweep angles at the cavitation number where the oscillation is severest

also have the same uncertainty except the shearing force acting on the base plate. The amount of this shearing force can approximately be estimated from the skin friction acting on a flat plate in turbulent boundary layer. After some calculation the result is shown by the following equation:

$$C'_D = 2D'/\rho U_\infty^2 A = 0.0053 \cos \tau \qquad (2)$$

where A is the plane area of the foil and D' is the total skin friction acting on the base plate. If we assume that all of the skin friction contribute to the drag, the drag coefficients expressed in Figs. 5(*b*), 6(*b*), 7(*b*), and 8(*b*) include the error C_D shown by equation (2).

Conclusions

Through the measurements and analyses of hydraulic loadings acting on the swept hydrofoil of Clark Y. 11.7 foil section, combined with the photographic observation of cavitation, the following conclusions are obtained:

1. The amplitude of the strong oscillation decreases with an increase in sweep angle.
2. On the 45 deg swept foil, the oscillation which shows the reasonance does not occur. This is due to the disappearance of periodic cavity break-off from the model surface.
3. The range of cavitation number where cavitation causes a severe oscillation on the swept foil can approximately be expressed by that on the unswept model, if the flow velocity normal to the foil is selected for calculating a cavitation number.
4. The lift-drag ratio on the highly swept foil at cavitating conditions shows a higher value than that on a slightly swept foil and remains higher at lower cavitation numbers for the constant angle of attack.
5. The reduced frequency at which the cavitation causes the strong oscillation on the swept foil can approximately be found from data for the unswept foil, if the flow velocity normal to the foil axis is employed for calculating the reduced frequency.

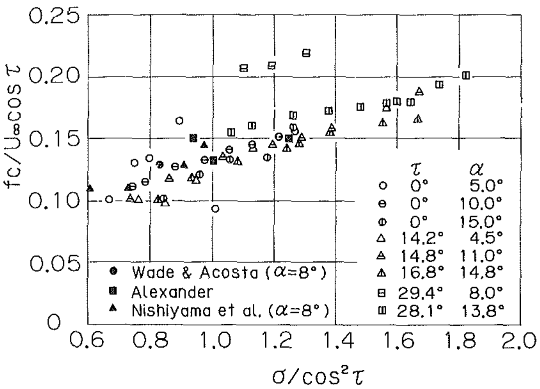

Fig. 13 Reduced frequencies based on the velocity component normal to the foil axis during the phase of maximum force oscillations

Acknowledgments

The authors would like to thank Professor A. Shima for his continuous support and suggestion. The authors are grateful to Mr. N. Hishinuma for his assistance with the preparation of the diagrams.

References

1 Numachi, F., "Cavitation Tests on Hydrofoils in Cascade," *Trans. ASME*, Vol. 75, 1953, pp. 1257-1269.

2 Knapp, R. T., "Recent Investigations of the Mechanism of Cavitation and Cavitation Damage," *Trans. ASME*, Vol. 77, 1955, pp. 1045-1054.

3 Wade, R. B., and Acosta, A. J., "Experimental Observations on the Flow Past a Plano-Convex Hydrofoil," ASME *Journal of Basic Engineering*, Vol. 88, No. 1, 1966, pp. 273-283.

4 Alexander, A. J., "Hydrofoil Oscillations Induced by Cavitation," *Proceedings of Conference on Cavitation*, Edinburgh, 1974, pp. 27-33.

5 Nishiyama, T., Yoshioka, S., and Akama, M., "Time Series Analysis of Hydrofoil Cavitation (1st Report, Self Oscillation Behavior in Transient Cavitation Region)," *Trans. JSME*, Series B, Vol. 49, 1983, pp. 2655-2661.

6 Ihara, A., "Effects of Yaw Angle to Unsteady Hydraulic Forces Acting on a Cavitating Circular Cylinder," *Proceedings of International Symposium on Cavitation*, Sendai, Vol. 1. 1986, pp. 145-150.

7 Crimi, P., "Experimental Study of the Effects of Sweep on Hydrofoil Loading and Cavitation," *Journal of Hydraulics*, Vol. 4, No. 1, 1970, pp. 3-9.

8 Numachi, F., Tsunoda, K., and Chida, I., "Cavitation Tests on Clark Y Profiles of Several Thickness Ratios," Reports of the Institute of High Speed Mechanics, Tohoku University, Vol. 8, No. 74, 1957, pp. 47-65.

9 Murai, H., Hirata, Y., and Mikashima, Y., "Research on Swept-back Blades Laid Between Parallel Walls, Report 1 (Experimental Research on Clark Y 11.7% Blade with Aspect Ratio of 2.0)," Reports of the Institute of High Speed Mechanics, Tohoku University, Vol. 17, No. 169, 1965, pp. 185-232.

10 Numachi, F., "Uber die Kavitationsentstehung mit besonderem Bezug auf den Luftgehalt des Wassers," Ingenieur-Archiv., Bd. VII, 1936, pp. 396-406.

11 Howarth, L., Modern Developments in Fluid Dynamics, Oxford University Press, 1956, p. 680.

12 Smith, R. A., Moon, V. T., and Kao, T. W., "Experiments on Flow about a Yawed Circular Cylinder," ASME *Journal of Basic Engineering*, Vol. 94, 1972, pp. 771-776.

The Synergistic Effect of Cavitation Erosion and Corrosion for Copper and Cupro-Nickel in Seawater

R. J. K. Wood
University of Southampton
Chemistry Department,
Southampton, England

S. A. Fry
Polytechnic South West,
Mechanical Engineering Department,
Plymouth, England

Experiments are described in which attempts have been made to investigate the fundamental mechanisms of the synergistic effect of cavitation erosion and corrosion. The design of an all-plastic cavitation tunnel is described which allows specimens to be held under potentiostatic control in a flowing seawater system. Experiments were conducted in a 10×20 mm working section with a 60° symmetrical wedge cavitation source at an upstream flow velocity of 14.7 m/s. An extensive test programme has been completed comprising three separate tests: Pure Erosion, Pure Corrosion and Combined Erosion and Corrosion, each conducted at two different cavitation intensities. These tests have concentrated on investigating the erosion/corrosion performance of copper in seawater. Preliminary results using cupro-nickel are also reported. It was found that a clearer indication of the synergistic effect was obtained from depth of penetration measurements than from mass loss measurements. The synergistic effect was found to be most marked when cavitation erosion occurs in the presence of mild corrosion. For the worse case studied, 50 percent of the depth of penetration was caused by synergistic mechanisms.

Introduction

In many engineering situations metal components are subjected to both cavitation erosion and corrosion simultaneously. For example, propeller blades, pump impellers, and valves on board ships suffer such combined attacks. The mass loss from such components is found to be greater than the summation of the mass losses due to individual attacks of cavitation erosion and corrosion. Therefore, there is a synergistic effect between the two forms of attack. Although considerable work has been carried out on the damage mechanisms of cavitation erosion and of corrosion in isolation, investigations into their combined effects have been limited. Shalnev [1] was the first to experiment on brass, bronze, and cast iron in boiled tap water and synthetic seawater. Results indicated a doubling of the mass loss for cast iron in sea water compared with tap water. Most investigations have concentrated on mild steels subjected to magnetostrictively induced cavitation, comparing mass losses obtained in corrosive (3 percent NaCl solution) and noncorrosive (distilled water) liquids (Martin [2], Okada [3], and Waring [4]). Simoneau [5] reports a multiplying factor of 5 when cavitation testing 1020 carbon steel in the corrosive liquid at 50°C. This factor is reduced to 1.5 for tests conducted at 22°C. However, no account of the pure corrosive mass loss is made and therefore the true synergistic effect cannot be evaluated. The synergistic contribution is the difference in mass loss between a combined cavitation erosion and corrosion attack and a simple summation of mass losses resulting from these mechanisms in isolation. See equation (1):

$$Mt = Me + Mc + Ms \qquad (1)$$

where

Mt = total mass loss
Me = pure cavitation erosion mass loss
Mc = pure corrosion mass loss
Ms = synergistic mass loss

Matsumura [6] further developed the magnetostrictive test procedure by removing the pure iron test specimen from a corrosive liquid bath (corrosion test), then exposing it to cavitation for a period and then returning it to the corrosive bath. This enabled the influence of cavitation on the corrosion process to be monitored. The dissolution rate was always increased but results were highly dependent on the static corrosion rate. A similar technique was used to investigate the influence of the environment on cavitation erosion. However, no clear dependence could be identified for erosion owing to the complex interplay of the test duration and the relative intensities of the cavitation erosion and corrosion.

The aim of the present work is to evaluate the true synergistic contribution to mass loss and to provide a better understanding of the mechanisms involved. It was decided that cavitation conditions should be produced hydrodynamically in a flowing system rather than using a magnetostrictive device since this may be more representative of real cavitation situations.

It had also been noted by the authors that cavitation conditions are affected by changing the working fluid from tap

---

Contributed by the Fluids Engineering Division for publication in the JOURNAL OF FLUIDS ENGINEERING. Manuscript received by the Fluids Engineering Division January 17, 1988.

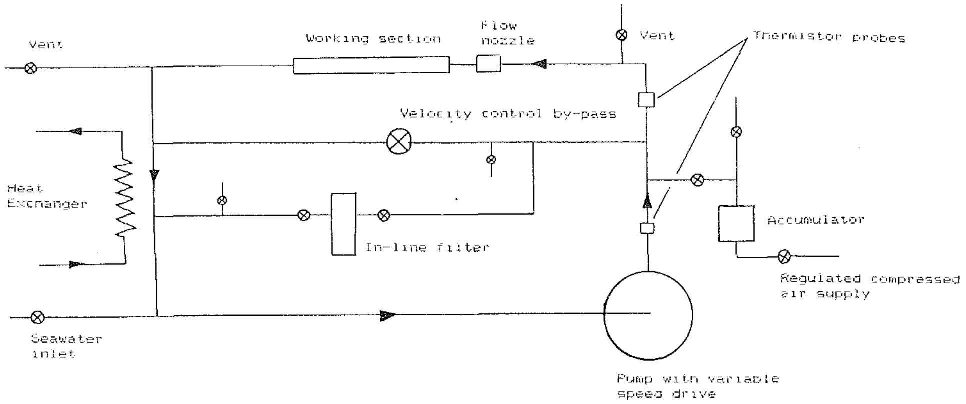

Fig. 1 Schematic diagram of flow loop

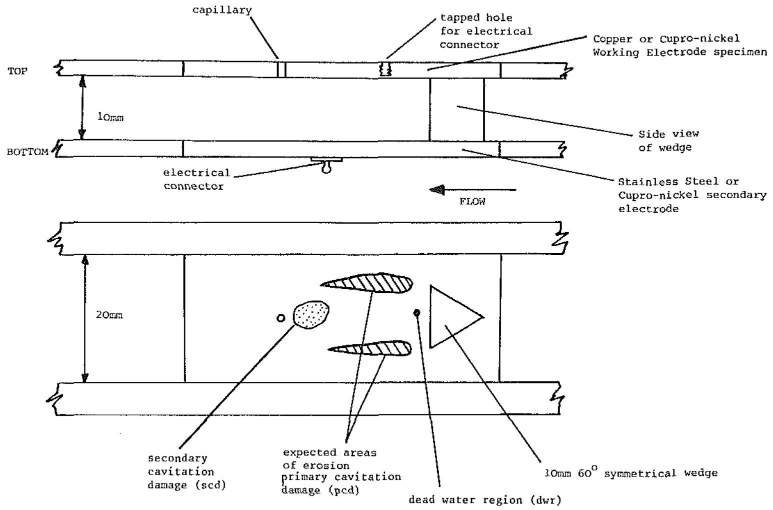

Fig. 2 Schematic diagram of the test section and corrosion cell

water to distilled water. For the present investigation, therefore, all tests are conducted using the same working fluid (sea water), and use potentiostatically controlled metal specimens to ensure accurate control of the corrosion rate. In the pure cavitation erosion tests cathodic protection is used to eliminate corrosion. Only a few previous papers have used potentiostatically controlled specimens subjected to hydrodynamic rather than magnetostrictively induced cavitation (Erdmann-Jesnitzer [7], Haferkamp [8]), but no comprehensive study under such conditions has been made.

Experimental

In order to obtain true hydrodynamic cavitation, as experienced in the field, and to enable accurate corrosion current measurements, an all-plastic cavitation flow tunnel was designed. The tunnel was constructed in uPVC plastic to avoid stray ion contamination of the corrosion cell mounted in the tunnel. The tunnel working section was constructed of Delrin giving a flow cross-section of 10 mm × 20 mm. Delrin was chosen for its good resistance to cavitation damage and its relatively low absorption of water. Incorporated in the working section design is a quick release specimen holder to enable regular weighing of specimens.

Figure 1 illustrates the flow loop. A flow nozzle with accompanying manometer upstream of the working section allows accurate measurement of the flow velocity through the section. The pressure upstream of the cavitation source is monitored by a precision pressure gauge off the low pressure line to the manometer. Upstream cavitation number σ (where $\sigma = \mathrm{Po} - Pv/{}^1/_2\rho v^2$) can then be calculated. The cavitation source used in this work is a 10 mm 60° symmetrical wedge which is known to be one of the most damaging geometries available (approximately twenty times more damaging than a circular cylinder of similar size). The fluid velocity through the working section is controlled by adjusting the speed of rotation of the circulating pump using the variable speed drive facility or by altering the valve setting on the by-pass. The tunnel pressure is regulated by compressed air pressure within an accumulator which acts as a transfer barrier. The temperature is maintained at a constant 25°C by a counterflow heat exchanger and refrigerator. This temperature is obtained after running the tunnel for approximately one hour. The air content of the circulated fluid is known to reach equilibrium within this time.

The specimen acts as the working electrode of a three electrode corrosion cell. The counter electrode of the cell is positioned directly opposite the working electrode as shown in Fig. 2. As the reference electrode of the three electrode corrosion cell measures the electrical potential it is sited as close to the working electrode surface as possible, thereby ensuring accurate control of that surface. Care has also been taken to locate the reference electrode away from any cavitation-affected areas on the surface, see Fig. 2. Perspex side walls of the working section allow cavity observation during tests. Under the cavitation conditions tested the cavities were unsteady, but the eye responds to a time average of events and it was possible to determine an "apparent" cavity length. A nondimensional cavity length (λ) is defined in Fig. 3.

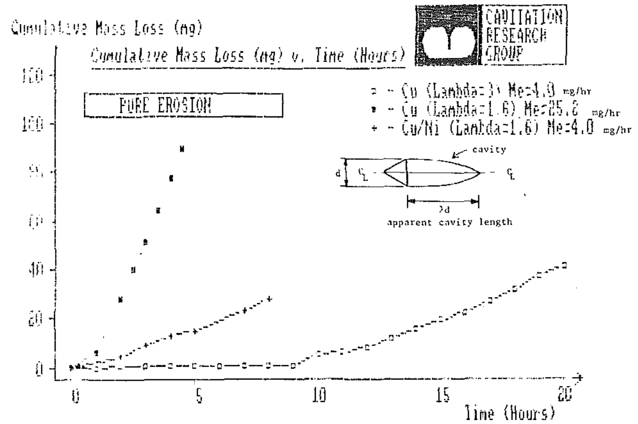

Fig. 3 CML versus time plots for Test I pure erosion for copper at $\lambda = 3.0$ ($\sigma = 6.00$) and 1.6 ($\sigma = 6.22$) and 70/30 Cu/Ni at $\lambda = 1.6$

It is most important that all tests should be carried out using similar quality sea water. Sea water was collected from Portland Harbour, south coast of the U.K., and delivered directly to the research facility where it was stored in an aerated, darkened tank. No experiments were conducted for at least seven days to allow living organisms in the sea water to reach a new level of equilibrium. The condition of the stored seawater was checked regularly by measuring the pH, conductivity, salinity, dissolved and total air content (yielding the free air content). These property measurements were taken to provide a reasonable indication of the quality of the sea water, and all tests were carried out with similar values (typical values are given in Table 1). To test this hypothesis a repeat tests was carried out using six weeks old sea water and freshly delivered sea water with similar measured properties. The results were the same in both cases.

The test programme outlined in Table 2 was devised so that copper and cupro-nickel specimens could be tested under different corrosion rates and at two cavitation intensities (i.e., $\lambda = 1.6$, $\sigma = 6.22$ and $\lambda = 3.0$, $\sigma = 6.00$). The corrosion rate is dependent on the overpotential (η) set on the potentiostat, where $\eta = E - E_{CORR}$.

E_{CORR} is the freely corroding potential and requires no potentiostatic control. The value of E_{CORR} is evaluated from a polarization curve where the measured corrosion currents for both positive and negative overpotentials are plotted on a log-linear scale. From such a plot the freely-corroding current can be gained (Fontana [9]). Tests were conducted at seven corrosion rates corresponding to overpotentials of 0, 5, 10, 15, 25, 50, and 100 mV. All tests were carried out with an upstream velocity of 1.47 m/s.

The materials used in these experiments were high conductivity copper to B.S.2874 and cupro-nickel 70/30 to B.S.2875.

Test I—Pure Erosion. The mass loss rate was obtained from plots of cumulative mass loss (CML) versus test duration. Figure 3 illustrates typical CML plots for copper under cavitation intensities $\lambda = 1.6$, $\sigma = 6.22$ (peak noise) and $\lambda = 3.0$, $\sigma = 6.00$. Also included are data points for Cu/Ni under $\lambda = 1.6$, $\sigma = 6.22$ conditions. This pure erosion data was obtained in sea water with the specimens held under cathodic protection to ensure no corrosive mass loss. An overpotential of $\eta = -140$ mV for copper and $\eta = -100$ mV for cupro-nickel, was sufficient to ensure cathodic protection without causing evolution of gas at the surface of the specimen (which, incidentally, had been found to affect the cavitation erosion mass loss). Each plot is typical of a ductile metal subjected to cavitation erosion. Initially no measurable mass loss can be detected (incubation period) which is followed by a short period of increasing mass loss rates until a steady state erosion period is established, where the mass loss rate is constant. From this region several data points are obtained and a linear regression applied to determine the mass loss rate. This required mass loss measurements to be taken hourly for $\lambda = 3.0$, $\sigma = 6.00$ and half-hourly for $\lambda = 1.6$, $\sigma = 6.22$ tests. The test duration allowed the mass loss to enter the steady state erosion period and for at least seven points to be obtained from within this region to enable the MLR to be evaluated, the MLR for pure erosion being denoted by Me.

Table 1

Temperature	19°C
Specific gravity	1.027 g/cm^3
Salinity	37 g/kg
Conductivity	4.3 S/m
Dissolved air	13.9 ml/l
Total air	18.1 ml/l
pH	8.00

Table 2 Test Programme

	Test	Cavitation Conditions	η	Readings Taken
I	Pure Erosion	Low intensity ($\lambda = 3.0$, $\sigma = 6.00$) and peak noise cavitation ($\lambda = 1.6$, $\sigma = 6.22$)	Cathodically protected	Balance
II	Pure Corrosion	Noncavitating	7 different values	Balance and current
III	Combined	Low intensity ($\lambda = 3.0$, $\sigma = 6.00$) and peak noise cavitation ($\lambda = 1.6$, $\sigma = 6.22$)	7 different values	Balance and current

Test II—Pure Corrosion. To enable pure corrosion conditions to be investigated non-cavitating flow conditions were established within the test section, $\sigma = 8.20$ (at the same upstream velocity as in Test I). The specimen was maintained at a constant overpotential by the potentiostat, which also measured the corrosion cell current. The cell current was logged every minute by a micro-computer. After obtaining 60 data points which are stored on floppy disc, a mean current value I and its associated standard deviation are evaluated. By using Faraday's law and integrating the current at each minute, the mass loss due to corrosion is obtained for every hour. By plotting these mass loss results versus time, a purely corrosion mass loss rate, denoted by Mc, was evaluated. Balance measurements were also taken at regular intervals to check the current derived mass loss values.

For the freely corroding case, ($\eta = 0$) in Tests II and III, the potentiostat was disconnected from the corrosion cell to allow the specimen to reach its freely corroding potential. To obtain the corrosion current during these tests required the reconnection of the potentiostat and the acquisition of polarization curves at regular intervals. As mass loss occurs while positive overpotentials are investigated, the specimen was weighed before and after each polarization curve was obtained.

Initial runs of Tests I and II revealed that the tests would span several days running and it was therefore necessary to store the specimens overnight. To avoid filming up, the specimens were stored in distilled water through which nitrogen was bubbled.

Test III—Combined Cavitation Corrosion and Erosion. The cavitation conditions set up in Test I are repeated at each of the corrosion conditions established in Test II. Both corrosion current and balance readings were taken as detailed in Test II. The mass loss rate from the balance readings, denoted by Mt, is the total mass loss rate from the specimen due to the combined attack of cavitation erosion and corrosion.

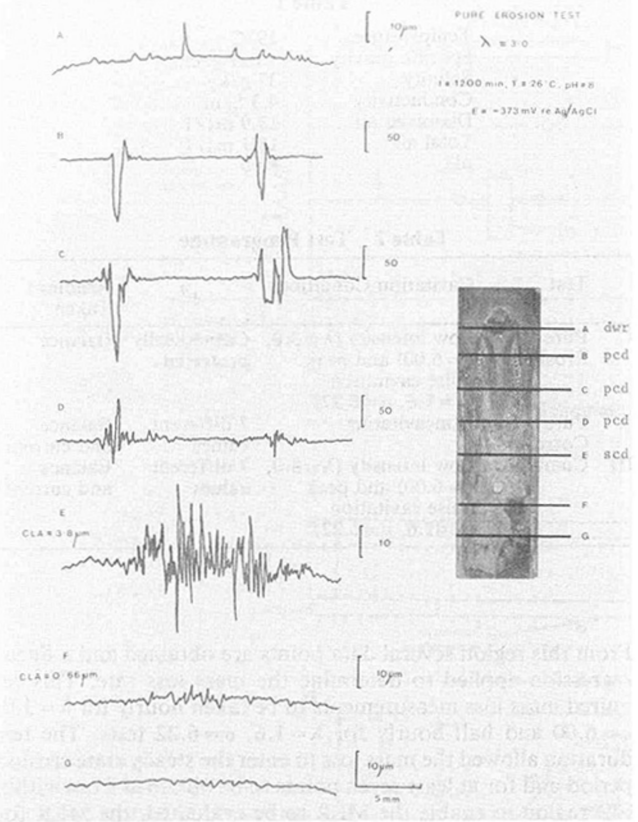

Fig. 4 Talysurf traces of the copper pure erosion Test I specimen for $\lambda = 3.0$ ($\sigma = 6.00$)

Results

The values of E_{CORR} obtained for copper was -230 mV re Ag/AgCl and -195 mV re Ag/AgCl for copper/nickel 70/30. A detailed analysis of the mass loss rate results was anticipated. The total mass loss given by equation (1) can be further split to give:

$$Mt = Me + Mc + (\Delta Me + \Delta Mc) \quad (2)$$

where

$$\left.\begin{array}{ll} \Delta Me = & \text{the additional erosive mass loss due to the presence of corrosion} \\ \Delta Mc = & \text{the additional corrosive mass loss due to the presence of cavitation erosion} \end{array}\right\} \text{synergistic terms}$$

From Tests I, II, and III these four mass loss rate components have been evaluated. However, these results exhibited considerable scatter making it difficult to interpret them meaningfully. With hindsight it is clear that this is due to the fact that corrosion acts over the entire specimen surface while erosion due to cavitation (at $\lambda = 3.0$, $\sigma = 6.00$) acts on only 7 percent of the surface. Obviously, synergism will only be exhibited where both damage mechanisms are at work. An alternative technique that allows the synergistic effect to be investigated is surface profilometry.

Talysurf Profiles

Talysurf profiles tranverse to the flow were obtained from Tests, I, II, and III specimens as shown in Figs. 4, 5, and 6 respectively using a Taylor-Hobson Talysurf 4 industrial profilometer. From the traces, the maximum depth of penetration measurements can be readily obtained. The specimen width (25 mm) is greater than the tunnel flow passage (20 mm), therefore each traverse includes two areas, one under each sidewall, not wetted by the electrolyte. These two areas at the beginning and end of each trace, provide a reference for the original polished surface from which the maximum depth measurements can be taken. Maximum depths were used to study local conditions (which differ considerably across the specimen due to changing hydrodynamic conditions) rather than a simple average which has little physical meaning.

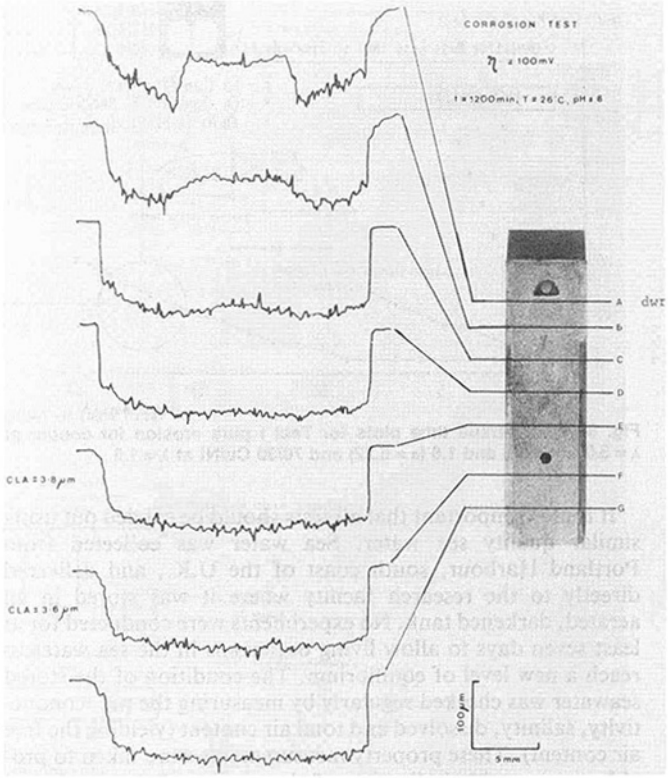

Fig. 5 Talysurf traces of the copper pure corrosion Test II specimen for $\eta = +100$ mV

Pure Erosion (Test I). Figure 4 presents the traces A to G for the Pure Erosion (Test I) case. Traces A, F, and G indicate that the initial polished surface of the specimen was slightly convex. The first point to note about the damage traces for pure erosion is that they exhibit a spiky characteristic. It may also be noted that the profile indicates that the metal has been raised above the undamaged surface datum. This has been observed previously (Selim [10]) and is a characteristic of ductile materials. From the other traces two regions of damage can be identified. Primary cavitation damage (pcd), see Fig. 2, is shown by traces B, C, and D while secondary cavitation damage is shown by trace E. The pcd comprises two deep but quite narrow areas of erosion. These are believed to result from bubble collapses in the regions of high shear between the dead water region and the outer flow. Within this region the collapse intensities of the bubbles is greatest causing the high damage rate of the pcd area.

Further downstream trace E shows a wider region of damage in the centre of the specimen. The damage here is less severe and the depth of penetration scale must be changed.

Pure Corrosion (Test II). The effect of pure corrosion is shown in Fig. 5. In contrast to the pure erosion traces the corrosion damage exhibits a smooth characteristic. It is apparent that the corrosion penetration rate is not uniform over the

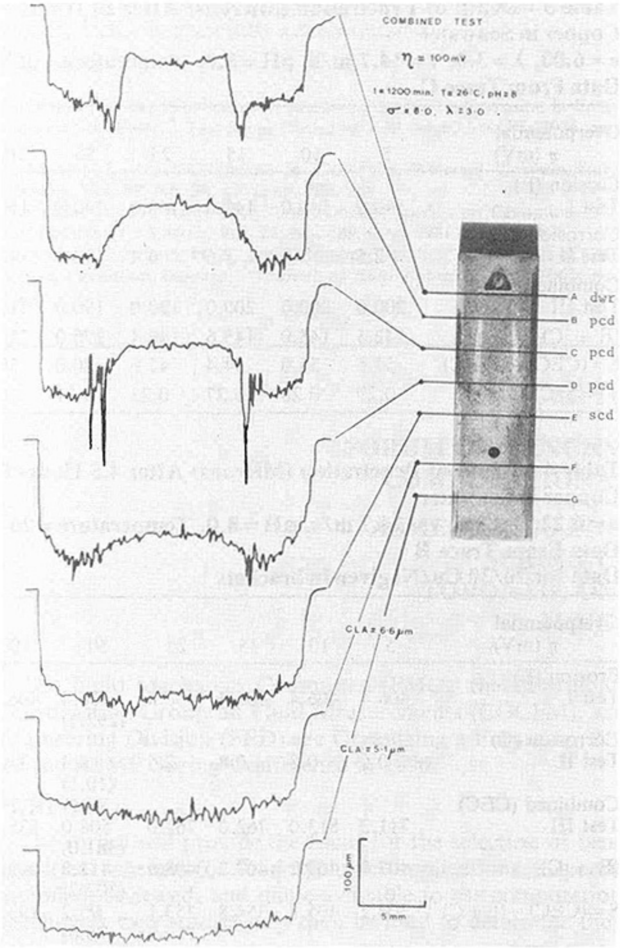

Fig. 6 Talysurf traces of the copper combined Test III specimen, $\eta = +100$ mV, $\lambda = 3.0$ ($\sigma = 6.00$)

specimen surface. The presence of the wedge (acting as the cavitation source) causes decreased corrosion to occur in the dead water region (behind the wedge) and increased corrosion at the throat of the flow passage where flow velocity is greatest. Clearly, the surface profile is a direct result of differing hydrodynamic conditions established over the specimen surface.

The areas of maximum penetration (see trace A) coincide with the regions of high shear flow. The diffusion-controlled copper dissolution rate would be greatest here, as the mass transport of ions from the specimen surface through to the fast moving bulk fluid would be most efficient in the presence of high turbulence as found in shear regions. Due to turbulent mixing of the wake with the outer flow, the regions of high turbulent concentration together with their corresponding regions of damage become less well-defined as we move in the downstream flow direction. By trace D the penetration rate is uniform over the surface as the flow pattern becomes independent of the wedge and influenced only by the vortex street set up in the wake by the wedge, making the traces slightly concave.

Combined Erosion and Corrosion (Test III). The effect of combining cavitation erosion and corrosion is shown in Fig. 6. It can be seen that under combined attack the traces again exhibit a relatively smooth damage characteristic.

The result of combined attack is best illustrated by comparing Figs. 5 and 6 together as shown in Fig. 7. With one exception the depth of penetration is always increased when the specimen is subjected to combined attack. This exception appears in the middle of trace C and is believed to result from an extension of the dead water region when it is bounded by cavities. The penetration rates in traces D, E, and F are increased due to the increased turbulent eddies produced in cavitating flows. The effect of this increased turbulence has diminished by trace G.

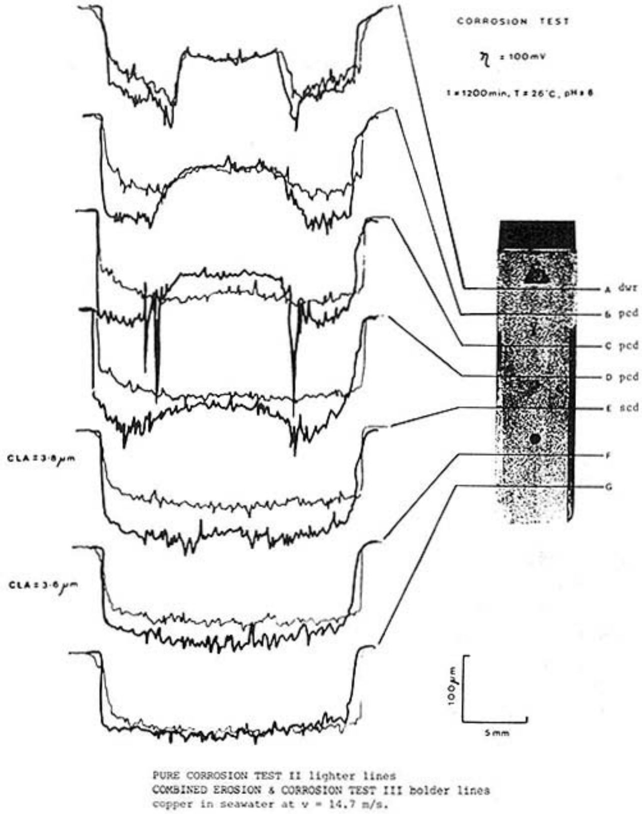

Fig. 7 Test II and III Talysurf traces for $\eta = 100$ mV, $\lambda = 3.0$ ($\sigma = 6.00$)

To obtain the synergistic depth of penetration requires an investigation of the surface where both cavitation erosion and corrosion act. Therefore, for the $\lambda = 3.0$, $\sigma = 6.00$ trace C was used, and for $\lambda = 1.6$, $\sigma = 6.22$ trace B was used.

The maximum depth of penetration for each type of test shall be referred to as E for the Pure Erosion (Test I), C for the Pure Corrosion (Test II) and CEC for the Cavitation Erosion-Corrosion (Test III). The combined depth of penetration is thus given by:

$$\mathrm{CEC} = \mathrm{E} + \mathrm{C} + \mathrm{S} \tag{3}$$

where S is the synergistic depth of penetration.

Table 3 lists the values of E, C and CEC for the $\lambda = 3.0$, $\sigma = 6.00$ experiments after 20 hours duration. Depths are given in microns.

The synergistic depth can be evaluated, and the ratio of the synergistic depth to the total depth is given by:

$$\gamma = \mathrm{S/CEC}$$

Values of S and γ are also given in Table 3. γ is seen to decrease with increasing η (i.e., as the damage to the surface becomes corrosion dominated). The results for $\lambda = 1.6$, $\sigma = 6.22$ are given in Table 4. To summarize, The results for both cavitation intensitites ($\lambda = 3.0$, $\sigma = 6.00$, and $\lambda = 1.6$, $\sigma = 6.22$) a plot of λ versus Mc/Mt is presented in Fig. 8. The ratio Mc/Mt indicates the fraction of the total mass loss rate due to corrosion. It can be seen that the synergistic effect (γ) decreases as the mass loss rate becomes corrosion-dominated (i.e., as Mc/Mt approaches unity). The synergistic effect reaches a maximum ($\gamma = 0.5$) when the mass loss is cavitation erosion dominated. Under these conditions (cavitation erosion

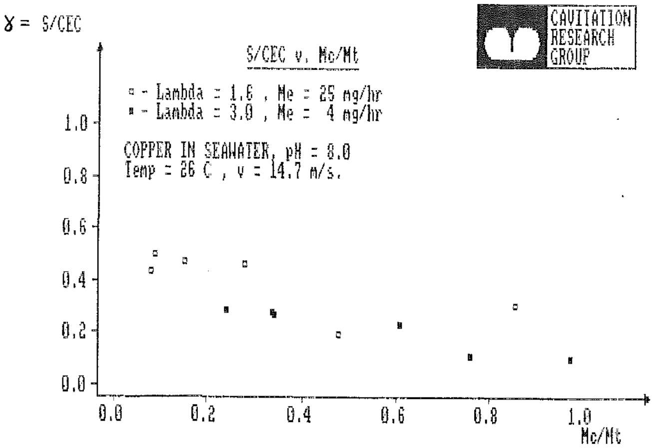

Fig. 8 S/CEC versus Mc/Mt plots for $\lambda = 1.6$ and 3.0 ($\sigma = 6.22$ and $\sigma = 6.00$) on copper

in the presence of mild corrosion) the synergistic effect can double the mass loss rate.

The above results indicate that the synergistic effect increases as the total mass loss rate becomes increasingly erosion-dominated. As indicated by equation (2) the synergistic mechanism responsible for this increase in penetration rate can take two forms: either the mechanism of enhanced cavitation erosion due to the presence of corrosion or the mechanism of enhanced corrosion due to the presence of cavitation erosion. The present tests do not distinguish between these two mechanisms so it is not possible to conclude which is dominant.

Cu/Ni Results

Unfortunately, depth of penetration results for 70/30 copper nickel were obtained at one value of overpotential only, $\eta = 50$ mV. Comparison of these results (Table 4 in brackets) with the corresponding results at $\eta = 50$ mV for copper (Table 4) reveals a similar synergistic contribution ($\gamma = 0.2$).

Conclusions

Tests under pure cavitation erosion, pure corrosion and combined attack have allowed the true synergistic effect to be evaluated for copper and 70/30 copper/nickel in a flowing sea water system. The use of potentiostatic control in an all-plastic tunnel has allowed accurate control of corrosion rates at different cavitation conditions.

As these proved difficult to interpret an alternative technique using Talysurf profiles was used. By measuring the maximum depth of penetration at the same position on each of the Tests I, II, and II specimens a synergistic depth (S) has been evaluated. A ratio, γ, of the synergistic depth (S) to the combined cavitation erosion-corrosion depth (CEC) measured from the Test III specimens is defined. By combining the results from the low and high intensity cavitation results, the dependence of γ on the corrosion rate over a large range has been reported. The corrosion rates covered in the experiments vary between 8 and 97 percent of the total mass loss rate from the Test III specimen. For high corrosion rates (i.e., the ratio Mc/Mt approaches unity) the values of γ are approximately 0.1 (i.e., 10 percent of the depth of penetration is due to the synergistic effect). However, lowering the corrosion rate increases γ. The maximum value of $\gamma = 0.5$ (i.e. the synergistic effect doubles the depth of penetration) was recorded at a corrosion rate such that $Mc/Mt = 0.09$. Therefore, it can be concluded that the synergistic effect is most marked when cavitation erosion occurs in the presence of mild corrosion.

Table 3 Depth of Penetration (Microns) After 20 Hours for Copper in Seawater
$\sigma = 6.00$, $\lambda = 3.0$, $v = 14.7$ m/s, pH = 8.0, temperature = 26°C
Data From Trace C

Overpotential η (mV)	5	10	15	25	50	100
Erosion (E) Test I	140.0	140.0	140.0	140.0	140.0	140.0
Corrosion (C) Test II	2.5	5.0	5.6	6.4	30.0	140.0
Combined (CEC) Test III	200.0	200.0	200.0	190.0	190.0	310.0
(E + C)	142.5	145.0	145.6	146.4	170.0	280.0
$S = (CEC) - (E + C)$	57.5	55.0	54.4	43.6	20.0	30.0
$\gamma' = S/CEC$	0.29	0.28	0.27	0.23	0.11	0.1

Table 4 Depth of Penetration (Microns) After 4.5 Hours for Copper in Seawater
$\sigma = 6.22$, $\lambda = 1.6$, $v = 14.7$ m/s, pH = 8.0, Temperature = 26°C
Data From Trace B
Data for 70/30 Cu/Ni given in brackets

Overpotential η (mV)	5	10	15	25	50	100
Erosion (E) Test I	406.4	406.4	406.4	406.4	406.4 (292.1)	406.4
Corrosion (C) Test II	0.6	0.8	0.8	2.5	6.4 (10.1)	35.6
Combined (CEC) Test III	711.2	813.0	762.0	762.0	508.0 (381.0)	635.0
(E + C)	407.0	407.2	407.2	408.9	412.8 (302.2)	442.0
$S = (CEC) - (E + C)$	304.2	405.8	354.8	353.1	95.2 (78.8)	193.0
$\gamma' = S/CEC$	0.43	0.50	0.47	0.46	0.19 (0.21)	0.30

The 70/30 Cu/Ni results indicate a similar value of γ compared with that evaluated for copper ($\gamma_{Cu} = 0.19$ and $\gamma_{70/30\ Cu/Ni} = 0.21$). This indicates that the synergistic effect on Cu/Ni is likely to be similar to that of copper.

From the above conclusions it is clear that to keep synergistic effects to a minimum, the design engineer should be wary of the condition when cavitation erosion occurs in a mildly corroding environment. This may explain the problems with synergistic effects under such conditions already reported (Simoneau [5]) in water turbines operating in brackish water.

For severely corroding environments the synergistic effect becomes insignificant and the corrosive and erosive mass losses can simply be added.

Uncertainties at 20:1 Odds

		Uncertainty	
Sigma	σ	±0.01	
Nondimensional cavity length	λ	±0.1	
Mass Loss Rate	M	±0.1	mg/hr
Overpotential	η	±0.5	mV
Depth of penetration			

Figure No.	Trace		
4	A, E, F, G	±0.05	μm
	B, C, D	±0.25	μm
5	A, B, C, D, E, F, G	±0.5	μm
6	A, B, C, D, E, F, G	±0.5	μm

Acknowledgments

The authors are grateful to Professor S.P. Hutton for his encouragement throughout this work, and to Mr. J. C. Rowlands and Mr. B. Angell for their support. Financial

assistance from the Procurement Executive, Ministry of Defence, U.K., is gratefully acknowledged.

References

1 Shalnev, K. K., "Resistance of Metals to Cavitation Corrosion in Fresh Water and Sea Water," Translated from *Dok.Aka.Navd*, Vol. 95, 1954, pp. 229-232.

2 Martin, J. A., "Cavitation in Corrosive Waters," *Schweizerische Bauzeitung*, Vol. 89, No. 24, 1971, pp. 587-590.

3 Okada, T., and Awazv, K., "Fundamental Studies on Cavitation Erosion," *Bulletin of J.S.M.E.*, Vol. 24, No. 189, Mar. 1981, pp. 461-467.

4 Waring, S., Preiser, H. A., and Thiruvongdam, A., "On the Role of Corrosion in Cavitation Damage," *Journal of Ship Research*, Dec. 1965, pp. 200-208.

5 Simoneau, R., Fihey, J. L., and Roberge, R., "The Effect of Corrosion in Low Intensity Cavitation Erosion," *ASME Symp. of Cavitation Erosion*, Boulder, Colo. June 1981, pp. 71-81.

6 Matsumura, M., "Cavitation Erosion-Corrosion," *Proc. 6th Int. Conference on Erosion by Liquid and Solid Impact*, Cambridge, 1983.

7 Erdmann-Jesnitzer, F., Louis, H., and Tai, P. T., "Cavitation Behaviour of Pure Iron by Electrochemical Methods," Eurorcor'77, 6th European Congress on Metallic Corrosion, London, 1977.

8 Haferkamp, H. H., Louis, H., and Tai, P. T., "Influence of Polarization and Intensity of Cavitation Attack on the Behaviour of Metallic Materials," I.Mech.E. Cavitation Conference, Edinburgh, U.K., 1983.

9 Fontana, M. G., and Greene, N. D., Chapter 10 of *Corrosion Engineering*, 2nd Edition, McGraw-Hill, 1978, pp. 342-344.

10 Selim, S.M.A., "Cavitation Erosion in Fluid Flow," Ph.D. Thesis, University of Southampton, U.K., 1981.

S. R. Bistafa
Assistant Professor,
ESCOLA POLITÉCNICA DA USP,
Depto. Eng. Mecânica,
C. P. 8174 - São Paulo
05508 - SP - BRAZIL

G. C. Lauchle
Senior Scientist and
Professor of Acoustics,
Applied Research Laboratory,
Penn State University,
State College, PA 16804 - USA

G. Reethof
Professor Emeritus,
Department of Mechanical Engineering,
Penn State University,
State College, PA

Noise Generated by Cavitation in Orifice Plates

An experimental investigation of the noise generated by cavitation in turbulent shear flows produced by confined sharp-edged orifice plates is reported. The acoustic source strength of cavitation was determined by means of reciprocity type measurements. Two experimental checks of the reciprocity method were performed. Proposed scaling relations, derived from dimensional analysis, were empirically adjusted and used to predict prototype acoustic performance based on the results of model tests. The dependence of the acoustic source strength on flow velocity and cavitation number was determined experimentally and compared with similar results reported in the literature.

Introduction

Control valves are one of the major contributors to the noise problem among industrial equipment, especially in petrochemical, chemical, and power plants. The two major sources of noise in the transport of liquids can be divided into noncavitating and cavitating sources. Noncavitating liquid flow generally results in relatively low noise levels, but it can be a major annoyance in household plumbing. It is generally accepted that the mechanism by which the noise is generated is a function of the turbulent velocity fluctuations. The high intensity turbulence in control valves occurs as a result of the high shear region produced by the throttling process.

Turbulence and high shear flow regimes can also incite cavitation which is normally the most intense source of noise in liquid flows. The predominant mechanism is the collapse of vapor bubbles. Investigators generally agree that the first formation of cavitation occurs as a result of microscopic free-stream nuclei becoming unstable due to intense turbulence pressure fluctuations in regions of discontinuity or separation in the control valve. The vapor bubbles formed become unstable and implode almost immediately as they convect into high pressure zones. Because thousands of bubbles may be collapsing simultaneously, the resulting noise level can be very high.

Noise has been associated with cavitation phenomena since the earliest studies performed by Reynolds [1]. Many theoretical and experimental studies have been developed on the subject. Fitzpatrick and Strasberg [2], using incompressible single bubble dynamics, predicted that the sound spectrum has a maximum at a frequency which is roughly equal to the reciprocal of the total lifetime of the cavity. Below this frequency the spectrum rises at a rate of 12 dB/octave. Above this frequency, the spectrum tends to decrease, at first at a rate of −1.2 dB/octave, and then more rapidly, at a rate of −6 dB/octave. This faster decay at higher frequencies is attributed to the influence of the compressibility of the medium.

Although the single bubble analysis gives considerable insight into the problem of cavitation noise, there are still doubts about its applicability to predict the noise characteristics of a cloud of bubbles normally encountered in cavitating systems.

Many researchers, including Morozov [3] and Baiter et al. [4], have treated cavitation as a random process, and have used statistical methods to derive its spectral properties. It is typically argued that although cavitation can consist of many collapsing cavitates, each cavity is a statistically independent event and in this case, the spectrum resembles that from a single cavity collapse.

A number of experiments [5–7] have determined noise spectra for profuse cavitation, and in general it is found that the spectrum rises to a maximum in the vicinity of a few kilohertz. In some other cases [6–9], flat regions are apparent between 20 and 100 kHz.

In this investigation orifice plates with different configurations are used to simulate the flow through control valves. One of the goals of this study is to determine experimentally the cavitation noise characteristics for this type of flow.

Since cavitation noise of the type studied here is not easily amenable to theoretical modeling, scaling relations are developed, experimentally adjusted, and corrected to take into account the influence of the gas content of the water on the acoustic source strength. The scaling relations are checked experimentally by performing tests at a different scale. The dependence of the acoustic source strength on flow velocity and cavitation number is established in this work.

The influence of gas content on cavitation noise is important because it affects the dynamics of individual bubbles. In

---

Contributed by the Fluids Engineering Division for publication in the JOURNAL OF FLUIDS ENGINEERING. Manuscript received by the Fluids Engineering Division March 4, 1986.

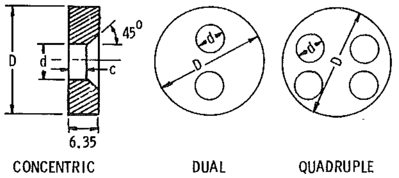

BASIC GEOMETRIC CHARACTERISTICS OF THE ORIFICE PLATES USED IN THE 152.5 mm (6 in.) WATER TUNNEL. *

OFIFICE PLATE	DIMENSIONS IN mm			d/D	DISCH. COEFF. Cd**
	D	d	c		
CONCENTRIC	152.5	50.8	2.3	0.33	0.600
	152.5	76.2	2.3	0.50	0.603
	152.5	101.6	2.3	0.67	0.605
DUAL	152.5	53.8	2.3	--	--
QUADRUPLE	152.5	38.1	2.3	--	--

(*) THE ORIFICE PLATES USED IN THE 305 mm (12 in.) WATER TUNNEL ARE SIMILAR IN 2:1 SCALE.

(**) THE DISCHARGE COEFFICIENTS ARE FOR FLANGE TAP LOCATIONS ACCORDING TO [11].

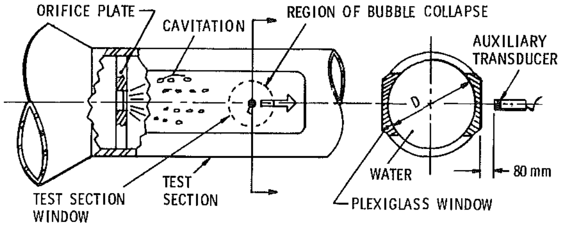

Fig. 1 Geometrical characteristics of the orifice plates and their location in the water tunnel test section

our specific case, this influence may be quite important due to the low pressure conditions immediately downstream of the orifice plate. This low pressure region promotes the release of dissolved air. As a consequence, the air content of the bubbles increases and the collapse of the bubbles is moderated by the increased air content. It may also influence the sound transmission characteristics of the medium. In this paper hydroacoustic results will be presented for only one, relatively high range of gas content level. Results for other, lower ranges of gas content level are given by Bistafa [10].

Experimental Procedure and Apparatus

The experimental investigation was conducted at the Garfield Thomas Water Tunnel of the Applied Research Laboratory at Penn State (ARL-Penn State). Two facilities were used with the basic objective of checking experimentally the proposed model/prototype scaling relationship for sound spectrum prediction. Both are recirculating water tunnels, one having 152.5 mm (6 in.) and the other 305 mm (12 in.) diameter circular test sections.

Thin orifice plates display the essential gross fluid characteristics of simple industrial control devices. The significant difference between the thin orifice plate and a valve is that valves are generally streamlined such that all of the flow separation processes occur within the valve body. Nevertheless, a control valve generates a shear flow similar to that created downstream of an orifice, or other sharp-edged aperture. These kinds of geometries produce a flow separation that promotes cavitation due to the local underpressures created in the high-shear region around the submerged jet. It was thus decided to use simple concentric orifice plates, and two variants: a plate with two diametrically opposed orifices and another with four equally spaced orifices. The purpose of the latter ones was to identify possible noise generation effects due to a multiplicity of orifices of the same flow areas. Figure 1 shows the geometrical characteristics of the orifice plates and their location in the water tunnel test section.

With the cavitation number of an orifice plate given by:

$$K = \frac{P_d - P_v}{P_u - P_d}, \tag{1}$$

measurements of the incipient (first occurrence) and desinent (disappearance of) cavitation numbers K_i and K_d, respectively, were made. (Please refer to the list of symbols for definitions of the variables used.) Measurements of P_u and P_d were performed with pressure taps on the flange supporting the orifice plate. Information on the location and design of the

Nomenclature

c = sound velocity in water
D = characteristic dimension or test section diameter
d = orifice diameter
e_1 = output voltage of transducer 1, caused by i_2
e_2 = output voltage of transducer 2, caused by i_1
f = frequency
g = acceleration of gravity
i_1 = electric input current of transducer 1
i_2 = electric input current of transducer 2
K = cavitation number for internal flows
K_i = incipient cavitation number
K_d = desinent cavitation number
k = ratio of specific heats
m = pressure differential exponent
n = cavitation number exponent
P = pressure outside the cavitation bubble
P_c = pressure inside the bubble
P_d = downstream pressure
P_g = gas pressure inside the bubble
P_0 = pressure collapsing the bubble ($P_0 = P - P_c$)
P_u = upstream pressure
P_v = vapor pressure
p = sound pressure
$\overline{p^2}$ = mean-square value of sound pressure
Q = ratio of dynamic head to minimum pressure in cavity at maximum bubble radius
r = noise observation distance
R_0 = bubble radius
t = time scale
U = source strength (or volume velocity)
$\overline{U^2}$ = mean-square value of source strength
V = average flow velocity through the orifice
α = air content of the liquid
$\beta = d/D$ = ratio of diameters
β = Henry's gas constant
Δf = frequency bandwidth
ΔP = pressure differential across the orifice plate
λ = scale factor
ρ = density
ν = kinematic viscosity
σ = surface tension
index m = refers to model scale
index p = refers to prototype scale
index 1 = refers to reciprocal transducer outside of tunnel
index 2 = refers to reciprocal transducer or source inside the tunnel

Subscript

s = saturated condition

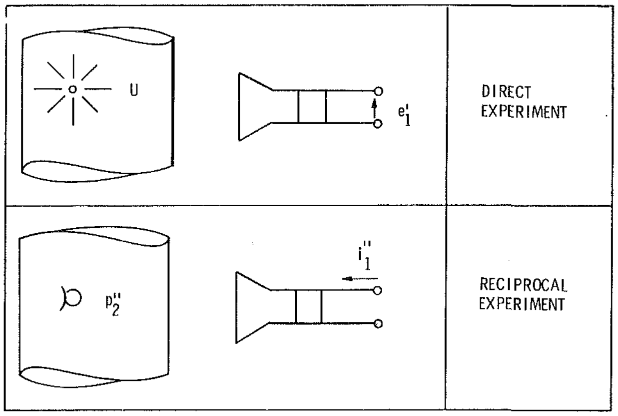

Fig. 2 Determination of the source strength of a point source in a water tunnel

pressure taps can be found [11]. Based on tabulated discharge coefficients as provided by [11], the velocity through the orifice could be determined. The cavitation number is varied in the water tunnels by either of two methods: vary the static pressure at constant velocity or vary the freestream velocity at constant static pressure. It is noted that the denominator of equation (1) is proportional to the dynamic head based on the average velocity through the orifice. These basic procedures and definitions are given, for example, by Holl [12].

Gas content was measured in parts per million (ppm) of water on a Molar basis, with a Thomas Van-Slyke manometer apparatus.

Detection of Limited Cavitation. Many methods for measuring cavitation inception are reported in the literature, e.g., references [5,13,14,15]. Some are based on optical means and others on acoustic means. In our experiments, it was first observed that before any vapor bubbles could be seen through the windows of the test section, a characteristic vaporous cavitation noise was heard and also detected by acoustic transducers located in the vicinity of the test section. With the help of a stroboscopic light we confirmed that "cavitation clusters" were present in the flow field simultaneously with the increase in noise level. Also, the auxiliary transducer used for the reciprocity experiments (to be discussed later) appeared to be very well correlated with the visual appearance of the "cavitation clusters" detected with the aid of the stroboscopic light. Hence, it was decided to use the auxiliary transducer as a means for detecting limited cavitation conditions. The incipient cavitation index was defined only under conditions where the rate of events were high enough to provoke a fairly continuous movement in the indicator of a Ballantine RMS voltmeter connected to the auxiliary transducer.

Like other methods, this approach has its subjectiveness in the determination of the limiting cavitating conditions.

Reciprocal Calibration Approach. In traditional methods, cavitation noise is measured with hydrophones placed in, or contiguous with the flow. To convert measured sound pressures in the facility to equivalent free-field conditions, it is necessary to calibrate the facility with an acoustic source of known characteristics. For closed jet test sections, the use of acoustic volume sources presents a problem for moderate to low frequency ranges because of the source size and wavelength in relation to the size of the test section. Also, vibration and flow-induced noise over the hydrophone create additional difficulties with this method.

The calibration approach used here is based on so-called reciprocity methods, proposed by Wolde [16]. Using lumped circuitry theory, he developed reciprocity relations for homogeneous and heterogeneous systems. One very useful relation which will be the basis for the determination of the acoustic source strength in the present work, can be found by developing reciprocity relations for a heterogeneous electro-acoustical system. This relation is:

$$U = \left(\frac{i_1''}{(p_2'')_{U_2''=0}} \right) (e_1')_{i_1'=0} \tag{2}$$

which equates the equivalent source strength (or volume velocity) to measured electro/acoustic parameters. The sufficient conditions for the validity of the above reciprocity relation are: linearity, passivity, and bilateral elements [16].

The quantities that appear in equation (2) are obtained by performing two experiments, as outlined in Fig. 2. In a first "direct" experiment, the unknown source (cavitation source) is present and the open circuit voltage (e_1') at the electrical terminal of the passive electro-acoustical or electro-mechanical transducer is measured. In a second, "reciprocal" experiment, the unknown source is stopped and replaced by an omnidirectional microphone or hydrophone. The transducer at position 1 is now driven by a current (i_1''), causing a sound pressure (p_2'') at position 2. Thus the source strength U of the cavitating source can be obtained from a direct and a reciprocal experiment on a electro-acoustical system in which $(e_1')_{i_1'}=0$ must be measured while the system is "open", i.e., loaded by such a high electrical impedance that the current at the electrical terminals is zero. The term $(p_2'')_{U_2''=0}$ must be measured with an omnidirectional hydrophone which is considered small and stiff so that the sound pressure at the particular position is not significantly affected by the presence of the hydrophone or its reaction on the medium.

The source strength of a monopole is related to the sound pressure in a freefield according to:

$$(\overline{U^2})^{1/2} = 2(\overline{p^2})^{1/2} r/\rho f \tag{3}$$

Because cavitation behaves acoustically as a monopole, the above approach seems appropriate for the studies conducted. With knowledge of the source strength, one can determine the free-field sound pressure using equation (3).

In the selected approach, an auxiliary reciprocal transducer is used as a sound source in the reciprocal experiment, and as a sound receiver in the direct experiment. This transducer is a medium-to-high frequency-range electrodynamic loudspeaker which provides sufficiently high sound pressure levels for frequencies from 2.5 kHz to 50 kHz. The measurement of the sound pressure inside the test section was accomplished with a Celesco LC-32 hydrophone. This hydrophone is piezoelectric and meets the requirements of reciprocity [16]. The signal from the hydrophone was high-pass filtered at 2.5 kHz to eliminate possible contamination due to low-frequency background noise.

In the reciprocal experiment the auxiliary transducer was driven with a constant voltage white noise signal, while the current to the speaker and the voltage output from the hydrophone were amplified and recorded simultaneously on a tape recorder. Care was exercised not to overdrive the speaker in order to avoid non-linear operation characteristics. A block diagram of this setup is shown in Fig. 3. The reciprocal experiment allows the determination of the ratio (i_1''/p_2'') in equation (2).

The next step in the determination of the source strength characteristics consists of measuring the voltage output of the auxiliary transducer while the orifice-plate is operating under cavitating conditions. The auxiliary transducer is now a sound receiver.

The duration of each recording was approximately 3 minutes, sufficient time for at least 256 samples to be used in the determination of spectra by a Nicolet Scientific model 660A dual channel FFT processor. The measured spectra were transferred to a Commodore PET computer and stored. These

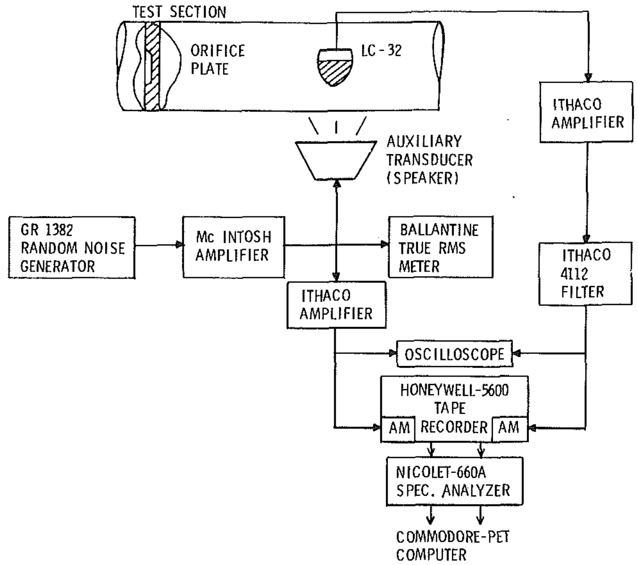

Fig. 3 Block diagram depicting the setup used for the determination of the transfer function

spectra were subsequently recalled and computations were made for the quantities of interest.

With the velocity held constant (constant pressure differential across the orifice plate), the pressure in the test section was lowered until the incipient condition was attained. The incipient pressure was then used to calculate K_i. Noise measurements were made for this condition and for lower cavitation numbers (more developed stages of cavitation) which were attained by decreasing the pressure further. The desinent cavitation number K_d was obtained by increasing the pressure, until no noise bursts due to cavitation could be detected. This procedure was repeated at each velocity and for each orifice plate.

Scaling of Cavitation Noise

The prediction of the acoustic radiation due to cavitation in hydraulic and fluid moving machinery, poses an important practical problem. Because of the complex flow fields and also because of the complex acoustic environments associated with such machinery, it is impractical to attempt a purely theoretical solution. We can, however, approach some of these problems using empirically established scaling relationships. Indeed, this has been the usual approach in many previous studies of cavitation noise.

Dimensional analysis indicates that the generation of cavitation noise should obey certain scaling laws if the relevant rules of similitude are followed. If we restrict our goal to the identification of those parameters (and their functional interrelationship) that dominate the noise generation process, it then seems possible to establish a scaling relationship that would permit one to make quantitative estimates of the noise characteristics expected at various scales of a specific hydraulic system. In this case, the system is a confined orifice plate operating under cavitating conditions. The scaling relationship sought is one that will allow us to predict the noise from similar systems of different size and operating conditions. In the following, we refer to such scaling as: "from model to prototype." The model-scale data required are those obtained from the smaller water tunnel experiments reported in other sections of this paper.

The conditions for modeling the acoustic characteristics of cavitation have been discussed previously by Levkovskii [17, 18]. His discussion is based on the use of Buckingham's PI Theorem [19]. There are dimensional quantities associated with the cavitation process itself, and there are additional quantities associated with the noise radiation. These quantities can be grouped into nondimensional PI parameters as follows:

For the Cavitation Process

$$\pi_1 = K \text{ (cavitation number)} \tag{4}$$

$$\pi_2 = R_0/D \text{ (cavity size effect)} \tag{5}$$

$$\pi_3 = Vt/D \text{ (characteristic time scale)} \tag{6}$$

$$\pi_4 = VD/\nu \text{ (Reynolds number)} \tag{7}$$

$$\pi_5 = V/\sqrt{gD} \text{ (Froude number)} \tag{8}$$

$$\pi_6 = V^2 D\rho/\sigma \text{ (Weber number)} \tag{9}$$

For the Cavitation Noise Process:

$$\pi_7 = r/R_0 \text{ (or } r/D \text{ because of } \pi_2\text{)} \tag{10}$$

$$\pi_8 = c\sqrt{\rho/P_0} \text{ (compressibility of medium)} \tag{11}$$

$$\pi_9 = fR_0\sqrt{\rho/P_0} \text{ (frequency parameter)} \tag{12}$$

$$\pi_{10} = p/P_0 \text{ (acoustic pressure)} \tag{13}$$

In the most rigorous sense, all ten PI parameters listed above must be accounted for in any scaling exercise. Approximate scaling, however, can be performed with only a few of the parameters. Those which are considered most important to the current study are π_{10}, π_9, π_7, π_2, and π_1. Parameter π_6 is not considered further because the surface tension is important only at the initial stages of cavity formation. Parameter π_5 is important when gravity influences the cavity formation, like cavitation that occurs at the top and bottom of big propellers. The Reynolds number (parameter π_4) could be considered important since the vortices that are formed in jet-type flows are dominated by viscous effects. It is at the center of these vortices where the first cavity formation occurs. However, it seems reasonable to assume that variations in Reynolds number will not have a meaningful effect unless the flow is at a critical or unstable regime. These assumptions are reinforced by the experimental findings of [5]. In this work the sound pressure was measured and plotted in nondimensional form as a function of dimensionless frequency at three values of cavitation number involving various combinations of static pressure and jet velocities. The data for different jet diameters, speeds, and pressures, collapse reasonably well, showing the generated noise could be considered independent of the Reynolds, Mach, and Weber numbers of the flow. Since the velocity can be the same for model and prototype, the parameter π_3 implies that the characteristic time scale will be proportional to the dimensions of the cavitating body. It is typically argued that parameter π_8 is not considered because water compressibility effects become important only at very high frequencies. Its neglect would, of course, impose a high-frequency limit to the scaling relationship. However, this argument is not generally true; π_8 affects the acoustic efficiency of collapsing bubbles. Therefore, if collapse noise is the dominant contributor to cavitation noise, the influence of π_8 becomes apparent at low frequencies as well. Some authors (e.g., [17]) take account of π_8 by assuming constant acoustic efficiency. This means at the same time that π_{10} is no longer applicable. On the other hand it is possible to proceed from π_{10} and to allow for π_8 by way of empirical adaption.

Using equation (13), the mean-square acoustic pressure measured over a bandwidth Δf (which is centered at frequency f) is related to that expected at prototype scale by:

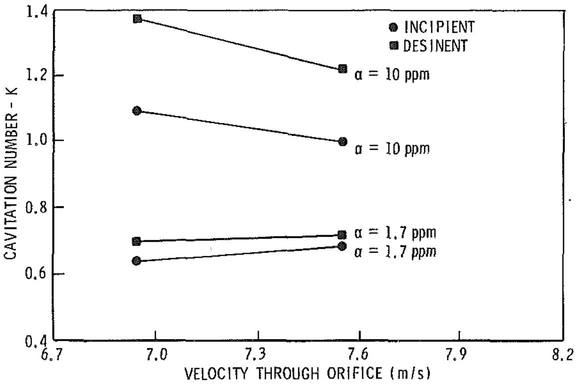

Fig. 4 Incipient and desinent cavitation numbers as a function of velocity for the concentric 203.2 mm (8 in.) orifice plate in the 305 mm (12 in.) water tunnel, with the air content of the water as a parameter. (Uncertainties at 20:1 odds: ±0.02; ±0.15 m/s.)

$$\frac{\overline{p_p^2}(f_p,\ \Delta f_p)}{\overline{p_m^2}(f_m,\ \Delta f_m)}=\left(\frac{\Delta P_p}{\Delta P_m}\right)^2. \tag{14}$$

Here, we have assumed $P_0 = P - P_c$ to be proportional to the pressure drop across the orifice plate, ΔP.

Equation (14) is valid provided that the cavitation number of the model and prototype are equal. However, right at the beginning of the experimental work it was found that the inception index of the model did not correspond to that of the prototype. This scale effect of the inception index is normally encountered in many model experiments used to predict the prototype performance. In order to minimize this scale effect we will make use of a hypothesis suggested in [20], which says: provided that K/K_i assumes equal values for prototype and model, equations (12) and (14) apply. Based on this hypothesis we are permitted to modify π_1 to read:

$$\pi_{11}=\pi_1/K_i=K/K_i. \tag{15}$$

A more careful examination of the frequency parameter π_9, reveals that the nondimensionalization of the frequency f can be made through use of the time of collapse of the cavity, which is given by:

$$\tau_c=R_0\sqrt{\rho/P_0}. \tag{16}$$

This theoretical time is based on the assumption that the cavity is empty. This is not generally true since it is known that vapor and noncondensable gases exist inside the cavity. According to [9], for a specific type of cavitation that occurs on hydrofoils, it was found that equation (16) under-estimates τ_c (upon substitution of observed values for R_0). We propose to improve the estimation of τ_c by including a function of the normalized cavitation number K/K_i:

$$\tau_c=F(K/K_i)\ R_0\ \sqrt{\rho/P_0}. \tag{17}$$

We assume that the function F, will be of the form: $F(K/K_i)=(K/K_i)^n$; and the frequency parameter, with the aid of equation (5), will then be given by:

$$\pi_{12}=f(K/K_i)^n\ D\sqrt{\rho/P_0}. \tag{18}$$

As discussed in the previous section, the experimental approach yields information on the source strength of cavitation noise. Equation (3) relates the source strength to sound pressure at frequency f. Also, π_7 can now be used, if we assume that model - scale measurements at distance r_m are used to predict prototype noise at $r_p = \lambda r_m$, where λ is the geometric scale factor given by $\lambda = D_p/D_m = R_{op}/R_{om}$ (because of π_2). Hence, equation (14) can be substituted into equation (3), and with the aid of equation (10) and (18), one can find:

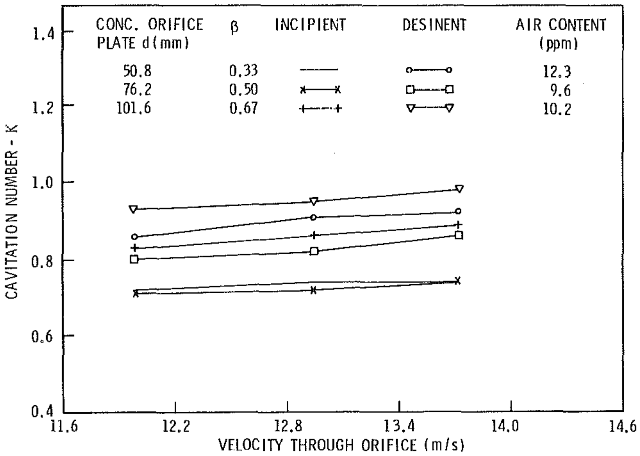

Fig. 5 Incipient and desinent cavitation numbers as a function of velocity for the concentric 50.8 mm (2 in.), 76.2 mm (3 in.), and 101.6 mm (4 in.) orifice plate, tested in the 152.5 mm (6 in.) water tunnel. (Uncertainties at 20:1 odds: ±0.02; ±0.15 m/s.)

$$\frac{\overline{U_p^2}(f_p,\ \Delta f_p)}{\overline{U_m^2}(f_m,\ \Delta f_m)}=\lambda^4\left(\frac{\Delta P_p}{\Delta P_m}\right)\left[\frac{(K/K_i)_p}{(K/K_i)_m}\right]^{2n}. \tag{19}$$

Equation (19) is the simplified scaling relationship that will be used in conjunction with the source strength spectral levels determined in the water tunnel experiments. The experiments are conducted in a manner that will help refine the exponents of the three ratios indicated in this equation. Because only two water tunnels were available, the exponent of λ could not be verified conclusively. However, both ΔP and K/K_i could be varied over reasonable ranges, so their exponents were determined and used to refine equation (19).

Experimental Results and Discussion

Results for Limited Cavitation Conditions. At the beginning of the experimental work it was verified that limited cavitation is very dependent on the total gas content of the water. Figure 4 shows incipient and desinent cavitation numbers for the concentric 203.2 mm (8 in.) orifice plate in the 305 mm (12 in.) water tunnel. It is seen that the limiting cavitation numbers increase with total gas content for a given velocity. As we shall see later, the air content not only influences the conditions for limited cavitation, but also influences the noise generated. The necessity of controlling the air content was clearly apparent. Most engineering problems concerning cavitation involve water having a relatively high gas content. Typical values are 10 to 14 ppm. A value around 10 ppm was chosen for the majority of the tests reported here. This level would correspond to a saturation level of about 68 percent at standard atmospheric pressure. It is not within the scope of the present work to make a thorough discussion about the effects of jet size, jet velocity, and the nuclei population as a function of dissolved gas content in the water, on cavitation inception. We shall simply show the basic experimental results and conclusions for limited cavitation in the orifice plates that we tested. A comprehensive discussion about these scale effects on cavitation inception can be found in [22].

Figure 5 shows incipient and desinent cavitation indices for the 50.8 mm (2 in.), 76.2 mm (3 in.), and 101.6 mm (4 in.) orifice plates tested in the 152.5 mm (6 in.) water tunnel at different velocities (pressure drops) through the orificies, with the ratio of diameters β, as a parameter. As we should expect, K_i was greater than K_d for all orifices tested at the same velocity.

Figure 5 shows an increase of the critical cavitation index

Table 1 Incipient and desinent cavitation numbers for the dual and quadruple orifice plates in the 152.5 mm (6 in.) water tunnel

ΔP – kPa (V – m/s)	dual orifice ($\alpha = 12$ ppm) K_i	plate K_d	quadruple orifice ($\alpha = 9.8$ ppm) K_i	plate K_d
185 (12.0)	1.66	*	1.44	1.65
216 (13.0)	*	*	1.25	*
243 (13.8)	*	*	*	*

* Not possible to determine due to pressure limitation in the water tunnel to 300 kPa.

Table 2 Incipient and desinent cavitation numbers for the test in the 305 mm (12 in.) water tunnel

ΔP-kPa (V-m/s)	concentric 152.4 mm orifice plate ($\alpha = 11$ ppm) K_i	K_d	concentric 203.2 mm orifice plate ($\alpha = 10$ ppm) K_i	K_d	dual orifice plate ($\alpha = 10$ ppm) K_i	K_d	quadruple orifice plate ($\alpha = 11$ ppm) K_i	K_d
62 (7.0)	0.99	1.26	1.09	1.37	1.59	1.89	1.62	1.89
74 (7.6)	-	-	1.00	1.22	-	-	-	-

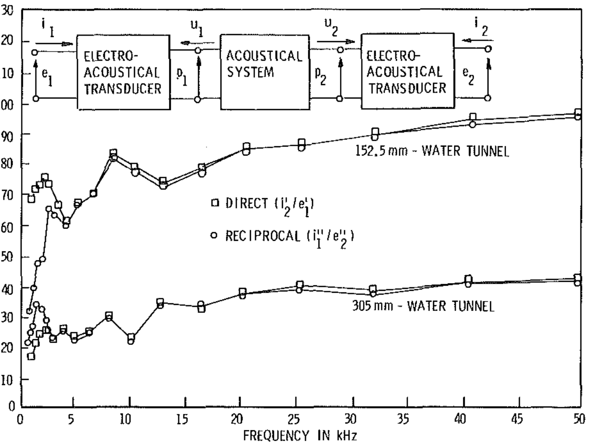

Fig. 6 Direct and reciprocal transfer functions for the 152.5 mm and 305 mm water tunnels. (Uncertainties at 20:1 odds: ±0.8 dB.)

with β. Although, with only one value of the pipe diameter D at issue, it characterizes the absolute size of the orifice as well. This fact is not so evident when we compare the indices for $\beta = 0.50$ and $\beta = 0.33$, but this discrepancy can be traced to the higher air content for the tests for $\beta = 0.33$. The increase of the limiting cavitation index with size is a well known fact in most cavitating systems. From the individual analysis of velocity and size effects, the next step would be an attempt of trying to scale the critical cavitation index with Reynolds number. Unfortunately, the small range of velocities covered by our tests did not allow us to do this conclusively. However Ooi [21], found experimentally in submerged water jets, that for a particular nozzle size and at a fixed air content, the incipient index is independent of the jet Reynolds number. This conclusion seems to contradict an earlier work done by Arndt [22] in which cavitation inception in free shear flows was found to be affected by the Reynolds number. In another work by Arndt [23], it was found that there exists a very strong dependence of the critical cavitation index on Reynolds number for sharp-edged disks normal to the flow. This behavior was explained by the fact that the shear layer in this case, is composed of vortices made up of rotational fluid originally in the boundary layer on the face of the disk. The data also show that there is a monotonic increase of the limiting cavitation number with Reynolds number, and no upper limit could be determined from the available data. As pointed out by Arndt [23], from a practical point of view, this situation is much more critical than the scaling problems associated with streamlined bodies. At present there is no definable upper limit on the critical index for free shear flows. This fact is also shown in Table 1 which presents data for conditions of limited cavitation for the dual and quadruple orifice plates in the 152.5 mm (6 in.) water tunnel. The impossibility of determining the incipient and desinent cavitation numbers for higher pressure drops is due to the fact that the pressure in the test section could not be increased beyond 300 kPa. Even from the available data, it is seen that the reported limits are much greater than the ones shown on Fig. 5 for the same pressure drops. The same trend is observed in Table 2 which is for the tests with the 152.4 mm (6 in.), 203.2 mm (8 in.), the dual, and the quadruple orifice plates in the 305 mm (12 in.) water tunnel. Even though the pressure drops are smaller than those for the tests in the 152.5 mm (6 in). water tunnel, the indices are considerably higher, especially for the dual and quadruple orifice plates.

Experimental Checks of Reciprocity. In theory, the reciprocity principle should be valid when the system is linear, passive, stable and bilateral. The reciprocity method has been used to determine the acoustic characteristics of cavitating flows in a water tunnel. In this application, more than one acoustic medium (air and water) is involved and elastic heterogeneous structures are present in the acoustic path. Lyamshev [24] has shown that reciprocity is valid in these types of situations, but it appears necessary to perform some experimental checks.

Wolde [16] proposed the following experimental check. The auxiliary transducer is located at the position where the actual measurements are to be performed. A Celesco LC-32 hydrophone is situated at the position of the cavitation noise source. Then, the acoustical system is reciprocal if:

$$\left(\frac{i_2'}{e_1'}\right)_{i_1'=0} = \left(\frac{i_1''}{e_2''}\right)_{i_2''=0} \tag{20}$$

where e_1 and i_1 are the voltage and current, respectively, associated with the auxiliary transducer; e_2 and i_2 are the same quantities associated with the LC-32. The ratios indicated by equation (20) are transfer functions for the direct and reciprocal experiments. Figure 6 shows these functions for both water tunnels. The agreement between the direct and reciprocal experiments is very good, except at frequencies below 2.5 kHz because of background noise contamination. The low-frequency limit for all data reported in this work is therefore 2.5 kHz.

The ultimate check of reciprocity as a method for determining the source strength of general sound sources is the prediction of the source strength of a source of known characteristics. The Celesco LC-32 hydrophone was used for this purpose. As a sound projector, it is basically a pulsating cylinder. Within the frequency range of interest, the directivity pattern is omnidirectional. When the acoustic wavelength is less than the observation distance, the source strength of a monopole is related to the sound pressure by equation (3). Thus, the sound pressure level can be measured and converted to source strength by equation (3). On the other hand, one can determine the source strength using the reciprocity method. A

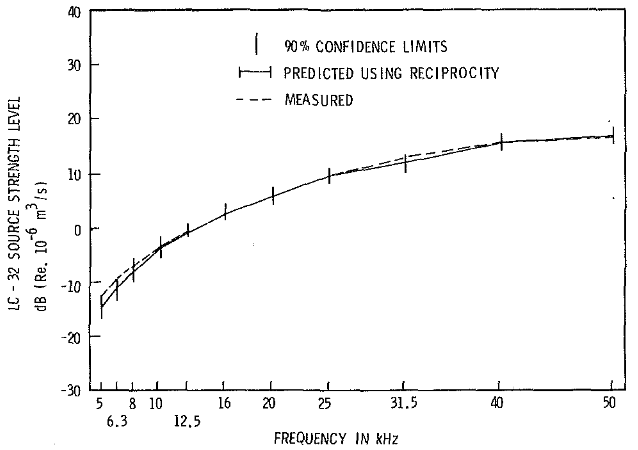

Fig. 7 1/3 octave-band mean-square source strength levels for the Celesco LC-32 hydrophone

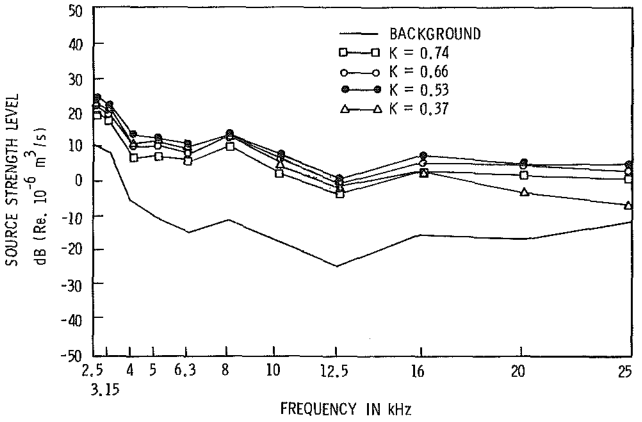

Fig. 8 1/3 octave-band mean-square source strength levels for the single 50.8 mm concentric orifice plate

comparison between the two methods is a check of the reciprocity method.

Typical 1/3 octave band results of this reciprocity check are presented in Fig. 7. These data represent the average of four spectra measured in the 152.5 mm (6 in.) and 305 mm (12 in.) water tunnels. Each spectrum of the average was obtained for different locations of the auxiliary transducer. The LC-32 was driven with approximately 35 volts (RMS) white noise over the frequency range of interest. Also indicated on this figure are the 90 percent statistical confidence intervals calculated for each 1/3 octave band assuming a Gaussian distribution for the measured source strength levels. As one can see, the dispersion is larger at low frequencies, due to the low transmitting response of the LC-32 for frequencies below 10 kHz. Also, below 10 kHz the acoustic wavelength becomes comparable to the diameter of the test section. The tunnel walls then begin to affect the performance of the projector. The free-field projecting response function of the projector becomes progressively less accurate as the frequency is lowered [25].

Source Strength Results for Cavitating Orifice Plates. Figure 8 shows the 1/3 octave band acoustic source strength spectra for various cavitation numbers at constant velocity through the concentric 50.8 mm (2 in.) orifice plate. The upper frequency was limited to 25 kHz due to a low signal-to-noise ratio at higher frequencies. Figure 9 shows similar spectra for the concentric 101.6 mm (4 in.) orifice plate. This orifice plate exhibits a good signal-to-noise ratio up to 50 kHz. In particular, these spectra show that as soon as the inception conditions set in, the measured source strength levels rise well above the background levels. The spectral shape is remarkably similar for all cavitation numbers considered. At low cavitation number the spectrum, although preserving its characteristic shape, seems to reach an upper (maximum) level. Observation of the cavities under these conditions suggests that a *supersaturated condition exists in the test section.* The bubble void fraction increases dramatically for low cavitation numbers which affect both the source strength and the sound transmission characteristics. This is particularly apparent at high frequencies where some decrease in spectral energy is observed.

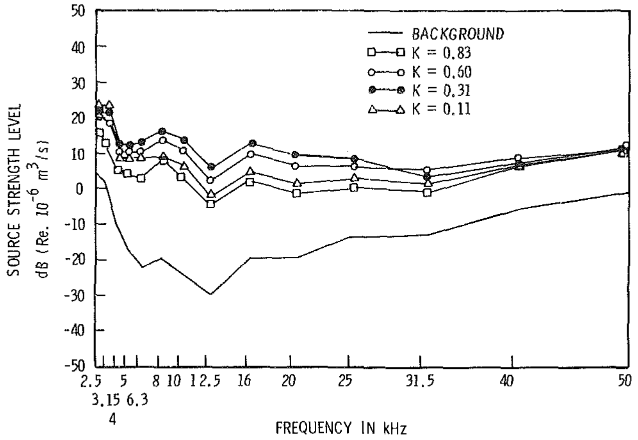

Fig. 9 1/3 octave-band mean-square source strength levels for the single 101.6 mm concentric orifice plate $\Delta P = 185$ kPa; $V = 12.0$ m/s; $K_i = 0.83$; $K_d = 0.93$; *air content* = 10.2 ppm. (Uncertainly at 20:1 odds: ±1.3 dB.)

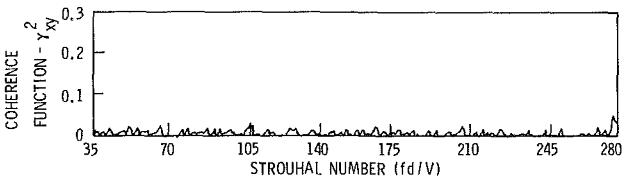

Fig. 10 Coherence function γ^2_{xy} between the cavitation noise produced by the dual orifice plate and the pump acoustic signal for the 305 mm (6 in.) water tunnel

The other orifice plates tested show similar behavior to those reported on in Figs. 8 and 9 [10].

One of the primary difficulties in studying scaling trends of cavitation noise in jet-type flows is the tendency of the noise spectrum to peak at a preferred frequency. This is explained by the fact that cavitation appears in the cores of the organized ring vortices emitted from the nozzle at a certain frequency. The corresponding Strouhal number based on jet diameter, and mean velocity is usually in the range from 0.3 to 0.8. Chahine and Johnson [26] used this fact to construct an acoustic chamber that feeds the jet forming nozzle in order to maximize the pressure fluctuation at a desired frequency. A concern here was whether excitations generated at the pump could be exciting the jet and introducing some peculiarities in the noise spectrum characteristics for the cavitating conditions. A first look at this problem revealed that the frequency range covered in our study correspond to a reduced frequency or Strouhal number in the range 35 to 280. This is well above the range within which the observed phenomenon is found. We also examined the coherence function between the acoustic signal generated at the pump and the auxiliary transducer signal. The latter is related to the signal of interest. For this

Table 3 Velocity exponent for cavitation noise

Reference	Cavitating source	Acoustic dependent variable	Velocity exponent	Comments
[27]	Rear-facing step	$\overline{p^2}$	3 to 4	*
[28]	Triangular prism	$\overline{p^2}\ (f,\Delta f)$	5.45	**
Present Study	Orifice-plate	$\overline{U^2}$	$2m = 3.7 \pm 0.7$	***

* These values were obtained at fixed cavitation numbers.
** For the octave band centered at 8 kHz. This exponent is associated with peak noise and erosion.
*** Valid for $\alpha/\alpha_s < 1$

Table 4 Cavitation number exponent for cavitation noise

Reference	Cavitating source	Acoustic dependent variable	Cavitation number exponent	Comments
[27]	Rear-facing step	$\overline{p^2}$	2.5	*
[29]	Jets	$\overline{p^2}$	-4.5	**
Present Study	Orifice-plate	$\overline{U^2}$	$2n = -1.2 \pm 0.5$	***

* In this work the dependence was assumed to be of the form: $p^2 \sim (K_i - K)^n$ and corresponds to vortex type cavitation.
** Obtained in the range: $0.15 < K < 0.3$.
*** Valid for $K/K_i < 1.0$ and $\alpha/\alpha_s < 1.0$

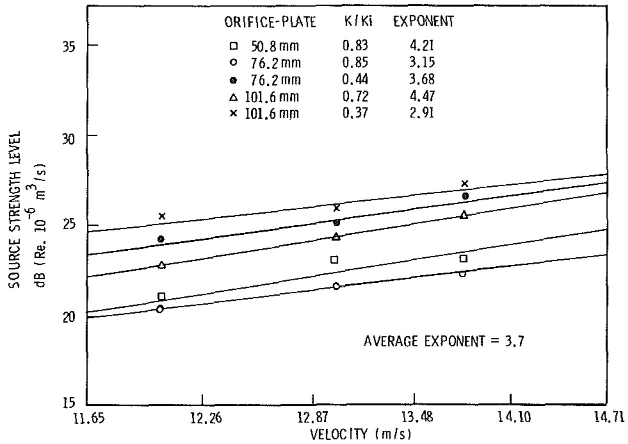

Fig. 11 Dependence of the mean-square source strength level on velocity for the single 50.8 mm, 76.2 mm, and the 101.6 mm orifice plates at different cavitation numbers. (Uncertainties at 20:1 odds: ±1.6 dB; ±0.15 m/s.)

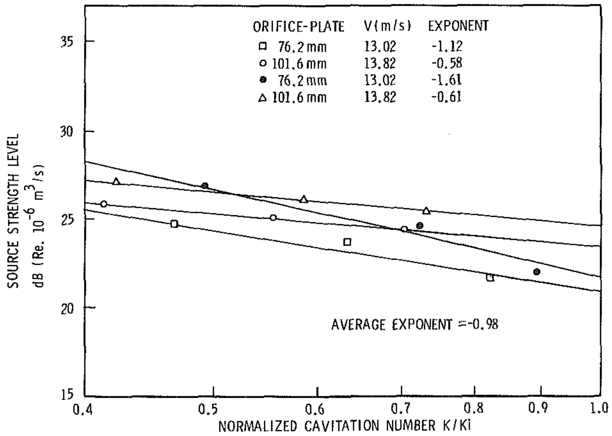

Fig. 12 Dependence of the mean-square source strength level on K/K_i for the single 76.2 mm and the 101.6 mm concentric orifice plates at different velocities. (Uncertainties at 20:1 odds: ±1.6 dB; ±0.02.)

operation to be succesful, it is necessary to use a transducer that is linearly related to the pump acoustic signal. A simple microphone located in the proximity of the pump was chosen. Figure 10 shows the coherence function γ_{xy}^2, between the cavitation noise produced by the orifice plate and the pump acoustic signal. It is seen that the coherence between the two signals is nearly zero, meaning that the output of the auxiliary transducer is not related to the excitations produced by the pump and hence is solely due to the cavitation noise generated by the orifice plate.

As discussed in a previous section, Reynolds number effects on the noise generated by cavitation in jet-type flows is of secondary importance. If that is the case, variations in cavitation noise generated by orifice-plates can be directly traced to the variations in the flow velocity (or pressure drop) and the cavitation number. Mathematically we can write this dependence as:

$$\bar{U}^2 \sim (\Delta P)^m (K/K_i)^{2n}. \tag{21}$$

Keeping one of these parameters constant (ΔP or K/K_i), one should be able to find the dependence of the source strength on the other parameter, and determine the exponents m and n. To accomplish this task we use only those data that exhibit a consistently repeatable behavior over the specific range of the parameter. When supersaturated conditions were attained in the test section, the acoustic characteristics became more random or inconsistent. The exponents were thus derived in the absence of any effects due to the release of dissolved air from the water and hence are valid only for undersaturated conditions downstream of the orifice plate. The acoustic data used for this study were those obtained for the orifice plates tested in the 152.5 mm (6 in.) water tunnel (model scale).

Representative 1/3 octave band center frequencies were selected; namely: 2.5, 6.3, 12.5, and 20 kHz. The mean-square

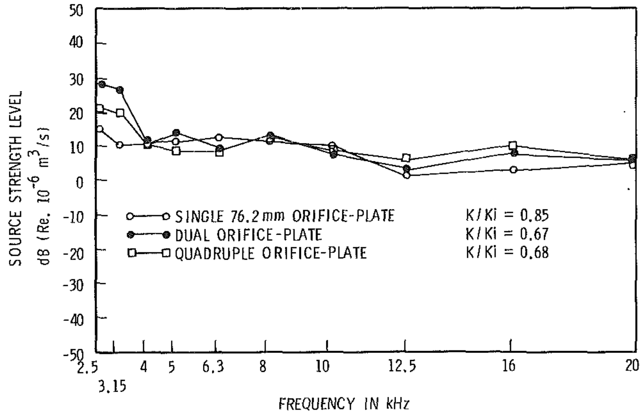

Fig. 13 1/3 octave-band mean-square source strength levels for three orifice plate configurations, all of the same flow area, and at $\Delta P = 185$ kPa. (Uncertainties at 20:1 odds: ±1.3 dB.)

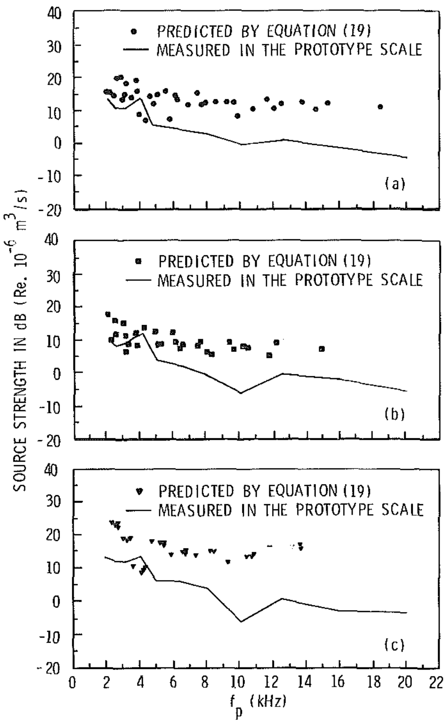

Fig. 14 Comparison between the proposed scaling relation with data measured in the 304.8 mm (12 in.) water tunnel at $\Delta P = 62$, 54, and 76 kPa with $K/K_i = 0.75$, 0.82, and 0.82, respectively, for the *(a)* dual, *(b)* quadruple, and the *(c)* single 203.2 mm orifice plate configuration. Theoretical relation (19) with equation (22).

value of the source strength over the entire spectral-measurement range was also used. The exponent for the presumed power law was determined then by averaging (arithmetically) those exponents established for each selected frequency band (including the over-all band levels).

Figure 11 shows typical results for the mean-square values of the source strength in dB as a function of velocity (or pressure drop, since $V \sim \Delta P^{1/2}$). The lines drawn through the data at each condition fit the majority of points in a mean-square sense and result in slopes which are quite similar. Similarly, Fig. 12 displays typical data representing the dependence of the mean square value of source strength in dB as a function of the normalized cavitation number.

Similar plots were obtained for each selected center frequency, giving power law exponents which were arithmetically averaged. This result was then finally averaged with the exponents shown on Fig. 11 (for ΔP), and on Fig. 12 (for K/K_i). Tables 3 and 4 give the final results in comparison with similar studies reported in the literature.

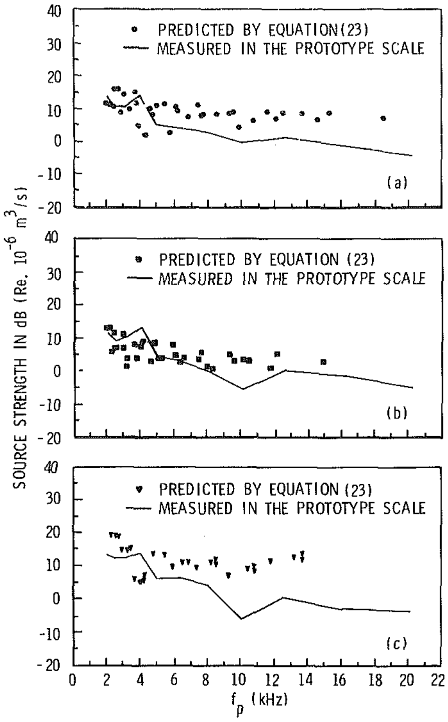

Fig. 15 Comparison between the proposed scaling relation with data measured in the 304.8 mm (12 in.) water tunnel at $\Delta P = 62$, 54, and 76 kPa with $K/K_i = 0.75$, 0.82, and 0.82, respectively, for the *(a)* dual, *(b)* quadruple, and the *(c)* single 203.2 mm orifice plate configuration. Modified relation (23) with $x = 4$, $y = 1.85$, and $2n = -1.2$ and equation (22).

The studies presented in Tables 3 and 4, are for shapes designed to minimize the effects of Reynolds number. Comparisons should be treated with caution because of different acoustic dependent variables, as well as the criteria adopted for the determination of the exponents. The variations in the velocity exponent can be traced to differences in nuclei concentration, which in turn can convert monopole radiation to dipole radiation as the concentration increases. Depending on the degree of conversion, the velocity exponent can vary between 4 and 6. Also, it is not known how the complicated compressibility effects affect the velocity exponent. With respect to the cavitation number dependence, it is not yet clear how one should include K_i in the scaling. There is speculation that $(K/K_i)^{2n}$ is most valid only near inception.

The main objective in considering the plate with two diametrically opposed orifices and the plate with four equally spaced orifices was to identify any possible influence that a multiplicity of orifices might have on cavitation noise. These plates were designed to have the same flow area and were tested under similar flow conditions. Figure 13 shows typical source strength spectra for these plates. It is quite clear that the cavitation noise created by multiple orifices is practically identical to the noise created by a single orifice. The conditions (cavitation number, pressure drop, etc.) were changed during the tests and trends similar to the single orifice plate results were observed.

Application of Scaling Relations for the Prediction of Cavitation Noise. Equation (19) will now be used to predict the spectral levels of cavitation noise expected in the 305 mm (12 in.) water tunnel, based on the test data obtained in the 152.5 mm (6 in) water tunnel. The test data obtained in the larger water tunnel will help verify the adequacy of the proposed scaling relation. The exponent of (K/K_i) is taken as

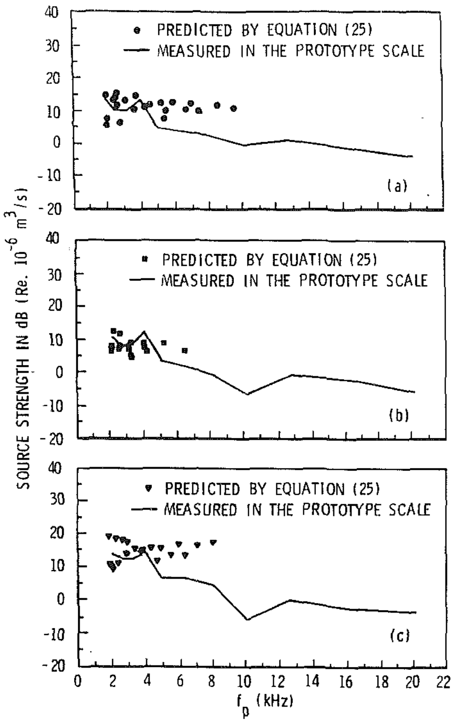

Fig. 16 Comparison between the proposed scaling relation with data measured in the 304.8 mm (12 in.) water tunnel at $\Delta P = 62$, 54, and 76 kPa with $K/K_i = 0.75$, 0.82, and 0.82, respectively, for the *(a)* dual, *(b)* quadruple, and the *(c)* single 203.2 mm orifice plate configuration. Equations (25) and (24) with $y = 1$ and $2n = -1.2$.

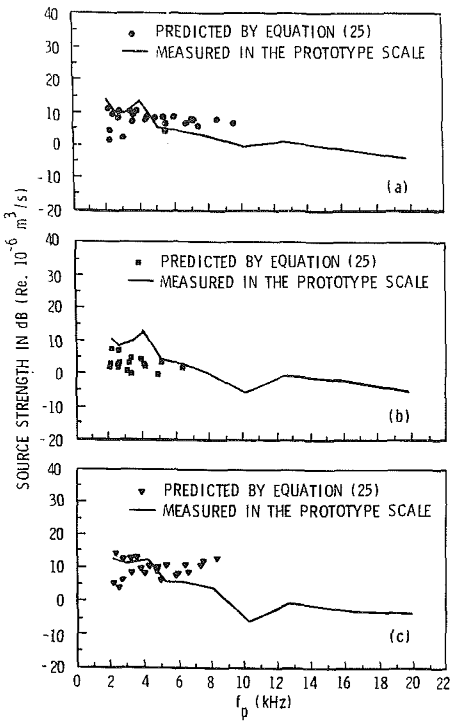

Fig. 17 Comparison between the proposed scaling relation with data measured in the 304.8 mm (12 in.) water tunnel at $\Delta P = 62$, 54, and 76 kPa with $K/K_i = 0.75$, 0.82, and 0.82, respectively, for the *(a)* dual, *(b)* quadruple, and the *(c)* single 203.2 mm orifice plate configuration. Equations (25) and (24) with $y = 1.85$ and $2n = -1.2$.

$2n = -1.2$ from the results discussed earlier and shown in Table 4. The frequency axis must also be scaled because of equation (18). With $\rho_m = \rho_p$ and P_0 being replaced by ΔP simplifies the frequency scaling. In particular,

$$\frac{f_p}{f_m} = \left(\frac{\Delta P_p}{\Delta P_m}\right)^{0.5} \left(\frac{(K/K_i)_p}{(K/K_i)_m}\right)^{0.6} \lambda^{-1}. \qquad (22)$$

Figure 14 shows the measured prototype source strength spectra for the dual, the quadruple, and the single 203.2 mm orifice plate configurations. These spectra are compared with those predicted with the aid of the data obtained in the smaller water tunnel (model scale). The normalized cavitation number (K/K_i) varies between 0.3 and 0.8, and the pressure differential ΔP varies between 185 kPa (26.6 psi) and 243 kPa (35.3 psi) in the mode tests. As can be seen, the theoretical scaling relation over predicts the prototype data.

The different exponents presented in Tables 3 and 4 suggest that equation (19) can be refined with respect to the exponents that appear for each parameter. This means that the scaling relation for source strength can be re-written as:

$$\frac{\overline{U_p^2}\,(f_p,\Delta f_p)}{\overline{U_m^2}\,(f_m,\Delta f_m)} = \lambda^x \left(\frac{\Delta P_p}{\Delta P_m}\right)^y \left(\frac{(K/K_i)_p}{(K/K_i)_m}\right)^z. \qquad (23)$$

From Table 3, the source strength scales approximately with the 3.7 power of velocity for undersaturated conditions. This observation would imply that $y = 1.85$ is the best numerical value for the exponent of the pressure differential, instead of the 1.0 as equation (19) suggests. In order to verify the dependence of the acoustic source strength on the fourth power of the geometric scale factor indicated in equation (19) we should maintain in the 305 mm (12 in.) water tunnel the same range of pressure differential utilized for the tests in the 152.5 mm (6 in.) water tunnel. Unfortunately, such conditions could not be attained in the larger water tunnel because of early impeller cavitation which results in a decrease of the signal-to-noise ratio. Consequently, the numerical value of $x = 4$ was retained and the tests conducted were for conditions where the orifice plates cavitated before the impeller. The exponent of (K/K_i) is taken as $z = -1.2$ from Table 4. Figure 15 shows the results for this revised scaling under the same testing conditions as Fig. 14. As one can see the predictions are in better agreement with the prototype data, particularly in the low frequency range.

The gas content of the water has a very pronounced influence on the bubble dynamics. This is because the higher the dissolved gas content, the greater is the amount of gas diffused into the cavitation bubbles. The gas present in the bubbles provides a cushioning effect in the final stages of collapse which reduces the noise generated, particularly in the high frequency range of the spectrum. On the other hand the gas content affects the liquid compressibility, which could be scaled using parameter π_8 (equation (11)). As we pointed out before, relaxing the liquid compressibility *may* introduce a scale effect. Since the gas content was not considered in the development of the scaling relation, we made use of a modification proposed by Løvik [30, 31] in order to account for differences in the gas content of the water between model and prototype. It should be mentioned that the modification to be introduced into the scaling relation is only related to the influence of gas content on bubble dynamics and not to the compressibility of the liquid. Løvik shows that the factor:

$$\left(\frac{Q_p}{Q_m}\right)^{1/2(k-1)} \text{with } k = 1.4 \text{ (for air),}$$

accounts for gas content effects on mean-square acoustic pressure. Note that: $Q = \rho V^2/2P_c$ where $P_c = P_g + P_v$. Here, $P_g \simeq \alpha\beta$; where α is the air content of the liquid (in ppm) and β is Henry's gas constant. Løvik points out that this empirical relation is known to apply only for $0.2 < 1/Q \leq 1$.

The frequency scaling is also affected by the gas content effect according to the following modificiation of equation (22):

$$\frac{f_p}{f_m} = \lambda^{-1} \left(\frac{\Delta P_p}{\Delta P_m} \right)^{0.5} \left(\frac{(K/K_i)_p}{(K/K_i)_m} \right)^{0.6} \left(\frac{1 + 1/Q_m}{1 + 1/Q_p} \right). \quad (24)$$

The general form of equation (23) is now altered using equations (3) and (24) with the mean-square acoustic pressure correction noted above. We find

$$\frac{\overline{U_p^2}\,(f_p, \Delta f_p)}{\overline{U_m^2}\,(f_m, \Delta f_m)} = \lambda^4 \left(\frac{\Delta P_m}{\Delta P_p} \right)^{y} \left(\frac{(K/K_i)_p}{(K/K_i)_m} \right)^{2n} \cdot \left(\frac{1 + 1/Q_p}{1 + 1/Q_m} \right)^{2} \left(\frac{Q_p}{Q_m} \right)^{1/2(k-1)}. \quad (25)$$

Equation (25) is a refined form of theoretically based equation (19) with $y = 1$ and $2n = -1.2$. It is also a refined form of the experimentally adjusted equation (23) with $y = 1.85$ and $2n = -1.2$. Figure 16 shows an application of equations (24) and (25) with $y = 1$ and $2n = -1.2$. Likewise, Fig. 17 shows the results for $y = 1.85$ (experimentally adjusted exponent) and $2n = -1.2$. The air content α for both the model and prototype was typically around 10 ppm, with the velocities in the model scale at around 13m/s (42.6 ft/s) and in the prototype scale at around 7 m/s (23.0 ft/s). The comparative analysis of both sets of data shows that the theoretical scaling relation, modified for gas content effects, continues to overpredict the prototype performance, while the relation with empirically adjusted exponents gives reasonable results with the exception of the quadruple orifice plate. Differences in source strength spectra among the three geometries considered are not clearly explainable within the experiment reported here. However, the nature of the cavitation noise (and also noncavitating noise) generated in turbulent jets is known to be sensitive to the geometry of the nozzle. Many references exist on this issue; the reader is referred to Chahine and Johnson [26] or Hussain [32] for a review. The reduction in the scaled frequency range that occurs when the air content effects are included in the frequency scaling formula suggests that the upper frequency limit in the model scale should be extended beyond the limit adopted for this study (50 kHz). This will then permit one to predict the prototype performance over a wider frequency range.

Summary and Conclusions

Research into the prediction and abatement of noise generated by cavitating flows in control devices is a rather recent development. There has been little effort to systematical study, both analytically and experimentally, the fundamental noise generation mechanisms associated with cavitating valves. Due to the complexity of the problem, it appears that a first study of the acoustics of this type of cavitating flow should be semi-empirical in nature.

The present work is concerned with experimental measurements of the acoustic source strength of cavitating flows generated by simple control devices. Scaling relations were developed, and used to estimate source strength levels expected in a larger but similar test environment. The proposed scaling relations were empirically adjusted and include the effects of water gas content level. Predictions using these formulas were compared with experimental results obtained at prototype scale. It is shown that the scaling relation obtained from purely dimensional analysis tends to over predict the prototype acoustic performance. The scaling formula with empirically adjusted exponents gives better results. The scaling formula which includes gaseous effects tends to narrow the frequency range of the prediction in the prototype scale, but the levels are predicted most accurately (relative to the other models).

It was found in this study that the acoustic source strength tends to increase approximately with the fourth power of velocity; and nearly linearly with the ratio K_i/K.

Some results of limited cavitation conditions are reported, and it was found that the incipient and desinent cavitation numbers tend to increase with orifice size and air content level; however, the influence of velocity could not be determined conclusively because of the small range of velocities covered by these tests. Therefore, a Reynolds number dependence could not be established.

Acoustic measurements in confined spaces like water tunnels require careful calibration in order to obtain free-field sound characteristics. A new method based on reciprocity was suggested and applied. This type of measurement requires a very simple and inexpensive setup and appears to provide reliable acoustic source strength estimates.

Acknowledgments

This work was performed at the Applied Research Laboratory and with the cooperation of the Noise Control Laboratory of the Pennsylvania State University, while the first author was pursuing his Ph.D. degree, under the sponsorship of CAPES, an agency of the Ministry of Education Affairs of Brazil.

The authors want to especially acknowledge the contributions of Dr. Hans J. Baiter of the Fraunhofer-Forschungsgruppe fur Hydroakustik in the discussion of the scaling relations, and Dr. Michael L. Billet of the Applied Research Laboratory at Penn State University for his continued support during the development of this work.

Finally, the first author wants to acknowledge the special grants from the Brazilian Agencies-CNPq and FAPESP that has supported his cavitation noise research program while at UNESP.

References

1 Reynolds, O., "Experiments Showing the Boiling of Water in an Open Tube at Ordinary Temperatures," *Papers on Mechanical and Physical Subjects*, Vol. II (1881-1900), Cambridge University Press, 1900, pp. 51-58.

2 Fitzpatrick, H. M., and Strasberg, M., "Hydrodynamic Sources of Sound," *Symp. on Naval Hydrodynamics*, Washington, D. C., 1956, pp. 241-280.

3 Morozov, V. P., "Cavitation Noise as a Train of Sound Pulses Generated at Random Times," *Sov. Phys. Acoust.*, Vol. 14, 1969, pp. 361-365.

4 Baiter, H. J., Gruneis, F., and Tilmann, P., "An Extended Basis for the Statistical Description of Cavitation Noise," *Int. Symp. on Cavitation Noise*, ASME, Phoenix, AZ, 1982, pp. 93-108.

5 Jorgensen, D. W., "Noise From Cavitating Submerged Water Jets," *J. Acoust. Soc. Am.*, Vol. 33, 1961, pp. 1334-1338.

6 Mellen, R. H., "Ultrasonic Spectrum of Cavitation Noise," *J. Acoust. Soc. Am.*, Vol. 26, 1954, pp. 356-360.

7 Esipox, I. B., and Naugolnykh, K. A., "Cavitation Noise in Submerged Jets," *Sov. Phys. Acoust.*, Vol. 21, 1976, pp. 404-405.

8 Hamilton, M. F., Thompson, D. E., and Billet, M. L., "An Experimental Study of Travelling Bubble Cavitation Noise," *Int. Symp. on Cavitation Noise*, ASME, Phoenix, AZ, 1982, pp. 25-33.

9 Blake, W. K., Wolpert, M. J., and Geib, F. E., "Effects of Boundary Layer Development on Cavitation Noise and Inception on a Hydrofoil," David W. Taylor Naval Ship Research and Development Center, Report 76-0051, 1976. Also, in *J. Fluid Mech.*, Vol. 80, 1977, pp. 617-640.

10 Bistafa, S. R., "An Experimental Study on the Noise Generated by Vaporous Cavitation in Turbulent Shear Flow Produced by Confined Orifices Plates," Ph.D. dissertation, Dept. of Mech. Engr., The Pennsylvania State University, Aug. 1984.

11 ASME, *Fluid Meters Their Theory and Application*, edited by Howard S. Bean, Sixth Edition, 1971.

12 Holl, J. W., "Nuclei and Cavitation," ASME *Journal of Basic Engineering*, Vol. 92, 1970, pp. 681-688.

13 Holl, J. W., "Cavitation State of Knowledge," *Limited Cavitation*, ASME Symposium, June 1969.

14 Tullis, J. P., "Cavitation Scale Effects for Valves," *J. Hydraulics Division*, ASCE, 1973, pp. 1109-1127.

15 Keller, A. P., "Investigations Concerning Scale Effects of the Inception of Cavitation," *Cavitation*, Inst. Mech. Engr., Heriot-Watt University, Edenburg, Scotland, 1974, pp. 109-117.

16 Wolde, T. Ten, "Reciprocity Experiments on the Transmission of Sound in Ships," Ph.D. thesis, Deft University, 1973.

17 Levkovskii, Y. L., "Modeling of Cavitation Noise," *Sov. Phys. Acoust.*, Vol. 13, 1968, pp. 337-339.

18 Levkovskii, Y. L., "Prediction of the Spectral Levels of Cavitation Noise," *Sov. Phys. Acoust.*, Vol. 26, 1981, pp. 495-497.

19 Buckingham, E., "Model Experiments and the Form of Empirical Equations," *Trans. ASME*, Vol. 37, 1915, pp. 263-296.

20 Strasberg, M., "Propeller Cavitation Noise After 35 Years of Study," ASME *Symposium on Noise and Fluids Engineering*, 1977, pp. 89-99.

21 Ooi, K. K., "Scale Effects on Cavitation Inception in Submerged Water Jets: A New Look," *J. Fluid Mech.*, Vol. 51, 1985, pp. 367-390.

22 Arndt, R. E. A., "Cavitation in Fluid Machinery and Hydraulic Structures," *Annual Review of Fluid Mechanics*, Vol. 13, 1981, pp. 272-328.

23 Arndt, R. E. A., "Cavitation Inception and How it Scales: A Review of the Problem with a Summary of Recent Research," *Symposium on High Powered Propulsion of Large Ships*, Part 2, The Netherlands, 1974.

24 Lyamshev, L. M., "A Question in Connection with the Principle of Reciprocity in Acoustics," *Sov. Phys. Doklady*, Vol. 4, 1959, p. 406.

25 Waterhouse, R. V., "Output of a Sound Source in a Reverberation Chamber and Other Reflecting Environments," *J. Acoust. Soc. Am.*, Vol. 30, 1958, pp. 4-13.

26 Chahine, G. L., and Johnson, V. E., "Noise Generated by a Self Resonating Cavitating Jet," *ASME Cavitation and Multiphase Flow Forum*, FED Vol. 9, 1984.

27 Lush, P. A., "Sound Generated by Cavitating Flows in a Duct," *Proc. of the Institute of Acoustic Specialists*, Meeting on Acoustic Cavitation, Poole, 1977.

28 Ramamurthy, A. S., and Bhaskaran, P., "Velocity Exponent for Erosion and Noise Due to Cavitation," ASME JOURNAL OF FLUIDS ENGINEERING, Vol. 69, 1979, pp. 69-75.

29 Franklin, R. E., and McMillan, J., "Noise Generation in Cavitating Flows—The Subjerged Jet," *Int. Symp. on Cavitation Noise*, ASME, Phoenix, AZ, 1982, pp. 17-23.

30 Løvik, A., "Scaling of Propeller Cavitation Noise," Noise Sources in Ships—1: Propellers, Nordforsk, Sweden, 1981.

31 Løvik, A., and Vassenden, J., "On the Influence of the Gas Content on Cavitation Noise and Erosion," *Proc. of the 6th Conference on Fluid Machinery*, Akademia Kiado, Budapest, 1979.

32 Hussain, A. K. M. F., "Coherent Structures and Turbulence," *J. Fluid Mech.*, Vol. 173, 1986, pp. 303-356.

Comparison of Computational and Experimental Unsteady Cavitation on a Pitching Foil

F. Stern
Associate Professor,
Research Engineer,
Department of Mechanical Engineering,
Institute of Hydraulic Research,
The University of Iowa,
Iowa City, Iowa 55242

Comparisons are made between a nonlinear method for predicting unsteady sheet cavitation and available experimental data for a pitching foil for the purposes of verifying the calculations and to further analyze the flow. A dynamical approach is employed in which the form of the instantaneous cavity surface is modeled as a semiellipse. The cavity length (major axis), thickness (semiminor axis), and position are determined such that the nonlinear cavity-surface boundary conditions are satisfied approximately. The pressure on the instantaneous cavity surface is prescribed using an unsteady thick-foil potential-flow method based on Green's second identity. The computational method yields best results in predicting the cavity dynamics, but underpredicts the cavity length. For fixed cavitation number, mean foil angle, and pitch amplitude, the cavity dynamics, such as maximum cavity size and cavity surface behavior, are shown to depend on the ratio of the cavity natural frequency for the foil fixed at the maximum pitch amplitude to the foil reduced frequency. For a certain value of this ratio, the cavitation response is shown to be a minimum. The experimental results confirm the computational trends up to the point that experimental data were obtained.

Introduction

In proportion to the total number of studies on cavitation, those devoted to unsteady cavitation are extremely small. Yet, the unsteady nature of cavitation is usually responsible for its deleterious consequences. This paper compares a nonlinear method for predicting unsteady sheet cavitation (Stern and Vorus, 1983) with available experimental data for a pitching foil (Shen and Peterson, 1978, 1980) for the purposes of verifying the calculations and to further analyze the flow. A dynamical approach is employed that is intended to model the gross features of unsteady sheet cavitation: cavity length, thickness, position, and surface behavior, including rates of deformation and movement. The approach differs significantly in a number of ways from the linear quasi-steady and unsteady cavitation theories. See Stern (1982) and Kerwin et al. (1986) for more complete reviews, including references up to their respective dates. More recently, Hsu and Shen (1988) have presented results from a linear quasi-steady partial-cavity theory, including comparisons with experimental data for a pitching foil.

In the following, the computational method is outlined and the flow geometry and experimental information are described. Then, comparisons are made for the noncavitating flow, steady cavitation, and unsteady cavitation, including inception, cavity dynamics, and cloud cavitation and noise. Lastly, some concluding remarks are made concerning: the implications of the present work with regard to practical applications; an overview of the most important results from a marine-propeller application (Stern, 1982); and the main differences between the results from the present approach and the linear theories.

Overview of the Computational Method

The theory presented in Stern and Vorus (1983) is fairly general and appropriate for a number of applications; however, features are incorporated in the formulation to facilitate its application to marine propellers. Therefore, the description provided is for marine propellers with the simplifications for the present pitching-foil application pointed out. Below, all variables are nondimensionalized, unless otherwise indicated, using the foil semichord $c/2$, steady section speed U, and fluid density ρ.

Problem Formulation and Dynamic-Potential Solution. Under the assumptions that the fluid is infinite, incompressible, and the flow irrotational, excluding the inflow wake field and the downstream vortex sheet representing the wake of the body, the velocity-potential boundary-value problem for unsteady sheet cavitation is separated into two parts—static and dynamic—which are solved sequentially in a forward time-stepping procedure. The static potential ϕ_s describes the flow around the cavity fixed instantaneously relative to the body (propeller) while the body moves (rotates) through a nonuniform wake field. The dynamic potential ϕ_d represents the instantaneous reaction of the cavity to the static potential and thus predicts the cavity's deformation and motion relative to the blade. For known cavity surfaces $S_c(t)$, the

---

Contributed by the Fluids Engineering Division for publication in the JOURNAL OF FLUIDS ENGINEERING. Manuscript received by the Fluids Engineering Division March 1, 1988.

static-potential boundary-value problem is solvable by standard methods since the boundary conditions are exclusively kinematic. Therefore, with regard to the dynamic-potential boundary-value problem, the static potential and its derivatives are considered as known at any time.

A solution is obtained for the dynamic potential by using the concepts of slender-body theory to define near and far-field potentials that are matched to form the complete solution. In the far field, the cavity is represented by a three-dimensional line distribution of sources. In the near field, the cavity is approximated at each cross section as a semiellipse with semimajor axis a (half-length), semiminor axis b (thickness), and position l along the section chord (Fig. 1). An important feature of unsteady cavitation (oscillating inner fluid boundary) is that even for long cavities of constant cross section, three-dimensional effects cannot be completely removed from the near-field problem, i.e., the cavity must have a finite length and a three-dimensional far-field representation. This is a result of the fluid being incompressible. An analytic solution is derived for the near-field dynamic potential in terms of elliptical coordinates (μ, η) and the unknowns $a(t)$, $b(t)$, and $l(t)$ that satisfies all of the conditions of the dynamic-potential boundary-value problem except the dynamic boundary condition on the surface of the cavity.

The dynamic boundary condition is satisfied in a least-square sense by requiring that its Fourier-cosine coefficients be zero. The first three coefficients provide conditions for determining a, b, and l. These conditions yield the cavity equations of motion in the form of three coupled nonlinear second-order ordinary differential equations with time as the independent variable. The cavity equations can be put in the form

$$\begin{aligned} \ddot{a} &= f_1(a, \dot{a}, b, \dot{b}, \dot{l}, \mathrm{Re}, \mathrm{Ar}, P_0, P_2) \\ \ddot{b} &= f_2(a, \dot{a}, b, \dot{b}, \dot{l}, \mathrm{Re}, \mathrm{Ar}, P_0, P_2) \qquad (1) \\ \ddot{l} &= f_3(a, b, \dot{b}, \dot{l}, \mathrm{Re}, P_1) \end{aligned}$$

where $\mathrm{Re} = Uc/\nu$ is the Reynolds number, Ar is the cavity aspect ratio, and

$$P_n = \frac{m}{\pi} \int_0^{\pi} P \cos n\eta d\eta$$

$$n = 0,\ 1,\ 2 \text{ and} \begin{cases} n = 0, & m = 1 \\ n > 0, & m = 2 \end{cases} \qquad (2)$$

are the first three Fourier coefficients of the fluid pressure

$$P = \sigma + C_p \qquad (3)$$

evaluated on the instantaneous cavity surface $S_c(t)$. In (3), σ is the cavitation number

$$\sigma = \frac{p_\infty - p_c}{\frac{1}{2}\rho U^2} \qquad (4)$$

where p_∞ and p_c are the ambient and cavity pressures, respectively; and C_p is the known static-potential pressure coefficient. The following terms, which are included in the more general form of the cavity equations, have been neglected in (1) for convenience: the cross-product term between the static and dynamic potentials; the slender-body theory interaction between cavity cross sections; and the surface-tension pressure.

The results are in the form of response curves, $(a, \dot{a}, b, \dot{b}, l, \dot{l})$ versus time which are obtained by numerical integration using a Runge-Kutta-Merson procedure in which the time step is automatically adjusted to keep the error within specified bounds (ca. 1 percent). For fixed Re and Ar, the cavitation response is controlled by the specification of $P = P(\mathbf{x}, t)$. When $P = P(\mathbf{x})$ is constant in time, the cavity equations have constant (i.e., fixed cavitation) solutions $(\bar{a}, \bar{b}, \bar{l})$. The constants are determined by the equations such that the first three harmonics of the fluid pressure are zero on the ellipse, i.e., the equations fit an ellipse, in a least-square sense, to the zero-pressure line in the fluid. When $P = P(\mathbf{x}, t)$ is not constant in time, the cavity equations have unsteady solutions. The character of the unsteady solution depends on the specific form of $P(\mathbf{x}, t)$ which for the problems of interest is of the

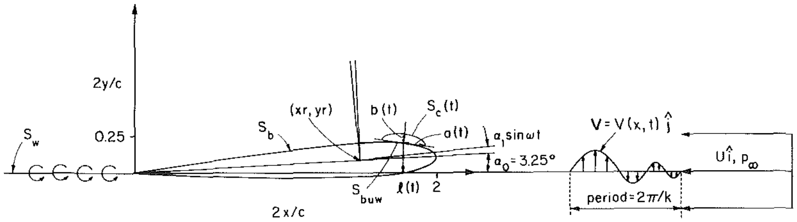

Fig. 1 Cavity and foil geometry

Nomenclature

(a, b, l) = cavity half-length, thickness, and position
$\dot{A}_c$ = cavity area velocity at collapse
A_k = maximum cavity area
Ar = cavity aspect ratio
c = foil chord length
C_p = static-potential pressure coefficient
k = reduced frequency
l_c = cavity position at collapse
L = cavity length
L_k = maximum cavity length
$\mathbf{n}$ = foil normal (n_x, n_y, n_z)
P = fluid pressure
Re = Reynolds number
S_b = foil surface
S_{buw} = unwetted portion of foil surface
S_c = cavity surface
S_w = foil wake
t = time
U = steady section speed (free-stream velocity)
$\mathbf{V}$ = section inflow
$\mathbf{x}$ = position vector
(xr, yr) = pitch axis
α = instantaneous angle of attack
α_0 = mean foil angle
α_1 = pitch amplitude
Γ = foil circulation
ν = fluid kinematic viscosity
ρ = fluid density
σ = cavitation number
ϕ = velocity potential
ϕ_d = dynamic potential
ϕ_{nc} = noncavitating potential
ϕ_s = static potential
ϕ_{sp} = perturbation potential
ω = excitation (pitch) frequency
ω_n = cavity natural frequency

general form

$$P = \text{Real} \sum_{n=0}^{N} P_n(\mathbf{x}) e^{inkt} \tag{5}$$

In (5), k is the section reduced frequency

$$k = \omega c/2U \tag{6}$$

where ω is the excitation frequency.

The integration of the cavity equations requires the determination of the static potential and its derivatives at each time step. It was stated earlier that the static-potential boundary-value problem can be solved by standard methods. However, it should be recognized that the semielliptical cavity form itself cannot be used in the solution of the static-potential problem because it is only an approximation to the cavity surface. Ostensibly, it provides the necessary information (cavity length, thickness, and position) that can be suitably represented. Presently, a thin-cavity approximation is used for the static potential. The details of this are discussed subsequently, followed by the noncavitating-potential solution. First, a brief review of some earlier results is provided as an aid in understanding the nature of solutions to the cavity equations (1).

In earlier work (Stern and Vorus, 1983), it was shown that the linear response of the cavity about the equilibrium values ($\bar{a}$, $\bar{b}$, $\bar{l}$) is damped periodic oscillations. The frequencies of the oscillations are referred to as the cavity natural frequencies ω_n. Both periodic and positively damped periodic solutions are stable. The linear damping terms are positive damping with Re^{-1} as the damping coefficient. The conclusion is that both the linear and nonlinear systems are stable. An exact analytical solution of the undamped linear system for circular isobars shows that, in general, ω_n depends on the normal pressure gradient at the cavity surface dp/dn, ($\bar{a}$, $\bar{b}$, $\bar{l}$), and Ar. In an extended sense, dp/dn can be regarded as determining the cavity stiffness and ($\bar{a}$, $\bar{b}$, $\bar{l}$) and Ar its mass. Since dp/dn is largest near the body, ω_n is relatively larger for small low Ar cavities as compared to large high Ar ones. The role of σ is in determining the cavity size. Also, the method was demonstrated numerically for both fixed and unsteady cavitation by using the steady noncavitating potential for a two-dimensional half-body as an approximation to the static potential.

The system response when perturbed from an already existing equilibrium configuration (i.e., the response of the homogeneous equations to initial conditions) shows that, for low values of Re, the response is basically linear. When $\text{Re} \sim 10$, the motion is overdamped exponential. When $\text{Re} \sim 10^2$, the motion is underdamped, uncoupled, and periodic. As Re increases ($>10^3$), so do the response amplitudes; consequently, the nonlinearities and coupling effects play a more important role. When $\text{Re} > 10^4$ the damping is negligible such that it is not possible to determine a logarithmic decrement. The effects of the nonlinearities and coupling are reflected in an irregular pattern in the oscillations, including secondary peaks in the curves and alternating maximums at each cycle between the curves. The oscillatory solutions all have frequencies close to the first-mode natural frequency ω_n. Fixed-cavity development was studied by varying the ambient pressure as a discontinuous ramp function with a specified fall time T_s. The response is damped oscillations at ω_n. The peak amplitude of the response depends on the ratio T_s/T_n, where T_n is the natural period ($=2\pi/\omega_n$). For small T_s/T_n, large peak amplitudes occur compared with quasi-steady response; for large T_s/T_n, quasi-steady response is achieved in the limit.

Unsteady cavitation was studied by varying the ambient pressure sinusoidally. The peak amplitude of the response depends on the ratio T_p/T_n, where T_p is the period of the pulse. For small T_p/T_n, small peak amplitudes occur compared with quasi-steady response; for $.5 < T_p/T_n < 1.75$, large peak amplitudes occur compared to quasi-steady response; for large T_p/T_n (>2), essentially quasi-steady response occurs. Two modes of cavity collapse were identified; first, a high frequency mode in which the cavity collapses toward the foil trailing edge, and second, a low-frequency mode in which the cavity collapses toward the foil leading edge. The importance of the ratio of the cavity natural frequency to the excitation frequency (i.e., ω_n/ω) is discussed further below with regard both to the present results and those obtained for a marine propeller (Stern, 1982).

Thin-Cavity Approximation for the Static Potential. The integration of the cavity equations requires the determination of the static potential and its derivatives at each time step. The boundary-value problem for the static potential ϕ_s is

$$\nabla^2 \phi_s = 0 \qquad \text{in } \forall \tag{7}$$

$$\frac{\partial \phi_s}{\partial n} = n \cdot \mathbf{V}(t) \qquad \text{on } S_b + S_c(t) \tag{8}$$

$$\phi_s = 0 \qquad \text{on } S_\infty (\text{upstream}). \tag{9}$$

In (8), S_b is the wetted portion of the foil surface, S_c is the cavity surface, n is the outward unit normal vector, and $\mathbf{V}$ is the inflow velocity relative to coordinates fixed in the foil (Fig. 1). In addition to satisfying conditions (7) through (9), the static potential must also satisfy a Kutta condition at the foil trailing edge, and proper consideration must be given for the foil wake.

For a thin cavity, the static potential can be assumed to be a perturbation on the noncavitating flow

$$\phi_s = \phi_{nc} + \epsilon \phi_{sp} \tag{10}$$

where ϵ is a small parameter related to the cavity thickness. The perturbation potential ϕ_{sp} satisfies the static-potential boundary value problem with the kinematic boundary condition (8) replaced by

$$\frac{\partial \phi_{sp}}{\partial n} = V_t n_{cx} + v_n \qquad \text{on } S_{buw} \tag{11}$$

$$= 0 \qquad \text{on } S_b \tag{12}$$

where S_{buw} is the unwetted portion of the foil surface, V_t is the noncavitating surface velocity, n_{cx} is the x component of the cavity normal, and v_n is the normal perturbation velocity on the cavity surface. Conditions (11) and (12) are obtained from (8) by a Taylor-series expansion about the foil surface and retaining terms of $0(\epsilon)$. In order to facilitate the use of the existing noncavitating flow computer program, (12) was ignored and, in (11), v_n was neglected and n_{cx} was approximated by the x component of the foil normal n_x. This simply adds the term $V_t n_x$ to the source strengths on the unwetted portion of the foil surface S_{buw}.

Noncavitating-Potential Solution. The noncavitating flow is calculated using an unsteady thick-foil potential-flow method. This provides an accurate representation of the unsteady-pressure field that is sensitive to changes in foil geometry (thickness, camber, angle of attack) and the nonuniform inflow. For propeller applications, three-dimensional propeller effects are included by correcting the harmonics of the section inflow through the use of an unsteady lifting-line method (Stern, 1982).

The noncavitating potential ϕ_{nc} in (10) is the solution to the static-potential boundary-value problem with the kinematic boundary condition (8) satisfied on the complete foil surface $S_b + S_{buw}$ (Fig. 1). Below, ϕ_{nc} is referred to as ϕ. For the present pitching-foil application, the kinematic boundary condition on the surface of the foil is

$$\frac{\partial \phi}{\partial n} = n_x + \alpha_1 \text{Real } [in_y + k(-(y-yr)n_x + (x-xr)n_y)]e^{ikt} \tag{13}$$

where α_1 is the pitch amplitude, and (xr, yr) is the location of the pitch axis. In obtaining (13), terms of $0(\alpha_1{}^2)$ have been neglected. For propeller applications, (13) is replaced by

$$\frac{\partial \phi}{\partial n} = n_x - n_y \text{Real} \sum_{n=1}^{N} V_n e^{ink(x+t)} \tag{14}$$

where V_n are the complex amplitudes of the Fourier-series expansion of the vertical component of the section inflow **V**. Considering (13) and (14), ϕ is assumed to be of the form

$$\phi = \text{Real} \sum_{n=1}^{N} \phi_n e^{inkt} \tag{15}$$

A solution for ϕ can be obtained based on Green's second identity for doubly connected regions

$$\phi = \frac{1}{m\pi}\left[\int_{S_b + S_{buw}} \left(\frac{\partial \phi}{\partial n} G - \phi \frac{\partial G}{\partial n}\right) ds = \int_{S_w} \Delta\phi \frac{\partial G}{\partial n} ds\right] \tag{16}$$

where $G = ln\sqrt{(x-\xi)^2 + (y-\eta)^2}$ is the Green's function, $\Delta\phi$ is the potential jump across the foil trailing wake sheet S_w, and $m=1$ or 2 depending on whether ϕ is evaluated on S_b or a field point, respectively. As depicted in Fig. 1, S_w is constrained to the $-x$ axis. From the condition of pressure continuity across S_w, $\Delta\phi = \Gamma(x+t)$ where Γ is the foil circulation

$$\Gamma = \text{Real} \sum_{n=1}^{N} \Gamma_n e^{inkt} \tag{17}$$

The surface values of ϕ in equation (16) and the circulation Γ (17) are determined from (16) evaluated on S_b in conjunction with the Kutta condition. The Kutta condition requires that the difference in tangential velocity between the upper and lower surface at the trailing edge be equal to the instantaneous loss in circulation $-d\Gamma/dt$. Once this is accomplished, field-point values for ϕ (or its derivatives) are obtained by direct application of (16). The necessary integrations in (16) or spatial derivatives of (16) can be performed analytically if ϕ and $\partial\phi/\partial n$ are assumed constant on line segments representing S_b. The pressure coefficient

$$C_p = \text{Real} \sum_{n=0}^{N} C_{p_n} e^{inkt} \tag{18}$$

is obtained from the Bernoulli equation. In (18), $C_{p0} = 2\phi_{0x} - \phi_{0x}{}^2 - \phi_{0y}{}^2$ and for the present pitching-foil application

$$C_{p_1} = 2\alpha_1[\phi_{1y} - ik\phi_1 - \phi_{0x}(y-yr)k + \phi_{0y}(x-xr)k + i\phi_{0x} - \phi_{0x}\phi_{1x} - \phi_{0y}\phi_{1y}] \tag{19}$$

and for propeller applications

$$C_{p_n} = 2V_n[-ik\phi_n + \phi_{nx} - \phi_{0x}\phi_{nx} - \phi_{0y}\phi_{ny} - \phi_{0y}e^{inkx}] \tag{20}$$

Terms of $0(\alpha_1{}^2)$ and $0(V_n{}^2)$ are neglected in (19) and (20), respectively.

Flow Geometry and Experimental Information

The experiments of Shen and Peterson (1978, 1980) were conducted at the David Taylor Research Center (DTRC) 36-in water tunnel with a Joukowski foil of 10.5 percent thickness and Ar 3.2. The foil was oscillated in pitching motion about an axis located 3/4 of the chord from the trailing edge. The instantaneous foil angle of attack α was given by

$$\alpha = \alpha_0 + \alpha_1 \sin\omega t \tag{21}$$

where α_0, α_1, and ω are the mean foil angle, pitch amplitude, and circular frequency of the pitch oscillation. The experimental geometry, coordinate system, and notations used for the computations are shown in Fig. 1. The most important nondimensional parameters describing this flow are the pitch amplitude α_1, the reduced frequency k (6), and the cavitation number σ (4).

In the first set of experiments (Shen and Peterson, 1978), surface-pressure measurements were compared with Geising's (1968) unsteady potential-flow solution for the fully wetted foil; and the effects of reduced frequency, cavitation number, and pitch amplitude on the cavitation inception angle, maximum cavity length, and occurrence of cloud cavitation were investigated. In the second set of experiments (Shen and Peterson, 1980), the effects of reduced frequency, cavitation number, and pitch amplitude on boundary-layer transition, and cavitation noise were considered. In the following, computational results for both steady and unsteady cavitation are presented for conditions chosen to simulate the experiments. Wherever possible, comparisons are made between the computational and experimental results.

Noncavitating Flow

Figure 2 shows a comparison between the present calculations, the method of Geising (1968), and the experimental data (Shen and Peterson, 1978) for the unsteady-pressure magnitude per radian $|C_{p_1}|/\alpha_1$ and phase angle for $\alpha_0 = 3.25$ deg, $\alpha_1 = 2$ deg, and three foil locations $x = (1.9334, 1.8, 1.5)$. The reduced frequency range is $0 \leq k \leq 2.5$. Similar results were obtained for $\alpha_1 = 1$ and .5 deg. The calculations were performed with ca. 100 line segments and took ca. 35 s of cpu time on a DEC-10 minicomputer for the steady solution ($k=0$) and a similar additional amount of time for each unsteady solution ($k \neq 0$). The theories compare well with the experiments; however, on the average, Geising's results for the pressure magnitude are closer to the experiments. The present results show somewhat smaller values. In Geising's singularity-distribution method, the location of the trailing wake sheet is determined as part of the solution, whereas in the present theory it is constrained to the $-x$ axis. This may account for the difference.

Steady Cavitation

Shen and Peterson (1978, 1980) report experimental results of steady cavitation for $\sigma = 1.13$, $\text{Re} = 2.8 \times 10^6$, and two values of foil angle $\alpha_0 = 3.8$ and 4.3 deg. The cavity length reported for $\alpha_0 = 4.3$ deg is $L_0/c = .39$. For this condition, extensive cloud cavitation was observed. The cloud-cavity shedding process was periodic with frequency 42 Hz. For $\alpha_0 = 3.8$ deg, the cavity length was $L_0/c = .25$ and only slight cloud cavitation was observed.

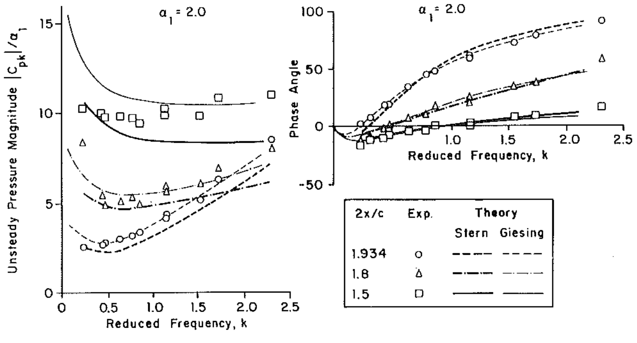

Fig. 2 Noncavitating flow unsteady-pressure magnitude and phase angle

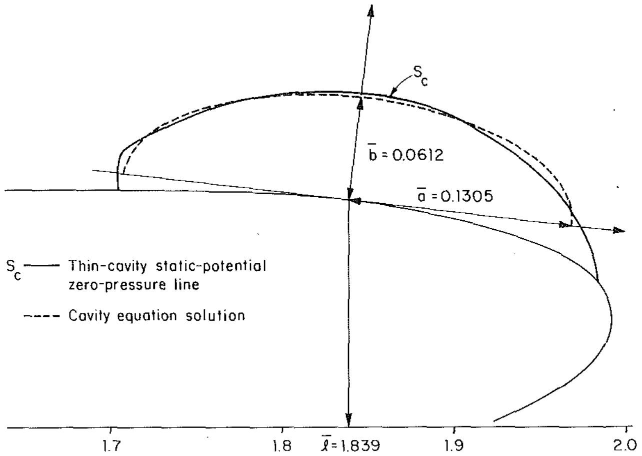

Fig. 3 Steady-cavity solution: $\alpha_0 = 4.8$ deg

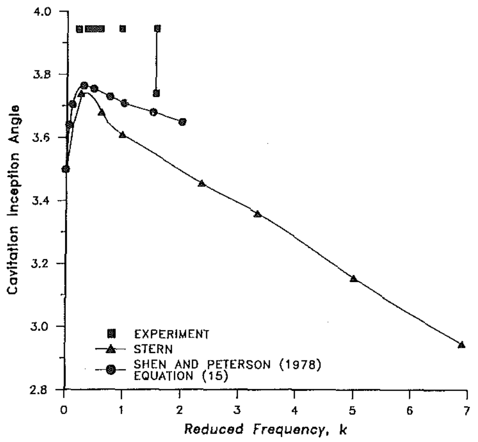

Fig. 4 Cavitation inception angles: $\alpha_1 = .95$ deg

Steady-cavity calculations were made with cavitation number $\sigma = 1.13$ and for two values of foil angle $\alpha_0 = 4.3$ and 4.8 deg. These angles correspond to the maximum foil angles attained by the oscillating foil when the mean foil angle $\alpha_0 = 3.25$ deg and the pitch amplitude $\alpha_1 = .95$ and 1.55 deg, respectively. Below, unsteady cavity results are presented for these values of α_0 and α_1. When $P(3)$ is constant in time, the cavity equations have constant solutions $(\bar{a}, \bar{b}, \bar{l})$. The constants are found from the cavity equations (1) with estimates of the solutions as initial conditions and large damping (small Re). The cavity equation response is periodic oscillations about the constant solution. Using Re = 100, the constant solution obtained for $\alpha_0 = 4.3$ deg is $(\bar{a}, \bar{b}, \bar{l}) = (.1152, .048, 1.848)$ and for $\alpha_0 = 4.8$ deg is $(\bar{a}, \bar{b}, \bar{l}) = (.1305, .0612, 1.839)$. The solution for $\alpha_0 = 4.8$ deg is shown in Fig. 3. The nondimensional natural frequencies

$$\hat{\omega}_n = \frac{\omega_n c}{2U} \tag{22}$$

obtained for $\alpha_0 = 4.3$ and 4.8 deg are 3.34 and 3.24, respectively. The calculations each took ca. 3 min of cpu time on a DEC-10 minicomputer.

Using the experimental value for $\mathrm{Re} = 2.8 \times 10^6$ (light damping) and a small displacement from the constant solution for the initial conditions, the cavity-equation response is large-amplitude nonlinear oscillations. The frequency of the oscillations is close to the natural frequency. This type of cavitation behavior suggests an instability of the cavity surface, such as cloud cavitation. This notion is supported by the fact that the natural frequency $\hat{\omega}_n$, when expressed in units equivalent to the experimental conditions, is 51 Hz. This is close to the cloud-cavitation shedding frequency of 42 Hz observed in the experiments. Below, further discussion is provided concerning cloud cavitation and cavitation noise. Also, it is shown that the cavity dynamics depend on the ratio $\hat{\omega}_n/k$.

The value of the computed cavity length $L_0/c = .1152$ for $\alpha_0 = 4.3$ deg is only about 30 percent of the experimental value $L_0/c = .39$. A part of this discrepancy is due to the approximate nature of the thin-cavity model used for the static potential. However, it is possible that a part of the discrepancy might be due to determining the cavity length by visual observations in the experiments.

Unsteady Cavitation

Unsteady-cavitation results were calculated with $\sigma = 1.13$, mean foil angle $\alpha_0 = 3.25$ deg, and two values of pitch amplitude $\alpha_1 = .95$ and 1.55 deg. For $\alpha_1 = .95$ deg, calculations were made for reduced frequency range $0 < k < 7$. For $\alpha_1 = 1.55$ deg, calculations were made for reduced frequency range $0 < k < 2.5$. These ranges were chosen after consideration of the linear-cavity-equation response. The peak amplitude of the linear response depends on the ratio $\hat{\omega}_n/k$. For small $\hat{\omega}_n/k$, small peak amplitudes occur compared to quasi-steady response. For $\hat{\omega}_n/k$ around 1, large peak amplitudes occur compared to quasi-steady response. For large $\hat{\omega}_n/k$, essentially quasi-steady response occurs.

Inception. Cavitation inception was determined computationally by the condition of the first occurrence of negative pressure on the foil surface. For $\sigma = 1.13$ and steady flow $(k = 0)$, inception occurred at foil angle $\alpha_0 = 3.28$ deg. The inception location was $x = 1.97$. Experimentally, for this same condition, inception occurred at $\alpha_0 = 3.5$ deg and $x = 1.96$. This kind of discrepancy is well known and has been discussed extensively in the literature. Consequently, the unsteady inception angles determined computationally were corrected by the difference between the computational and experimental steady inception angles. Shen and Peterson (1978) present experimental inception angles for $\sigma = 1.13$ and for $\alpha_1 = .95$ and 1.55 deg. Also, an analytical equation for predicting the unsteady inception angle is presented. This equation (equation (15) of Shen and Peterson (1978)) is based on unsteady potential theory and the experimental steady inception angle. Figure 4 shows a comparison for $\alpha_1 = .95$ deg between the unsteady inception angles obtained computationally, experimentally, and from equation (15) of Shen and Peterson (1978). All three results demonstrate that for $k < 2$ there is a delay in inception due to foil oscillation. This delay increases with pitch amplitude α_1 (figure not shown). Shen and Peterson (1978) point out that for high frequency the amount of cavitation inception delay is reduced. The computational results show that the reduction is substantial and that for $k > 2$ the unsteady inception angle is actually less than the steady inception angle. This effect is quite pronounced for the $\alpha_1 = 1.55$ deg condition.

Although the present computations and the results of Shen and Peterson (1978) show similar trends, there are some differences. Both calculation methods predict the maximum inception delay to occur at $k \simeq .25$ for both values of α_1. However, for $k > .25$ the present computations predict a much larger reduction in inception angle than equation (15) of Shen and Peterson (1978). This is surprising since the two methods use unsteady potential-flow theories which were shown above to be in good agreement. The experimental results show, in general, larger inception angles than the theories. Shen and Peterson (1978) point out that part of the discrepancy may be due to the lack of accurate resolution in measuring foil angles in the experiments. This is the reason that, in some cases, the experimental results are given as a range of angles instead of a single value.

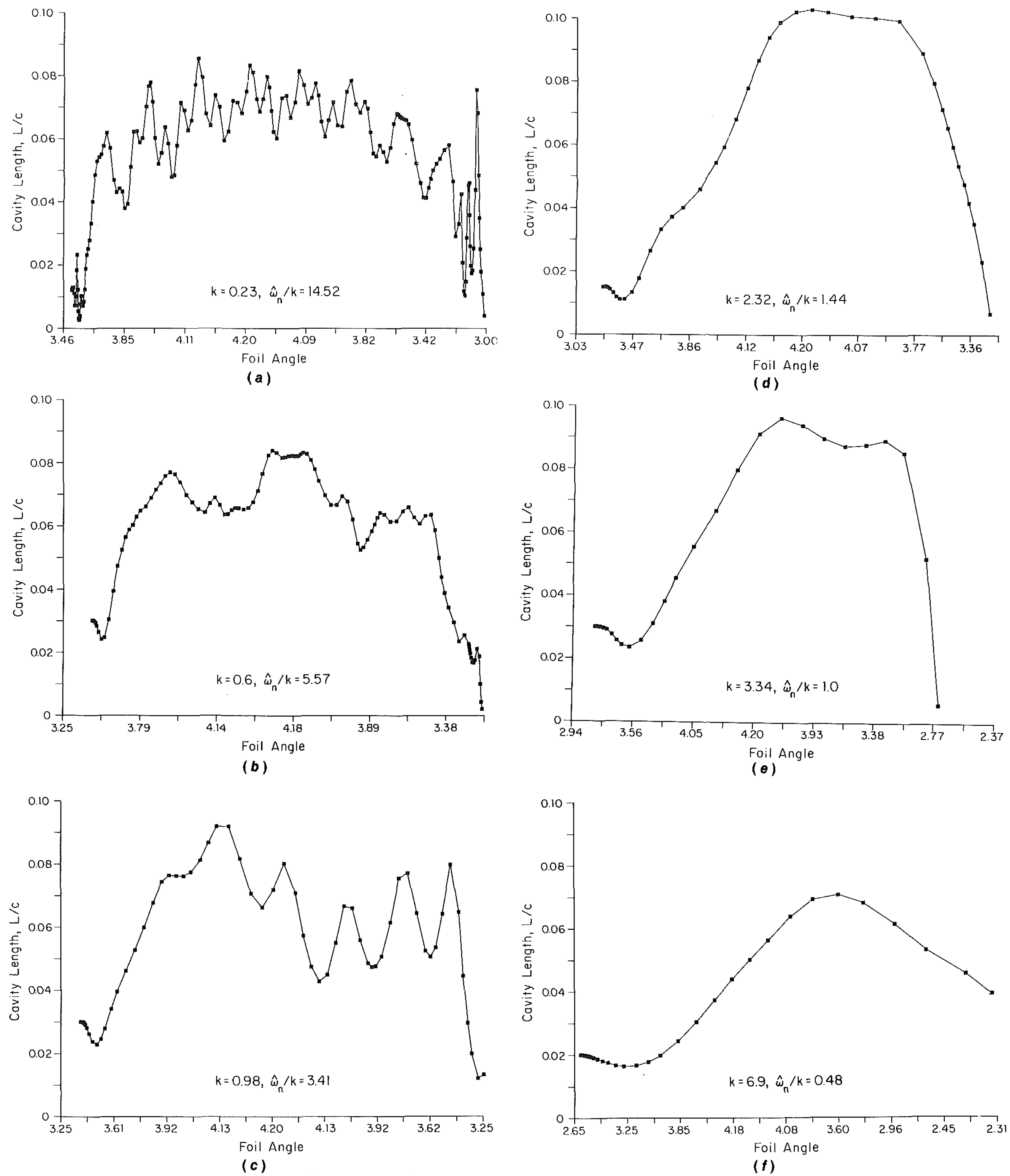

Fig. 5 Cavity-length response: $\sigma = 1.13$ and $\alpha_1 = .95$ deg

The inception position was found in the computations to move back from the leading edge towards the trailing edge as the reduced frequency increased. For $\alpha_1 = .95$ deg, the inception position moved from $x = 1.962$ for $k = .23$ to $x = 1.89$ for $k = 6.9$. This trend was even more pronounced for $\alpha_1 = 1.55$ deg. In fact, for $\alpha_1 = 1.55$ deg and $k = 6.9$, upper surface inception occurred at a foil angle of 2.1 deg (before $\alpha_{\min}$) and at $x = .5$ and lower surface inception occurred at a foil angle of 4.5 deg (before $\alpha_{\max}$) and at $x = 1.95$. This change in the inception position was not observed in the experiments. Shen and Peterson (1978) report that inception initiated at $x = 1.96$ for all k investigated ($.23 < k < 2.3$).

Dynamics. Computational results for unsteady cavitation were obtained for $\alpha_1 = .95$ deg and seven values of reduced frequency $k = .23$, .6, .98, 2.32, 3.34, 5.0, and 6.9. The calculations took ca. 1-5 min of cpu time depending on the value of k (lower k values required more time) on a DEC-10 minicomputer. The cavity-length response L/c for each frequency (except $k = 5.0$) is shown in Figs. 5(a–f). The other response curves are similar in character. For the lower values of reduced frequency ($k = .23$, .6, and .98), the cavity response is seen from Figs. 5(*a*) through 5(*c*) to be large amplitude oscillations during the cavity life cycle. The frequency of the oscillations is close to the natural frequency. The oscillatory cavity response at low reduced frequency (large $\hat{\omega}_n/k$) is a result of the fact that the cavity has sufficient time to adjust to the impressed pressure field. For the higher values of reduced frequency ($k = 2.32$, 3.34, 5.0, and 6.9), the cavity response is seen from Figs. 5(*d*) through 5(*f*) to be a relatively slow, stable-growth phase followed by a rapid-collapse phase.

Results were also obtained for $\alpha_1 = 1.55$ deg and three values of reduced frequency $k = .23$, .98, and 2.32 (figures not shown). The $\alpha_1 = 1.55$ deg cavity response is similar in character to the $\alpha_1 = .95$ deg response; however, as a result of the larger pitch amplitude, the cavity size is increased. Furthermore, the response velocities tend to be larger than the $\alpha_1 = .95$ deg values, resulting in larger amplitude cavity oscillations at the low frequencies ($k = .23$ and .98) and a more rapid collapse phase at the high frequency ($k = 2.32$).

Figure 6 shows a comparison of the computational and experimental maximum cavity lengths as a function of reduced frequency (the computational maximum cavity length nondimensionalized using the foil chord is simply $L_k/c = 2a_k/c$). The values of the steady, maximum cavity length L_0/c are also shown. The computational results clearly underpredict the cavity length. This has already been pointed out and discussed above for the steady-cavity solution. The same discussion is also valid for the unsteady-cavity solution. Figure 7 shows a comparison of the computational and experimental maximum cavity lengths for $\alpha_1 = .95$ deg, normalized using the steady-cavity results. This removes the absolute cavity size as a variable without affecting the cavity dynamics. The computational maximum cavity area A_k, normalized using the steady cavity area A_0, is also shown. In Fig. 7, abscissa scales for both the reduced frequency k and the ratio $\hat{\omega}_n/k$ are shown. The results clearly show the dependence of the cavity dynamics on the ratio $\hat{\omega}_n/k$. Both the experimental and computational results indicate a minimum cavitation response for a low value of reduced frequency. The computations have a minimum cavitation response for $k \simeq .5$ and the experiments for $k \simeq 1$. The computations show that, as k increases from the value at the minimum cavitation response, the cavitation response increases, reaching a maximum at $k \simeq 2.5$ ($\hat{\omega}_n/k = 1.3$). Then, for even higher values of reduced frequency (low $\hat{\omega}_n/k$), the cavitation response decreases again. For $k = 6.9$, the response is below the $k = .5$ minimum. The experimental results seem to confirm the computational trends in that they show an increase in cavitation response for k greater than its value at the minimum cavitation response; however, experimental results were not obtained for $k > 1.65$.

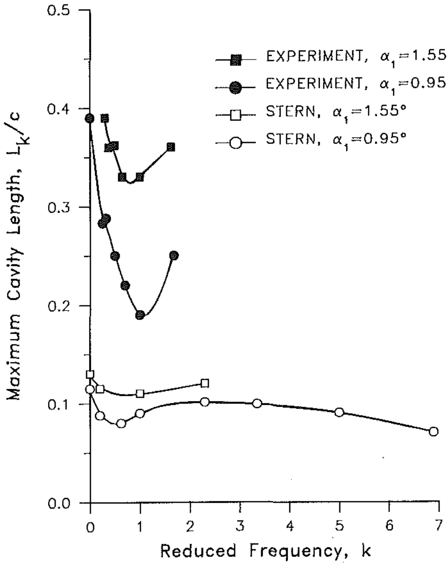

Fig. 6 Maximum cavity length

Figure 8 shows the same comparisons as Fig. 7 except for the $\alpha_1 = 1.55$ deg condition (the experimental steady-cavity length for the $\alpha_0 = 4.8$ deg condition was obtained by linear extrapolation of the $\alpha_0 = 3.8$ and 4.3 deg results). The same cavity dynamic behavior discussed in connection with Fig. 7 is found in Fig. 8 for the frequency range $0 \leq k < 2.5$. The major difference between Figs. 7 and 8 is the amount of reduction in

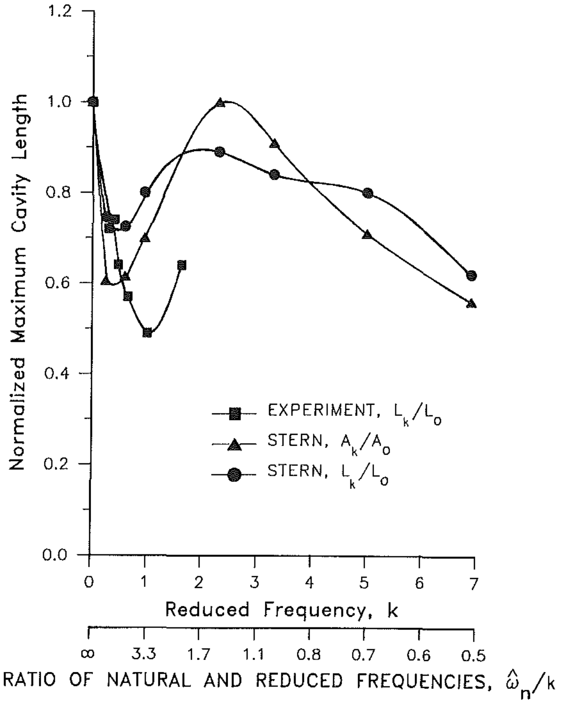

Fig. 7 Normalized maximum cavity length: $\alpha_1 = .95$ deg

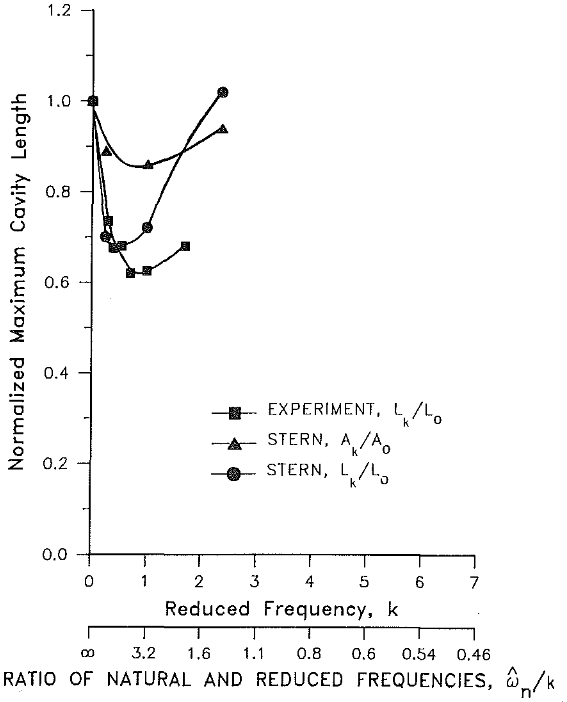

Fig. 8 Normalized maximum cavity length: $\alpha_1 = 1.55$ deg

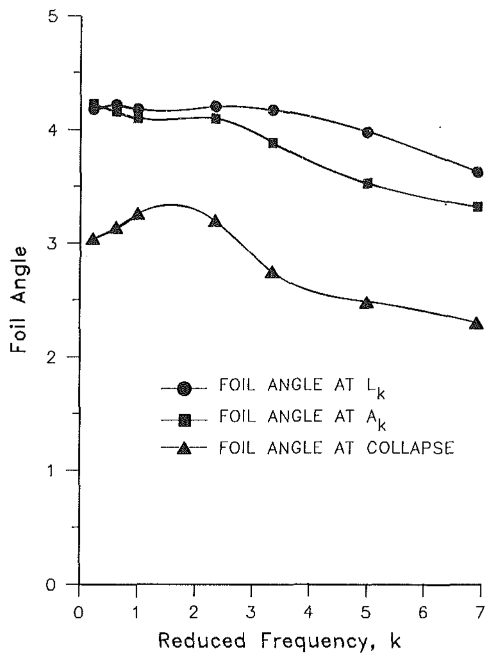

Fig. 9 Foil angles when cavity area and length are maximum and at collapse: $\alpha_1 = .95$ deg

cavitation response at the minimum. Both the computational and experimental results predict less reduction in response at the minimum. This, no doubt, is due (at least for the computational results) to the larger amplitude cavity oscillations at low frequencies found for $\alpha_1 = 1.55$ deg. If results had been obtained for $\alpha_1 = 1.55$ deg and $k > 2.5$, it is not expected that the cavity dynamics would be similar to the $\alpha_1 = .95$ deg results, at least for the high frequency $k = 6.9$. Examination of the $\alpha_1 = 1.55$ deg and $k = 6.9$ unsteady surface pressures indicated a large upper surface cavity originating near the foil trailing edge and moving forward to the leading edge. Lower surface leading-edge cavitation was also indicated.

Figure 9 shows, for the $\alpha_1 = .95$ deg computational results, the foil angles when the cavity area and length were maximum and the foil angle at cavity collapse. It is seen that the cavity area and length are maximum when the foil angle is at its maximum 4.2 deg except for high reduced frequencies. At the higher reduced frequencies, the cavity area and length are maximum at smaller foil angles reached after the foil passes its maximum position. The foil angle at collapse shows a similar trend in that the collapse angle is reduced at the higher reduced frequencies. Figure 10 is similar to Fig. 9 except for $\alpha_1 = 1.55$ deg and it also includes experimental results. The trends are similar to those discussed in connection with Fig. 9; however, the experimental results predict larger reductions in foil angles than the computations and at lower values of reduced frequencies.

Figure 11 shows the calculated cavity position on the foil at the time of collapse l_c. The results for both values of pitch amplitude are similar and show that for $k = .23$ the collapse is back from the foil leading edge. This is due to the large amplitude oscillatory behavior of the cavity at this low frequency. As the frequency increases, the collapse position initially moves towards the foil leading edge and then for higher frequencies it moves back from the leading edge again. However, in all cases collapse is never further back on the foil than $x = 1.8$. In other applications (Stern and Vorus, 1983; Stern, 1982), the high-frequency collapse position was found to be much further back on the foil. Apparently, for leading edge cavitation on a Joukowski foil, the cavity collapse occurs close to the leading-edge pressure suction peak for all frequencies. Experimental values for the cavity collapse position were not reported.

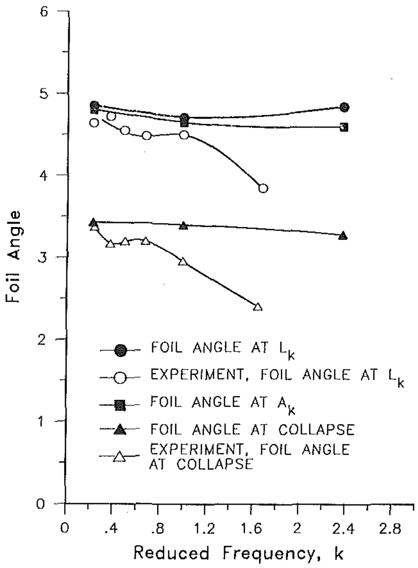

Fig. 10 Foil angles when cavity area and length are maximum and at collapse: $\alpha_1 = 1.55$ deg

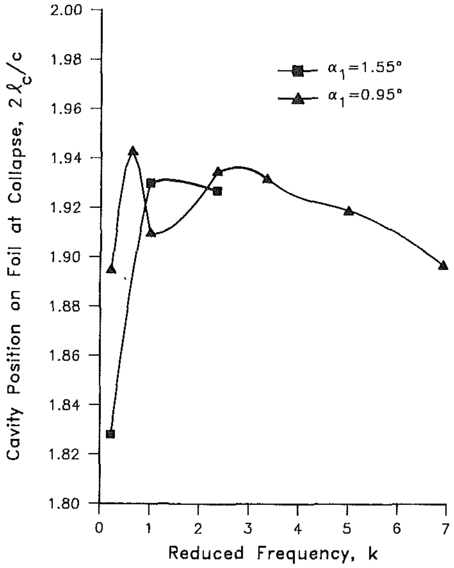

Fig. 11 Cavity position at collapse

Cloud Cavitation and Noise. Shen and Peterson (1978, 1980) report that many of the experimental cavities were accompanied by cloud cavitation. Cloud cavitation refers to the condition when an instability in the cavity surface occurs and a portion of the cavity separates, develops the appearance of a cloud, and subsequently is shed downstream. For the steady-cavity condition ($k = 0$) and for low reduced frequencies, the cloud-cavitation shedding could be periodic. For higher reduced frequencies, the cavities were reported to be relatively stable up until the final stages of the cloud cavitation collapse. For $\sigma = 1.13$, $\alpha_1 = .95$ deg, and at low reduced frequencies ($k < 1.2$), only light cloud cavitation was reported to have been present in the experiments. For this same condition and at reduced frequency $k = 1.646$, heavy cloud cavitation was reported. For $\sigma = 1.13$, $\alpha_1 = 1.55$ deg, and at all values of reduced frequency, heavy cloud cavitation was reported in the experiments.

Cavitation noise measurements were also made in the experiments (Shen and Peterson, 1980). Cavitation noise was reported to increase with the occurrence and intensity of cloud cavitation. For unsteady cavitation, the peak noise occurred near cavitation collapse. When the relative sound power is plotted versus reduced frequency, Shen and Peterson (1980) show the existence of a "noise bucket"; for the steady condition and at low reduced frequencies, the noise level is relatively high; for the mid-range reduced frequencies (for $\alpha_1 = .95$ deg, $k = .494$, and for $\alpha_1 = 1.55$ deg, $k = .659$ and .988), the noise level is minimum; for higher reduced frequencies ($k = 1.646$), the noise level increases above the $k = 0$ value. The differences between the $\alpha_1 = .95$ deg and $\alpha_1 = 1.55$ deg noise response are seen to be at the low and high frequencies, where the $\alpha_1 = 1.55$ deg noise response shows an increase over the $\alpha_1 = .95$ deg values (Shen and Peterson (1980) Figs. 25, 27, 28, and 30).

The computational results appear to contain trends that are similar to the experimental trends concerning cloud cavitation and cavitation noise. The low frequency ($k = .23$) response (Fig. 5(*a*)) shows large amplitude oscillations of the cavity surface. The oscillations are particularly intense during the cavity-collapse phase. This type of behavior suggests an instability of the cavity surface, such as cloud cavitation. Cavitation noise and possibly the occurrence of cloud cavitation are related to the intensity of the oscillations. The response velocities are a measure of the intensity of the oscillations. As pointed out earlier, the $\alpha_1 = 1.55$ deg response velocities were larger than those for $\alpha_1 = .95$ deg resulting in even larger amplitude oscillations at low frequency. This implies an increase in cavitation noise and possibly cloud cavitation. For the medium frequencies ($k = .6$ and .98), where the cavitation response was shown to be minimum, the oscillatory behavior and response velocities are lower than the $k = .23$ condition (Figs. 5(*b*-*c*)). This suggests for the medium frequencies a reduction in cavitation noise and possibly cloud cavitation. For the resonance frequencies ($k = 2.32$ and 3.34), where the cavitation response was shown to be maximum, the oscillatory behavior is not present; however, extremely large velocities are found at collapse. This suggests a different type of cavity instability than was found at low frequencies which is associated with the rapid and violent collapse of the large cavity. For $\alpha_1 = .95$ deg and for the high frequencies ($k = 5.0$ and 6.9), where the cavitation response was shown to be reduced, the response velocities are also reduced. This suggests a reduction in cloud cavitation and noise also. For $\alpha_1 = 1.55$ deg and for high frequencies, calculations were not made; however, as discussed earlier, an examination of the unsteady foil surface pressures for $k = 6.9$ indicated much more extensive and no longer leading edge cavitation. This suggests a completely different type of cavitation response, probably accompanied by extensive cloud cavitation and cavitation noise.

The computational method can be used to calculate cavitation noise. Shen and Peterson (1980) report that the peak noise occurs near cavitation collapse. A measure, in part, of the predicted cavitation noise at collapse is the response velocities at collapse. Figure 12 shows the cavity area velocity at collapse $\dot{A}_c$ for both values of α_1. The results shown in Fig. 12 suggest a higher noise level for the $\alpha_1 = 1.55$ deg condition than for $\alpha_1 = .95$ deg at low ($k = .23$) and at near resonance ($k = 2.3$) frequencies.

Shen and Peterson (1980) state that there is essentially no correlation between maximum cavity length and the relative sound power. The present computations and Figs. 25 and 31 of Shen and Peterson (1980) do not indicate this. It appears that, for a fixed σ, α_1, and Re, the cavitation response including cavity size, noise levels, and cloud cavitation depend on the ratio $\hat{\omega}_n/k$. A minimum response is indicated for a low value of k. For k below this value, particularly for $\alpha_1 = 1.55$ deg, the response levels increase toward the $k = 0$ values. A maximum response is indicated for $\hat{\omega}_n/k$ around 1. For $\alpha_1 = .95$ deg and $\hat{\omega}_n/k < < 1$, the response is below its value at the minimum. For $\alpha_1 = 1.55$ deg and $\hat{\omega}_n/k < < 1$, leading-edge cavitation is no longer present and large response levels are indicated.

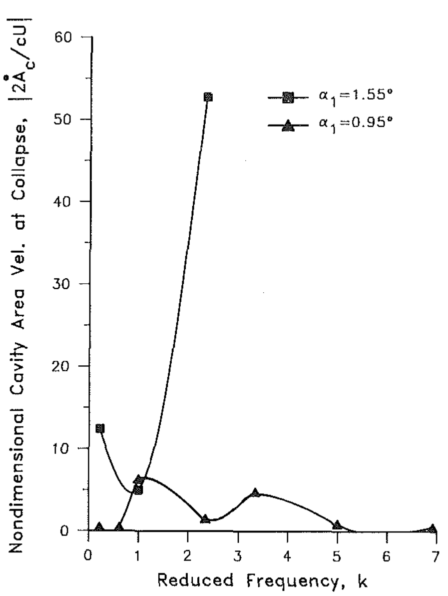

Fig. 12 Cavity area velocity at collapse

Concluding Remarks

The computational method yields best results in predicting the cavity dynamics, but underpredicts the cavity length. For fixed cavitation number, mean foil angle, and pitch amplitude, the cavity dynamics, including maximum cavity size, cavitation noise and cavity surface behavior, depend on the ratio of the cavity natural frequency, for the foil fixed at the maximum pitch amplitude, to the reduced frequency $\hat{\omega}_n/k$. The experimental results appear to confirm the computational trends up to the point that the experimental data were obtained.

The present work indicates a minimum cavitation response for a certain value of reduced frequency k depending on the cavity natural frequency $\hat{\omega}_n$. The natural frequency is obtained from the steady cavity response for fixed cavitation number, foil geometry, and angle of attack. This has direct implications with regard to propeller cavitation. That is, for a particular hull (wake field) and propeller operating conditions, the foil sections can be chosen so as to insure a minimum cavitation response.

Comparisons have also been made with model and full-scale experimental data for the marine propeller of the Naval Auxiliary Oiler (AO-177) (Stern, 1982). Close agreement is shown for cavitation inception, radial and chordwise extent, duration, and cavity dynamics, including surface behavior and collapse position. Observed trends due to propeller geometry and ship wake are also correctly reflected by the calculated results. However, the predicted cavities are thick such that the maximum cavity volume is about 2.2 cubic feet. Although no experimental information for the cavity thickness or volume variation is available, the predicted values seem excessive in comparison to the overall dimensions of the propeller. It should be noted that, for propeller applications, there is additional uncertainty due to the lack of knowledge of the effective propeller inflow.

Generally, the linear quasi-steady and unsteady cavitation theories for marine propellers predict even larger cavities than those predicted by the present theory and show a phase difference for the volume variation as compared to observations, e.g., Kerwin et al. (1986) predict the maximum cavity thickness for the AO-177 to be 6 cubic feet. Also, these theories have provided only very limited information concerning the cavity dynamics, apart from the general trend of slow growth followed by rapid collapse. In fact, in most cases, the leading edge of the cavity is constrained to coincide with the leading edge of the foil which may adversely affect the cavity dynamics, especially the collapse position. Interestingly, Hsu and Shen (1988) have shown good agreement between their linear theory and experimental data for a pitching foil. This is attributed to the inclusion of nonlinear foil-thickness effects in the pressure distribution and the fact that the comparisons are made for conditions corresponding to small leading-edge sheet cavitites with essentially quasi-steady dynamics, i.e., correspondingly closely to the restrictions of their theory. It should be recognized that the present approach does not suffer from these restrictions. Furthermore, the present comparisons are for relatively large sheet cavities with significant dynamical effects.

In conclusion, in most circumstances, nonlinear cavity dynamics play an important role in unsteady cavitation. Thus, the preservation of such features, as has been done in the present approach, are important for the development of computational methods for unsteady cavitation. Considerable uncertainty exists concerning the accuracy of the predicted instantaneous cavity extent, especially thickness and volume variation. This is particularly true for marine propellers. In this regard, it is essential that experimental information, which is sorely lacking, be obtained to verify the calculations. In the present approach, it is clear that a more accurate static-potential solution than the thin-cavity model used presently is needed. It may be possible to accomplish this along the lines described by Uhlman (1987). Also, it may be advantageous to use more general forms to model the cavity surface, e.g., forms with cusped leading and/or trailing edges.

Acknowledgments

This research was performed during the time the author was employed by Science Applications, Annapolis, Maryland. Partial support was provided both by Science Applications internal research funds and DTRC. Initial support was provided by the American Bureau of Shipping.

References

Giesing, J. P., "Two-Dimensional Potential Flow Theory for Multiple Bodies in Small-Amplitude Motion," Douglas Aircraft Company, Report No. DAC-67028, 1968.

Hsu, C. C. and Shen, Y. T., "Unsteady Partial Cavity Flow on Foils," *Proc. 17th ONR Sym. Naval Hydrodynamics*, The Hague, Aug. 1988.

Kerwin, J., Kinnas, S., Wilson, M. B., and McHugh, J., "Experimental and Analytical Techniques for the Study of Unsteady Propeller Sheet Cavitation," *Proc. 16th ONR Sym. Naval Hydrodynamics*, Berkeley, CA, June 1986, pp. 387-414.

Shen, Y. T., and Peterson, F., "Unsteady Cavitation on an Oscillating Hydrofoil," *Proc. 12th ONR Sym. Naval Hydrodynamics*, Washington, D.C., June 1987, pp. 362-384.

Shen, Y. T., and Peterson, F., "Influence of Hydrofoil Oscillation on the Boundary Layer Transition and the Cavitation Noise," *Proc. 13th ONR Sym. Naval Hydrodynamics*, Tokyo, Oct. 1980, pp. 221-241.

Stern, F., "Comparison of Computational and Experimental Unsteady Cavitation," *Proc. 14th ONR Sym. Naval Hydrodynamics*, Ann Arbor, MI, Aug. 1982, pp. 613-652.

Stern, F., and Vorus, W. S., "A Nonlinear Method for Predicting Unsteady Sheet Cavitation on Marine Propellers," *J. Ship. Res.*, Vol. 27, No. 1, Mar. 1983, pp. 56-74.

Uhlman, J. S., "The Surface Singularity Method Applied to Partially Cavitating Hydrofoils," *J. Ship. Res.*, Vol. 31, No. 2, June 1987, pp. 107-124.

W. P. Wolfe

C. E. Hailey
Mem. ASME

W. L. Oberkampf
Mem. ASME

Aerodynamics Department,
Sandia National Laboratories,
Albuquerque, New Mexico 87185

Drag of Bodies of Revolution in Supercavitating Flow[1]

The drag of bodies of revolution at zero degree angle of attack in supercavitating flow has been calculated. The potential flow about the body and cavity is calculated using an axial distribution of source/sink elements and is coupled with laminar and turbulent boundary-layer solutions for the body. Excellent agreement for drag coefficient is demonstrated between theory and a water-tunnel experiment, also between theory and a high-speed water-entry experiment. Results show skin-friction drag is the dominant drag component for high-speed water entry or high-speed underwater travel.

Introduction

When a vehicle is propelled at high speed under water or enters the water at high speed, it generates cavitating flow. The cavity typically forms at some axial location on the surface of the body and remains in existence for many body lengths aft of the base. In the literature such a cavity is referred to as a "supercavity." It is well known that the cavity formation fundamentally affects the hydrodynamic forces and moments and flight stability of the body. The ability of theoretical methods, however, to predict cavitating-flow forces and moments is very limited. Theoretical predictions for drag, the most basic of hydrodynamic forces, have been limited to very few shapes. This paper describes a numerical method for predicting the drag of bodies of revolution at zero angle of attack in cavitating flow.

The earliest theoretical results for slender bodies of revolution were obtained by Plesset and Schaffer (1948). They calculated the drag of cones over a range of cavitation numbers, σ. They used similitude considerations linking the axisymmetric flow with corresponding problems in plane two-dimensional flow. They assumed that the pressure distribution along the generator of the cone was the same as that on a wedge having the same half-angle at the same cavity pressure coefficient. Armstrong (1954), also using a similitude approach, improved the velocity distribution on the cone by comparing a power series expansion near the apex of a wedge to that of a cone. This noticeably improved agreement between theory and experiment for drag on cones with half-angles less than 15 degrees.

Johnson and Rasnick (1961) predicted the inviscid drag of paraboloids at zero angle of attack and zero cavitation number. They used methods of classical hydrodynamics to determine the pressure distribution over ellipsoids. They approximated the body of interest by a paraboloid and truncated the length of the body when the surface pressure coefficient became negative. This yielded a shape which did not cavitate on the sides of the body even for cavitation numbers near zero. A cavity would form on the base, however, and extend downstream some distance depending on σ. Chou (1974) used slender-body theory to calculate the flow over bodies of revolution and their attached cavities. He assumed the pressure in the cavity to be known from the cavitation number and the boundary of the liquid/gas interface was assumed to be a streamline. Given an arbitrary cavitation number, he employed an iterative solution of a nonlinear integral equation to determine the source/sink distribution producing the body and cavity boundary.

Struck (1970) and Rattayya, Brosseau, and Chisholm (1981) removed the assumption of slender bodies by using surface singularities to form the body and cavity streamline. Knowing the cavitation number, an iterative procedure was developed for solving the mixed boundary-value problem resulting from the specification of pressure, or velocity, at the unknown location of the cavity boundary. Struck calculated the drag of a flat circular disk and a sphere for various values of σ. Rattayya, Brosseau, and Chisholm did not present any results for drag but calculated body pressure distributions and cavity shapes for blunted ogive/cylinder geometries.

The present paper describes results for calculating the cavitating flow field and drag on a class of bodies of revolution at zero angle of attack. The method is applicable over a range of geometries; from pointed noses to noses with moderate bluntness and various afterbody geometries. Predictions are made over the range of cavitation numbers approaching zero to fully-wetted flow. The results are valid for incompressible flow, velocities typically less than 300 m/s. Potential flow about the body and cavity is calculated using source/sink singularities distributed along the axis. A significant extension of previous work in cavitating flow is the inclusion of laminar and turbulent boundary-layer solutions on the body. This allows the calculation of a total drag coefficient which includes skin-friction and pressure drag on the body and cavity drag on the base. Predictions and experimental data for drag are compared for cones and a paraboloid. Experimental data from both water tunnel and high-speed water-entry tests are used in evaluating the present method. The

---

[1] This work was performed at Sandia National Laboratories for the U.S. Department of Energy under contract number DE-AC04-76DP00789.

Contributed by the Fluids Engineering Division for publication in the JOURNAL OF FLUIDS ENGINEERING. Manuscript received by the Fluids Engineering Division September 4, 1987.

results of this work indicate that skin-friction drag is an important component of the total drag for high-speed water entry or high-speed underwater travel.

Method of Solution

Potential-Flow Solution. The potential-flow solution is obtained by modeling the body of revolution and cavity by an axial distribution of source/sink elements. The solution is divided into two separate stages. The first stage calculates a fully-wetted flow solution with no cavity. The pressure results from the first-stage calculation are used to start the second stage. The second-stage calculation iterates to the converged cavity shape and location. The cavity is found such that the pressure on the cavity streamline is everywhere equal to the specified pressure, p_c. Details of Stage One and Two are described below.

Stage One. The fully-wetted potential solution for the body flow field without cavity is found using the inviscid section of the code SANDRAG (Wolfe and Oberkampf, 1985a, 1985b, 1987). Detailed derivations of the potential flow equations, which are omitted in this paper, can be found in the report of Wolfe and Oberkampf (1985a). The body of revolution is modeled by an axial distribution of source/sink elements whose strengths vary linearly over the length of each element. The strengths of adjacent elements are equal at their juncture. For a body with N source elements, N linear algebraic equations with $N+1$ unknowns are obtained by requiring that the zero streamline pass through N surface points on the body. In cylindrical coordinates, the equation for the body surface streamline (zero streamline) is given by

$$\Psi(x_i, r_i) = 0 = \frac{U_\infty r_i^2}{2} + \frac{1}{4\pi}\sum_{j=1}^{N+1} A_{ij}\gamma_j \tag{1}$$

In this expression, the $N+1$ unknowns are the source strengths, γ_j, $j=1, 2, \ldots N+1$. The body surface control points are given by (x_i, r_i), $i=1, 2, \ldots N$, and A_{ij} is a coefficient matrix which is a function of body geometry. The remaining equation used to close the system is obtained by specifying an additional surface control point aft of the body, approximating the separating streamline.

Equation (1) is solved directly to yield the source strengths, γ_j. Once these strengths are known, the velocity components at the surface control points are determined from

$$u(x_i, r_i) = \frac{1}{r_i}\left(\frac{\partial \Psi}{\partial r}\right)_i \tag{2}$$

$$v(x_i, r_i) = -\frac{1}{r_i}\left(\frac{\partial \Psi}{\partial x}\right)_i \tag{3}$$

Bernoulli's equation yields the pressure at the body surface control points. A quadratic interpolation routine is used to define the surface pressure between surface control points. The pressure distribution is then used to start the second-stage calculation.

Stage Two. Once the fully-wetted potential-flow solution is calculated, the solution for the body with cavity is found. The cavity boundary is treated as an impermeable extension of the body surface. The pressure along the cavity boundary is assumed to be a constant, specified value. This is equivalent to specifying u and v and solving equations (1)–(3) as a coupled set for the unknown cavity coordinates and source strengths. Because these equations cannot be solved explicitly for γ and r as functions of u and v, they must be solved by iteration.

An initial estimate for the cavity surface is made and control points are distributed on the estimated cavity boundary. The body/cavity juncture is initially defined to be where the static pressure from the Stage 1, fully-wetted flow calculation, is equal to the specified cavity pressure, p_c. Depending on the cavitation number, control points are specified on the cavity boundary up to five body diameters aft of the base. As the cavitation number increases, the cavity length must be decreased. The current cavity model does not close the cavity at the aft end. Numerical experimentation has shown that the shape of the cavity beyond approximately five body diameters aft of the body does not affect the pressure distribution over the vehicle. Source/sink elements are placed along the cavity axis. The initial estimate of the cavity shape is a circular arc which leaves the body with the body slope and has zero slope

Nomenclature

a = turbulent boundary layer parameter
A_{ij} = coefficient matrix
B = turbulent boundary layer overlap parameter
C_D = total drag coefficient $= D/qS$
C_{D_0} = total drag coefficient evaluated at $\sigma = 0$
C_f = local skin friction coefficient $= \tau_w/q$
D = drag force
H = boundary layer shape factor
k^+ = nondimensional surface roughness
k_c = index of control point at body/cavity juncture
k_s = equivalent sand grain roughness
L = body length
m = boundary layer transition parameter
p = pressure
q = dynamic pressure $= \rho U_\infty^2/2$
r = radial coordinate
rms = root mean square value
Re_l = Reynolds number based on length
s = surface length
S = reference area
u = longitudinal velocity component
U = velocity
v = radial velocity component
V_{cavity} = total velocity along cavity streamline
x = axial coordinate
γ = source strength
δ = boundary layer thickness
δ^* = boundary layer displacement thickness
η = boundary layer transition parameter
κ = turbulent boundary layer overlap parameter
λ = boundary layer parameter
μ = absolute viscosity
ν = kinematic viscosity
Π = turbulent boundary layer parameter
ρ = density
Θ = boundary layer momentum thickness
Ψ = stream function
σ = cavitation number $= (p_\infty - p_c)/q_\infty$
τ = shear stress

Super and Subscripts

$(\ )_{ij}$ = indices
$(\ )_\infty$ = freestream value
$(\ )_c$ = cavity
$(\ )_{tr}$ = value at transition
$(\ )_i$ = value at point of instability
$(\ )'$ = d/ds

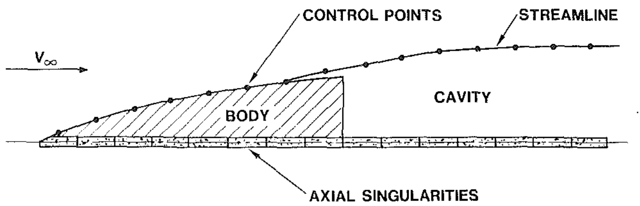

Fig. 1 Body and cavity inviscid flow

at the final cavity control point. The surface control points are distributed so that one control point is located at the body/cavity juncture. The remaining control points are distributed in a scheme similar to that described in the report of Wolfe and Oberkampf (1985a) to minimize streamline undulation between control points. The body/cavity with source elements and surface control points is illustrated in Fig. 1.

The matrix which defines the surface of the body plus cavity is formed from two sets of equations. The first rows of the matrix are given by equation (1) for those control points, (x_i, r_i), $i = 1, 2, \ldots, k_c$, which are on the body surface. Here k_c is the index of the control point at the body/cavity juncture. The rows of the matrix which define the cavity surface are given by the inverse method outlined by Zedan and Dalton (1978), whereby for a given pressure or velocity distribution the appropriate body shape is determined iteratively. In this application, the specified cavity pressure, p_c, for a given freestream pressure and velocity, defines a cavitation number. Using Bernoulli's equation, the cavitation number defines the total velocity along the cavity streamline, V_{cavity}, as $V_{\text{cavity}} = U_\infty\sqrt{1+\sigma}$. The longitudinal velocity, u_i, is then specified at each cavity control point in the form

$$u_{i_{\text{cavity}}} = V_{\text{cavity}} \cos\left(\frac{dr}{dx}\right)_i \qquad (4)$$

The system of equations defining the cavity surface is then given by

$$u_{i_{\text{cavity}}} r_i = U_\infty r_i + \frac{1}{4\pi}\sum_{j=1}^{N+1}\frac{\partial A_{ij}}{\partial r_i}\gamma_j \qquad (5)$$

where $\partial A_{ij}/\partial r_i$ can be expressed exactly as a function of the estimated cavity surface. The control point at the body/cavity juncture is required to satisfy both equation (1) and equation (5). Without this requirement, the solution will not converge. Since the cavity surface generated by the solution of the system of equations (1) and (5) must also satisfy the zero streamline requirement, the location of the zero streamline provides the next estimate of the cavity surface. The procedure is repeated until a converged solution is obtained.

The body/cavity which satisfies equations (1) and (5) is said to be converged if the average calculated longitudinal component of velocity, rms (u_i), is sufficiently close to the average specified cavity velocity, rms $(u_{i_{\text{cavity}}})$, so that the relative error criterion

$$\frac{|\text{rms}(u_{i_{\text{cavity}}}) - \text{rms}(u_i)|}{\text{rms}(u_{i_{\text{cavity}}})} \leq 1\times10^{-6}$$
$$i = k_c + 1, \ldots .N \qquad (6)$$

is satisfied on the cavity surface. Equation (6) is satisfied very rapidly, usually after three or four iterations. All calculations were perfomed using 14 significant digits.

A set of physical constraints are imposed on the solution to keep the cavity shape from passing through the body surface. These physical constraints allow the body/cavity juncture to move on the body. The first physical constraint is the requirement that the cavity radius be everywhere greater than the body radius except at the body/cavity juncture,

$$r_{\text{cavity}} > r_i \text{ for } i = k_c + 1, \ldots .N \qquad (7)$$

If the convergence requirement given by equation (6) is satisfied, but equation (7) is not met, the body/cavity juncture is moved aft a small step. The second physical constraint is the requirement that the pressure on the body, forward of the cavity, be greater than the specified cavity pressure.

$$p_i > p_c \text{ for } i = 1, 2, \ldots k_c - 1 \qquad (8)$$

If equations (6) and (7) are satisfied, but equation (8) is not met, the body/cavity juncture is moved forward a small step. In either case, the body surface control points are redistributed so that a control point is located at the point of cavity attachment. Then the solution procedure is repeated, beginning with a new estimate for the cavity shape.

The iterative procedure necessary to satisfy equation (6) is quite fast. An alternate formulation of the inverse problem is to specify the radial velocity component, $v_{i_{\text{cavity}}} = V_{\text{cavity}} \sin(dr_i/dx_i)$, at each cavity control point. This formulation was tried, but then abandoned, because the convergence given by equation (6) was very slow. An attempt was made to specify both the longitudinal velocity and the radial velocity in the same solution. The longitudinal velocity was fixed at alternating cavity control points, the radial velocity was specified at the remaining cavity control points. The convergence requirement

$$\frac{|(\text{rms}\sqrt{u^2_{i_{\text{cavity}}} + v^2_{i_{\text{cavity}}}} - V_{\text{cavity}})|}{V_{\text{cavity}}} \leq 1\times10^{-4} \qquad (9)$$

was satisfied after several iterations for slender shapes. For a 15 deg half-angle cone, however, this requirement could not be met.

Boundary-Layer Solution. Once the converged cavity solution has been obtained from the potential solution, the boundary-layer calculations are performed. Both laminar and turbulent boundary-layer solutions are obtained on the body using momentum-integral techniques. The boundary-layer solutions account for the effects of pressure gradient and surface roughness. The effects of surface roughness on the development of the boundary layer are dependent upon the type of roughness present. Only the effects of distributed, three-dimensional roughness, e.g., sand, have been considered in the present work.

The solution for the laminar portion of the boundary layer is obtained from Thwaites' one parameter solution of the momentum-integral equation (1949; White, 1974). For steady flow over an axisymmetric body with impermeable walls, it is assumed that the boundary-layer thickness, δ, satisfies the condition $\delta \ll r$ where r is the local radius of the body. The momentum-integral equation can be reduced to the form

$$\Theta^2 = \frac{0.45\mu}{r^2 U^6 \rho}\int_0^s r^2 U^5 ds \qquad (10)$$

where Θ is the boundary-layer momentum thickness, U is the surface velocity from the potential solution, and s is the surface length. Once the momentum thickness is obtained from equation (10), the remaining laminar boundary-layer parameters (shape factor and surface shear stress) are obtained from a tabulated correlation among the parameters (Schlichting, 1968).

The point of transition is calculated in the present work by the approximate method of Schlichting (1968, see also White (1974)). First, the point of instability, s_i, where the unsteady Tollmien-Schlichting waves first appear, is determined. This determination is made using the local Reynolds number based on displacement thickness, Re_{δ^*}. At each step in the laminar calculation, the local values of Re_{δ^*} and the parameter η, defined as

$$\eta = \frac{2m}{1+m}, \tag{11}$$

where

$$m = \frac{sU'}{U} \tag{12}$$

are calculated. This local η is used to determine the local value of $\mathrm{Re}_{\delta^*,\mathrm{crit}}$ from a correlation of stability parameters for Falkner-Skan profiles (White, 1974). The flow is unstable when $\mathrm{Re}_{\delta^*} > \mathrm{Re}_{\delta^*,\mathrm{crit}}$. Once s_i is known, the transition point, s_{tr}, is determined by examining Re_Θ. A transition value of Re_Θ is determined from

$$\mathrm{Re}_\Theta(tr) = \mathrm{Re}_\Theta(s_i) + 450 + 400\exp^{60\lambda_m} \tag{13}$$

where

$$\lambda_m = \frac{1}{s_{tr} - s_i} \int_{s_i}^{s_{tr}} \lambda(s)ds \tag{14}$$

When $\mathrm{Re}_\Theta(s) \geq \mathrm{Re}_\Theta(tr)$, the flow has transitioned. The method for including distributed surface roughness in the transition model is discussed in the references by Wolfe and Oberkampf (1985a, b).

Once the flow has transitioned, the turbulent boundary-layer solution is initiated. The method chosen in the present work is a modification of White's Karman-type method for non-equilibrium pressure gradient flows. The method has been modified to account for the effects of surface roughness. For turbulent flow, small roughness elements at the surface will break up the thin viscous layer and cause strong changes in the velocity profile. As with the laminar boundary-layer equations, the method assumes that $\delta \ll r$. In terms of a Reynolds number based on radius, White states that the method gives accurate results as long as $rU/\nu > 10^3$.

The following equations form a closed set and are solved simultaneously to obtain the turbulent boundary-layer characteristics.

Momentum:

$$\frac{d\Theta}{ds} + \Theta\left(\frac{2+H}{U}\frac{dU}{ds} + \frac{1}{r}\frac{dr}{ds}\right) = \frac{C_f}{2} \tag{15}$$

Skin Friction:

$$C_f = \frac{2}{\lambda^2} \tag{16}$$

Shape Factor:

$$H = \frac{\lambda}{\lambda - a(\Pi)} \tag{17}$$

where, from the law of the wake, λ and $a(\Pi)$ are

$$\lambda = \frac{1}{\kappa}\ln\left[\frac{\kappa H}{1+\Pi}\mathrm{Re}_\Theta\right] + B + \frac{2\Pi}{\kappa} \tag{18}$$

$$a(\Pi) = \frac{2 + 3.179\Pi + 1.5\Pi^2}{\kappa(1+\Pi)} \tag{19}$$

Overlap Parameters:

$$\kappa = 0.40 \tag{20}$$

$$B = 5.5 - \frac{1}{\kappa}\ln(1 + 0.3k^+) \tag{21}$$

where k^+ is a nondimensional surface roughness given by

$$k^+ = \frac{k_s U}{\nu}\frac{1}{\lambda} \tag{22}$$

and k_s is the equivalent sand grain roughness of the surface.

Equilibrium Correlation of Cole's Law-of-the-Wake:

$$\Pi_{eq} = 0.8(\eta + 0.5)^{0.75} \tag{23}$$

where

$$\eta = -\frac{\lambda^2 H\Theta}{U}\frac{dU}{ds} \tag{24}$$

Lag condition for nonequilibrium flows:

$$\frac{d\Pi}{ds} = 0.1\left(\frac{\Pi_{eq} - \Pi}{\Theta}\right) \tag{25}$$

The constant of 0.1 used in equation (25) is different from that used by White. White states that he used a constant of 0.01; however, the results in his text could not be duplicated using this value. A value of 0.1 provides much better agreement with experimental data and with the calculated values given by White.

The iterative solution to these equations is started with the value of Θ obtained from the laminar solution and an initial estimate of $H = 1.4$. This is the value of the shape factor for a fully developed turbulent boundary layer on a flat plate with a zero pressure gradient. The solution begins at the point of transition and proceeds to each succeeding body station that has fully-wetted flow. At each station, a solution is obtained by iterating among equations (16)-(25). Once the iteration has converged, the solution is advanced to the next body station by numerically integrating equation (15).

Potential-Flow/Boundary-Layer Coupling. After the laminar and turbulent boundary-layer solutions are calculated, the displacement thickness is added to the wetted flow portions of the body. This changes the radial location of the control points used in the potential-flow solution and couples the viscous effects to the inviscid body and cavity flow. The potential-flow solution is calculated as previously described in Stage Two of the Potential-Flow Section for this new, "effective" body. The body/cavity juncture is initially selected as that found by the pure potential-flow solution. A new cavity shape and location is then found which satisfies the convergence criteria given by equations (6)-(8).

The boundary-layer solution gives the skin-friction component of drag and slightly alters the pressure component of drag. The skin-friction drag is calculated for the wetted portion of the body only, based on the assumption that the cavity-covered section of the body does not contribute to the skin-friction component. The surface roughness introduced in the boundary-layer solution only affects the boundary-layer transition and turbulent skin friction. No coupling between surface roughness and cavitation inception is made. Likewise there is no attempt in this work to couple boundary-layer separation with cavitation inception.

The present method has been implemented on a VAX 8600 computer. Typical run times depend on how much the cavity location changes during the iteration procedure. When the iteration procedure requires that the cavity move from far forward on the body toward the base, roughly nine minutes of cpu time is required. When the cavity location does not move, the cpu time is reduced to roughly two minutes. The body and cavity are typically modeled with 30 source elements for the potential-flow solution and 200 surface points for the boundary-layer solution. The code calculates the water viscosity as a function of the water temperature and salinity. The water-vapor pressure calculation accounts for the effects of water temperature, salinity, and freestream pressure.

Results

Presented here are comparisons of theoretical and experimental drag coefficients. The experimental data for comparisons are taken from both water-tunnel and high-speed water-entry tests. Figure 2 compares theory and water-tunnel data for a family of cones with half-angles of 15 deg or less. Cones with half-angles larger than 15 deg are too blunt for the

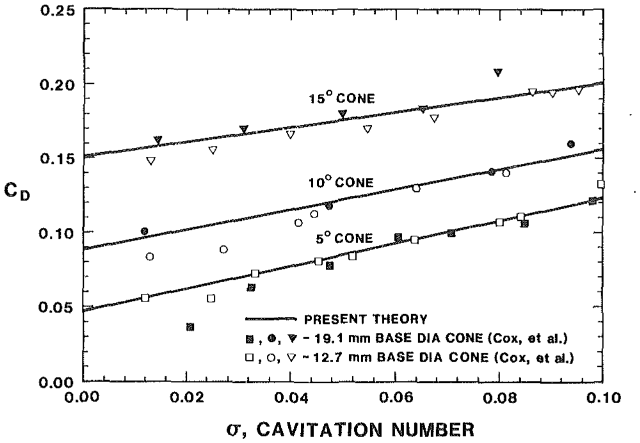

Fig. 2 Drag coefficient of 5, 10, and 15 deg cones versus σ in a water tunnel

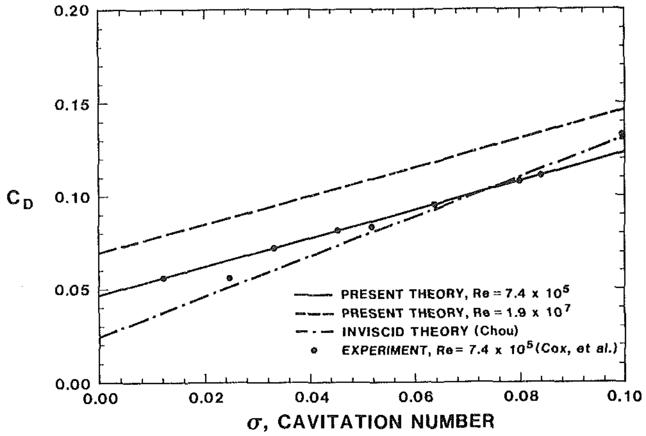

Fig. 3 Drag coefficient of 5 deg cone compared with previous theory and high Reynolds number results

potential-flow theory employed here. The comparison with the experiment of Cox and Maccoll (1957) is quite good for all three cones. The experimental results were obtained by fixing the tunnel velocity at 11.58 m/s (38 fps), with variations in σ obtained by lowering the tunnel freestream pressure, p_∞. The numerical results were calculated in a similar fashion, assuming the cavity pressure was vapor pressure. The numerical and experimental results for the 12.7 mm (1/2 in) base-diameter cones had a constant Reynolds number of 7.4×10^5, based on length. The solution calculates a laminar boundary layer along the cone body with a cavity beginning at the base for the 5, 10, and 15 deg cones. The calculation was also made for the 19.1 mm (3/4 in) base diameter family of cones, but is not shown in Fig. 2. The calculated drag coefficient for the 19.1 mm base diameter cones is indistinguishable from the calculated drag of the 12.7 mm base-diameter cones with the scale used in Fig. 2. This result suggests the experimental drag coefficients for the 12.7 mm an the 19.1 mm diameter cones should be essentially the same. Therefore, the differences in the experimental results for the two size cones shown in Fig. 2 are data scatter.

The present theory and experimental results indicate the relationship $C_D = C_{D_0}(1+\sigma)$, first proposed by Reichardt (1946), does not hold for slender shapes. Reichardt's theory holds for blunter shapes where most of the body is in the cavity and C_{D_0} is fairly large and composed essentially of pressure drag. Slender shapes, such as the family of cones in Fig. 2, support only a base cavity so that a large component of drag is due to skin friction. The present analysis shows that the relationship $C_D = C_{D_0} + \sigma$, proposed by Armstrong (1954), also is not applicable. The lines in Fig. 2 have approximate slopes of 0.76, 0.67, and 0.50 for cone angles of 5, 10 and 15 deg, respectively.

The importance of skin-friction drag can be seen in Fig. 3, which compares theory and water-tunnel data for the 5 deg half-angle cone previously shown in Fig. 2 ($\mathrm{Re}_l = 7.4 \times 10^5$). Also plotted in the figure are inviscid-flow predictions from Chou (1974), adjusted to include the base-drag contribution where the base-drag component is the value of σ. Chou's predictions are lower than the measurements for σ near zero and the slope of the curve is incorrect because skin-friction drag was ignored. It is important to note that the inviscid-drag predictions of Chou and the inviscid drag of the present theory are very similar, both in magnitude and slope. For a value of $\sigma = 0.01$ a calculation for drag was made by "turning off" the boundary layer portion of the code, which gave $C_D = 0.035$. Chou's theory, which is most valid for small values of σ, predicts $C_D = 0.036$ for the same cavitation number, $\sigma = 0.01$. Similarly for $\sigma = 0.02$, the inviscid-drag prediction of the present theory gives $C_D = 0.042$ while Chou's theory gives $C_D = 0.046$. From the present calculation, it was found that the cone drag as $\sigma \rightarrow 0$ is composed of 56 percent forebody pressure drag and 44 percent skin-friction drag. For fully-wetted flow, not shown in Fig. 3, the drag coefficient for the 5 deg cone is predicted to be 0.278. The components of drag have completely reversed from that at $\sigma = 0$. For fully wetted flow, 3 percent is forebody pressure drag, 8 percent is skin-friction drag, and 89 percent is base (cavity) drag.

Also plotted in Fig. 3 is the calculated drag for a 5 deg half-angle cone at a higher Reynolds number, $\mathrm{Re}_l = 1.9 \times 10^7$. This Reynolds number corresponds to a freestream velocity of 304.8 m/s, which is a representative velocity for high-speed water entry. Note also that this Reynolds number is in the region where there is a jump in skin-friction drag due to the transition from laminar to turbulent flow. The purpose of this curve is to show the importance of Reynolds number in high-speed, cavitating flow, over a wide range of σ values. The water-tunnel experiment was conducted for a constant freestream velocity of 11.58 m/s, which results in a drag component due to a laminar boundary layer. For high-speed water entry, or high-speed underwater travel, a fully turbulent boundary layer exists on the body which gives rise to a large component of skin-friction drag as seen in Fig. 3. Even for $\sigma = 0.1$, a case dominated by base drag for the laminar Reynolds number case, the turbulent skin-friction component represents 30 percent of the total drag for the high-speed flow case.

Figure 4 shows calculated cavity shapes for the 5 deg half-angle cone discussed above as a function of cavitation number. Variations in σ were accomplished by changing the freestream pressure with the freestream velocity fixed at 11.58 m/s ($\mathrm{Re}_l = 7.4 \times 10^5$) and the cavity pressure equal to vapor pressure. The figure shows a base cavity for all three cavitation numbers. For $\sigma = 0.1$ and $\sigma = 0.05$, the starting cavity location was at the base of the cone. For $\sigma = 0.001$, the starting cavity location was forward on the body of the cone. The iteration scheme moved the cavity location to the base of the cone so that equations (6)-(8) would be satisfied. For $\sigma = 0.1$, the solution shows the cavity beginning to close about 0.5 body lengths aft of the base. The present theory cannot predict complete cavity closure. The cavity streamline cannot touch the body axis because of the singularity distribution along the axis which results in infinite velocity for any stream line approaching the axis. The theory shows that as $\sigma \rightarrow 0$, the cavity grows in length and fullness, which is in agreement with water-tunnel test observations.

Cavity shape is determined by the potential-flow solution and is almost completely a function of σ, with little Reynolds number influence. The Reynolds number influence comes

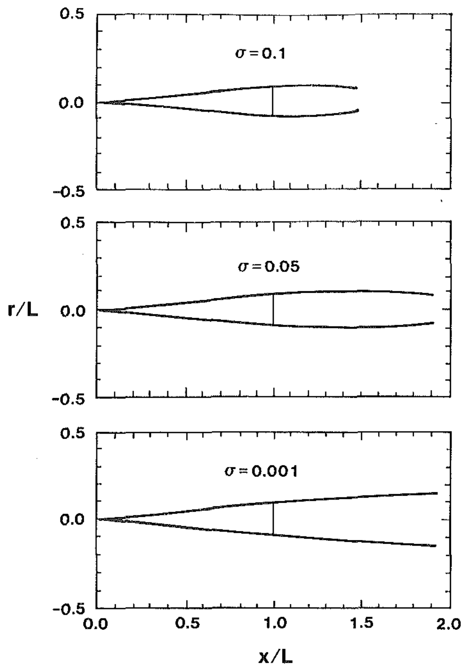

Fig. 4 Calculated cavity shape and location as a function of σ for 5 deg cone

from the coupling of the potential-flow solution with the boundary-layer solution. Calculations of cavity shape for the same set of σ shown in Fig. 4 were made for a higher Reynolds number ($Re_l = 1.9 \times 10^7$, $V_\infty = 304.8$ m/s). These results were indistinguishable from those plotted in Fig. 4. This is not surprising since the boundary-layer solution results in only a slight change in body shape. The Reynolds number contribution is very important in calculating skin-friction drag. Similar results were found for the 10 and 15 deg cones.

The experimental results of Goeller, Hassett, and Steves (1972) for high-speed water entry of a vehicle are compared with theory in Fig. 5. The body is a paraboloid that was fired into the water at an entry speed of 316.4 m/s and an angle, from the horizontal, of 18.8 deg. Excellent agreement is shown between theory and experiment from water entry to low speed. This agreement demonstrates the first successful prediction of drag on bodies during high-speed water entry. The results are plotted as a function of velocity rather than cavitation number. Plots as a function of σ give an indistinguishable cluster of data points in the region $0 \leq \sigma \leq 0.05$ which represents a considerable range of velocity data points (316.4 m/s to about 137.2 m/s). The theoretical results calculate a base cavity for the entire range of σ values. For small values of σ, the starting cavity location is on the body, but the converged cavity solution, which satisfies equations (6)-(8), locates the cavity on the base of the paraboloid. Photographs taken of the paraboloid moving at 244 m/s after vertical entry (90 deg from the horizontal) show cavitation on the model body. However, it appears the cavitation is caused by a joint in the model.

The cavity pressure during water entry was assumed to be the vapor pressure of the liquid. This assumption was based on the high-speed water-entry cavity pressure measurements of Doak and Ferguson (1973) who showed that very shortly after water entry the pressure in the cavity was near vapor pressure. The present agreement between theory and experiment for drag corroborates the cavity pressure measurement of Doak and Ferguson.

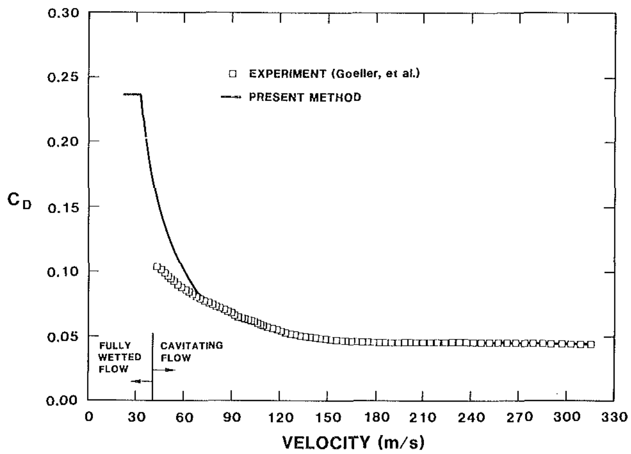

Fig. 5 Drag coefficient of a paraboloid during high-speed water entry

Conclusions

The present paper describes work concerning fluid dynamics of cavitating flow. The flow field and drag of bodies of revolution at zero angle of attack are predicted for cavitation numbers from fully-wetted flow to $\sigma \rightarrow 0$. Excellent agreement for drag coefficient is demonstrated between theory and water-tunnel experiment. It is shown that skin-friction drag is the dominant drag component as the cavitation number approaches zero. Also, turbulent skin-friction drag is an important component for high-speed bodies with base cavities for a wide range of cavitation numbers. Excellent agreement is also demonstrated between theory and a high-speed water-entry experiment. This agreement corroborates the experimental measurement that the cavity pressure is equal to the water vapor pressure, contrary to low-speed water entry.

References

Armstrong, A. H., 1954, "Drag Coefficients of Wedges and Cones in Cavity Flow," Royal Armament Research and Development Establishment, Fort Halstead, Rept. No. 21-54.

Chou, Y. S., 1974, "Axisymmetric Cavity Flows Past Slender Bodies of Revolution," *Journal of Hydronautics*, Vol. 8, No. 1, pp. 13-18.

Cox, R. N., and Maccoll, J. W., 1957, "Recent Contributions to Basic Hydroballistics," *Symposium on Naval Hydroballistics*, NAS-NRC Publication 515, Washington, D.C., Chap. IX, pp. 215-239.

Doak, D. W., and Ferguson, G. M., 1973, "Water Entry Cavity Pressure Measurements," ASME 1973 Cavitation and Polyphase Flow Forum.

Goeller, J. E., Hassett, R. J., and Steves, H. K., 1972, "Oblique Water Entry of High-Speed Cones and Paraboloids," Naval Ordnance Lab., Rept. NOLTR-72-188.

Johnson, V. E., and Rasnick, T. A., 1961, "The Drag Coefficient of Parabolic Bodies of Revolution Operating at Zero Cavitation Number and Zero Angle of Yaw," NASA-TR-R-86.

Plesset, M. S., and Schaffer, P. A., 1948, "Cavity Drag in Two and Three Dimensions," *Journal of Applied Physics*, Vol. 19, pp. 934-939.

Rattayya, J. V., Brosseau, J. A., and Chisholm, M. A., 1981, "Potential Flow About Bodies of Revolution with Mixed Boundary Conditions-Axial Flow," *Journal of Hydronautics*, Vol. 15, Nos. 1-4, pp. 74-80.

Reichardt, H., "The Laws of Cavitation Bubbles at Axially Symmetric Bodies in a Flow," MAP Reports and Translations No. 766, 1946.

Schlichting, H., 1968, *Boundary Layer Theory*, McGraw-Hill, Inc., New York, 6th Edition.

Struck, H. G., 1970, "Discontinuous Flows and Free Streamline Solutions for Axisymmetric Bodies at Zero and Small Angle of Attack," NASA-TN-D-5634.

Thwaites, B., 1949, "Approximate Calculation of the Laminar Boundary Layer," *Aeronautical Quarterly*, Vol. 1, pp. 245-280.

White, F. M., 1974, *Viscous Fluid Flow*, McGraw-Hill, Inc., New York.

Wolfe, W. P., and Oberkampf, W. L., 1985a, "Drag Prediction for Projectiles and Finned Bodies in Incompressible Flow," AIAA Paper No. 85-0104.

Wolfe, W. P., and Oberkampf, W. L., 1985b, "SANDRAG-A Computer Code for Predicting Drag of Bodies of Revolution at Zero Angle of Attack in Incompressible Flow," Sandia National Laboratories, Albuquerque, N.M., SAND85-0515.

Wolfe, W. P., and Oberkampf, W. L., 1987, "Drag Predictions for Projectiles and Finned Bodies in Incompressible Flow," *J. Spacecraft and Rockets*, Vol. 24, pp. 14-22.

Zedan, M. F., and Dalton, C., 1978, "Incompressible Irrotational Axisymmetric Flow about a Body of Revolution: The Inverse Problem," *Journal of Hydronautics*, Vol. 12, Nos. 1, pp. 41-46.

Viscous and Nuclei Effects on Hydrodynamic Loadings and Cavitation of a NACA 66 (MOD) Foil Section

Y. T. Shen
David Taylor Research Center,
Bethesda, MD 20084-5000

P. E. Dimotakis
California Institute of Technology,
Pasadena, CA 91125

A series of experiments has been conducted on a two-dimensional NACA 66 (MOD) foil to examine the effects of viscosity and nuclei on cavitation inception. In this paper the main discussions center on two foil angles having different types of pressure loadings to represent a propeller blade section operating at design and off-design conditions. At one degree design angle of attack the foil experiences a rooftop-type gradually varying pressure distribution. At three degrees off-design angle of attack the foil experiences a sharp suction pressure peak near the leading edge. Cebeci's viscid/inviscid interactive code is used to compute the viscous scale effects on the development of the boundary layer, lift, drag and pressure distribution on the foil. Chahine's multibubble interaction code is used to compute the effect of nuclei, test speeds, foil size and foil surface on traveling bubble cavitation. Both computer codes are found to agree satisfactorily with the experimental measurements reported here. Two assumptions commonly used to predict full scale surface cavitation from model tests are examined experimentally and theoretically. The first assumption states that cavitation inception occurs when the static pressure reaches the vapor pressure. On the contrary, the experiments showed that the water flowing over the foil surface sustained significant amounts of tension during inception of midchord bubble cavitation as well as leading edge sheet cavitation. The second assumption states that there is no scale effect on the values of negative minimum pressure coefficient. In the case of a rooftop-type pressure loading, the second assumption is supported by the pressure numerical calculations. However, in the case of a pressure loading with a strong suction peak near the leading edge the value of negative minimum pressure coefficient is as much as 12 to 15 percent lower on a model than at full scale.

Introduction

Most heavily loaded hydrofoils or propellers will develop tip vortex, leading edge sheet and midchord bubble cavitation at high speed. The occurrence of cavitation produces undesirable changes in hydrodynamic performance, noise generation, and physical damage from vibration and erosion. Therefore, the ability to predict the occurrence of cavitation becomes an important engineering problem. Because the physical processes involved with cavitation inception are complex, the prediction of cavitation performance has relied heavily on model experiments and extrapolation of the results to full scale.

Two assumptions are commonly used in model tests of surface cavitation for full scale prediction. The first assumption states that cavitation inception occurs when the static pressure reaches the vapor pressure. The cavitation inception index, σ_i, is assumed equal to the negative minimum pressure coefficient, $-Cp_{\min}$; the difficulty with this assumption is that cavitation takes a variety of forms and values of σ_i even with the same model tested in the same facility. Acosta and Parkin [1] pointed out that differences in Reynolds number and free stream nuclei distributions in a real fluid are responsible for producing the various appearances of cavitation on a single headform model.

A foil operated at its design condition experiences midchord bubble cavitation at high speeds. This type of cavitation is extremely sensitive to the free stream nuclei concentrations [2]. Model tests on axisymmetric headforms by Huang indicate that the effect of different model sizes on bubble cavitation is small and negligible [3]. However, other experiments show bubble cavitation to be strongly affected by model size and test speed [2, 4]. To resolve these discrepancies and understand the effect of nuclei on cavitation more clearly, bubble dynamics calculations have been applied to specific test models. A single bubble dynamics code based on Rayleigh-Plesset theory has been used in some headform studies [2, 4]. Using single bubble dynamics theory, that assumes infinite surroundings to compute bubble growth and collapse along a

---

Contributed by the Fluids Engineering Division for publication in the JOURNAL OF FLUIDS ENGINEERING. Manuscript received by the Fluids Engineering Division August 9, 1988.

model surface, may not be valid because of the proximity of the solid boundary. Recently, a dynamics theory that includes multibubble interactions has been developed by Chahine [5]. The theory uses matched asymptotic expansions to relate the effect of neighboring bubbles. This theory is used here with the experimental data to evaluate the effect of nuclei on cavitation inception and the foil boundary on bubble growth. That is, the foil surface is modeled in the calculations as the midplane of two identical bubbles, one bubble being real and flowing over the foil, and the other bubble being the first bubble's imaginary mirror image in the foil.

Viscous effects are also important in cavitation testing. For foils, the viscous effects on leading edge sheet cavitation have been extensively investigated experimentally [see a review paper in reference 6]. It is often quoted that no leading edge sheet cavitation takes place if the boundary layer on the foil is laminar. Based on the experimental experience, the onset of leading edge sheet cavitation is often associated with laminar separation or natural transition to turbulence [7, 8]. It is a purpose of this paper to examine nuclei and viscous effects on cavitation appearance and the assumption of $\sigma_i = -Cp_{\min}$.

The second assumption often used in cavitation prediction states that $-Cp_{\min}$ can be computed from potential flow theory. The same $-Cp_{\min}$ value at model and full scale has been commonly assumed and used to relate the model tests and full scale predictions. The accuracy of this assumption for a lifting surface has not been carefully examined and reported in the literature. It is a purpose of this paper to theoretically examine this assumption. To accomplish this, a viscid/inviscid interactive computer code recently developed by Cebeci is used [9]. This code computes the development of the boundary layer and the subsequent modification of the pressure distribution, lift and drag. The resultant pressure distribution is used in Chahine's multibubble interaction program to predict the onset of bubble cavitation.

Recently a two-dimensional foil test program was conducted in a high speed water tunnel [10]. To validate the accuracy of numerical calculations the measured pressure distribution is compared to the theoretical predictions from Cebeci's code, and the measured bubble cavity sizes as a function of chord location are compared to the results of the multibubble interaction predictions. For completeness, a brief description of the foil model and test facility is given.

As a practical matter, two-dimensional foil theory is often applied in surface ship propeller design. Recall that due to shaft inclination and wake defects, a propeller blade section experiences angle of attack variations in every cycle of rotation. The blade operates during one revolution on the average at the design condition with a small angle of attack, say $\alpha = 1$ deg, and a rooftop-type pressure distribution. During one revolution the blade will also operate at off-design angles of attack, up to say, $\alpha = 3$ deg, with a sharp suction pressure peak at the leading edge. To cover these two operating conditions, the following discussion will focus on foil performance at $\alpha = 1$ and 3 degrees.

Foil Model and Test Facility

The foil model used in this test program is a NACA 66 (MOD) section of 9 percent thickness. A NACA a = 0.8 meanline is used with a camber ratio of $f/c = 0.020$. This section has been widely used in marine propellers. The model has a 6-in. chord (152 mm) and a 6-inch span and is made from 17-4 PH stainless steel. To ensure an accurate surface contour, the model was cut from a block by a numerically controlled machine using 850 passes on the foil surface. The maximum deviation from the specified section profile measured normal to the surface at three stations along the span was found to be less than 0.0004 of the chord length.

The experiments were performed in the High Speed Water Tunnel in the Graduate Aeronautical Laboratories of the California Institute of Technology. This water tunnel is equipped with a two-dimensional working section. The test section is 50-in. long by 30-in. high with a 6-in. span (1270 × 762 × 152 mm) and is well suited for investigating the section characteristics of hydrofoils, and particularly for studying cavitation. The model can be viewed through top, bottom and side windows to observe cavitation. Test descriptions such as model mounting, force and pressure distribution measurements, tunnel velocity, tunnel pressure measurements, and accuracy of data acquisition are given in reference [10].

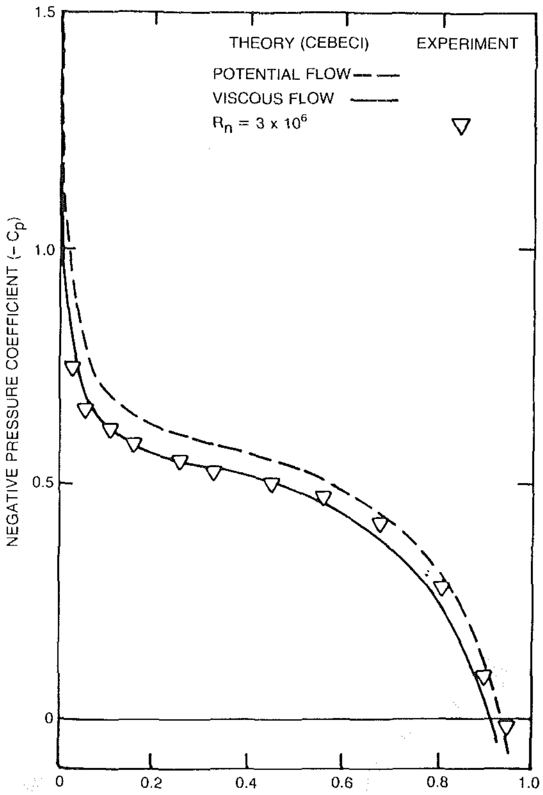

Fig. 1 Pressure distribution at $\alpha = 3$ degrees

Uncertainty Estimates. The force balance was calibrated within the test range to the accuracy of ±0.16 Kg for lift and ±0.045 Kg for drag. The foil angle of attack was set to within 0.01 deg as indicated. The accuracy was ±0.3 percent for the tunnel reference pressure and ±0.5 percent for the tunnel reference velocity. The pressure difference between the static pressure at each model tap and the test section reference pressure was measured via a Scanivalve pressure scanner, using a Druck differential pressure transducer. This was calibrated against a precision Hg manometer to 138 kpa. Accuracy throughout this range was within ±0.21 kpa. The actual pressure hole locations were within ±0.0076 cm of designated positions. The measured cavitation bubble locations were within ±2 percent of the chord length.

Real Fluid Effect on Cavitation At Foil Angle of 3 Degrees

Model Cavitation Observation. Figure 1 shows the measured pressure distribution in a noncavitating flow condition with the foil set at 3 deg. This test run was conducted at a tunnel speed of 60 feet per second (18.3 m/s) which gives a Reynolds number R_n, based on the chord, of 3×10^6. A strong suction pressure peak near the leading edge was noted. This

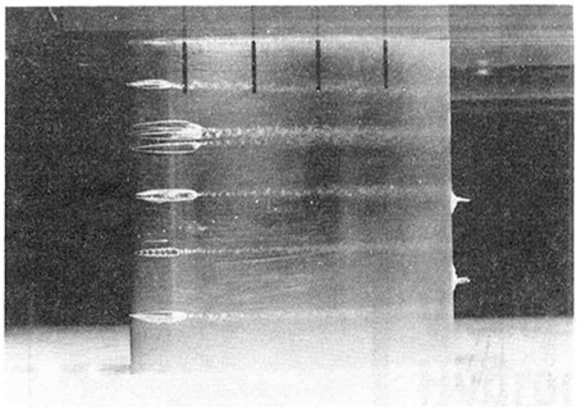

Photo 1 Leading edge attached cavities: $\alpha = 3$ deg, $V = 18.3$ m/s, $R_n = 3 \times 10^6$, $\sigma_v = 0.66$

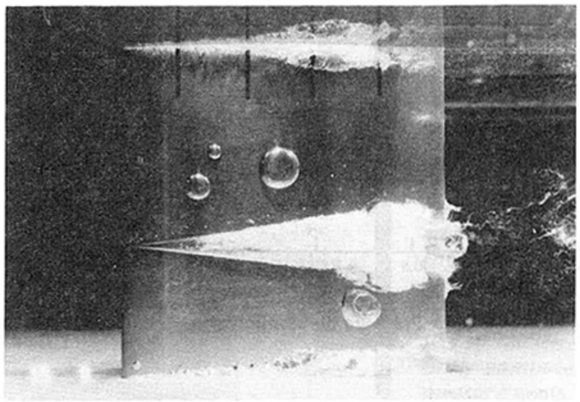

Photo 2 Midchord bubble cavitation: $\alpha = 3$ deg, $V = 9.15$ m/s, $R_n = 1.5 \times 10^6$, $\sigma_v = 0.44$

type of pressure distribution is often experienced when a propeller is operated in a nonuniform wake.

The cavitation experiments were conducted in the High Speed Water Tunnel to determine the kind of cavitation expected with this type of pressure loading and cavitation inception was determined visually under stroboscopic illumination. The cavitation number σ_v was computed from recorded tunnel pressure, speed, temperature and the related vapor pressure and water density. The symbols σ_v and $-Cp_{\min}$ are defined as

$$\sigma_v = \frac{P_\infty - P_v}{1/2\ \rho\ V^2}\ ; \quad -Cp_{\min} = \frac{P_\infty - P_{\min}}{1/2\ \rho\ V^2}$$

where P_∞, P_v, $P_{\min}$, ρ, and V are tunnel pressure, water vapor pressure, minimum pressure on the foil surface, water density, and tunnel speed, respectively.

At a tunnel speed of 60 ft/s (18.3 m/s), corresponding to $R_n = 3 \times 10^6$, cavitation inception was detected at $\sigma_i = 0.74$, which is much lower than the computed value of $-Cp_{\min} = 1.135$. More fully developed cavities at $\sigma_v = 0.66$ are shown in Photo 1. The cavities appear as a group of several individual cavities and are seen to initiate right at the foil leading edge. In the next test run, the tunnel speed was set at 30 ft/s (9.15 m/s), corresponding to $R_n = 1.5 \times 10^6$. No cavitation was detected at $\sigma_v = 0.74$ or 0.66. The tunnel pressure had to be lowered to $\sigma_i = 0.58$ to produce an occasional flushing of a transient bubble. More developed cavities at $\sigma_v = 0.44$ are shown in Photo 2. Except for a cavity triggered by a pressure tap on the foil surface, the cavitation observed in this test was composed of midchord traveling bubbles.

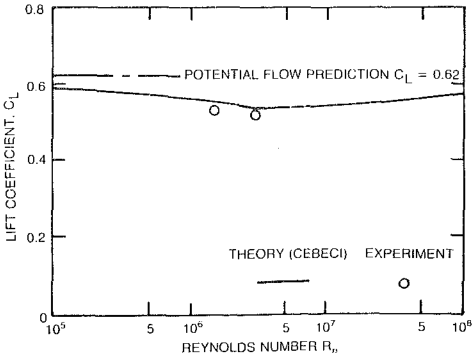

Fig. 2 Scale effect on lift coefficient at $\alpha = 3$ degrees

Not only was there a significant difference in measured cavitation inception indices (0.74 versus 0.58), but the forms of cavitation in these two tests were totally different. In one, sheet cavities occurred at the leading edge and in the other, traveling bubbles occurred at the midchord. The speed is seen to exert a strong influence on cavitation. Furthermore, the measured cavitation inception indices of 0.74 and 0.58 are significantly different from $-Cp_{\min}$ of 1.135. We will first discuss whether $-Cp_{\min}$ is sensitive to Reynolds number scale effect and then discuss the scale effect on cavitation appearance and the relationship between $-Cp_{\min}$ and measured cavitation inception indices σ_i.

Theoretically Computed Scale Effect on $-Cp_{\min}$ and C_L. The viscid/inviscid interactive computer code developed by Cebeci was used to compute the scale effect on the growth of the boundary layer on the modification of the pressure distribution on the foil surface at $\alpha = 3$ deg. The computed pressure distribution at $R_n = 3 \times 10^6$ is plotted in Fig. 1 along with the measured data at noncavitating conditions. Although the theory slightly overpredicts the suction pressure in the forward part and slightly underpredicts the suction pressure in the rear part of the foil, the agreement between the computed and measured values is considered satisfactory for practical use.

The computed transition locations on the upper surface x_{tru}, on the lower surface x_{trl}, the lift and drag coefficients C_L and C_D and the negative minimum pressure coefficients $-Cp_{\min}$ are given in Table 1 as a function of R_n. Since no laminar flow separation occurs at a foil angle of 3 deg, the location of transition is computed using Michel's transition criterion [9]. At $R_n = 5 \times 10^5$, the flow is laminar up to 62 percent of the chord on the upper foil surface and up to 99 percent of the chord on the lower foil surface. With such an extended laminar flow region on the foil, the computed C_L value of 0.58 is close to the potential flow value of 0.62. As the Reynolds number increases, the flow transition locations move forward and result in a reduction of C_L. However, at $R_n = 1 \times 10^7$, transition occurs at 4 percent of the chord from the leading edge with 96 percent of the chord in turbulent flow. A further increase in Reynolds number results in only a slight forward movement of the transition location. The trend of C_L versus R_n is reversed. A further increase in R_n results in an increase in C_L. At extremely high Reynolds numbers, the solution again approaches the potential flow limit. The computed C_L value is given in Fig. 2. The experimentally measured C_L values of 0.527 and 0.521 at $R_n = 1.5 \times 10^6$ and 3×10^6, respectively, are also given in Fig. 2 for comparison with the numerical calculations. Again, the agreement is quite satisfactory.

The computed $-Cp_{\min}$ value is shown in Table 1. At a model Reynolds number of $R_n = 3 \times 10^6$, the computed $-Cp_{\min} = 1.135$ at $x/c = 0.0045$. Even at a full-scale R_n of 10^8, the $-Cp_{\min}$ value reaches only 1.258, which is still substantially lower than the $-Cp_{\min}$ value of 1.538 computed by potential flow theory. Table 1 shows that $-Cp_{\min}$ is sensitive to

Table 1 Computed scale effect on boundary layer developments and hydrodynamic loadings at $\alpha = 3$ deg

R_n	$x_{tru/c}$	$x_{trl/c}$	C_L	C_D	$-Cp_{\min}$
5×10^5	0.621	0.990	0.582	0.00600	1.281
1.5×10^6	0.304	0.941	0.550	0.00609	1.203
3×10^6	0.133	0.892	0.531	0.00614	1.135
5×10^6	0.055	0.764	0.538	0.00633	1.116
1×10^7	0.0382	0.707	0.544	0.00583	1.118
3×10^7	0.0178	0.585	0.554	0.00527	1.218
1×10^8	0.0125	0.395	0.566	0.00482	1.258
Potential flow	-----	-----	0.626	-----	1.538

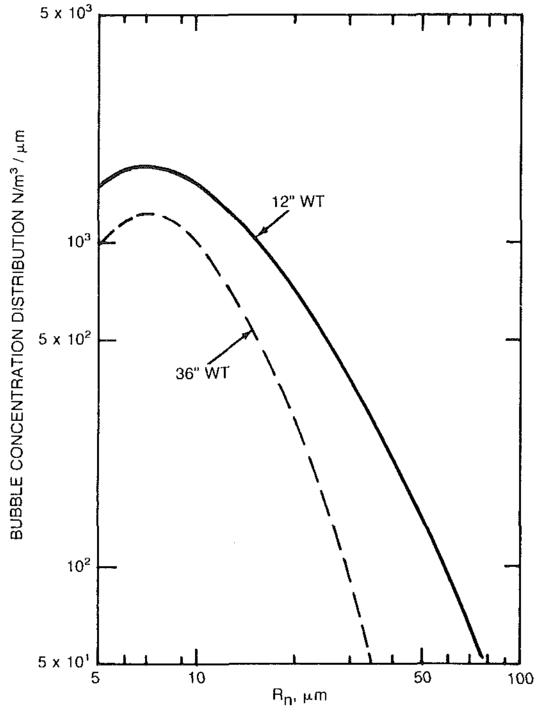

Fig. 3 Measured bubble spectra at DTRC 12 – and 36 – inch water tunnels (from reference [2])

Reynolds number. The computation from potential flow theory predicts $-Cp_{\min}$ values substantially higher than the values predicted at finite values of Reynolds number. This important result shows that cavitation scaling between model and full scale requires consideration of viscous effects on $-Cp_{\min}$ values.

Real-Fluid Effects on Cavitation Appearance. If a cavity is to be created in a homogeneous liquid, the liquid must be ruptured, and the stress required to do this is not measured by the vapor pressure but by the tensile strength of the liquid at that temperature [11]. According to Plesset [12] liquids can theoretically withstand a tension of the order of thousands of atmospheres. In practice, however, the formation of cavities requires only moderate tension [11, 13, 14] due to the presence of weak spots in liquids commonly known as "nuclei." Free gas bubbles in the free stream are a good source of nuclei [2, 15, 16]. An example of bubble nuclei distributions measured in the David Taylor Research Center (DTRC) 12-inch and 36-inch water tunnels is shown in Fig. 3 [2]. Figure 3 is used only as an example, as bubble nuclei distributions are very sensitive to water treatments. As noted by the logarithmic scale, gas bubbles greater than 50 μm are rare.

Cavitation Observation at 30 ft/s (9.15 m/s), $R_n = 1.5 \times 10^6$. Table 1 shows that laminar flow on the upper surface covers the first 31 percent of the chord at this test condition. In this laminar region the boundary layer effect on bubble dynamics can be neglected. In a fully established turbulent region, high frequency pressure fluctuations are superimposed on mean static pressure. According to Huang

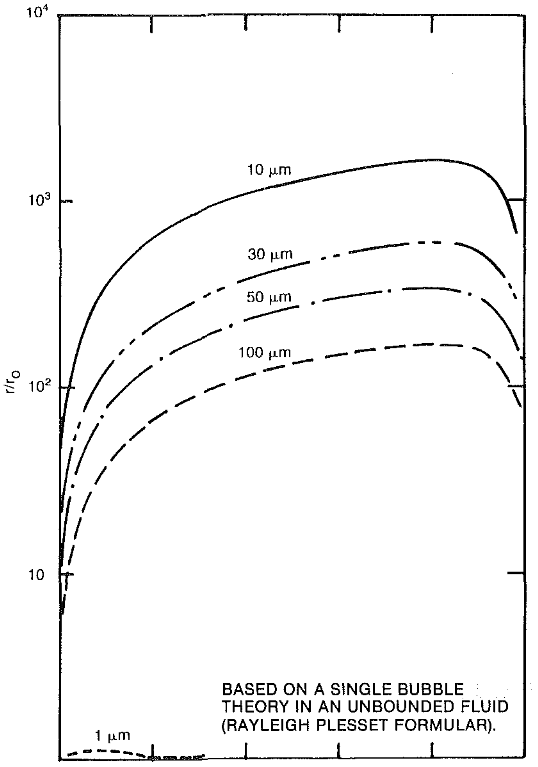

Fig. 4 Computed influence of initial bubble sizes on the subsequent bubble growth at $\alpha = 3$ deg, $V = 9.15$ m/s, $\sigma_v = 0.44$ for $r_0 = 1, 10, 30, 50, 100$ μm.

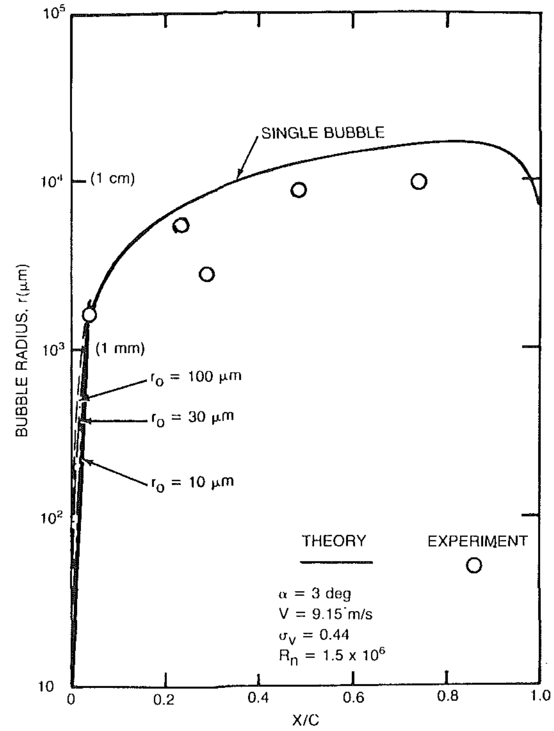

Fig. 5 Bubble radius variation during the passage over the foil at $V = 9.15$ m/s

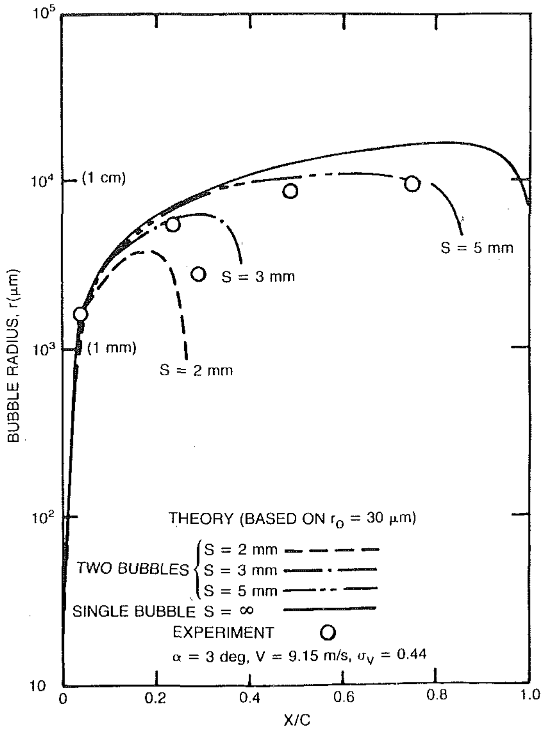

Fig. 6 Influence of vertical distance S from foil surface on bubble growth during the passage over the foil

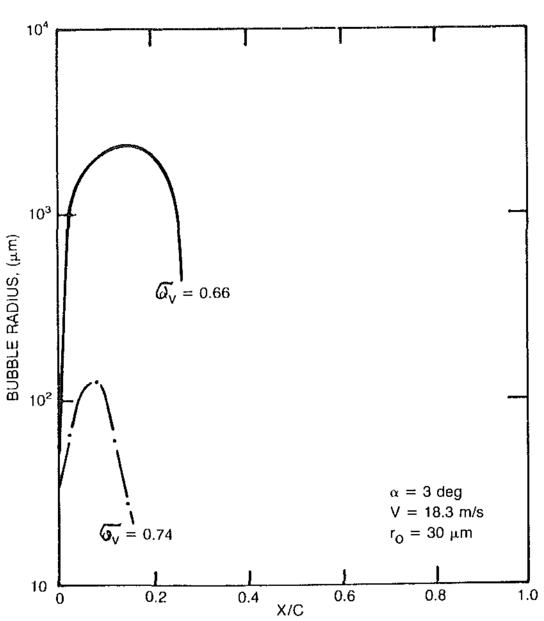

Fig. 7 Computed bubble radius variation during the traverse through the foil at $V = 18.3$ m/s, $\alpha = 3$ degrees

and Peterson [17] the average magnitude of pressure fluctuations is only about 1.5 percent of the dynamic head. In this study only the mean static pressure was used to estimate bubble growth and collapse from Chahine's computer code.

In the known pressure field given in Fig. 1, the histories of bubble radius motion during their passage over the foil are illustrated in Figs. 4 and 5 for initial bubble sizes of $r_0 = 1$, 10, 30, 50, and 100 μm, where r_0 denotes the initial bubble radius in the free stream. The computations are based on the Rayleigh-Plesset dynamic theory for a single spherical bubble in an unbounded fluid subjected to given pressure and velocity fields. It is remarked that in the limiting case of a single bubble, Chahine's solution reduced to the Rayleigh-Plesset equation. The numerical computations for these two figures are based on a free stream velocity of 9.15 m/s, tunnel pressure of 0.21 atmospheres, water temperature of 20°C, and gas polytropic constant of 1.4. The corresponding cavitation number is 0.44 which is the same value as in Photo 2. Except for 1 μm bubbles all sizes of bubbles experience explosive growth and collapse. Furthermore, a short distance from the leading edge, transient bubbles with radii, r_0, equal to or greater than 10 μm are predicted to almost merge into a single curve and reach the same maximum size of 17 mm. This result agrees with the previous finding that $r_{\max}$ does not depend on initial radius r_0 when r_0 is well beyond the critical radius for static instability [4, 18]. The radii of five bubbles visible in Photo 2 are plotted in Fig. 5 for comparison. The single spherical bubble dynamics theory seems to overpredict the bubble sizes by 60 to 70 percent at $x/c = 0.49$ and 0.74. Furthermore, according to the single bubble theory as shown in Fig. 5, the bubble size at $x/c = 0.29$ should not be smaller than the bubble size at $x/c = 0.24$, but it is, as shown in Photo 2.

Experiments clearly show that cavitation bubbles are convected downstream along trajectories at very short vertical distances above the foil surface. The proximity of the solid boundary is expected to modify the history of bubble radius change. To incorporate the solid boundary effect, the foil surface is mathematically replaced by locating an imaginary bubble on the other side of the foil an equal distance from the foil surface.

Numerical examples of bubble growth computed from Chahine's multibubble code are shown in Fig. 6 for $r_0 = 30$ μm and vertical spacings S of 2, 3 and 5 mm above the foil surface. Initially the bubbles are spherical, but the neighboring effect of the images distorts the bubbles as they grow in size. Blake's observation from high speed movies reveals that near the wall the bubbles had a prolate spherical shape [19]. The bubbles' radii measured from Photo 2 are given in Fig. 6. The following observations are derived from Fig. 6:

(*a*) Single bubble dynamics theory overpredicts the history of bubbles radius change by a noticeable margin.

(*b*) The proximity of the foil surface retards the bubble growth rate.

(*c*) Because of the influence of vertical spacing S from the foil surface, a bubble in an upstream location can become larger than a bubble observed in a downstream location as shown in Photo 2.

(*d*) The agreement between measured and predicted history of bubble motion is greatly improved with the consideration of bubble and foil surface interaction.

Cavitation Observation at 60 ft/s (18.3 m/s). At a tunnel speed of 60 ft/s ($R_n = 3 \times 10^6$) leading edge cavitation was detected at $\sigma_i = 0.74$. Photo 1 was taken at a lower value of $\sigma_v = 0.66$ with more developed cavities. The computation from single bubble dynamic theory indicates that the free stream bubbles will not undergo any meaningful growth at $\sigma_v = 0.74$ as shown in Fig. 7 for $r_0 = 30$ μm. Even at $\sigma_v = 0.66$, the maximum bubble size attained is only 2.3 mm. The tunnel pressure would have to be reduced further to produce visible midchord traveling bubbles. However, the foil surface has already produced leading edge cavitation at $\sigma_v = 0.74$.

At $R_n = 3 \times 10^6$, flow transition occurs at $x/c = 0.13$. Photo 1 shows that the cavities are initiated right at the leading edge of the foil. We therefore infer that the occurrence of cavitation is not directly related to the transition of laminar flow to turbulent flow. Photo 1 shows that this type of cavitation is characterized by long streams issuing from many points. Klebanoff and Tidstrom have shown experimentally [20] that a flat plate boundary layer velocity profile develops a local separating velocity profile downstream of an isolated

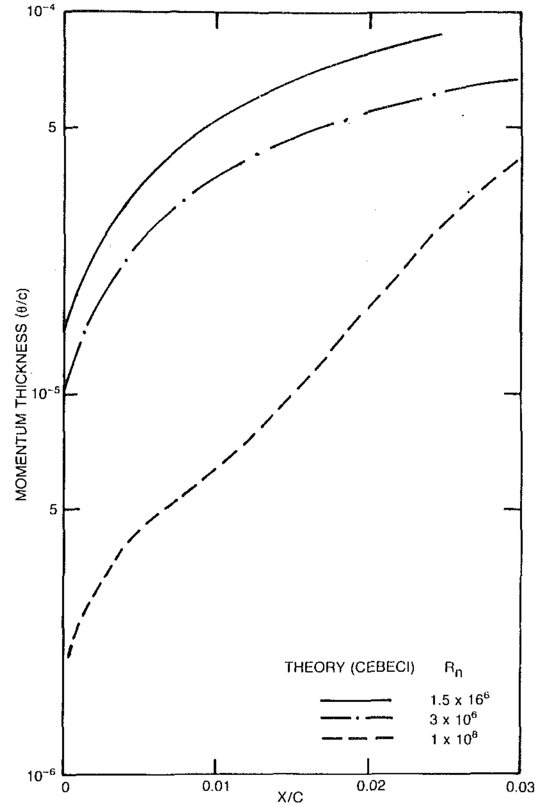

Fig. 8 Computed scale effect on momentum thickness distributions at $\alpha = 3$ degrees

roughness. This fact strongly suggests that the cavities in Photo 1 were triggered by local rough spots in the laminar flow region [21, 22]. This reasoning is further supported when we consider the momentum thickness distribution along the foil surface as shown in Fig. 8. The momentum thickness at the leading edge is noticeably thinner at $R_n = 3 \times 10^6$ than at 1.5×10^6. Even though the foil surface was carefully fabricated, experimental results indicate that at $\alpha = 3$ deg the foil surface can be regarded as relatively smooth at $R_n = 1.5 \times 10^6$ but relatively rough at $R_n = 3 \times 10^6$.

At $\alpha = 2$ a weak suction pressure peak is measured and predicted around the leading edge. However, experiments detected cavitation in the form of midchord traveling bubbles at 9.15 m/s as well as 18.3 m/s at $\alpha = 2$ deg. It appears that at $\alpha = 2$ deg the occurrence of leading edge cavities will require testing at R_n values greater than 3×10^6. On the other hand, with a strong suction pressure peak at $\alpha = 4$ deg, leading edge cavitation occurred at both $R_n = 1.5$ and 3×10^6. The occurrence of midchord bubble cavitation at $\alpha = 4$ deg will require testing at R_n values much lower than 1.5×10^6. It appears that the foil angle of 3 deg is a special case which encompasses midchord bubble cavitation and leading edge cavities within the test range of $R_n = 1.5$ to 3×10^6.

At a foil angle of 3 deg, once a separation zone is formed behind a rough spot, Parkin's model can be used to explain the nuclei effect on leading edge cavitation [23]. The freestream nuclei can enter the separation zone through the reentrant jet region and become trapped inside the separation zone. The headform observations of Arakeri and Acosta [15] reveal that inception occurs at the reattachment point with high wall pressure fluctuations. Through gas diffusion and most importantly rectified diffusion from high pressure fluctuations the nuclei then undergo explosive growth when the local pressure is in the neighborhood of vapor pressure [24]. When the nuclei reach a certain size, they rise from the dead water zone and are convected downstream forming visible bubbles. Photo 1 shows clearly that each individual sheet cavity is in the shape of a triangular wedge induced by a three-dimensional roughness. Behind the triangular wedge is a pair of trailing horseshoe vortices made visible by the cavitation bubbles [25].

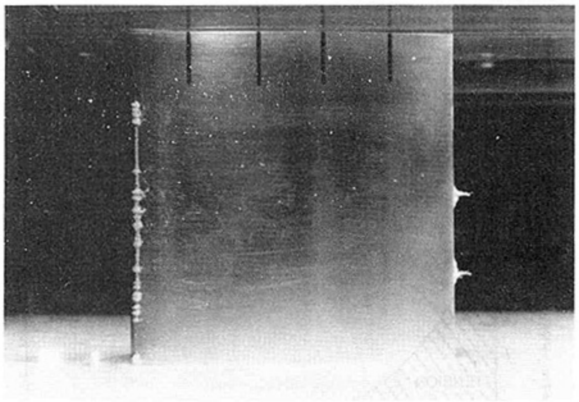

Photo 3 Leading edge cavitation occurring at roughness spots and laminar flow separation zone: $\alpha = 6$ deg, $V = 12.2$ m/s, $R_n = 2 \times 10^6$, $\sigma_v = 2.44$

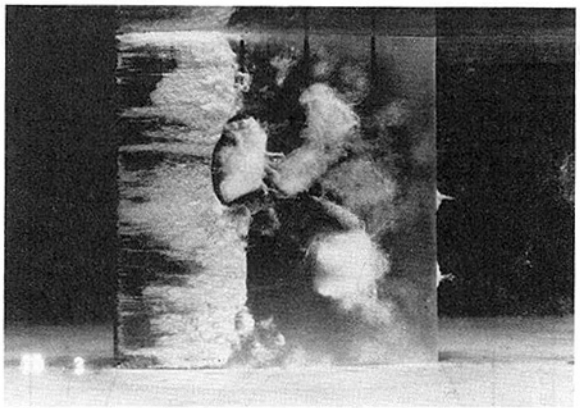

Photo 4 Developed partial cavity: $\alpha = 6$ deg, $V = 12.2$ m/s, $R_n = 2 \times 10^6$, $\sigma_v = 1.22$

Results from a test at $\alpha = 6$ deg amplify further the effect of roughness on cavitation. Flow visualization [26] and boundary layer calculations show that, within the present test range, laminar flow separation occurs at $\alpha = 6$ deg. This is clearly seen from the cavitation shown in Photo 3 for $\sigma_v = 2.44$ and $R_n = 2 \times 10^6$. Cavities are seen to initiate at two distinct locations along the chord, one at the laminar separation zone which shows as a straight band [16], and the other at local rough spots at the leading edge which shows as wedge shapes at each spot. Photo 3 shows that, at high R_n of 2×10^6 and high foil angle, cavities can occur either at local rough spots or in a laminar separation zone.

Photo 4 shows a developed partial cavity flow under further reduced tunnel pressure at $\alpha = 6$ deg, $\sigma_v = 1.22$ and $R_n = 2 \times 10^6$. The mean cavity length is about 40 percent of the chord. The appearance of the cavity in Photo 4 is very similar that observed on a full scale propeller blade as discussed in a paper by Kuipper [27]. As seen in Photo 4, the whole cavity is a composite of numerous cavities initiated from the leading edge at the rough spots. Recently, it has been argued that the mathematical treatment of a leading edge partial cavity should start at the laminar separation zone. The present study shows clearly that at high R_n values it is more plausible to consider that the partial cavity originates at local roughness spots which

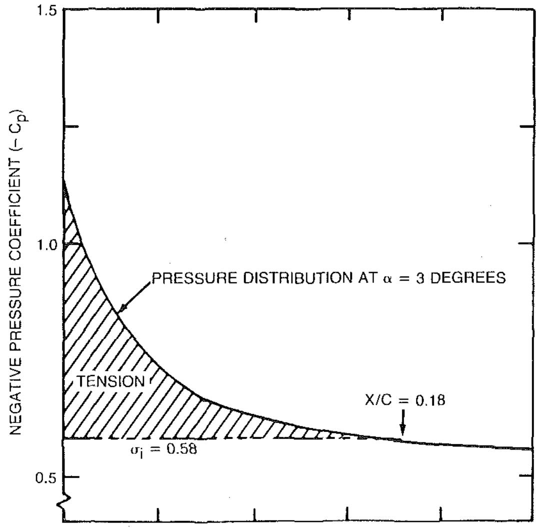

Fig. 9 Tension sustained by water at cavitation inception for $V=18.3$ m/s, $R_n=1.5\times10^6$, $\sigma_v=0.58$ and $\alpha=3$ degrees

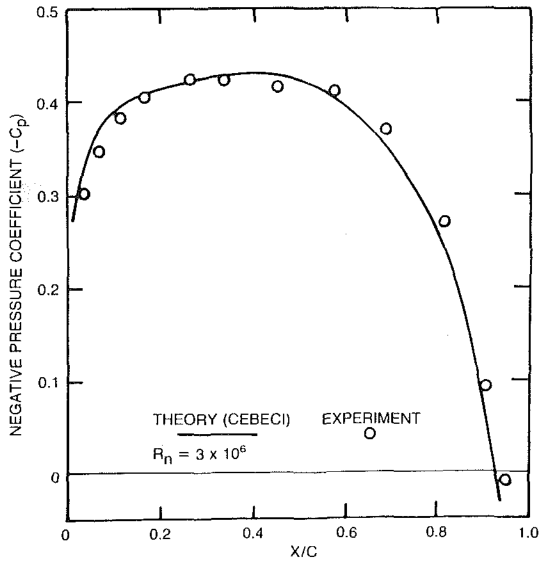

Fig. 10 Pressure distribution at $\alpha=1$ degree

at high R_n values are likely to be found in the vicinity of $-Cp_{\min}$.

Cavitation Inception Indices and $-Cp_{\min}$. At $R_n = 1.5\times10^6$ (9.15 m/s) cavitation inception occurred as midchord traveling bubbles at $\sigma_i=0.58$. As shown in Fig. 9, the water is under tension in the region between the leading edge and $x/c=0.18$. The maximum tension, occurring at the location of $-Cp_{\min}$, is estimated by $(-Cp_{\min}-\sigma_i)\cdot1/2\ \rho\ V^2=(1.35-0.58)\cdot1/2\ \rho\ V^2=3.36$ psi (23 Kpa). Knapp [11] measured the cavitation susceptibility of laboratory water by a venturi meter and found that tensile strength at the stage of cavitation inception varied from 0 to 40 psi (0 to 276 Kpa) depending on the treatment of water samples. The air content of the water in the present test program was in the range of 12 to 14 ml/l, which is close to 100 percent air saturation. This is probably why the water sustained a tension of only 3.36 psi. If the water were deaerated, a cavitation inception index of less than 0.58 would be expected at $R_n=1.5\times10^6$ [2, 16].

As R_n increased to 3.0×10^6 (18.3 m/s) cavitation inception occurred as leading edge cavities at $\sigma_i=0.74$. The numerical predictions given in Fig. 7 show no midchord bubble cavitation under this condition. At the location of $-Cp_{\min}$ the water was estimated to sustain a tension of $(1.135-0.74)\ 1/2\ \rho\ V^2=9.58$ psi (66 Pka). With the free stream nuclei entering the flow separation zone, there is ample time for bubbles to undergo explosive growth. The cavitation inception index associated with leading edge sheet cavities is thus expected to be relatively insensitive to the nuclei concentration. The measured σ_i value is expected to depend on the location of flow separation that triggers cavitation.

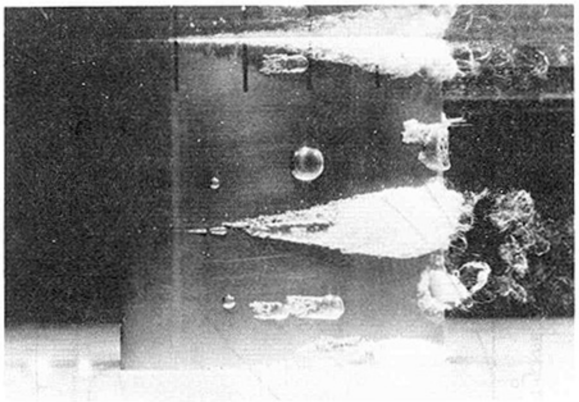

Photo 5 Midchord bubble cavitation: $\alpha=1$ deg, $V=10.67$ m/s, $R_n=1.75\times10^6$, $\sigma_v=0.31$

Increasing the R_n value reduces the boundary layer thickness. The location of cavitation inception triggered by rough spots is expected to move toward the location of $-Cp_{\min}$ as R_n is increased. This reasoning seems supported by the fact that, when a uniformly distributed artificial roughness was introduced on the foil surface around the leading edge [10], cavitation inception detected at $R_n=1.5$ and 3.0×10^6 occurred at the leading edge in the form of sheet cavities with measured σ_i values of 1.130 and 1.236, respectively. These values agree well with the $-Cp_{\min}$ of 1.135. With the introduction of artificially distributed roughness the location of rough spots to trigger cavitation is forced to occur at the location of $-Cp_{\min}$. The agreement between measured σ_i and predicted $-Cp_{\min}$ is then improved. The influence of artificial roughness on hydrodynamic loadings and cavitation will be discussed in a separate report. At very high R_n values, cavitation inception is expected to occur at the location of $-Cp_{\min}$ and the cavitation inception index is expected to be around $\sigma_i=-Cp_{\min}+\Delta\sigma$ where $\Delta\sigma$ denotes the influence of local roughness [17, 21, 28]. More studies are needed to quantify the relationship between $\Delta\sigma$ and the local roughness. In view of the significant scale effect on hydrodynamic loading, the correct $-Cp_{\min}$ values must be used to relate model data to full scale predictions.

Real-Fluid Effects on Cavitation at Foil Angle of 1 Degree

Model Cavitation Observations. The measured pressure distribution in a noncavitating condition with the foil setting at $\alpha=1$ deg is shown in Fig. 10. The shape of the pressure distribution curve resembles a rooftop and is often called rooftop-pressure distribution. The pressure distribution computed from Cebeci's viscid/inviscid interaction code is plotted in Fig. 10 for comparison with experimental measurements. The values are consistent with the previous findings at $\alpha=3$ deg in that the pressure coefficients are slightly overpredicted at the front part of the foil and underpredicted in the rear part. The predicted $-Cp_{\min}$ value is 0.43 and the measured $-Cp_{\min}$ is 0.42, the difference is only a few percent. Overall

Table 2 Computed scale effect on boundary layer developments and hydrodynamic loadings at $\alpha = 1$ deg

R_n	$x_{tru/c}$	$x_{trl/c}$	C_L	C_D	$-Cp_{\min}$
5×10^5	0.761	0.918	0.382	0.00522	0.448
1.75×10^6	0.604	0.706	0.351	0.00451	0.434
3×10^6	0.510	0.646	0.349	0.00458	0.433
3×10^7	0.112	0.254	0.348	0.00523	0.430
1×10^8	0.058	0.109	0.354	0.00483	0.432
Potential flow	-----	-----	0.390	-----	0.450

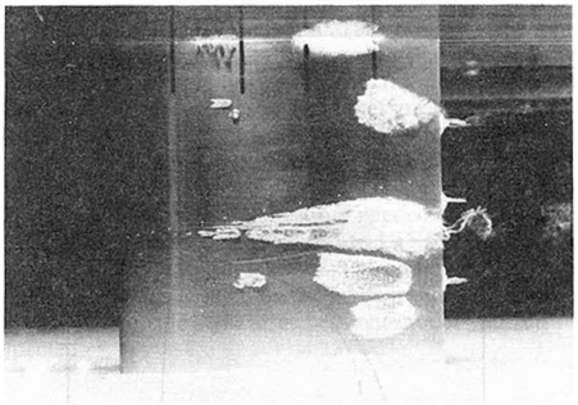

Photo 6 Midchord transient attached Cavities: $\alpha = 1$ deg, $V = 18.3$ m/s, $R_n + 3\times10^6$, $\sigma_v = 0.40$

the agreement between experimental measurements and theoretical predictions is good.

At a tunnel speed of 10.67 m/s ($R_n = 1.75\times10^6$), cavitation inception was detected at $\sigma_i = 0.38$ which is noticeably lower than the measured $-Cp_{\min}$ of 0.42. A test with more developed cavities at $\sigma_v = 0.311$ is shown in Photo 5, where three distinctive spherical bubbles are visible. The bubble dynamics theory will be used to compare the measurements taken from Photo 5.

Figure 10 shows that the local pressure around the leading edge is so much higher than the vapor pressure that there is no danger that leading edge sheet cavitation will be induced by the local surface roughness. At a tunnel speed of 18.3 m/s, cavitation inception was observed on the foil as transient attached bubbles at midchord with $\sigma_i = 0.41$ to 0.415, which is very close to the measured $-Cp_{\min}$ values of 0.42. Photo 6 shows more developed cavities at $\sigma_v = 0.40$. Distinctive spherical bubbles are rarely observed at high speeds [27] partly because of the thin boundary layer and partly because of the high shear stress. Occasionally, small spherical bubbles may appear. Photo 6 shows one distinct spherical bubble at $x/c = 0.38$.

Theoretically Computed Scale Effect on $-Cp_{\min}$ and C_L. The computed locations of natural transition, C_L, C_D, and $-Cp_{\min}$ for $\alpha = 1$ deg are given in Table 2. The boundary layer at $R_n = 5\times10^5$ is almost laminar over the whole foil surface. The computed C_L value is 0.382, which is close to the potential flow value of 0.390. The same trend is noted in $-Cp_{\min}$. As R_n increases, the surface area covered with turbulence becomes larger and the C_L value drops to 0.351 at $R_n = 1.75\times10^6$ and 0.348 at $R_n = 3\times10^7$ before it rises to 0.354 at $R_n = 1\times10^8$. The same trends in C_L and R_n are also noted when $\alpha = 3$ deg.

Within the range of $R_n = 1.75\times10^6$ to 1.0×10^8, the computed $-Cp_{\min}$ values vary only between 0.430 to 0.434. The variation is so minor that within this Reynolds number range, $-Cp_{\min}$ can be treated as a constant equal to 0.432. However, it is emphasized that the use of the potential flow value of 0.450 will overpredict $-Cp_{\min}$ by 4 percent.

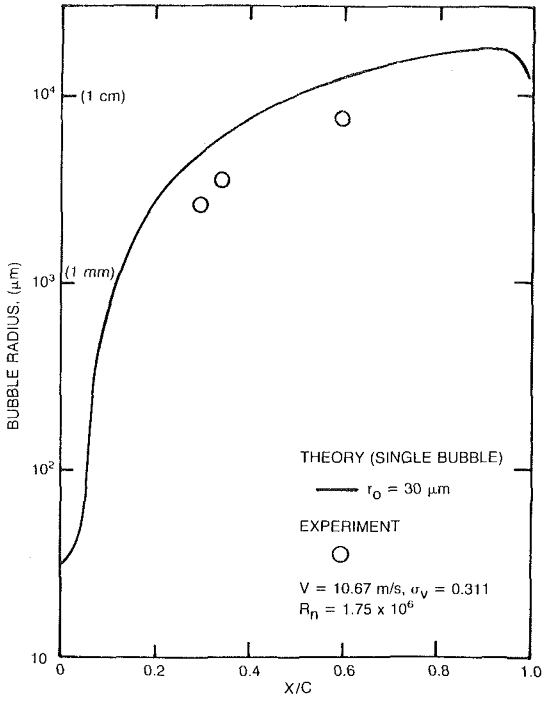

Fig. 11 Bubble radius variation during passage over the foil at $V = 10.67$ m/s, $\sigma = 0.311$ and $\alpha = 1$ degree

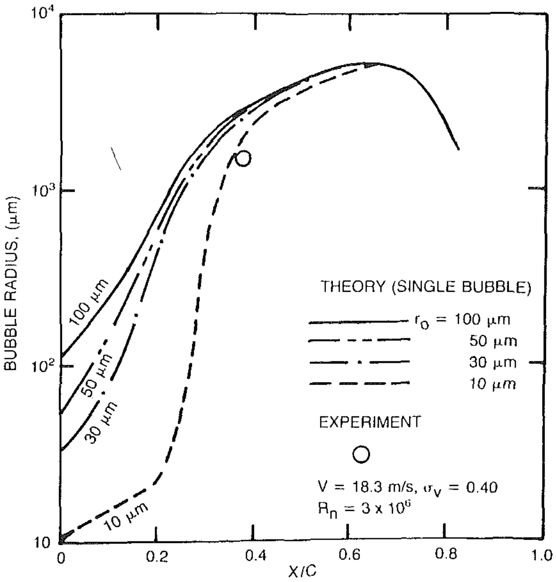

Fig. 12 Bubble radius variation during passage over the foil at $V = 18.3$ m/s, $\sigma_v = 0.40$ and $\alpha = 1$ degree

Real-Fluid Effect on Cavitation Appearance and Cavitation Inception Indices. Numerical calculations show that the presence of a foil surface retards the rate of bubble growth. The magnitude of this influence depends heavily on the vertical distances between the bubble and the foil surface. Thus, it is important to include a bubble image if the physical size of the bubble radius history is to be calculated. However, numerical calculations also show that once a nuclei becomes unstable, it grows almost exponentially. If the supply of free stream nuclei is adequate both in concentration and spatial distribution, it is expected that cavitation inception detected visually may be well predicted by a single bubble dynamic

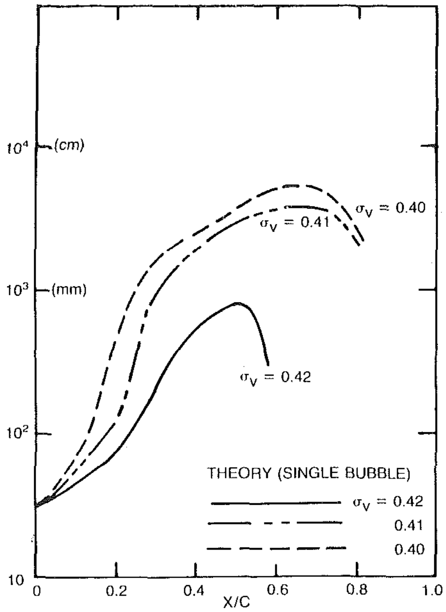

Fig. 13 Computed influence of cavitation number on bubble radius variation during the traverse through the foil at $V = 18.3$ m/s, $r_0 \approx 30\ \mu$m, $\alpha = 1$ degree

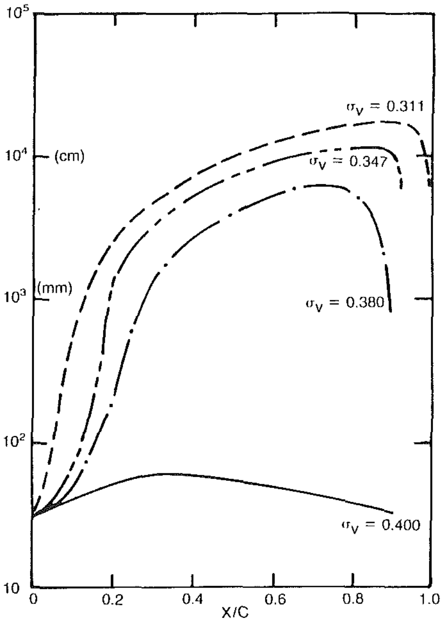

Fig. 14 Computed influence of cavitation number on bubble radius variation during the traverse through the foil at $V = 10.67$ m/s, $r_0 = 30\ \mu$m, $\alpha = 1$ degree

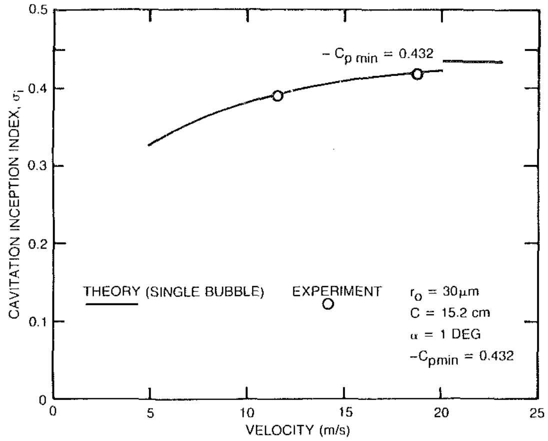

Fig. 15 Computed tunnel speed effect on midchord bubble cavitation at $\alpha = 1$ degree, $r_0 = 30\ \mu$m

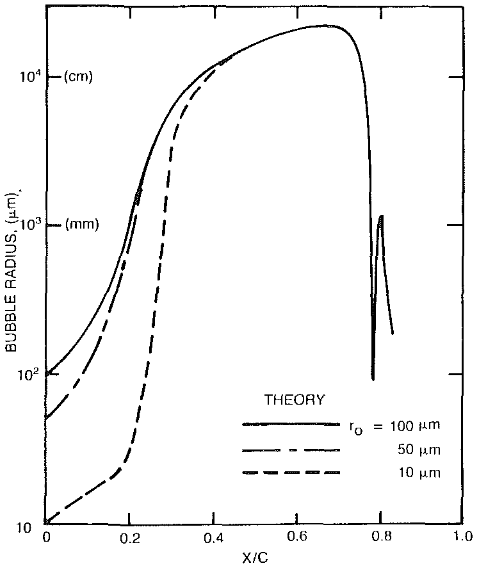

Fig. 16 Computed bubble radius variation during the traverse through a full scale foil at $V = 26.6$ m/s, $C = 1$ meter, $\sigma_v = 0.40$, $R_n = 2.9 \times 10^7$, $\alpha = 1$ degree

equation. In this section for the case of $\alpha = 1$ deg, our focus of attention is viscous and nulei effects on cavitation inception. Therefore, we only present numerical calculations based on a single bubble dynamic equation for the case of $\alpha = 1$ deg.

The bubble dynamics computer code was used to investigate bubble cavitation. In the known pressure field given in Fig. 10, the bubble radius variation during its passage over the foil is illustrated in Fig. 11 for the test condition of Photo 5 and in Fig. 12 for the test condition of Photo 6. The sizes of three distinct spherical bubbles measured from Photo 5 and of one distinct spherical bubble from Photo 6 are plotted in Figs. 11 and 12 for comparison with numerical calculations. Once again the single bubble dynamics theory consistently overpredicts the history of the bubble wall motion by 60 to 70 percent. Figure 10 clearly shows that the local pressure around the leading edge is so much higher than the vapor pressure that there is no danger of leading edge sheet cavitation to be induced by the local surface roughness even at high speeds.

The computed histories of bubble wall motion at $V = 18.3$ m/s are shown in Fig. 13 for $\sigma_v = 0.40$, 0.41, and 0.42. It is assumed that cavitation occurs when $r_{\max}$ is of the order of 1 mm, which is the lower limit of visual observation. Figure 13 indicates that midchord bubble cavitation will occur when $\sigma_i = 0.41$ to 0.42. This value is in excellent agreement with the experimentally observed value of $\sigma_i = 0.41$ to 0.415. Figure 14 shows the predicted occurrence of cavitation at a test speed of 10.67 m/s at $\sigma_i = 0.38$ to 0.40 which is in good agreement with the experimentally observed value of 0.38. The theory predicts cavitation inception to occur at $\sigma_i = 0.33$ at a test speed of 5 m/s. The computations are based on initial bubble size of 30 μm. The use of this initial bubble size to predict cavitation inception is justified by the fact that nuclei with radii greater than 50 μm are rare in water tunnels and in ocean water [2, 29, 30].

A surface tension effect on bubble cavitation is shown in Fig. 15, which illustrates the strong effect of test speed on cavitation inception index. The trend in Fig. 15 is in good agreement with the experimental work of Billet and Holl on axisymmetric bodies [21]. At high speed, as in Huang's experiments [3], the surface tension effect on bubble cavitation is small. The need to conduct the model tests at high speed to minimize the free stream nuclei effect on cavitation is clearly demonstrated in Fig. 15.

The effect of model size in cavitation will now be discussed. As a numerical example, consider a propeller blade section at the 0.7 radius with an advance coefficient J of 0.92. The relative velocity on this blade section at a ship speed of 20 knots is 26.6 m/s. Assume a chord size of 1 meter and an ambient pressure at the shaft center of 1.467 atmospheres. The corresponding cavitation number and Reynolds number in this example are 0.40 and 2.9×10^7, respectively. The computed histories of bubble wall motion for this full scale example are illustrated in Fig. 16. With the same pressure field used in the computations, the general trends of bubble growth in Figs. 12 and 16 are quite similar. At $\sigma_v = 0.4$ cavitation will be detected at both model and full scale. However, because of the length of the low pressure region, the time needed for a cavitation bubble to transverse it and grow is 5 to 10 times longer in full scale operation than in model tests. The computed $r_{\max}$ at full scale is 4 to 5 times greater than for the model. A significant difference in acoustic signatures between model and full scale is expected.

Concluding Remarks

This paper theoretically and experimentally investigated viscous and nuclei effects on hydrodynamic loading and cavitation of a NACA 66 (MOD) foil. In this paper the main discussion centered at two foil angles having different types of pressure loadings to represent a propeller operating at design and off-design conditions. At three degrees angle of attack the foil experienced a sharp suction pressure peak near the leading edge, but without leading-edge laminar boundary layer separation. At one degree angle of attack the foil experienced a roof-top type, gradually varying pressure distribution. For the present test data the computed hydrodynamic loadings from Cebeci's viscid/inviscid interactive code and the cavitation events from Chahine's multibubble interaction code were found to agree satisfactorily with the experimental measurements.

Two assumptions are commonly used in model tests of surface cavitation for full scale prediction. The first assumption states that cavitation inception occurs when the static pressure reaches the vapor pressure. On the contrary the present experiments show that the water flowing over the foil surface sustains a significant amount of tension when inception of midchord bubble cavitation as well as leading edge sheet cavitation occurs. The present results support Knapp's classic statement that the occurrence of cavitation is not measured by vapor pressure but by the tensile strength of water.

In the case of a laminar flow over the foil, cavitation appearance is of midchord bubbles. This fact is well known. The measured cavitation inception indices were well predicted by the Rayleigh-Plesset equation. Inception of bubble cavitation was delayed at low tunnel speeds. This fact calls for high test speeds to minimize the nuclei effect on bubble cavitation.

The presence of foil surface retarded the bubble growth rate. The introduction of a bubble image in dynamic calculations explained a fact that because of vertical spacing s from the foil surface, a bubble in an upstream location can become larger than a bubble observed in a downstream location as shown in Photo 2. It is important to include the image effect if the physical size of the bubble radius history is to be calculated. However, due to the fact that once a nuclei becomes unstable, it grows almost exponentially. The cavitation inception detected visually can be well predicted by the Rayleigh-Plesset equation.

Based on the present experimental and theoretical investigations the process involved in producing leading edge sheet cavities can be described as follows. The boundary layer thickness becomes thinner as the Reynolds number is increased and local flow separation can be induced by rough spots on the foil surface at high speeds. Once the flow separates, high wall pressure fluctuations have been detected at the reattachment zone. Stable free stream nuclei are known to enter the separation zone from the re-entraint jet. There will be ample time for these stable nuclei to grow. When the local pressure in the flow separation zone is in the neighborhood of the vapor pressure, the nuclei will undergo explosive growth through the mechanisms of gas diffusion and most importantly rectified diffusion from high pressure fluctuations as discussed by Strasberg [4]. An attached sheet cavity is then formed.

In the case of a rooftop-type pressure loading, flow separation can be induced by rough spots at the leading edge. However, the local pressure in this separated region is well above the vapor pressure so that only midchord bubble cavitation was detected throughout the whole test program.

In the case of a pressure loading with a strong suction peak, midchord bubble cavitation was detected at $\sigma_i = 0.58$ for a low tunnel speed of 9.15 m/s. Leading edge sheet cavitation was detected at $\sigma_i = 0.74$ for a high tunnel speed of 18.3 m/s. When artificially distributed roughness was introduced around the leading edge, cavitation inception detected at $v = 9.15$ m/s and 18.3 m/s occurred both at the leading edge of sheet cavities with σ_i respectively of 1.130 and 1.236. These values agree well with the computed $-Cp_{\min}$ value of 1.135. The measured σ_i value depends on the location of the rough spots that trigger cavitation. With the introduction of artificially distributed roughness the location of rough spots to trigger cavitation is forced to occur around the location of $-Cp_{\min}$. The agreement between the measured σ_i value and predicted $-Cp_{\min}$ value is then improved.

The second assumption states that there is no scale effect on the values of $-Cp_{\min}$. The predicted location of flow transition moves forward from the midchord to the leading edge as R_n increases. Due to the boundary layer displacement effect, the values of C_L, C_D and C_p are R_n dependent. In the case of a pressure loading with a strong suction pressure peak, the change in pressure loading takes place mostly in a very short region around the leading edge. Numerical calculations show that the values of $-Cp_{\min}$ are as much as 12 to 15 percent lower on a model ($R_n = 3\times10^6$) than at full scale ($R_n = 10^8$). However, in the case of a rooftop-type pressure loading the change in the pressure loading is distributed over the whole chord and the scale effect on the values of $-Cp_{\min}$ computed numerically is found to be small.

Acknowledgments

This work was supported by the Office of Naval Research under the Applied Hydromechanics Research Program, administered by Code 1504 of the David Taylor Research Center. The authors express their appreciation to Messrs. H. F. Gaebler, H. T. Hamaguchi and Dr. D. B. Lang of the Graduate Aeronautical Laboratories of the California Institute of Technology for their assistance in carrying out model experiments and to Dr. T. T. Huang for the benefit of his technical discussions. The authors owe thanks to Drs. T. Cebeci and G. Chahine for allowing us to use their computer codes. Finally, the authors express their appreciation to Mr. J. H. McCarthy and Dr. W. B. Morgan for their continuous technical guidance and encouragement during the course of cavitation research at DTRC.

References

1 Acosta, A. J., and Parkin, B. R., "Cavitation Inception—A Selective Review," *Journal of Ship Research*, Vol. 19, No. 4, Dec. 1975, pp. 193-205.

2 Ling, S. C., Gowing, S., and Shen, Y. T., "The Role of Microbubbles on Cavitation Inception on Head Forms," 14th Symposium on Naval Hydrodynamics, Ann Arbor, Michigan, 1982.

3 Huang, T. T., "The Effects of Turbulence Stimulators on Cavitation Inception of Axisymmetric Headforms," ASME JOURNAL OF FLUIDS ENGINEERING.

4 Kodama, Y., Tamiya, S., Take, N., and Kato, H., "The Effect of Nuclei on the Inception of Bubble and Sheet Cavitation on Axisymmetric Bodies," ASME JOURNAL OF FLUIDS ENGINEERING, Vol. 103, 1981.

5 Chahine, G. L., "Cloud Cavitation Theory," 14th Symposium on Naval Hydrodynamics, Ann Arbor, Michigan, 1982.

6 Kuiper, G., "Reflection on Cavitation Inception," ASME Cavitation and Multiphase Flow Forum, Albuquerque, New Mexico, FED—Vol. 23, June 1985.

7 Huang, T. T., and Shen, Y. T., "Application of Turbulence Stimulator to Reduce Scale Effect on Cavitation Inception," *Proceedings of the International Symposium on Propeller and Cavitation Inception*, Apr. 1986, pp. 182-189.

8 Kuiper, G., "Scale Effects on Propeller Cavitation on Propeller Cavitation Inception," 12th Symposium on Naval Hydrodynamics, Washington, DC, 1978, pp. 400-425.

9 Cebeci, T., Clark, R. W., Chang, K. C., Halsey, N. D., and Lee, K., "Airfoils with Separation and the Resulting Wakes," *Journal of Fluid Mechanics*, Vol. 163, 1986, pp. 323-347.

10 Dimotakis, P. E., Gaebler, H. F., Hamaguchi, H. T., Lang, D. B., and Shen, Y. T., "Two Dimensional NACA 66 (MOD) Hydrofoil High Speed Water Tunnel Tests," CIT Report HSWT 1142, Feb. 1988.

11 Knapp, R. T., Daily, J. W., and Hammitt, F. G., *"Cavitation,"* McGraw-Hill, 1970.

12 Plesset, M. S., "The Dynamics of Cavitation Bubbles," ASME *Journal of Applied Mechanics*, Vol. 16, 1949.

13 Shen, Y. T., Gowing, S., and Pierce, R., "Cavitation Susceptibility Measurements by Venturi," Int'l Symposium on Cavitation, ASME, New Orleans, Louisiana, Dec. 1984.

14 Shen, Y. T., and Gowing, S., "Cavitation Susceptibility of Ocean and Laboratory Waters," 21st American Towing Tank Conference, Washington, DC, Aug. 1986.

15 Arakeri, V. H., and Acosta, A. J., "Viscous Effect in the Inception of Cavitation on Axisymmetric Bodies," ASME JOURNAL OF FLUIDS ENGINEERING, Vol. 103, 1981, pp. 280-287.

16 Holl, J. W., and Carroll, J. A., "Observations of the Various Types of Limited Cavitation on Axisymmetric Bodies," ASME JOURNAL OF FLUIDS ENGINEERING, Vol. 103, 1981, pp. 415-423.

17 Huang, T. T., and Peterson, F. B., "Influence of Viscous Effects on Model Full-Scale Cavitation Scaling," *Journal of Ship Research*, Vol. 20, 1976, pp. 215-223.

18 Chahine, G. L., and Shen, Y. T., "Bubble Dynamics and Cavitation Inception in Cavitation Susceptibility Meters," ASME JOURNAL OF FLUIDS ENGINEERING, Vol. 108, 1986, pp. 444-452.

19 Blake, W. K., Wolpert, M. J., and Geib, F. E., "Cavitation Noise and Inception as Influenced by Boundary-Layer Development on a Hydrofoil," *Journal of Fluid Mechanics*, Vol. 80, 1977, pp. 617-640.

20 Klebanoff, P. S., and Tidstrom, K. D., "Mechanism by which a Two-Dimensional Roughness Element Induced Boundary Layer Transition," *The Physics of Fluids*, Vol. 13, 1972, pp. 1173-1188.

21 Billet, M. L., and Holl, J. W., "Scale Effects on Various Types of Limited Cavitation," ASME JOURNAL OF FLUIDS ENGINEERING, Vol. 103, 1981, pp. 405-414.

22 Arndt, R. E. A., Holl, J. W., Bohn, J. C., and Bechtel, W. T., "Influence of Surface Irregularities on Cavitation Performance," *Journal of Ship Research*, 1979, p. 157.

23 Parkin, B. R., "The Onset of Bubble-Ring Cavitation on Hemispherical Headforms, ASME JOURNAL OF FLUIDS ENGINEERING, Vol. 104, 1982, pp. 115-122.

24 Strasberg, M., "The Influence of Air-Filled Nuclei on Cavitation Inception," DTMB Report 1078, May 1957.

25 Ling, S. C., "On Inception of Cavitation Within a Thin Turbulent Boundary Layer," *Int'l Symposium on Cavitation Inception*, ASME, New Orleans, Louisiana, Dec. 1984.

26 Shen, Y. T., "Wing Sections for Hydrofoils—Part 3: Experimental Verifications," *Journal of Ship Research*, Vol. 29, 1985, pp. 39-50.

27 Kuiper, G., "Effects of Artificial Roughness on Sheet Cavitation," Inst. of Mechanical Engineering, Second Conference on Cavitation, Edinbourough, 1983.

28 Holl, J. W., "The Inception of Cavitation on Isolated Surface Irregularities," ASME *Journal of Basic Engineering*, Vol. 82, 1960, pp. 169-183.

29 O'Hern, T. J., Katz, J., and Acosta, A. J., "Holographic Measurements of Cavitation Nuclei in the Sea," *ASME Cavitation and Multiphase Flow Forum*, Albuquerque, New Mexico, FED—Vol. 23, June 1985.

30 Weitendorf, E. A., "Conclusions from Full-Scale and Model Investigations of the Free Air Content and of the Propeller-Excited Hull Pressure Amplitudes Due to Cavitation," *Int'l Symposium on Cavitation Inception*, New York, Dec. 1979.

R. J. Sumner

C. A. Shook

Department of Chemical Engineering,
University of Saskatchewan,
Saskatoon, SK Canada, S7N 0W0

M. C. Roco

Department of Mechanical Engineering,
University of Kentucky,
Lexington, KY 40506

Concentration Fluctuation Spectra in Turbulent Slurry Pipeline Flow

Using probes responding to changes of slurry electrical resistance with concentration, time spectra of longitudinal concentration fluctuations in turbulent slurry flows have been measured. The sensors, with an effective domain approximately 1 mm in diameter, showed the spectra to be relatively insensitive to location within the pipe cross section. High frequency spectra were found to be relatively insensitive to slurry concentration and particle diameter. Low frequency spectra showed fluctuation amplitudes which increased with solids concentration.

Introduction

In modeling pipeline flows of slurries with high solids concentrations, there is no satisfactory method for deciding a priori whether a given flow is laminar or turbulent. In contrast with single phase flows, there is no abrupt difference in the velocity dependence of flow resistance for slurries in laminar and turbulent flow. Other criteria are evidently necessary.

The effect of the presence of solid particles in a turbulent flow has been discussed frequently (see Azbel, 1983) but experimental evidence of the effect upon the turbulence is meagre. For open channel flows, inferences have often been drawn from the fact that local velocities are reduced in the region of high solids concentration (and mixture density) near the bottom of the channel (Einstein and Chien, 1955 and Lau, 1983). Since the derivative of velocity with respect to distance from the wall is thereby increased, if this change is attributed to a variation of the von Karman coefficient κ:

$$\kappa = (u_*/y)/(du/dy) \qquad (1)$$

κ values appear to decrease with the addition of solids. This change has often been denoted as a "damping" of the turbulence. For open channel flows, reductions in flow resistance have been reported to accompany this κ variation. However, alternative explanations of the distortion of the velocity distribution have been proposed (for example, Parker, 1984). Furthermore for pipeline flows, where high solids concentrations are more easily achieved than in open channels, reduced flow resistances are not observed when solids of higher density are added to the fluid. In searching for a reconciliation of these differences of interpretation of experimental results, it seems possible that the appropriate criterion involves the Richardson number:

$$\mathrm{Ri} = -g(d\rho/dy)/\rho(du/dy)^2 \qquad (2)$$

rather than the solids concentration and the particle properties as suggested by Einstein and Chien (1955). Single phase flows with $\mathrm{Ri} > 0.042$ are nonturbulent (Schlichting, 1978).

A related problem for slurry flows concerns the appropriate viscosity for use in describing the flow. If the particles are very fine and the settling velocity is low, the mixtures can be tested viscometrically and their pipeline flows are predictable with continuum models. However, with slurries of large particles, continuum models are known to be inadequate and the matter of predicting the laminar/turbulent transition point has not been resolved satisfactorily.

The present investigation was undertaken to examine the particle concentration fluctuations which arise in turbulent slurry flows. All the slurries were of the settling type, although a considerable range of settling tendency was produced by varying the density and diameter of the particles. Although other mechanisms for generating spatial inhomogeneities can be postulated, the simplest mechanism arises from the fluid turbulence itself.

Previous Work

One of the earliest experimental investigations of turbulence in slurry flows was that of Kazanski and Bruhl (1972) who used sets of sensor electrodes mounted on the pipe wall in the presence of a transverse magnetic field. Although the domain sensed by a given set of electrodes could only be defined approximately, they were able to detect velocity fluctuations in slurries. As the velocity was reduced towards deposition, low frequency (less than 1 Hz) "macroturbulent" fluctuations were detected. Concentration fluctuations accompanying these variations can often be observed visually. They have been attributed to a form of Helmholtz instability in flows where substantial concentration and velocity gradients occur. Such variations are most pronounced in slurries of particles of high settling velocity. Somewhat higher frequency fluctuations were detected in vertical flows through a conventional magnetic flux flowmeter (Peters, 1979). Fourier transforms of these signals showed frequencies of the order of 10 Hz. For disturbances travelling at the mean flow velocity at the conditions of their experiments, this suggests fluctuations with wavelengths a few multiples of the pipe diameter. These wavelengths would be much shorter than Kazanski's "macroturbulent" fluctuation. Flow disturbances arising

---

Contributed by the Fluids Engineering Division and presented at the Third International Symposium on Liquid-Solid Flows, Winter Annual Meeting, Chicago, Ill., November 27–December 2, 1988 of THE AMERICAN SOCIETY OF MECHANICAL ENGINEERS. Manuscript received by the Fluids Engineering Division March 20, 1988.

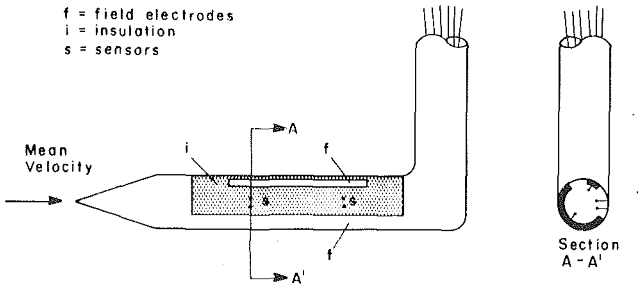

Fig. 1 L-probe used for sensing local concentration fluctuations

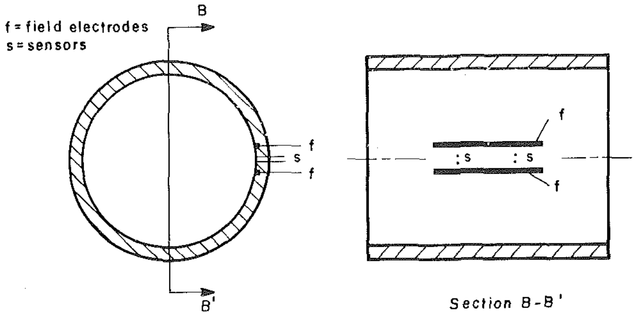

Fig. 2 Wall probe used for sensing local concentration fluctuations

from velocity field distortions by the elbow upstream of the flowmeter were suggested as a cause of the fluctuations observed by Peters. Fluctuations amplitudes increased with mean particle concentration, particle diameter and density.

Experimental Method

(i) Background. The sensors used in this investigation were of the type described by Brown et al. (1983) and Gillies et al. (1984). They employ the principle of an increase in electrical resistance arising from the presence of a dispersed nonconducting component in a conducting fluid. The relationship between volume fraction and resistance was derived by Maxwell (1892). In order to respond to high frequency fluctuations, however, it is essential to eliminate polarization of the sensor electrodes. This is achieved by displacing the sensor electrodes (s) (Fig. 1) in the direction of an applied potential gradient between the field electrodes (f) (Fig. 1). In this way the very high impedance of the circuit containing the sensor electrodes ensures that virtually no current flows in the sensor circuit, thereby minimizing polarization.

As particles move through the domain of the sensors, the local concentration fluctuates, causing the resistance and potential to fluctuate. In previous studies, cross-correlation of the fluctuations observed at the two pairs of sensor electrodes, displaced axially in the flow, has been used to determine the local particle velocity. These measurements showed that concentration fluctuations persist for the time required to travel between the sensors. With water slurries, particle retardation by friction with the probe was very small.

Because of the orientation of the sensor electrodes, it is the fluctuation in the direction of the mean flow velocity component (longitudinal direction) to which they respond.

For this device to function satisfactorily the domain of the sensors must be small enough for a variation in the local solids concentration to occur as a result of the turbulent mixing processes in the flow. The sensors used in this study were 26 gauge platinum wires imbedded in insulation (i) and flush with the surface to which the flow was parallel. They were displaced from each other by approximately 1 mm, as shown in Fig. 1. Two sets of sensors (s) were mounted 10 mm apart on the L-probe which could be traversed within the flow.

Two more sets of electrodes were mounted into the wall of the pipe (Fig. 2) so that a non-intrusive measurement could be made. The potential gradient in this case was applied through identical field electrodes (f). Of course the sizes of the field electrodes were different for the L-probe and the wall probe but the essential features were the same. The diamter of the L-probe was 4.5 mm. The field electrode displacements were similar in the wall probe and the L-probe.

An indication of the size of the domain sensed by the probe was obtained by examining the variance of concentration measurements when beds of spherical particles were allowed to settle into stationary beds around the wall probes. Using particles 3 mm and 0.3 mm in diameter, it was determined that the sensor domain was in fact of the order of the sensor electrode spacing (1 mm).

(ii) Conditions. Potential fluctuations for flowing slurries were obtained in a recirculating test loop pipeline of I.D. 50 mm. The mean in-situ concentration was fixed in each experiment by the quantity of solids added to the system and the known volume of the loop. Tests were conducted using slurries of clean silica sands with narrow size distributions and also with slurries of polystyrene beads and chips. The properties of the particles are shown in Table 1. These provided a wide range of concentration and velocity distributions within the pipe. Temperatures were maintained constant near 20°C. This is necessary since the fluid conductivity, which is a function of temperature, must be constant for concentration measurements. The wall probe was located in a long straight section of horizontal pipe well downstream (180 pipe diameters) of the inlet 90 degree elbow.

(iii) Measurement Techniques. Local time average concentrations at the sensors were determined using a 1000 Hz AC square wave source applied to the field electrodes in the man-

Nomenclature

C_r = local solids concentration (volume), also mean in-situ solids concentration
D = pipe diameter (m)
D_p = mean particle diameter (mm)
$E(n)$ = voltage potential amplitude at frequency n (V_{rms})
$F(n)$ = fraction of total power spectral density function between frequencies n and $n+dn$ (s)
g = gravitational acceleration (m/s^2)
L_x = integral length scale from the spatial correlation (m)
n = frequency (Hz)
$P(n)$ = power spectral amplitude at frequency n based on 1Ω load resistance (W)
Ri = Richardson number
u = time average local velocity (m/s)
u_* = friction velocity (m/s)
V = bulk velocity (m/s)
y = elevation above the bottom of the pipe (m)
κ = von Karman coefficient
ρ = mixture density (kg/m^3)
τ = integral time scale from the autocorrelation function (s)

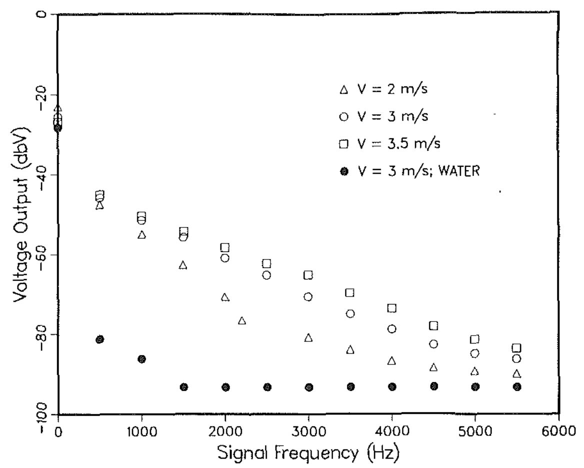

Fig. 3 Spectra obtained in a slurry of 0.19 mm sand, $C_r = 20$ percent, $y/D = 0.25$. Precision of ordinate: ±2 dbV; abscissa: ±12.5 Hz.

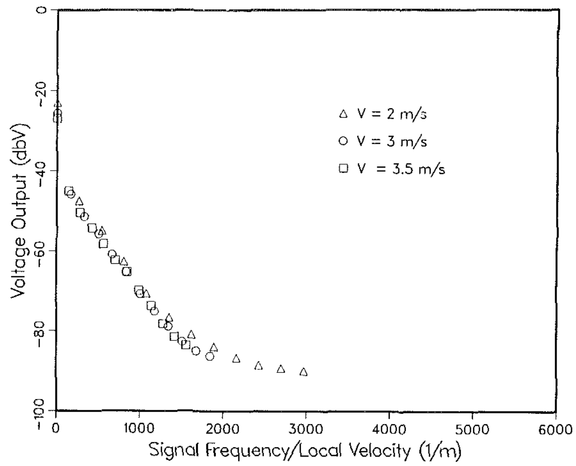

Fig. 4 Spectra of Fig. 3 expressed in terms of wave number. Precision of local velocity: ±3 percent, V: ±1 percent.

ner described by Nasr-El-Din (1987). Local particle velocities were determined with the probes. Mean flow velocities were obtained with a magnetic flux flowmeter.

The signals from the sensor electrodes were amplified before spectral analysis or correlation. The same amplifier settings were used in all the measurements reported here. Spectral analysis (Fourier transform) was performed with a digital signal analyzer (Rockland Scientific Corporation Model 5830B). Most of the spectra were recorded at two ranges: 0 to 10 kHz and 0 to 200 Hz, denoted henceforth as the high frequency and low frequency ranges. Cross-correlations for local velocity determinations were performed with the Rockland analyzer and with a Hewlett Packard 3721A Correlator.

The Rockland signal analyzer determines the power spectrum of a signal by first sampling and digitizing the time domain signal. The analyzer then performs a discrete Fourier transform to obtain the frequency domain spectrum $E(n)$. The power spectrum $P(n)$ is reported in units of logarithmic decibel volts (dBV) where:

$$\begin{aligned} \mathrm{dBV} &= 20 \log (\mathrm{E(n)}/1.0\,(\mathrm{V_{rms}})) \\ &= 10 \log (\mathrm{P(n)}/1.0\,(\mathrm{V_{rms}}^2)) \qquad (3) \end{aligned}$$

The signal analyzer simulates the operation of a bank of filters. The power spectrum is displayed in 200 filters with a bandwidth of 1 Hz for the 200 Hz frequency span and 400 filters with a 25 Hz bandwidth for the 10 KHz frequency span. The output is presented in both analog and digital form. Since the time average spectrum was of interest in this study, 64 spectra were averaged for the low frequency range, and 128 spectra were averaged for the high frequency range. This degree of averaging was found to suppress random components from an individual instantaneous spectrum to give a stable and reproducible average power spectrum. The standard deviation of the mean power spectrum data points ranged between 0.5 and 1.2 dBV.

In addition to the spectral and the cross-correlations for particle velocity, the analyzer can perform autocorrelations of the potential fluctuations. These can be used to determine the integral length scale of the flow L_x, by assuming the concentration fluctuations are convected with the local particle velocity.

Table 1 Properties of particles

Material	Density (kg/m^3)	Dp (microns)
Sand	2650	190
		400
		900
Polystyrene	1050	300
		1400

Experimental Results

(i) Experiments With Sand. Figure 3 displays the spectra obtained in the lower half of the pipe ($y/D = 0.25$) in a slurry of fine sand. The zero frequency amplitudes are a measure of the fraction of the total applied potential which occurs between the sensors, in a time average sense. This depends upon the time average concentration at the point as well as the mean concentration between the field electrodes and the amount of polarization of the latter. Since the mean concentration for the whole pipe is fixed, differences in bulk velocity between runs will cause the local concentration to vary. These will produce differences in the zero frequency components. Because the mean local concentrations were measured by another method it was not necessary to infer concentration from the zero frequency amplitudes.

In Fig. 3 we note that for the water, the amplitude of the potential fluctuation quickly falls to the limit of resolution for the particular settings of the instrument (−95 dBV). The water results show the magnitude of electrode polarization and noise effects from instrumentation. For the slurries, at all three velocities the amplitudes decrease continuously with increasing frequency. If the concentration fluctuations are carried with the local time averaged velocity, the appropriate independt variable should be the wave number (n/u) as in the case of turbulent velocity fluctuation spectra (Taylor. 1938). Figure 4 shows the data plotted in this way. The fact that individual spectra can be collapsed to a single curve suggests that the sensor response is satisfactory for this frequency range.

For the fine sand used in these tests, local velocities could be determined with good precision at all three mean velocities. When coarse particles were used, these produced slurries which were highly stratified. In this case local velocities were more difficult to determine precisely, and the corresponding diagrams showed somewhat more scatter.

Because some change in local concentration occurs when the bulk velocity is varied in the pipeline loop, it was desirable to investigate the effect of the mean concentration on spectra in a systematic way. Figure 5 shows that the effect of mean concentration is small but significant for the fine sand. At this position ($y/D = 0.25$) local concentrations were somewhat greater than the mean values, but considerable variation in local concentration between runs occurred in these tests. The effect of particle size is shown in Fig. 6, together with the results obtained with water. For the sand slurries in Fig. 6 there is some difference in local concentration. However,

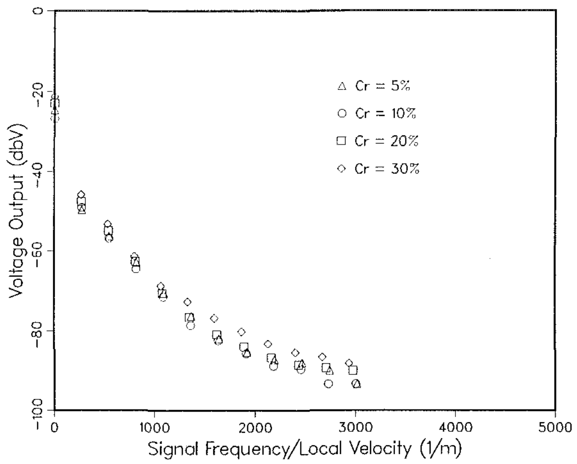

Fig. 5 Effect of mean concentration (C_r) on spectra observed with 0.19mm sand, $V = 2$ m/s, $y/D = 0.25$. Range 0-10 kHz. Precision of ordinate ±2 dbV; local velocity: ±3 percent, C_r: ±1 percent (absolute).

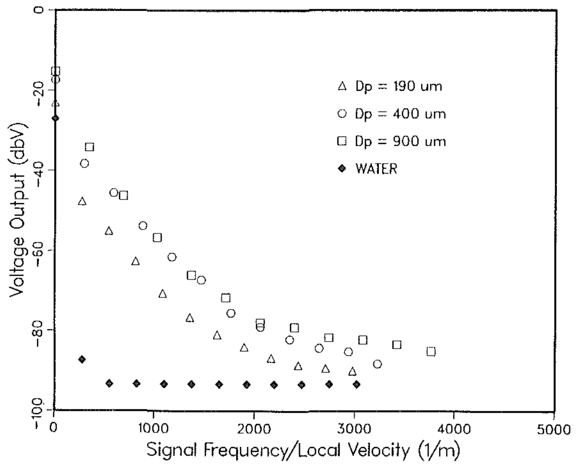

Fig. 6 Effect of particle size (D_p) on spectra observed with sand slurries, $V = 2$ m/s, $C_v = 18$-20 percent, $y/D = 0.25$. Range 0-10 kHz. Precision of ordinate: ±2 dbV, local velocity ±5 percent.

bearing Fig. 5 in mind, their effect upon the spectra should be small. We therefore conclude that the amplitude of concentration fluctuations increases only slightly with particle size in this frequency range.

On physical grounds, it seems unlikely that very fine particles would display substantial concentration fluctuations in turbulent flow. First, the domain of the sensors would always contain large numbers of particles. Furthermore, concentration fluctuations would be difficult to generate because of the inertia of the particles relative to the fluid. Similarly, very large and dense particles would resist displacement by all but the largest and most intense fluid velocity fluctuations. We conclude that the range of particle sizes in Fig. 6, which covers most settling slurries of industrial importance, lies in the intermediate category where fluid turbulence plays an important role.

If we assume these fluctuations arise from fluid turbulence, the high wave number range corresponds to the energy dissipation region. Velocity fluctuation spectra in turbulent single-phase pipe flows have somewhat different shapes (Laufer, 1955) but also show steeply decreasing amplitudes at high wave numbers. Although the energy dissipation rates are much higher in coarse particle slurries than in fine particle ones, mechanistic models since Newitt et al. (1955) have assumed that the higher friction is due to Coulomb friction between particles and the pipe wall. This hypothesis is consistent with the spectra considered so far. The fact that there is little difference between these concentration fluctuation spectra suggests that the dissipation process in the fluid is insensitive to the presence of the particles. We observe that no damping of the high frequency fluctuations by the solid particles seems to occur in this concentration range. It should also be noted that the differences in particle size, concentration and mean velocity between experiments produced profoundly different values of the derivative of time average velocity u with respect to position in these experiments. The fine sand slurries had a fairly uniform concentration distribution and a more nearly symmetrical velocity distribution. Figure 7 shows results typical of the two larger sands.

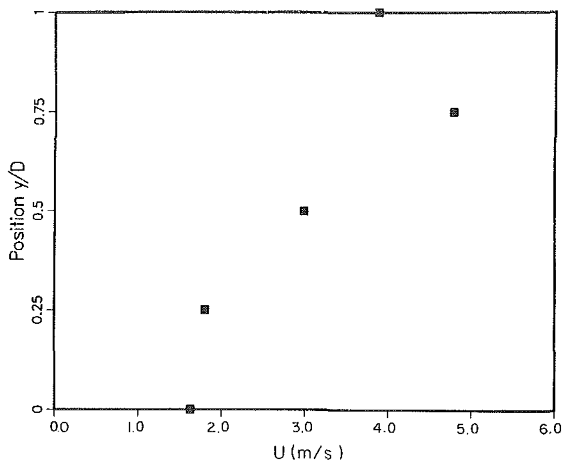

Fig. 7(a) Velocity distribution on the vertical axis for a slurry of 0.9 mm sand. $C_r = 30$ percent, $v = 3$ m/s. Precision of measurement 3 percent.

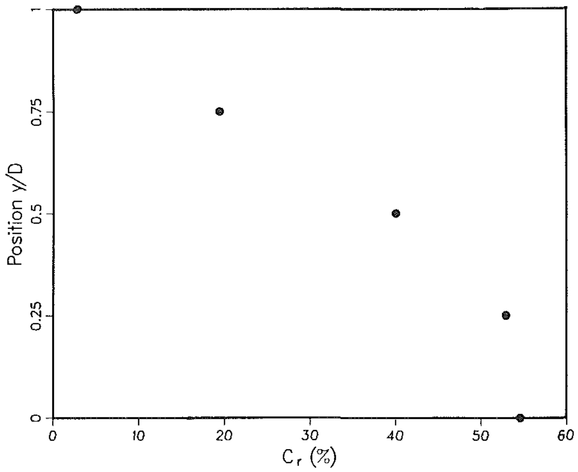

Fig. 7(b) Concentration distribution on the vertical axis for the slurry of Fig. 7(a). Precision of measurement 2 percent (absolute).

Integrated concentration and velocity distributions for these sands have shown good agreement with the known mean values. Evidently these differences between slurries do not produce significant changes in the high wave number portion of the spectrum.

The low frequency portion of the fluid velocity spectrum in single phase flows, obtained by previous workers, does not show the sharp decline with wave number which characterizes the dissipation region. The eddies which produce low frequency fluctuations are larger, with longer lifetimes than those in the dissipation region. It was therefore of interest to investigate the low frequency region separately.

Figure 8 shows slurry concentration spectra obtained with a range of 0-200 Hz using the coarse sand. The measurements were taken at $y/D = 0.25$, 0.75 and at the top and bottom of

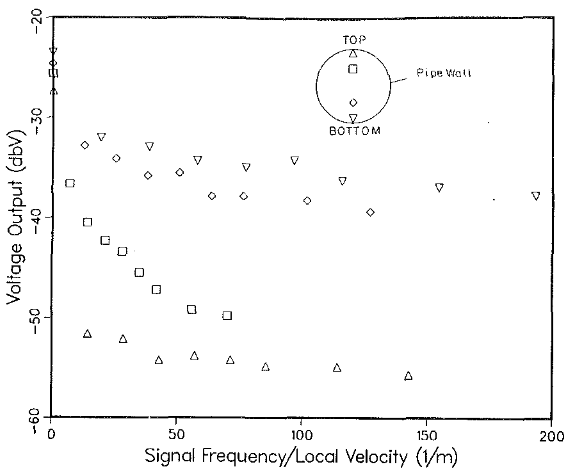

Fig. 8 0-200 Hz spectra observed with 0.9 mm sand, $V = 2$ m/s, $C_r = 30$ percent. Precision of ordinate ±2 dbV; velocity; ±5 percent.

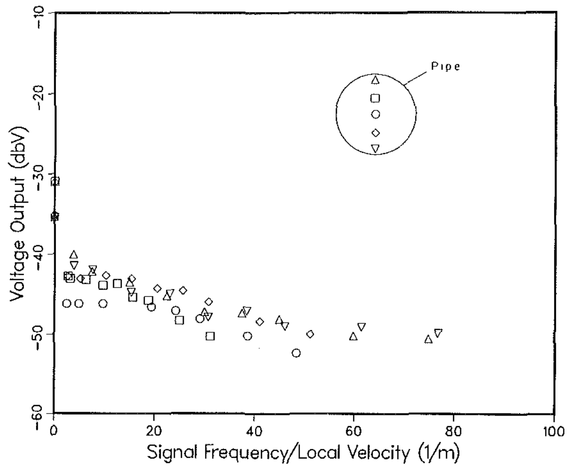

Fig. 9 0-200 Hz spectra observed with 0.3 mm polystyrene slurries, $V = 3.5$ m/s, $C_r = 35$ percent. Precision of ordinate ±2 dbV; velocity ±3 percent.

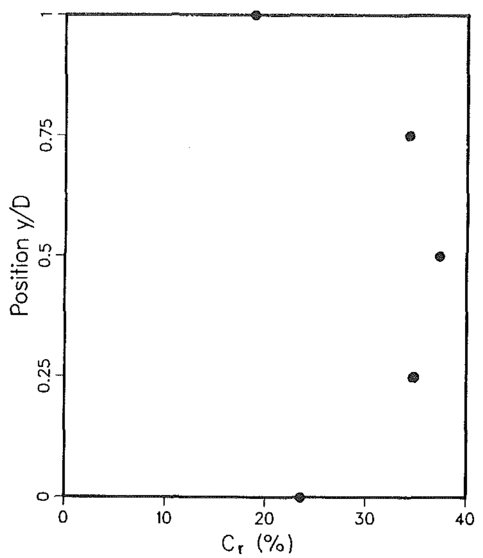

Fig. 10(*a*) Concentration distribution on the vertical axis for a slurry of 1.4 mm polystyrene chips. $C_r = 30$ percent, $V = 3$ m/s. Precision of measurement 2 percent (absolute).

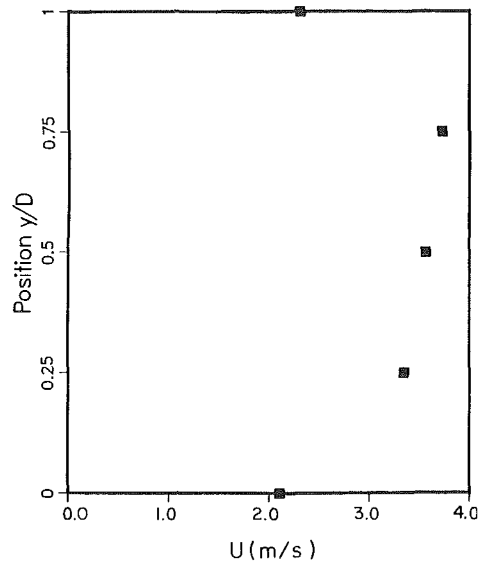

Fig. 10(*b*) Velocity distribution on the vertical axis for the slurry of Fig. 10(*a*). Precision of measurement 3 percent.

the pipe as shown in the insert legend. Figure 7 shows that local concentrations decrease considerably with height for this slurry and evidently the amplitude of the fluctuations decreases correspondingly. In contrast with the high frequency spectra, these measurements show an increase in the amplitude of the concentration fluctuations with solids concentration. We cannot interpret these differences until we can determine whether the difference is due to the presence of high solids concentrations or to an effect produced by high concentrations with this particular slurry. Such an effect could be differences in average shear rates (*du*/*dy*) which result from the increased density in the high concentration regions of this slurry.

(ii) Experiments With Plastic Particles. To simplify the situation we therefore examined the effect of solids concentration using slurries of nearly neutrally buoyant (density 1050 kg/m^3) polystyrene particles of diameter 1.4 mm and 0.3 mm. These slurries would not have high time average shear rates and their Richardson numbers would exclude any possibility of laminarization. The high frequency spectra of these slurries were similar to those shown previously for sands.

Low frequency region spectra are shown in Fig. 9 in the range 0-200 Hz, for a 35 percent slurry of fine polystyrene particles. There is little concentration variation over the cross-section in this case and there is little difference between the spectra obtained at the five positions in the pipe. It seems that the concentration fluctuations have similar amplitudes at all positions although the velocities sensed by the wall probe were only 70 percent of the mean values. At concentrations of 10 and 50 percent by volume the spectra were similar to those of Fig. 9 but about 10 dBV lower in amplitude. For slurries in this range of concentrations, therefore, any damping of low frequency concentration fluctuations by the particles is minor.

This evidence suggests that the difference shown in Fig. 8 is *not simply a concentration effect*. Because the particles used in obtaining Fig. 8 were considerably coarser than those employed in Fig. 9, a further investigation was conducted using 1.4 mm polystyrene particles. Concentration and velocity distributions for these slurries are shown in Fig. 10. These are of course profoundly different from those of Fig. 7. Concentration distributions with nearly neutrally-buoyant particles show the effect of the "dispersive stress" in slurries, first detected by Bagnold, 1954. For the sand slurries this stress is small in comparison with the immersed weight effect.

The low frequency spectra obtained with the coarse polystyrene particles are shown in Fig. 11. The amplitudes are somewhat higher than those observed with the fine particles.

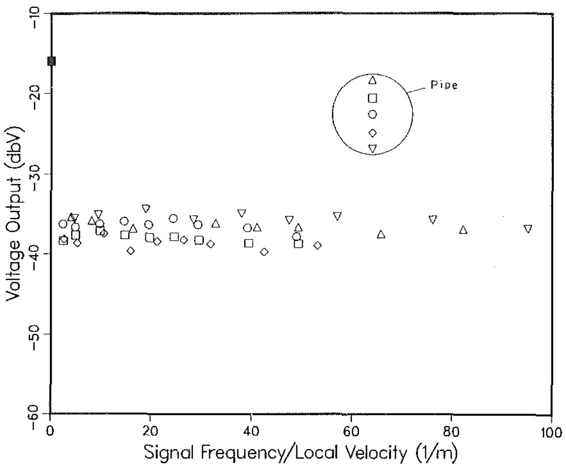

Fig. 11 0-200 Hz spectra observed with 1.4 mm polystyrene slurries, $V = 3.5$ m/s, $C_r = 34$ percent. Precision of ordinate ±2 dbV; velocity ±3 percent.

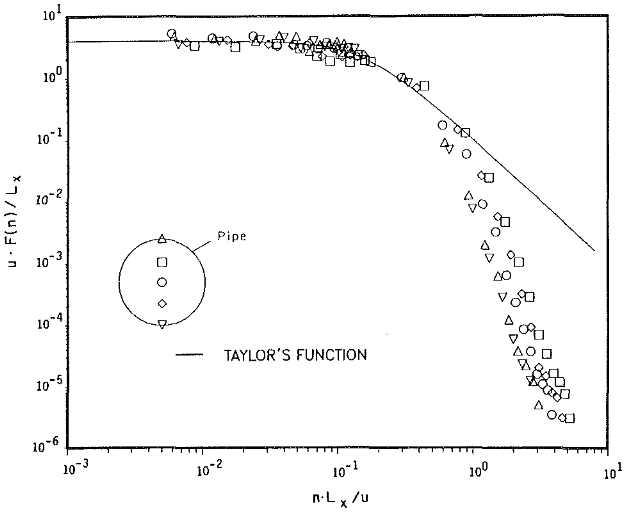

Fig. 12 Comparison of low frequency and high frequency spectra (coarse polystyrene) with Taylor's function for isotropic turbulence

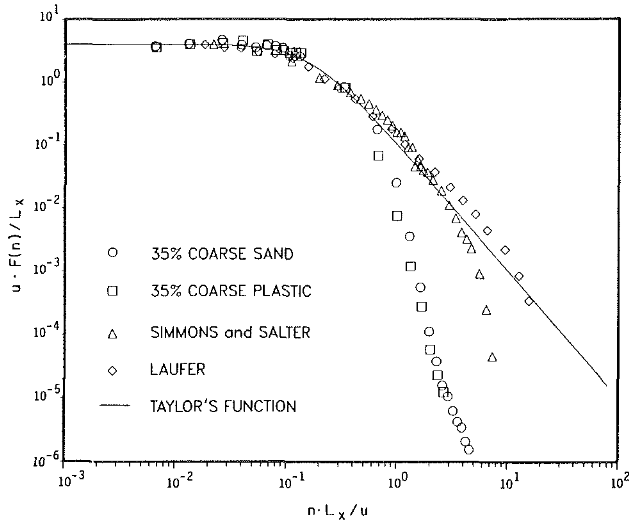

Fig. 13 Comparison of spectra observed at the bottom of the pipe with wind tunnel and pipe velocity fluctuation spectra

There was also a tendency for the amplitude to increase with concentration, as for the finer particles. The experiments conducted with the low density particles therefore suggest that the effect shown in Fig. 8 is not a particle size or concentration effect. Instead, the variation in low frequency amplitude appears to be related to a flow parameter such as density gradient or time average shear rate.

(iii) Comparison With Velocity Fluctuation Spectra of Other Researchers. A common method of presenting power spectra for velocity fluctuations is in terms of the function $F(n)$ which represents the normalized distribution of energy with respect to frequency.

$$\int_0^\infty F(n)dn = 1 \qquad (4)$$

The power spectra of this study were converted to $F(n)$ by dividing $P(n)$ by the bandwidth of the filter to give power spectral density (PSD). Using numerical integration, the area under the PSD curve was determined. The PSD amplitudes were divided by this area to give the $F(n)$ function.

In Taylor's (1938) plot, $F(n)$ is presented in terms of the dimensionless groups $F(n)/\tau$ or $uF(n)/L_x$ and n/τ or nL_x/u. τ is the integral time scale, while L_x is integral length scale and u is the time averaged local velocity. In the present study L_x was determined by integrating the area under the autocorrelation function obtained with the spectral analyzer in a separate set of experiments. Typical length scales were of the order of 0.002 m. There was no consistent trend of these with mean velocity or particle properties.

Figure 12 shows the dimensionless spectra of a 35 percent slurry of 1.4 mm polystyrene particles compared to Taylor's function. The portion of the spectra corresponding to the low frequency fluctuations appears to follow Taylor's function quite closely but at higher frequencies the spectra deviate significantly. The deviation appears to be greatest at the walls.

The power spectra measured at the bottom of the pipe ($y/D = 0$) with 0.9 mm sand and 1.4 mm polystyrene slurries are compared with Taylor's function and the velocity fluctuation results obtained by Simmons and Salter (1938) in a wind tunnel 2 m downstream of a 73 cm grid in Fig. 13. Laufer's (1955) pipe turbulence data obtained at the axis of the pipe have also been converted to a form which allows the comparison.

Since the frequency response of the probes is not known, we cannot reject the possibility that the systematic deviation in the high frequency region (above 500 H_z) may be in part an experimental artifact. Since these particles have dimensions comparable to the sensor domain, it is likely that the high frequency fluctuations represent variations in the distance between individual particles. Thus it is also reasonable to infer that these data show the diminishing ability of the small, high frequency eddies to perturb large particles.

Although there was a systematic variation of concentration fluctuation amplitude, none of the experimental conditions produced complete damping, even at the pipe wall and at very high solids concentrations. We observe, however, that high values of the gradients of velocity and concentration tend to occur together. In none of the experiments did the Richardson number exceed 0.042.

Conclusions

1 Concentration fluctuations persist in slurry flows to very high solids concentrations.

2 The fluctuation spectra in turbulent slurry flows are insensitive to particle concentration, particle diameter or particle density in the high frequency region.

3 Low frequency spectra show significant concentration and particle diameter effects. Except for fine particles at high concentrations, the amplitudes increase with increasing concentration.

4 Spectra observed at the pipe wall were similar to those measured within the flow.
5 Normalized concentration spectra resemble turbulent velocity fluctuation results obtained by other workers in homogeneous fluids, in the low frequency region.

References

1 Azbel, D., and Liapis, A. I., *Handbook of Fluids in Motion*, N. P. Cheremisinoff and R. Gupta, (eds.), Ann Arbor Sci, Ann Arbor Michigan, 1983, pp. 915-925.

2 Bagnold, R. A., "Experiments on a Gravity-Free Dispersion of Large Solid Spheres in a Newtonian Fluid Under Shear," *Proc. Roy. Soc.* (A), Vol. 225, 1954, pp. 49-63.

3 Brown, N. P., et al., "A Probe For Point Velocities in Slurry Flows," *Can. J. Chem. Eng.*, Vol. 61, No. 4, Aug. 1983, pp. 597-601.

4 Einstein, H. A., and Chien, N., "Effects of Heavy Sediment Concentration Near the Bed on Velocity and Sediment Distribution," Univ. of California Inst. of Eng. Research, M. S. D. Sediment Series No. 8, 1955.

5 Gillies, R. G., Husband, W. H. W., Small, M., and Shook, C. A., "Some Experimental Methods for Coarse Coal Slurries," *Proc. 9th Int. Conf. on Hyd. Transport of Solids in Pipes*, BHRA Fluid Engineering, Cranfield, U. K., Paper A2, 1984, pp. 33-46.

6 Kazanski, I., and Bruhl, H., "The Influence of Highly Concentrated Rigid Particles on the Macroturbulent Characteristics in Pipe Flow," *Proc. 2nd Int. Conf. on the Hydraulic Transport of Solids in Pipes*, BHRA Fluid Engineering, Cranfield, U. K., Paper A2, 1972, 2.15-2.30.

7 Lau, Y. L., "Suspended Sediment Effect in Flow Resistance," *J. Hyd. Div.*, A.S.C.E., Vol. 109, No. 5, May 1983, pp. 757-763.

8 Laufer, J., "The Structure of Turbulence in Fully Developed Pipe Flow," N.A.C.A., Report 1174, 1955, Report 1174.

9 Maxwell, J. C., A Treatise on Electricity and Magnetism, 3rd Ed., Clarendon Press, Oxford, 1892, pp. 440-441.

10 Nasr-El-Din, H., Shook, C. A., and Colwell, J., "A Conductivity Probe for Measuring Local Concentrations in Slurry Systems," *Int. J. Multiphase Flow*, Vol. 13, No. 13, No. 3, May/June 1987, pp. 365-378.

11 Newitt, D. M., et al., "Hydraulic Conveying of Solids in Horizontal Pipes," *Trans. Inst. Chem. Engrs.*, Vol. 33, 1955, pp. 93-113.

12 Parker, G., and Coleman, N. L., "Simple Model of Sediment Laden Flows," *J. Hyd. Div.*, A.S.C.E., Vol. 112, No. 5, May 1986, pp. 356-375.

13 Peters, J., and Shook, C. A., "Electromagnetic Sensing of Slurry Concentration," *Can. J. Chem. Eng.*, Vol. 59, No. 4, Aug. 1981, pp. 430-437.

14 Schlichting, H., *Boundary Layer Theory*, 7th Ed., Chapter 17, McGraw-Hill, New York, 1978, p. 513.

15 Shook, C. A., "Experiments with Concentrated Suspensions of Particles with Density Slightly Greater Than the Carrier Fluid," *Can. J. Chem. Eng.*, Vol. 63, No. 6, Dec. 1985, pp 861-869.

16 Simmons, L. F. G., and Salter, C., "An Experimental Determination of the Spectrum of Turbulence," *Proc. Roy. Soc.*, Series A, Vol. 165, 1938, pp. 73-89.

17 Taylor, G. I., "The Spectrum of Turbulence," *Proc. Roy. Soc.*, Series A, Vol. 164, 1938, pp. 477-490.

A Portable Slurry Wear Test for the Field

B. W. Madsen
Bureau of Mines,
U.S. Department of the Interior,
Albany, OR 97321-2198

A new portable slurry wear test apparatus developed by the Bureau of Mines, U.S. Department of the Interior, makes it possible to gather materials wear and corrosion data at a mineral processing site. The portable wear cell is identical in design to a laboratory cell reported previously. It allows simultaneous evaluation of 16 specimens in a continuous flow of fresh slurry. Data obtained from selected metals and polymers showed high-chromium white cast irons to perform particularly well in tests with an aqueous lead-zinc sulfide ore slurry. However, ultra-high-molecular-weight polyethylene that exhibited superior wear resistance in comparable laboratory tests with an aqueous slurry of silica sand did not perform as well in field tests. Such results show how misleading it can be to use laboratory data to predict relative rates of wear in industrial slurries, even under nominally identical flow conditions. Field testing is therefore needed. In situ electrochemical corrosion measurements on a low-alloy steel showed that the field and laboratory slurries were similarly corrosive.

Introduction

The Bureau of Mines is conducting research aimed at reducing the wear and corrosion of mining and mineral processing equipment. Moving minerals in a slurry is an efficient means of transporting them and is used in many mineral processing operations. However, the movement of such slurries can cause significant erosion and corrosion. Erosion is caused by the solid particles striking a container, and corrosion can occur if the liquid reacts chemically with the container. Several studies have been made of erosion-corrosion phenomena (Jackson, 1974; Hoey et al., 1975; Liu and Hoey, 1975; Bass, 1977; Hocke and Wilkinson, 1978; Lebedev et al., 1980; Elkholy, 1983; Moroz, 1983; Singleton and Blickensderfer, 1985), using a variety of experimental methods (Postlethwaite et al., 1974; Postlethwaite, 1981; Tsai et al., 1981; Pitt and Chang, 1985, 1986a, b; Spencer and Sagues, 1987). However, few quantitative measurements have been made in industrial environments. The present author developed a flow-through laboratory apparatus (Madsen, 1985, 1987a; Madsen and Blickensderfer, 1987) that yields constant rates of wear because worn particles are not recycled. This apparatus also permits corrosion measurements to be made during erosion. Such measurements have demonstrated that large synergistic effects can develop between erosion and corrosion (Madsen, 1987b, 1988).

The present study extends the author's work to an industrial mineral processing environment. For this purpose a portable version of the slurry wear apparatus was constructed. The erosion and corrosion of 17 metals and 3 polymers were compared under nominally identical flow conditions in slurries of complex sulfides in mill water and of silica sand in tap water. The new apparatus can be tapped into an industrial slurry flow and left to run for long periods of time. This makes it possible to test at the low velocities of flow (1 to 5 m•s^{-1}) often encountered in industrial situations.

Apparatus, Materials, and Procedures

Apparatus. The portable slurry wear test apparatus consists of the cell shown in Figs. 1 and 2 plus a pump, a motor

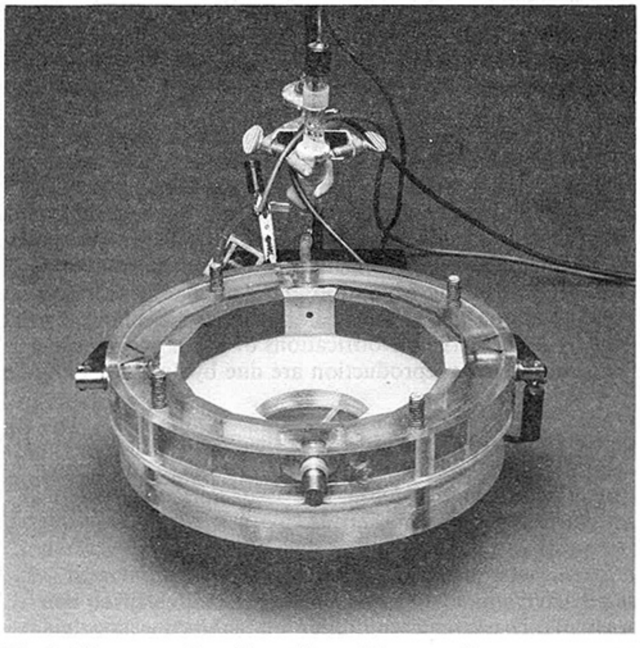

Fig. 1 The wear cell configured for making corrosion measurements

---

Contributed by the Fluids Engineering Division and presented at the Winter Annual Meeting, Chicago, Ill., November 27–December 1, 1988 of THE AMERICAN SOCIETY OF MECHANICAL ENGINEERS. Manuscript received by the Fluids Engineering Division January 4, 1989.

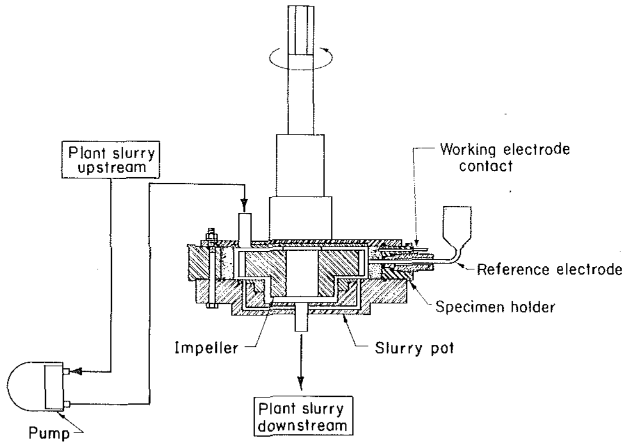

Fig. 2 Schematic diagram of the wear cell

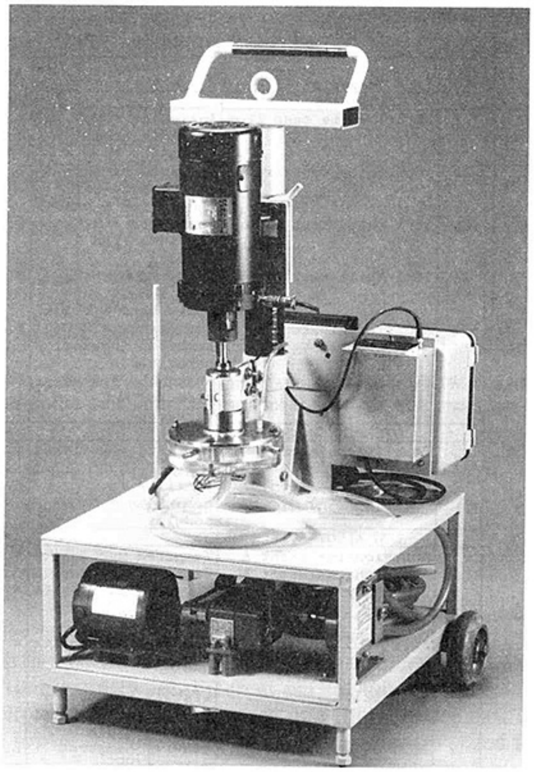

Fig. 3 Portable slurry wear test apparatus

to drive the impeller, a speed controller and velocity indicator, a pH meter, a thermometer, and a strip chart recorder, all mounted on a portable cart as shown in Fig. 3. This cart is equipped with leveling bolts and a lifting eye. To permit electrochemical testing, a potentiostat-galvanostat (EG&G Princeton Applied Research Model 273[1]) and an IBM[1] compatible microcomputer equipped with a National Instruments IEEE-248[1] interface board are also provided. Together, these control the potential applied to the working electrode and measure the resulting current through it. Both the voltage and current are recorded in digital form on magnetic discs for later processing. The potentiostat and the computer are compact and readily portable to facilitate setting up experiments in field environments. The strip chart recorder provides a continuous record of temperature and pH.

Figure 1 shows the wear cell in the configuration used when making corrosion measurements. This cell is common to both the portable and the laboratory versions of the apparatus. During both wear and corrosion testing an impeller moves a continuous stream of fresh slurry past 16 specimens set into the rim. The slurry enters the cell at its perimeter from the top and exits via four radial channels and a central hole in the bottom, Fig. 2. Each specimen is a 10-mm thick plate beveled to fit its neighbors and has a wear surface of 6.66 cm^2 (23.8 mm × 28 mm). Each of the 16 specimens can be a different material. Metal specimens are coated on their nonwearing surfaces with an insulating layer of nylon. Figure 1 also shows the saturated calomel electrode (SCE) used as the reference electrode in the corrosion studies and the Luggin probe connecting it to the slurry through the center of the specimen serving as the working electrode. The cross-sectional area of the Luggin probe is 0.12 cm^2, leaving the area of the working electrode as 6.54 cm^2. The two specimens serving as counter electrodes and their connections are also visible in the photograph. A514 type B steel was chosen for these electrodes because it is a freely corroding material that allows an electric current to pass with little or no resistance. Although some iron enters the slurry when these electrodes are anodically polarized, the high rate of flow of the slurry minimizes the concentration that can accumulate. The remaining 13 spaces are filled with nonconducting polymeric spacers.

Materials

Specimens. Table 1 summarizes the phase and chemical compositions of all the metals used in the tests. Also included are their Brinell harnesses, as measured using a load of 3×10^4 N. Six of the 17 metals tested (Nos. 1, 2a–c, 3, and 4) were white cast irons. These ranged in Cr content from 2 to 20 wt pct. They were variously heat-treated to produce different distributions of carbides in austenitic and/or variously tempered martensitic matrices. Two other cast irons (Nos. 5 and 6) contained no Cr. The alloys containing Cr consisted of flakes of graphite in a pearlitic matrix and those containing no Cr consisted of graphite nodules in a matrix containing both pearlite and cementite. The other six metals (Nos. 7–12) were low alloy steels that were heat-treated to produce variously tempered martensites. In one case (No. 10) the alloy contained a dispersion of fine carbide particles. The final three metals were two high Cr-content austenitic stainless steels (Nos. 13 and 14) and an age-hardened Al alloy (No. 15).

Table 2 lists the some of the properties of the three polymers used. These were a high-density, extra-high-molecular-weight polyethylene (HDPE, No. 16), an ultra-high-molecular-weight polyethylene (UHMWPE, No. 17), and a chlorinated polyvinyl chloride (No. 18).

Nomenclature

A = ampere
K = degree Kelvin
g = gram
h = hour
L = liter
mA = milliampere
min = minute
mL = milliliter
mm = millimeter
mm^3 = cubic millimeter
mV = millivolt
μm = micrometer
μS = microsiemen
pct = percent
s = second
Ω = ohm

---

[1] Reference to a specific product does not imply endorsement by the Bureau of Mines.

Table 1 Phase and chemical compositions and Brinell hardness of the alloys tested

No.	Material	Phase Composition	HB[1], Gpa	Density, g/cm^3	Composition, wt pct								Heat Treatment
					C	Cr	Ni	Mn	Si	Mo	Cu	Al	
	WHITE CAST IRONS												
1	20-2-1 White cast iron	Austenite + M_7C_3 carbides (rod & blade)	6.82	7.76	2.8	20.0	1.00	0.7	0.70	2.0	ND	ND	1285 K, 8h; AC; 815 K, 4h; AC
2a	18-1 White cast iron	Tempered martensite + M_7C_3 carbides (rod & blade)	7.45	7.68	3.43	17.6	0.34	0.86	0.21	1.07	ND	ND	1285 K, 4h; AC; 785 K, 12 h; AC
2b	18-1 White cast iron	Austenite + M_7C_3 carbides (rod & blade)	5.08	7.75	3.43	17.6	0.34	0.86	0.21	1.07	ND	ND	As cast
2c	18-1 White cast iron	Tempered martensite + M_7C_3 carbides (rod & blade)	5.38	7.68	3.43	17.6	0.34	0.86	0.21	1.07	ND	ND	920 K, 12h; AC;
3	Modified NiHard 4	Martensite + M_7C_3 carbides (coarse, dendritic)	5.82	7.72	3.7	9.42	5.31	2.01	1.12	0.66	ND	ND	1050 K, 6h; AC
4	NiHard 1	Austenite + fine globular M_7C_3 carbides	6.53	7.78	3.16	1.36	3.70	0.56	0.25	0.04	ND	ND	720 K, 4h; AC; 550 K, 4h; AC
	OTHER CAST IRONS												
5	Pearlitic high-C cast iron	Pearlite + C flakes	4.40	7.45	3.1	ND	ND	0.70	0.60	ND	ND	ND	1310 K, 2h; WQ
6	Nodular cast iron, 0.45 S	Pearlite + cementite + C nodules	2.85	7.23	2.85	ND	0.4	0.2	1.2	0.1	ND	ND	As cast
	LOW ALLOY STEELS												
7	Abrasion-resistant A	Tempered martensite	4.76	7.84	0.33	0.98	0.14	0.61	0.38	0.20	0.16	0.03	Proprietary
8	Abrasion-resistant B	Tempered martensite	5.34	7.86	0.31	1.84	0.26	0.99	1.64	0.37	ND	ND	Proprietary
9	Low-alloy experimental	Tempered martensite	4.61	7.89	0.23	2.0	0.24	0.45	0.05	0.06	0.29	0.06	1175 K, 1h; WQ; 370 K, 1h; AC
10	AISI 1095	Tempered martensite	4.44	7.86	1.07	<0.1	<0.1	0.30	0.20	<0.1	<0.04	0.04	1175 K, 1h; WC; 370 K, 1h; AC
11	AISI 52100	Lightly tempered martensite + fine M_7C_3 carbides	6.70	7.84	1.05	1.39	0.13	0.34	0.26	<.1	0.12	<0.02	1130 K, 1h; OQ; 370 K, 1h; AC
12	ASTM A514 type B	Heavily tempered martensite	2.69	7.84	0.19	0.50	0.10	0.90	0.30	0.10	0.02	0.03	As received
	OTHER ALLOYS												
13	316 Stainless steel, wrought	Austenite	1.40	8.03	0.04	17.2	12.4	1.6	0.40	2.3	ND	ND	As received
14	Mn-N Stainless steel, (NP599), forged	Austenite	2.29	7.91	0.09	16.4	2.16	8.71	0.41	0.21	0.31	ND	AC from 1470 K
15	6061 - T651 Al alloy (1 Mg)	Al solid solution + Mg_2Si precipitate	0.92	2.67	ND	0.20	ND	ND	0.6	ND	0.28	>97	SHT & aged

[1] HB- Brinell hardness with load of 3×10^4 N (3000 kg force)

ND - Not determined; FC - Furnace cooled; AC - Air cooled; WQ - Water quenched; OQ - Oil quenched; SHT - solution heat-treated

Table 2 Properties of the polymers studied

Property	HDPE (No. 16)	UHMWPE (No. 17)	CPVC (No. 18)
Chemical formula	$(CH_2)n$	$(CH_2)n$	$(CH_2\ CHCl)n$
Molecular weight	330,000	$3 \times 10^6 - 5 \times 10^6$	-----
Density, g/cm3	0.933	0.923	1.67
Shore D hardness	63	67	85
Tensile strength at yield, MPa	23	24	45-48*
Ultimate tensile strength, MPa	31	39	55
Young's modulus, MPa	827	760	2480
Flexural modulus, MPa	965	900*	2860
Elongation at yield, pct	5-10*	25	1-5*
Elongation to failure, pct	800	470	2-40*
Fracture toughness, MPa m ½	2-5*	1-2*	2-4*

*Data generic to the class of polymer.

Specimens of both classes of materials were prepared by abrading on dry SiC papers down to 400 grit (38 μm), cleaning ultrasonically in water containing a standard laboratory detergent, and rinsing successively in water and ethanol. They were then dryed in a hot air stream and weighed to the nearest 0.1 mg. Specimens were used several times without re-preparing their surfaces. Previous work (Madsen 1985; 1987a, b; Madsen and Blickensderfer, 1987) has shown that small changes in surface topography do not affect their rates of wear. Corrosion measurements were made only on A514 type B steel specimens. These were prepared in the same fashion as the wear test specimens, except that a hole was drilled in the center of each to provide access for the Luggin probe.

Slurries

The industrial slurry came from a grinding-flotation mill in the Cascade Mountains near Lyons, OR. The particles were smaller than 600 μm and contained chlorite and other clays, calcite and other carbonates, quartz, ferromagnesian silicates, sphalerite, galena, chalcopyrite, pyrite, hematite, and organic matter. The clays accounted for one-third to one-half of the total mass, the harder quartz and ferromagnesian silicates for about one quarter, and the sulfides for about 10 to 20 pct. More than half of the total mass was in the minus 325-mesh size fraction, and less than 1 percent was coarser than 50 mesh. The pH varied between 7.36 and 7.8 and the specific conductance was $\sim 65\ \mu S \bullet m - ^1$. The solids content of the slurry varied no more than 1 wt pct during any one test. Between tests, however, this parameter varied from 19 to 25 wt pct. In general, the particles in this slurry exhibited sharper edges and corners and a more angular shape than did the silica sand particles in the laboratory slurry. This latter slurry consisted of 2 wt pct of 212- to 300-μm (minus 50- to plus 70-mesh) American Foundryman's Society (AFS) silica sand in tap water.

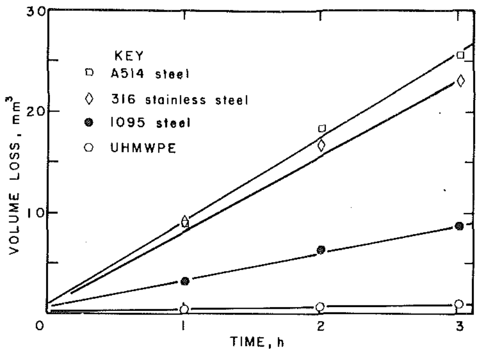

Fig. 4 Typical data from a laboratory wear test conducted at 294 K using an impeller tip speed of 12 $\text{m}\cdot\text{s}^{-1}$. The slurry was 2 wt pct AFS silica sand in tap water.

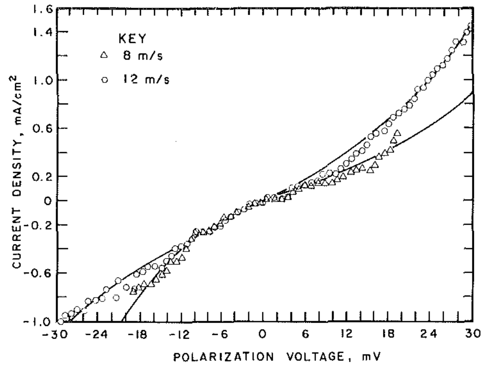

Fig. 5 Anodic and cathodic polarization curves for A514 type B steel exposed to the field slurry at impeller tip speeds of 8 and 12 $\text{m}\cdot\text{s}^{-1}$

When making electrochemical corrosion measurements in the laboratory slurry, 0.06*M* Na_2SO_4 was used instead of tap water. The specific conductance was thereby raised to ~50 $\mu\text{S}\cdot\text{m}^{-1}$, reducing the drop in potential through the slurry. Previous work (Madsen, 1987b) has shown that the use of this low concentration of sodium sulfate does not affect wear rates.

Procedures

Wear Testing. Both the field and the laboratory tests were conducted at 294 K at a flow rate of 4500 $\text{mL}\cdot\text{min}^{-1}$. This rate was controlled by the slurry feed pump and was independent of the motion of the impeller. At this flow rate the retention time of the slurry in the wear cell was ~2 s. In both environments, tests were conducted at impeller tip speeds of 8 $\text{m}\cdot\text{s}^{-1}$ and 12 $\text{m}\cdot\text{s}^{-1}$. Field test A lasted for 208 min and used the lower speed and a slurry containing 25 wt pct solids. Field test B, which used a slurry containing 19 wt pct of solids, was run for 98 min at the higher speed. All laboratory tests lasted for 3 h and were interrupted at 1 h intervals to monitor mass loss. Before reweighing, worn laboratory test specimens were cleaned and dried in the same fashion as they were initially. The worn field test specimens were dried at the test site with a paper towel. They were then returned to the laboratory for cleaning, drying, and weighing according to the standard protocol. Wear rates were expressed conventionally as volume loss per unit time. This was calculated for the field tests as the ratio of total volume loss to test time, and for the laboratory tests as the slope of a plot of volume loss versus test time. This slope was determined by linear regression. Two or three A514 type B steel specimens were included in each test to provide an indication of experimental scatter.

Corrosion Testing

Polarization scans were made in both field and laboratory slurries. The field slurry contained 15 wt pct of solids and the laboratory slurry 2 wt pct. Impeller tip speeds ranged from 4 to 14 $\text{m}\cdot\text{s}^{-1}$. The scanning rate was always 1 $\text{mV}\cdot\text{s}^{-1}$ and the range of potential scanned was from about −30 mV to +30 mV relative to the open circuit corrosion potential (E_c). At each current density ($j = I/A$, where I is the current and A the area of the working electrode), the polarization voltage ϕ was calculated from the measured voltage by subtracting the product IR. R is the resistance of the path through the solution between the reference and working electrodes. Previous work (Madsen, 1987a, b) has shown it to remain constant at ~1 Ω over the narrow range of potential involved. The corrosion current (I_c) and current density ($j_c = I_c/A$) at the corrosion potential (i.e., when $\phi = 0$) were then calculated by using nonlinear regression (Mansfeld, 1973; Gerchakov et al., 1981; Rocchini, 1987; Madsen, 1988) to fit the polarization data to the equation

$$I = I_c\,[\exp(2.303\,\phi/B_a) - \exp(-2.303\,\phi/B_c)], \qquad (1)$$

where B_a and B_c are the anodic and cathodic Tafel slopes, respectively.

Results

Wear. The results of the field tests are summarized in Table 3, with the specimens ranked according to increasing wear rate. Note that a somewhat different partial suite of materials was used at each impeller tip speed, and that a white cast iron is at the top of the list. Increasing the impeller tip speed from 8 to 12 $\text{m}\cdot\text{s}^{-1}$ and the solids content of the slurry from 19 to 25 wt pct increased the rates of wear of the polymers by a factor of 2 to 4X. A514 type B steel was the only metal field-tested at both speeds, and for this material the increase in speed and solids content resulted in a 3.7-fold increase in wear rate.

Figure 4 shows typical data obtained in laboratory tests conducted at 12 $\text{m}\cdot\text{s}^{-1}$. Note the linearity of the data for each material. Table 3 presents wear rates obtained for the full complement of 20 materials from experiments conducted at impeller tip speeds of 8 and 12 $\text{m}\cdot\text{s}^{-1}$ in laboratory slurries which did not contain sodium sulphate. Where more than one specimen of any given material was tested, the wear rate is quoted as the mean plus and minus one standard deviation. Note that raising the impeller tip speed from 8 to 12 $\text{m}\cdot\text{s}^{-1}$ increases the wear rates of the polymers by 2 to 4X and those of the metals by 4 to 9X. As a result, the change in impeller tip speed changes the ranking of the test materials. Note also the excellent performance of ultra-high molecular weight polyethylene at both speeds.

Corrosion. Figure 5 shows the experimental data obtained from the polarization scans and the curves fitted to these via equation (1). Average values of B_a and B_c were 68 and 66 mV per decade of current in the field tests and 54 and 100 mV per decade of current in the laboratory tests, respectively. Table 4 summarizes the corresponding values of E_c and corrosion rate. The latter values were obtained by using Faraday's law to convert j_c to units of $\text{mm}^3\cdot\text{h}^{-1}$ as described in the Discussion section. Note that increasing the impeller tip speed shifts E_c to a more negative value in both slurries, that E_c is slightly more negative in the field test slurry than in the laboratory slurry at low impeller tip speeds, and that the corrosion rate does not vary much at impeller tip speeds greater than 4 $\text{m}\cdot\text{s}^{-1}$.

Discussion

The results reported in Table 3 exhibit two striking features. The first is the order of magnitude higher wear rate exhibited by the polymers in the field tests than in the laboratory tests. The percentage increase is comparable for all three polymers at both 8 and 12 $\text{m}\cdot\text{s}^{-1}$, although the lower speed field test was conducted in a significantly less dense slurry than was the

Table 3 Wear rates measured in field and laboratory tests

No.	Material	Wear rate, $\mathrm{mm^3 \cdot h^{-1}}$ Field Test A, 25 wt pct solids, $8\ \mathrm{m \cdot s^{-1}}$	Laboratory tests @ 2 wt pct solids $8\ \mathrm{m \cdot s^{-1}}$	$12\ \mathrm{m \cdot s^{-1}}$
2b	18-1 White cast iron	0.33	0.17	0.70
2a	18-1 White cast iron	0.56	0.14	0.85
4	NiHard 1	0.79	0.35	1.36
2c	18-1 White cast iron	0.82	0.22	0.89
14	Mn-N Stainless steel	0.95	1.67	7.82
9	Low-alloy experimental steel	1.01	1.33	5.39
7	Abrasion resistant steel A	1.10	1.00	4.07
17	UHMWPE	1.11	0.07 ± 0.07	0.18 ± 0.12
12	A514 type B steel	1.73 ± 0.03	1.93 ± 0.19	8.44 ± 0.46
6	Nodular cast iron	1.84	1.58	6.64
16	HDPE	2.63	0.30 ± 0.11	1.01 ± 0.25
18	CPVC	12.0	1.66 ± 0.45	6.56 ± 1.90
		Field Test B, 19 wt pct solids, $12\ \mathrm{m \cdot s^{-1}}$		
1	20-2-1 White cast iron	1.39	0.08	0.75
3	Modified NiHard 4	1.97	0.11	0.98
17	UHMWPE	2.63	0.07 ± 0.07	0.18 ± 0.12
11	AISI 52100 steel	2.98	0.36	2.21
10	AISI 1095 steel	3.40	0.53	2.68
8	Abrasion resistant steel B	4.11	0.60	3.58
5	Pearlitic high C cast iron	4.36	0.43	2.74
13	316 Stainless steel	5.55	1.30	6.96
12	A514 type B steel	6.44 ± 0.28	1.46 ± 0.06	8.40 ± 0.55
16	HDPE	8.56	0.30 ± 0.11	1.01 ± 0.25
15	6061-T651 Al	32.8	6.44	31.31
18	CPVC	47.4	1.66 ± 0.45	6.56 ± 1.90

Table 4 Corrosion potentials and rates for A514 type B steel as function of slurry type and impeller tip speed. Values given for E_c are within 1 mV unless otherwise stated.

Impeller tip speed, $\mathrm{m \cdot s^{-1}}$	E_c, mV vs SCE		Corrosion rate, $\mathrm{mm^3 \cdot h^{-1}}$	
	Field slurry	Laboratory slurry	Field slurry	Laboratory slurry
0*	< -600	< -600	ND	0.053 ± 0.037
4	−494	−470	<0.148	0.282 ± 0.093
8	−494	−475	0.218 ± 0.121	0.138 ± 0.065
12	−515	−492	0.208 ± 0.040	0.130 ± 0.014
14	−515	−515	0.211 ± 0.062	0.212 ± 0.003
16	ND	−525	ND	0.155 ± 0.050

ND Not determined

*With slurry feed pump and impeller shut off. The value of E_c drifted under these conditions between −600 and −630 mV versus SCE.

higher speed field test. Evidently, the wear rates of the polymers are not markedly dependent on solids content in such dense slurries. In contrast to the polymers, the metals exhibited smaller and less consistent changes in wear rate in response to the same change in slurry. Those high-chromium, high-carbon content materials containing large volume fractions of carbide particles—the white cast irons, NiHard I and modified NiHard 4—wore about twice as fast in the field tests as in the laboratory tests at both 8 and 12 $\mathrm{m \cdot s^{-1}}$. In contrast, both the high-chromium, low-carbon, austenitic materials (316 stainless steel and the Mn-N stainless steel) and the low-chromium cast irons and steels showed less variation in wear rate with change in slurry. Indeed, both A514 type B steel and the low-alloy experimental steel exhibited less wear in the field test slurry than in the laboratory slurry when tested at 8 $\mathrm{m \cdot s^{-1}}$. 316 stainless steel did the same when tested at 12 $\mathrm{m \cdot s^{-1}}$. The 6061-T 651 Al alloy also showed little change of wear rate with slurry type.

The polymers do not corrode in either the field or the laboratory tests. Therefore, their order-of-magnitude-higher wear rate in the former suggests that the two kinds of slurry particles lead to different mechanisms of erosion. Examination of the eroded surfaces revealed the presence of fine shavings on the surfaces of the polymeric specimens used in the field tests. This suggests that the more angular particles present in the field slurry cause more micromachining (type II cutting) and less plowing and/or type I cutting than do the rounder AFS sand particles (Finnie, 1958; Hutchings, 1979).

From Faraday's law, the density of A514 type B steel ($7.86 \times 10^3\ \mathrm{kg \cdot m^{-3}}$), and the area (A) of the working electrode (6.54 $\mathrm{cm^2}$), it follows that a corrosion current density of 1 $\mathrm{mA \cdot cm^{-2}}$ is equivalent to a volume loss rate of 0.86 $\mathrm{mm^3 \cdot h^{-1}}$. In all of the present experiments the oxygen content of the slurry was close to the solubility limit of $\sim 9 \times 10^{-6}\ \mathrm{g \cdot g^{-1}}$ (Dean, 1973). At the chosen flow rate of 4500 $\mathrm{mL \cdot min^{-1}}$ this is enough to sustain a corrosion current density of ~1270 $\mathrm{mA \cdot cm^{-2}}$ (~1090 $\mathrm{mm^3 \cdot h^{-1}}$). Thus the measured corrosion rates reported in Table 4 suggest that ≤0.02 percent of the available oxygen was ever consumed.

The lack of any systematic variation of corrosion rate with increase in impeller tip speed above 4 $\mathrm{m \cdot s^{-1}}$ suggests that in both slurries the corrosion reaction is under activation control (Fontana and Greene, 1978). In contrast, the rate of corrosion of A514 type B steel in stationary, near-neutral aqueous solutions is cathodically controlled by the rate of diffusion of oxygen to the corroding surface (Fontana and Greene, 1978). The observation that E_c never shifts far enough in the positive direction for passivation to occur (Wranglen, 1985) is also consistent with the suggestion that the present reaction is under

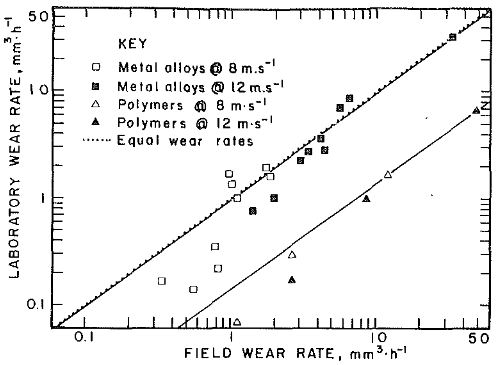

Fig. 6 Comparison of the wear rates measured in the field and laboratory tests

activation control. However, it is not clear why E_c becomes more negative at the highest impeller tip speeds. Perhaps erosion-induced surface roughening increases either the anodic and/or the cathodic exchange current density, leading to reduced activation polarization of either or both electrode processes (Fontana and Greene, 1978). Alternatively, the shift may have a hydrodynamic origin, perhaps related to increased turbulence at higher impeller tip speeds.

Comparison of the appropriate data from Tables 3 and 4 also suggests that, in the case of A514 type B steel, corrosion accounted for no more than 10 percent of the volume loss measured in either slurry at an impeller tip speed of 8 m$\cdot$s^{-1} and for only 2-3 percent of that measured at 12 m$\cdot$s^{-1}. However, previous cathodic protection studies carried out in the laboratory slurry (Madsen, 1987b) show that passing a positive current through the slurry from the counter electrodes to the working electrode reduces the wear rate. For example, passing a positive current of density ≥ 25 mA$\cdot$cm^{-2} reduces the rate of wear of A514 type B steel from 28 to 19 mm$^3\cdot$h^{-1} at an impeller tip speed of 15.6 m$\cdot$s^{-1}. Thus corrosion appears to have a much bigger effect on erosion than does erosion on corrosion.

The mechanism(s) responsible for this synergism is (are) as yet far from clear. Nevertheless, the results obtained to date do lead to two conclusions. First, similar values of the corrosion rates were measured in slurries containing insulating quartz sand particles and slurries containing semiconducting sulfide ore particles. This shows that the net effect of any galvanic corrosion processes occurring during contact of slurry particles with the working electrode is small. Second, 0.06M Na$_2$SO$_4$ does not affect wear rates (Madsen, 1987b). This shows that any precipitation of iron sulfate at or near the surface of the working electrode is likewise unimportant.

To end on a more practical note, attention is drawn to the plot of wear rates in the laboratory tests (y) versus wear rates in the field tests (x) presented in Fig. 6. The dotted line represents equal rates of wear in the two tests ($y = x$) and the two solid lines were drawn by using the least squares technique to fit separate equations of the form $y = ax$ to the data obtained from the metallic and polymeric specimens. It is clear that there is a better correlation between the two rates at the higher impeller tip speed. Figure 6 also emphasizes the much greater variation of wear rate with slurry type exhibited by the polymers as compared to the metals: the line fitted to the data obtained from the polymers lies much farther from the dotted line than does the line fitted to the data obtained from the metals.

Conclusions

Field testing remains a necessary part of the reliable selection of materials to resist the combined effects of slurry erosion and corrosion. The advantage of the present, portable apparatus is that it permits the erosive and corrosive effects of industrial slurries to be determined at the flow velocities of greatest interest under reproducible flow conditions. This is done without having to transport large quantities of such slurries to a distant laboratory. The disadvantage is that the test does not, in general, duplicate the flow conditions characteristic of the industrial application. For this reason it may fail to predict correctly the relative service lives of different materials. However, since the actual slurry of interest is used, the predictions made are likely to be better than those obtained in tests with a substitute slurry.

Acknowledgments

The author wishes to thank his colleagues for their support and encouragement. He gives special thanks to Darrell P. Hoskins, physical science technician, for his sustained efforts in conducting the slurry wear tests. He is also grateful to the owners and operators of the Shiny Rock Mining Company, in particular George Atiyeh and Joe Webber, for the use of their grinding-flotation mill facilities near Lyons, OR.

References

Bass, M. L., 1977, "Erosion-Corrosion of Cast Pump Alloys," presented at Pacific Northwest Metals and Minerals Conf., Seattle, WA. 24 pp. Available from BuMines, Albany Research Center, 1450 Queen Avenue SW, Albany, OR 97321, USA.

Dean, J. A. (ed.)., 1973, *Lange's Handbook of Chemistry*, 11th Edition, McGraw-Hill, New York, NY, pp. 10-7.

Elkholy, A., 1983, "Prediction of Abrasion Wear for Slurry Pump Materials," *Wear*, Vol. 84, pp. 39-49.

Finnie, I., 1958, "The Mechanism of Erosion of Ductile Metals," *Proc. 3rd U.S. National Congress of Applied Mechanics*, ed. by R. M. Haythornthwaite, ASME, New York, NY, pp. 527-532.

Fontana, M. G., and Greene, N. D., 1978, *Corrosion Engineering*, McGraw-Hill, New York, NY.

Gerchakov, S. L., Udey, L. R., and Mansfeld, F., 1981, "An Improved Method for Analysis of Polarization Resistance Data," *Corrosion*, Vol. 37, p. 696.

Hocke, H., and Wilkinson, H. N., 1978, "Testing Abrasion Resistance of Slurry Pipeline Materials," *Tribology Int.*, Vol. 5, pp. 289-294.

Hoey, G. R., Dingley, W., and Freeman, C., 1975, "Corrosion Inhibitors Reduce Ball Wear in Grinding Sulfide Ore," *CIM Bull.*, Vol. 68, pp. 120-123.

Hutchings, I. M., 1979, "Mechanisms of the Erosion of Metals by Solids Particles," *Erosion: Prevention and Useful Applications*, ASTM STP 664, ed. by W. F. Adler, ASTM, Philadelphia, PA, pp. 59-76.

Jackson, L. D. A., 1974, "Controlling Abrasion in Slo (sic) Slurry Pipeline Systems," *Can. Min. J.*, Vol. 95, pp. 42-45.

Lebedev, A. N., Shchyerbakov, O. B., and Balashov, G. V., 1980, "Corrosive and Erosive Wear of Steel in Ore Milling Equipment," *Zashch. Met.*, Vol. 16, pp. 327-330.

Liu, A. W., and Hoey, G. R., 1975, "Mechanisms of Corrosive Wear of Steel Balls in Grinding Hematite Ore," *Can. Met. Quart.*, Vol. 14, pp. 281-285.

Madsen, B. W., 1985, "A Study of Parameters Using a New Constant-Wear-Rate Slurry Test," *Wear of Materials 1985*, ed. by K. C. Ludema, ASME, New York, NY, pp. 345-354.

Madsen, B. W., 1987a, "Measurement of Wear and Corrosion Rates Using a Novel Slurry Wear Test Apparatus," *Materials Performance*, Vol. 26, No. 1, pp. 21-28.

Madsen, B. W., 1987b, "Measurement of Erosion-Corrosion Synergism With a Slurry Wear Test Apparatus," *Wear of Materials*, 1987, ed. by R. C. Ludema, ASME, New York, NY, pp. 777-786.

Madsen, B. W., 1988, "Synergism Between Electrochemical Corrosion and Slurry Wear," *Proc. 43rd NACE Annual Conf.*, NACE, Houston, TX, Vol. 3, pp. 242/1-242/15.

Madsen, B. W., and Blickensderfer, R., 1987, "A New Flow-Through Slurry Erosion Wear Test," *Slurry Erosion: Uses, Applications, and Test Methods*, ASTM STP 946, ed. by J. E. Miller and F. E. Schmidt, Jr., ASTM, Philadelphia, PA, pp. 169-184.

Mansfeld, F., 1973, "Tafel Slopes and Corrosion Rates From Polarization Resistance Measurements," *Corrosion*, Vol. 29, p. 397.

Moroz, P., 1983, "Wear Mechanisms in Steel and White Iron Grinding Balls in Wet Ore Grinding Applications," presented at Post Deadline Session, Int. Conf. on Wear of Materials, Reston, VA.

Pitt, C. H., and Chang, Y. M., 1985, "Electrochemical Determination of Erosive Wear of High Carbon Steel Grinding Balls," *Min. and Met. Proc.*, Vol. 2, pp. 166-173.

Pitt, C. H., and Chang, Y. M., 1986a, "Corrosive-Erosive Wear of Grinding Ball Metals at High Jet Velocities," *Proc. 41st NACE Annual Conf.*, NACE, Houston, TX, Vol. 3, pp. 232/1-232/15.

Pitt, C. H., and Chang, Y. M., 1986b, "Jet Slurry Corrosive Wear of High-Chromium Cast Iron and High-Carbon Steel Grinding Ball Alloys," *Corrosion*, Vol. 42, pp. 312.

Postlethwaite, J., 1981, "Direct Measurement of the Corrosion Current for Oxygen-Reduction Corrosion," *Electrochemical Corrosion Testing*, ASTM STP 727, ed. by F. Mansfeld and U. Bertocci, ASTM, Philadelphia, PA, pp. 290-302.

Postlethwaite, J., Tinker, E. B., and Hawrylak, M. W., 1974, "Erosion-Corrosion in Slurry Pipelines," *Corrosion*, Vol. 30, pp. 285-290.

Rocchini, G., 1987, "A Computerized Tool for Corrosion Rate Monitoring," *Corrosion*, Vol. 43, p. 326.

Singleton, D. J., and Blickensderfer, R., 1985, "Wear and Corrosion of 12 Alloys During Laboratory Milling of Phosphate Rock in Phosphoric Acid Waste Water," RI 8919, U.S. Bureau of Mines, Washington, DC.

Spencer, D. K., and Sagues, A. A., 1987, "Erosion by Sand and Coal Slurries," *Corrosion-Erosion Wear of Materials at Elevated Temperatures*, ed. by A. V. Levy, NACE, Houston, TX, pp. 367-385.

Tsai, W., Humphrey, J. A. C., Cornet, I., and Levy, A. L., 1981, "Experimental Measurement of Accelerated Erosion in a Slurry Pot Tester," *Wear*, Vol. 68, pp. 289-303.

Wranglen, G., 1985, *An Introduction to the Corrosion and Protection of Metals*, Chapman and Hall, London, England.

J. T. Park

R. J. Mannheimer

T. A. Grimley

T. B. Morrow

Southwest Research Institute,
San Antonio, Texas 78228-0510

Pipe Flow Measurements of a Transparent Non-Newtonian Slurry

An experimental description of the flow structure of non-Newtonian slurries in the laminar, transitional, and full turbulent pipe flow regimes is the primary objective of this research. Experiments were conducted in a large-scale pipe slurry flow facility with an inside pipe diameter of 51 mm. The transparent slurry formulated for these experiments from silica, mineral oil, and Stoddard solvent exhibited a yield-power-law behavior from concentric-cylinder viscometer measurements. The velocity profile for laminar flow from laser Doppler velocimeter (LDV) measurements had a central plug flow region, and it was in agreement with theory. The range of the transition region was narrower than that for a Newtonian fluid. The mean velocity profile for turbulent flow was close to a 1/7 power-law velocity profile. The rms longitudinal velocity profile was also similar to a classical turbulent pipe flow experiment for a Newtonian fluid; however, the rms tangential velocity profile was significantly different.

Introduction

An investigation of the structure of non-Newtonian slurries in the laminar, transitional, and turbulent flow regimes in pipes was the focus of this research. An understanding of the multiphase flow of solids in a liquid is essential to the basic technology for the economical transport of solids, such as coal, through pipelines. Experiments were performed in a slurry pipe-flow facility. Detailed quantitative information is provided on the effects of particles on the structure of non-Newtonian slurry flows. Such knowledge can lead to better design criteria for more efficient pipeline systems.

A large scale experimental facility, which is shown schematically in Fig. 1, is required for proper scale-up of non-Newtonian flows. Since non-Newtonian fluids are shear rate dependent, experimental results at the same Reynolds number will be different in large diameter pipes where the shear rates are lower than in small diameter pipes.

The flow of a non-Newtonian slurry in a 51-mm diameter-pipe in the laminar, transitional, and turbulent flow regimes was the focus of the experimental program. A transparent model slurry was developed from a clear liquid and silica particles. Fine particles with diameters, D_p, between one and two microns, make the slurry non-Newtonian and provide a yield stress. The index of refraction of the liquid was matched to the index of refraction of the silica particles and the wall of a glass test section. Matching of refractive indices permitted the use of the two-component laser Doppler velocimeter (LDV) for measurement of mean velocity and turbulence properties including the Reynolds stress components in the slurry flow. In addition, the rheology of the fluids was characterized.

LDV measurements in transparent slurries through pipes have been reported previously by Yianneskis and Whitelaw (1984) and Abbas and Crowe (1985). These measurements included only mean velocity profile measurements with a single-component LDV system. No turbulence quantities for the two-phase flow experiments were presented, and the pipe diameters were, respectively, 17.5 and 25.4 mm. Rheological properties of the slurries were not measured by these investigators. Since their slurries contained relatively large particles ($96 < D_p < 270$ microns), the slurries were probably Newtonian. Also, the fluids were pure chemicals with no capability for control of the index of refraction of the fluid over a broad range. Yianneskis and Whitelaw (1984) were able to maintain a difference in refractive indices within 0.0005 through temperature control.

Experiments

Experimental Facility. A schematic of the SwRI pipe slurry facility is shown in Fig. 1. The pump was a Moyno Progressing Cavity Pump which had a flow rate of 15.8 lps (250 gpm) at 400 rpm. A pulsation dampener, which was designed specifically for this facility, removed flow pulsations due to the pump. The entrance pipe was a seamless stainless steel pipe with an inside diameter of 52.35 ± 0.08 mm (2.061 ± 0.003 in.) and length of 13.75 m (42.90 ft) or a length to diameter ratio of 250.

The transparent test section follows the entrance pipe. The test section consisted of a glass tube which was enclosed by a 122-cm (48 in.) long Plexiglas square box. The tube was a Vycor glass tube by Corning with the following dimensions: length of 91 cm (36 in.), inside mean diameter of 50.6 mm (1.993 in.), and wall thickness of 3 mm (0.12 in.). It was slightly elliptical with a maximum diameter of 50.93 mm (2.005 in.) and a minimum diameter of 50.29 mm (1.980 in.). The measured refractive index of the glass tube was 1.4557.

The primary purpose of the test section design was the elimination of refractive index problems caused by the curvature of the tubing. The flow loop and the cavity around the tubing in the Plexiglas box were filled with fluids whose

---

Contributed by the Fluids Engineering Division and presented at the Winter Annual Meeting, Chicago, Ill., November 27-December 1, 1988 of THE AMERICAN SOCIETY OF MECHANICAL ENGINEERS. Manuscript received by the Fluids Engineering Division January 4, 1989.

Table 1 Dantec optical parameters in air for a three-beam system with 33.05 mm beam separation and 80 mm focal length

Parameter	Blue	Green	Units
Wavelength	488.0	514.5	nm
Probe Diameter	33.5	35.3	μm
Probe Length	231.7	244.2	μm
Fringe Spacing	1.706	1.798	μm
Number of Fringes	19.6	19.6	

refractive indices are the same as the glass tube. The cavity contained a glycerine and water mixture.

The entrance to the test section was a Plexiglas dye injector which also functioned as a transition piece between the stainless steel pipe and glass tube which had slightly different diameters. The length of the transition section was 50.8 mm (2.0 in.); consequently, the mean convergent half angle is 0.98 degrees. The decrease in diameter is 3.3 percent from the stainless steel pipe to the glass tube.

The return leg of the flow loop was constructed from 73 mm (2.9 in.) inside diameter schedule 80 pipe of polyvinyl chloride (pvc) plastic. The return leg included a Micro Motion D300 mass flowmeter with a maximum flow rate of 53 kg/s (7000 lb/min).

Instrumentation. The primary measurements for these experiments were velocity profile measurements with a two-component, two-color Dantec LDV. The optical system can be operated in a three-beam or four-beam configuration in backscatter mode. The optical parameters in air are summarized in Table 1 for the three-beam system with an 80 mm lens and 33.05 mm beam separation.

LDV data were acquired with a Dantec 55L90a Counter Processor which included frequency shift. Data acquisition and the traverse system were controlled by a QIC 1800 IBM-AT compatible computer with a 30 Mb hard disk. The traverse system was three dimensional with a traverse range of 600 mm (24 in.) in each direction with a resolution of 4 μm. The LDV measurements were correlated with electronic pressure drop measurements along the entrance tube and the mass flowmeter.

Optically Transparent Slurries. LDV measurements in circular pipes or fluids which contain transparent solids require matching the indices of refraction for the fluid and solid. Edwards and Dybbs (1984) have recently reviewed the problems and solutions associated with index of refraction matching.

The liquid phase of the slurry for these experiments consisted of 60 percent Stoddard solvent by weight and 40 percent mineral oil. The density of the liquid phase was 0.812 gm/cm^3, and the viscosity was 4.1 cP. The refractive index was measured as 1.445. The solid phase of the slurry was Hi Sil T-600 silica from PPG Industries with a mean particle size of 1.13 μm based on population and 1.79 μm based on volume.

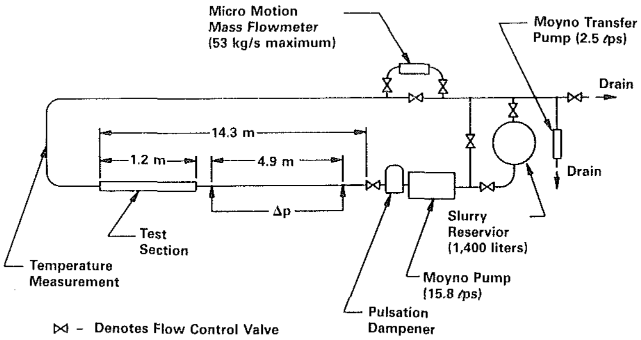

Fig. 1 Schematic of SwRI pipe slurry facility

The slurry for the pipe flow experiments contained 5.65 percent Hi Sil T-600 silica by weight, and the effective volume fraction was estimated to be 14 percent. The resultant density was 0.831 gm/cm^3. From a concentric cylinder viscometer measurements, the fluid had a yield-power law behavior of the form

$$\tau = \tau_0 + k\gamma^n. \tag{1}$$

where τ_0 is the yield stress, γ is the shear rate, and k and n are constants. Data were corrected for slip by a procedure described by Mannheimer (1984). The values of the constants in equation (1) as they were determined by linear regression analysis with a coefficient of determination of 0.996 were as follows:

$$\tau_0 = 100 \text{ dynes/cm}^2,\ n = 0.630, \text{ and } k = 1.670 \text{ dyn} - \text{s}^n/\text{cm}^2.$$

Results

Pressure Drop and Centerline Velocity Measurements. A benchmark experiment with a Newtonian fluid was completed for verification of the flow quality of the loop and for validation of experimental procedures. The fluid was a mixture of 92.0 percent glycerine by weight and 8.0 percent water. This mixture provided a match to the index of refraction for the glass test section, and its viscosity allowed flows in the laminar, transitional, and turbulent flow regimes within the flow capacity of the pump.

The results for the pressure drop measurements for the transparent non-Newtonian slurry are presented in Fig. 2 for increasing and decreasing flow rates which correspond to a range of pipe Reynolds numbers from 100 to 3500. The ordinate in the figure is $\mathrm{Re}_D C_f/16$ whose value is 1 in the laminar flow regime for Hagen-Poiseuille theory from Schlichting (1960). The pipe friction factor is related to the skin friction coefficient by $f = 4C_f$.

In Fig. 2 for the Reynolds number range $400 < \mathrm{Re}_D < 2000$, the experimental data are within 5 percent of the expected value. The two sigma error bars (20 to 1 odds) were computed from the method of Kline and McClintock (1953) and Moffat (1985). Transition to turbulence, which is defined by a sharp

Nomenclature

C_f = skin friction coefficient, $2\tau/\rho U_m{}^2$
D = pipe diameter
f = pipe friction factor
F = non-dimensional pressure, gradient, equation (2)
k = constant, equation (1)
n = exponent, equation (1)
p = pressure
r = radial coordinate
R = pipe radius
Re_D = pipe Reynolds number, $U_m D/\nu$
u = axial or longitudinal velocity
u^* = shear stress velocity, $(\tau/\rho)^{1/2}$
U = mean local axial velocity
U_c = centerline velocity
U_m = mass average pipe velocity
v = radial velocity
w = tangential velocity
x = axial coordinate
Y = yield number, equation (3)
z = normal coordinate
γ = shear rate
δ = plug radius
ν = kinematic viscosity
ρ = density
τ = wall shear stress
τ_0 = yield stress

Superscripts

$'$ = rms

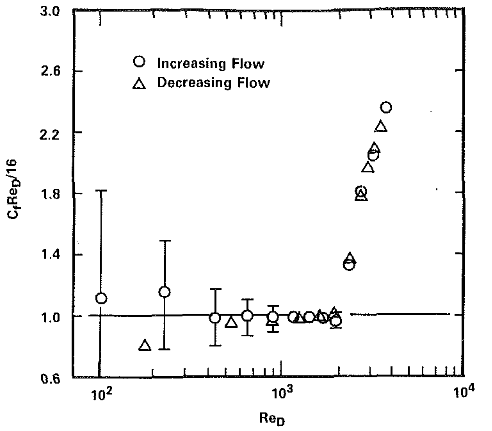

Fig. 2 Pipe skin friction as a function of Reynolds number for a 52.3 mm diameter stainless steel pipe with a glycerine-water mixture

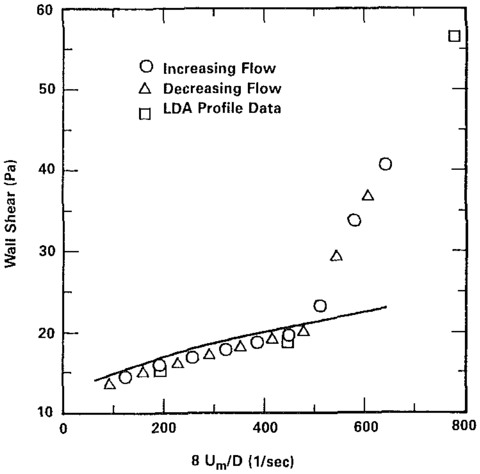

Fig. 3 Wall shear stress from pressure drop measurements as a function of pipe shear rate in 52.3 mm diameter stainless steel pipe with a transparent non-Newtonian slurry. Line: laminar flow theory from viscometer measurements

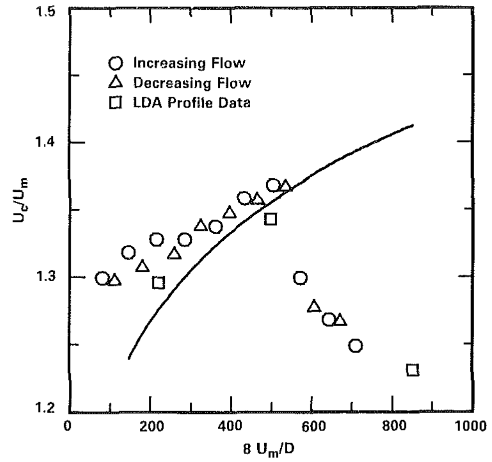

Fig. 4 Centerlinne velocity measurements for a 50.6 mm diameter glass tube with a transparent non-Newtonian slurry. Line: laminar flow theory from viscometer measurements

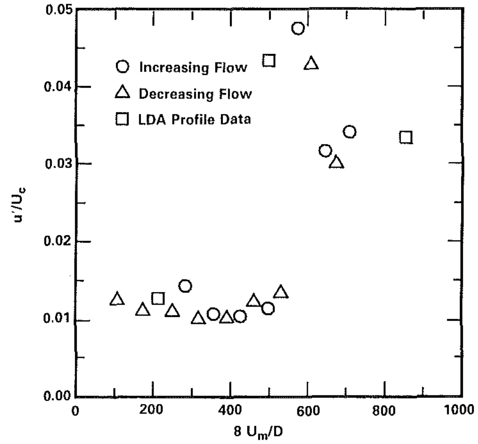

Fig. 5 Centerline relative longitudinal turbulence intensity for a 50.6 mm diameter glass tube with a transparent non-Newtonian slurry

increase in $Re_D C_f/16$, occurred at a Reynolds number of 2000 which agrees with the value on the Moody (1944) diagram.

The results for the pipe pressure drop measurements for the transparent non-Newtonian slurry are shown in Fig. 3. Wall shear stress in Pascals is plotted as a function of the pipe shear rate, $8U_m/D$, where U_m is the mass average velocity and D is the pipe diameter. Transition occurs at a shear rate of 480 s^{-1} or a mean pipe fluid velocity of 316 cm/s. The appropriate Reynolds number definition for presentation of this data in nondimensional form is being evaluated.

The centerline velocity of the transparent test section was measured with the LVD over a range of velocities at a station which was nominally 46 cm (18 in.) or 9 diameters from the entrance. In Fig. 3 for the laminar flow regime, the data are reasonable agreement with the theory reported by Soto and Shah (1976); however, the theoretical values of shear stress are consistently higher. In that theory, the relevant nondimensional constants are a nondimensional pressure gradient or friction factor defined by

$$F = |dp/dx|\,(D/4k)\,(D/U_m)^n \quad (2)$$

and a nondimensional yield stress or yield number defined by

$$Y = (\tau_0/k)\,(D/U_m)^n \quad (3)$$

where dp/dx is the pressure gradient. The yield number and friction factor are related by the following equations:

$$1 = [n/2F^3][F-Y]^{(n+1)/n}[(F-Y)^2/(3n+1) + 2Y(F-Y)/(2n+1) + Y^2/(n+1)] \quad (4)$$

$$\delta/R = Y/F = \tau_0/\tau \quad (5)$$

where δ is the plug radius. From the constants of the yield-power-law model in equation (1), U_m, and D, equation (4) is solved numerically by Newton's method, and the pressure gradient is calculated from equation (2). The pressure gradient is related to the wall shear stress by

$$\tau = (D/4)\,|dp/dx|\,. \quad (6)$$

The centerline velocity, U_c, and relative longitudinal turbulence intensity, u'/U_c, as a function of the mean pipe flow velocity from LDV measurements are presented in Figs. 4 and 5. In Fig. 4, the data for centerline velocity are compared to the theory from Soto and Shah (1976) given by

$$U_c/U_m = [n/2F(n+1)][(F-Y)^{(n+1)/n}] \quad (7)$$

for $r \leq \delta$. Again the data are in reasonable agreement with theory.

Both Figs. 4 and 5 clearly show the onset of transition at a velocity of 3.2 m/s or a shear rate of $8\,U_m/D = 500\ s^{-1}$. The onset of transition is at a slightly higher velocity than in the pressure drop data since the diameter of the glass test section is

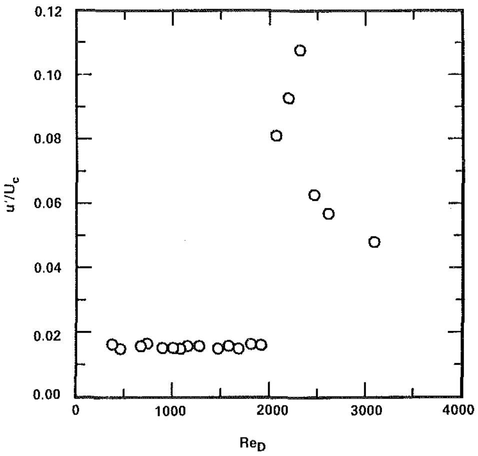

Fig. 6 Centerline relative longitudinal turbulence intensity for a 50.6 mm diameter glass tube with a glycerine-water mixture

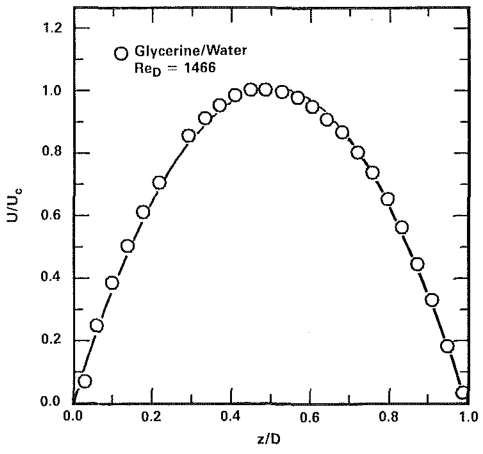

Fig. 7 Nondimensional laminar velocity profile in a 50.6 mm diameter glass tube for a refractive-index matched glycerine-water mixture at $Re_D = 1466$. Line: parabola

slightly smaller than the stainless steel pipe where the pressure drop is measured.

Transition to fully developed turbulent flow is not definitive in the pressure drop or the mean velocity data in Figs. 3 and 4. However, the centerline longitudinal relative turbulence intensity indicates that the flow transitions to fully developed turbulent flow at $8\ U_m/D = 650$ or $U_m = 4.1$ m/s. Consequently, the transition region for these experiments is $3.2 < U_m < 4.1$ m/s whereas for the Newtonian fluid (glycerine/water mixture) the transition region is $2000 < Re_D < 3000$ in Fig. 6. Thus, transition exists over a much narrower velocity range for the non-Newtonian slurry. The transition range is 50 percent of transition velocity for the Newtonian fluid in comparison to 28 percent for the slurry. The peak relative turbulence intensity for the non-Newtonian fluid is much lower than that for the Newtonian fluid in the transition region.

The rms velocity in the laminar flow regime in Fig. 5 with values between 1.0 and 1.5 percent and in Fig. 6 with values less than 2.0 percent is probably the noise level of the LDV system. Measurements with hot-film anemometry would be required for an accurate value of the flow noise.

Velocity Profile Measurements. The results of the LDV profile measurements are presented in Figs. 7 through 9. In these figures, the velocities are nondimensionalized with the centerline mean velocity, U_c. The abscissa in these figures traverses from the bottom of the pipe ($Z/D = 0$) to the top ($Z/D = 1.0$) in the vertical centerline where the abscissa is normalized with the pipe diameter.

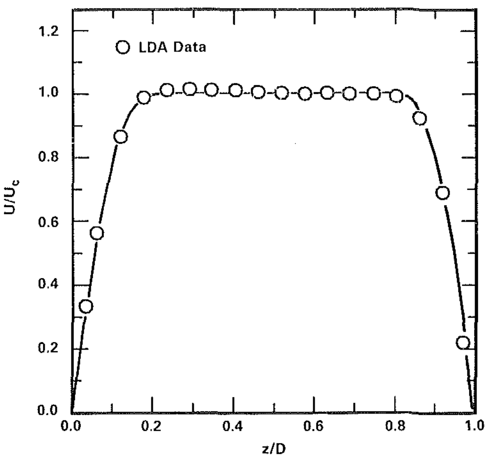

Fig. 8 Nondimensional laminar velocity profile in a 50.6 mm diameter glass tube for a transparent non-Newtonian slurry at a mean velocity of 1.37 m/s. Line: laminar flow theory from viscometer measurements

With the current experimental arrangement, five of the six unique Reynolds stress components $\langle u_i u_j \rangle$ can be measured. In general, these include $(u')^2$, $(v')^2$, $(w')^2$, $\langle uv \rangle$, and $\langle uw \rangle$. According to Laufer (1954), the only relevant statistical terms in Reynolds' equation for pipe flow are $(v')^2$, $(w')^2$, and $\langle uv \rangle$. The velocity components u and v are measured by a lateral traverse of the horizontal centerline while u and w are measured by a vertical traverse along the vertical centerline. To date, only a vertical traverse has been completed.

The Reynolds stress term $\langle vw \rangle$, which requires an on axis LDV measurement, is zero from symmetry since positive and negative values of the same magnitude are equally likely. Similarly $\langle uw \rangle$ is zero. The only interesting covariance, $\langle uv \rangle$, has not yet been measured.

The laminar velocity profile measurements for a Newtonian fluid are shown in Fig. 7. The data are in excellent agreement with a parabolic profile. The velocity ratio, U_c/U_m, of the centerline measurement from the LDV to the mass average velocity from the flowmeter was 1.92 in comparison to a theoretical value 2 from Schlichting (1960), and the velocity ratio from the LDV and pressure drop measurements was 1.89.

The mean velocity profile for the laminar flow case at a mean flow of 1.37 m/s is shown in Fig. 8. The data are in agreement with the laminar flow theory from Soto and Shah (1976) given by

$$U/U_m = [n/2F(1+n)][(F-Y)^{(n+1)/n} - (Fr/R - Y)^{(n+1)/n}] \tag{8}$$

for $r \geq \delta$ and equation (7). The theoretical curve was computed from the concentric-cylinder viscometer measurements. The ratio U_c/U_m, which is the square symbol in Fig. 4 at $8\ U_m/D = 217$, differed from the theory in equation (7) by 1.8 percent.

The profile measurements for turbulent flow are presented in Fig. 9 where they are compared to the results of Laufer (1954) for air, a Newtonian fluid, at a pipe Reynolds number of 40,600. The LDV data were corrected for bias errors by the method of Johnson et al. (1984). The velocity profile data of Fig. 9 also corresponds to the square symbols near $8U_m/D = 800$ in Figs. 3, 4, and 5. The mean pipe flow velocity in the test section is 5.44 m/s.

The mean velocity profile in Fig. 9(*a*) is very nearly a 1/7 power-law velocity profile. Most of the data for the mean tangential velocity profile, which is not shown, is within ±0.5 percent U_c for the spatially averaged value. The variation in

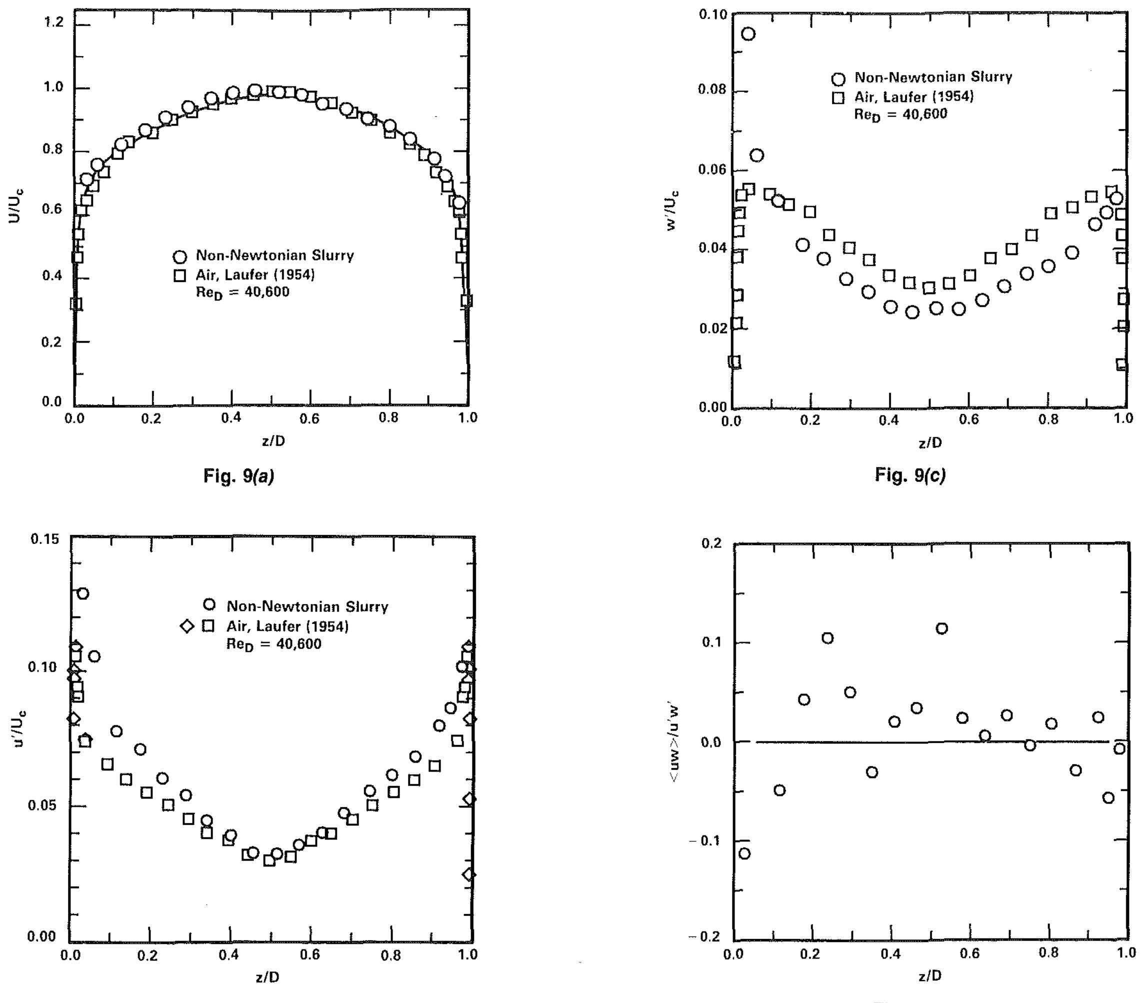

Fig. 9(a)

Fig. 9(c)

Fig. 9(b)

Fig. 9(d)

Fig. 9 Nondimensional turbulent velocity profiles in a 50.6 mm diameter glass tube for a transparent non-Newtonian slurry at mean velocity of 5.44 m/s in comparison to a Newtonian fluid. *(a)* Axial mean component, *(b)* axial relative turbulence intensity, *(c)* tangential relative turbulence intensity, *(d)* Axial-tangential velocity correlation coefficient.

the tangential component is less than the equivalent rms noise of the instrumentation.

Near the center of the tube ($0.2 < Z/D < 0.8$), the axial or longitudinal relative turbulence intensity in Fig. 9(*b*) is very similar to that for turbulent flow of a Newtonian fluid. However, near the wall the relative intensity for the slurry of 13 percent is slightly higher than the 11 percent Laufer's data (1954). In law of the wall variables, Laufer's value of $u'/u^* = 2.6$ is slightly higher that for the slurry ($u'/u^* = 2.5$).

The differences in the tangential profile are more significant. Over 80 percent of the core of the flow ($0.1 < Z/D < 0.9$), the relative turbulence intensities in Fig. 9(*c*) are lower for the slurry although the shapes of the profiles are similar. Near the wall both w'/U_c and w'/u^* are significantly higher for the slurry. The maximum value of w'/U_c is about 9.4 percent for the slurry versus 5.5 percent for a Newtonian fluid, and the maximum value of w'/u^* is 1.8 for the slurry in comparison to 1.3 for Laufer's data (1954).

The rms profiles in Figs. 9(*b*) and 9(*c*) are unsymmetrical. The lower values for the traverse along the upper half ($0.5 < Z/D < 1.0$) may be caused by improper filter settings on the counters. Filter settings are optimized during the experiment since Doppler frequency diminishes as the tube wall is approached. Previous one-component measurements of u'/U_c were symmetrical, and the results were similar to the lower half of the survey ($0 < Z/D < 0.5$) in Fig. 9(*b*).

The correlation coefficient for the two velocity components is shown in Fig. 9(*d*). Theoretically, $\langle uw \rangle$ should be zero. As the figure indicates, most of the values in the profile are near zero.

Conclusions

The measurements in this paper are the first reported velocity profile measurements for a non-Newtonian slurry. A transparent slurry has been developed which exhibits yield-power-law behavior. The pressure drop data and velocity profile measurements in the laminar flow regime are in agreement with theory on the basis of rheological properties measured with a concentric-cylinder viscometer.

The transition region for the slurry is much narrower than the transition region for a Newtonian fluid. The peak relative turbulence intensity at the center of the pipe was lower for the non-Newtonian slurry.

Some of the results for turbulent flow were similar to those of Laufer (1954) in air at a pipe Reynolds number of 40,600. At a mean pipe flow velocity of 5.44 m/s, the mean velocity profile was very near a 1/7 power law velocity profile. The rms longitudinal velocity profile was also similar to Laufer's (1954), but the rms tangential was significantly different. The relative turbulence intensity for the tangential component was higher at the wall and lower at the center for the slurry.

Since the present slurry data for turbulent flow were acquired at a velocity only slightly higher than the transition region, comparison to Laufer's data (1954) may not be appropriate. A better comparison would be data for a turbulent Newtonian flow at a Reynolds number of 4,000 where the mean profile is a 1/5 power law (Hinze, 1975). The mean profile for the slurry probably evolves to a 1/7 power law more rapidly since its laminar profile is blunter than the parabolic profile for a Newtonian fluid.

Acknowledgments

This research was supported by the U.S. Department of Energy under grant DE-FG22-86PC90962 and by the Advisory Committee for Research at Southwest Research Institute. The DOE technical monitor for this project was Mr. Swenam Lee of the Pittsburgh Energy Technology Center, and the DOE program manager was Mr. Shelby Rogers.

References

Abbas, M. A., and Crowe, C. T., 1985, "Experimental Study of the Flow Properties of a Homogeneous Slurry Near Transitional Reynolds Number," *Cavitation and Multiphase Flow Forum—1985*, J. W. Hoyt and O. Furuya, ed., ASME, New York, pp. 137-141, also, *International Journal of Multiphase Flow*, Vol. 13, No. 3, 1987, pp. 357-364.

Edwards, R. V., and Dybbs, A., 1984, "Refractive Index Matching for Velocity Measurements in Complex Geometries," *TSI Quarterly*, Vol. 10, No. 4, pp. 3-11.

Hinze, J. O., 1975, *Turbulence*, Second Edition, McGraw-Hill, New York, pp. 715-724.

Johnson, D. A., Modarress, D., and Owen, F. K., 1984, "An Experimental Verification of Laser-Velocimeter Sampling Bias and Its Correction," ASME JOURNAL OF FLUIDS ENGINEERING, Vol. 106, No. 1, pp. 5-12.

Kline, S. J., and McClintock, F. A., 1953, "Describing Uncertainties in Single Sample Experiments," *Mechanical Engineering*, Vol. 75, No. 1, pp. 3-8.

Laufer, J., 1954, "The Structure of Turbulence in Fully Developed Pipe Flow," NACA Report 1174.

Mannheimer, R. J., 1983, "Effect of Slip on Flow Properties of Cement Slurries Can Flaw Resistance Calculations," *Oil and Gas Journal*, Vol. 81, No. 49, pp. 144-147.

Moffat, R. J., 1985, "Using Uncertainty Analysis in the Planning of an Experiment," ASME JOURNAL OF FLUIDS ENGINEERING, Vol. 107, No. 2, pp. 173-178.

Moody, L. F., 1944, "Friction Factors for Pipe Flow," *Trans. ASME*, Vol. 66, No. 8, pp. 671-684.

Schlichting, H., 1960, *Boundary Layer Theory*, Fourth Edition, McGraw-Hill, New York.

Soto, R. J., and Shah, V. L., 1976, "Entrance Flow of a Yield-Power Law Fluid," *Applied Scientific Research*, Vol. 32, No. 1, pp. 73-85.

Yianneskis, M., and Whitelaw, J. H., 1984, "Velocity Characteristics of Pipe and Jet Flows With High Particle Concentration," *Liquid-Solid Flows and Erosion Wear in Industrial Equipment*, M. C. Roco, ed., ASME, New York, pp. 12-15.

Flow Speed Measurement and Rheometry by Pulsed Neutron Activation

K. G. A Porges

S. A. Cox

C. Herzenberg

C. Kampschoer

Argonne National Laboratory,
Argonne, IL 60439

Pulsed Neutron Activation (PNA) is a means of noninvasive flow velocity measurement based on tagging the flowing medium with a short-lived radioactivity. Previous work with salt or dye-tagging showed poor accuracy in turbulent and failed in laminar flow when conventional data processing was used. However, use of a data acquisition and processing scheme that is based on tag dispersion modelling can produce absolute values over a wide range of flow speeds and regimes with high accuracy. For non-Newtonian/laminar flow, rheological information can also be obtained. The inherently non-intrusive nature of PNA tagging makes this scheme available for slurry measurements. The performance of PNA in slurry flow at up to 60 percent solid content was compared to full-flow diversion and weighing. Errors ranged from less than 0.2 percent at high Reynolds' numbers to about 2 percent for paste flow. Rheological parameters (yield shear stress or flow behavior index) could be determined with an accuracy that compared to that of a spindle viscometer with grab-samples. The PNA scheme thus offers a unique means of studying slurry flow in a dedicated laboratory facility, or of providing calibration for other flowmeters in an industrial plant through temporary installation by a team of expert consultants.

I Introduction and General Description

The present report describes a technique for flow speed measurement that spans the entire range of velocities and flow regimes found in ducted flow, with an error that varies from better than 0.2 percent for highly turbulent flow to about 2 percent for non Newtonian/laminar flow. The scheme dispenses entirely with calibration or "meter factors" and thus produces an absolute readout; equipment can be clamped onto ducts whence emplacement of this scheme in an Industrial Plant will not interrupt plant operation.

Pulsed Neutron Activation (PNA) is a tag transit-time measurement scheme, closely related to older dye- or salt-tagging schemes that required the installation of an injector and downstream detector. In the thirties, radioactive tagging was introduced as a means of avoiding at least the detector installation (since gamma radiation is readily detected through the duct wall). In 1970, Boswell and Pierce [1] first demonstrated the use of neutron bursts to activate the flowing medium itself, thereby eliminating all installations. Soon thereafter, the capability of PNA for high accuracy, inherent in an injection that takes very little time and does not disturb the flow, was exploited by a group at ANL [2-4] who made effective use of tag dispersion modelling [5-8] and moments ratio data processing for turbulent flow. Several other groups [9-21] continued this work. The principal efforts of our own group were directed towards the application of PNA to slurry flow (22-26), in which connection we were able to develop different models to cope with laminar and laminar non-Newtonian flow. Tag dispersion modelling inevitably assumes a quasi-homogeneous medium, hence, PNA measurements under conditions where partial or full flow separation obtains tend to be inaccurate. While this remains to be resolved, flow separation is rarely encountered in industrial practice.

A basic requirement of PNA is the presence within the flowing medium of a tag acceptor—a nuclear species that interacts with fast neutrons to produce a short-lived, gamma-emitting radioactivity. The list of such nuclides is short but includes some common elements such as oxygen, sodium, silicon and fluorine, amongst others. If no tag acceptor is present, a Teflon collar, installed in the duct opposite the neutron source, works reasonably well for turbulent flow, including gas-entrained particle flow.

The equipment includes a neutron burst generator, downstream gamma detector and acquisition and data processing electronics, as well as a considerable amount of shielding material. Most of the gamma channel can be purchased; portable, lightweight neutron burst generators of adequate output, designed for oil-well exploration, are also available off-the-shelf. Data acquisition and processing can be implemented through PC-based software and available plug-in boards. Alternatively, logic circuitry that interacts with a Multiscaler is readily fabricated and offers some flexibility for exploratory work. Such a system was used in the tests described in this report.

Contributed by the Fluids Engineering Division and presented at the Winter Annual Meeting, Chicago, Ill., December 5–10, 1988 of THE AMERICAN SOCIETY OF MECHANICAL ENGINEERS. Manuscript received by the Fluids Engineering Division January 4, 1989.

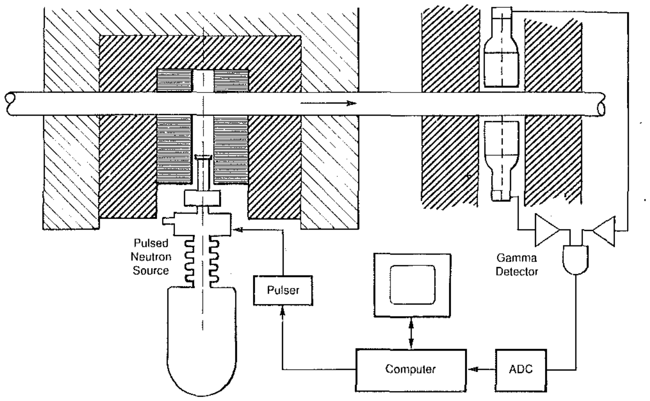

Fig. 1 PNA system (schematic)

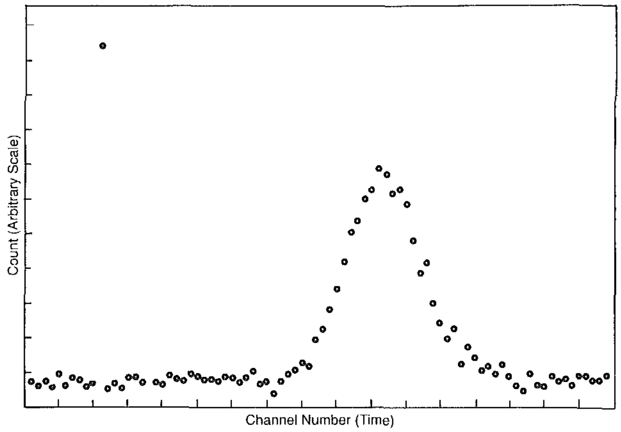

Fig. 2 Turbulent flow PNA profile

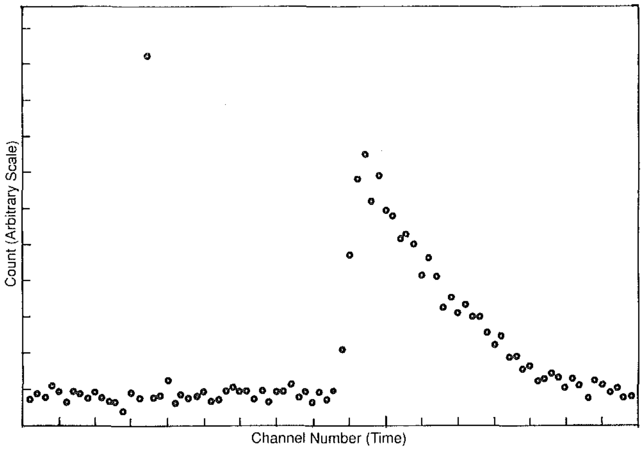

Fig. 3 Laminar/Newtonian PNA profile

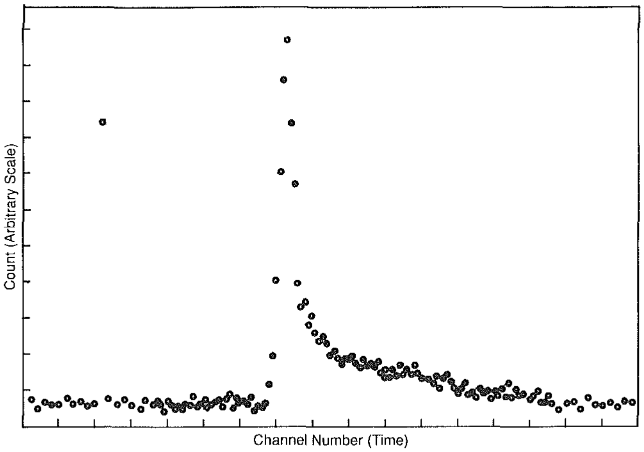

Fig. 4 Laminar/Bingham PNA profile

In comparison to other means of flow measurement, it has to be acknowledged that both neutron source and gamma detector are costly as well as easily damaged. To achieve accuracy and to minimize radiation hazards, effective shielding and collimation must be provided; this calls for experience and/or shielding design calculations that require a Mainframe computer.

The time required for a single measurement varies both with the amount of tag acceptor present in the medium and with the neutron yield and gamma detection efficiency. Measurements with top-of-the-line neutron sources (10^{10} n/burst) and efficient gamma detectors (5″ by 5″ NaI or BGO scintillators) on water slurries can yield acceptable accuracy with one or two bursts, hence, a few seconds. Measurements for, say, laminar, non-Newtonian flow of coil-oil slurry, using average equipment (10^7 n/burst), may take as much as 45 min.

Considering these various positive and negative characteristics of the method, one can see two principal application areas:

(*a*) as a semi-permanent installation at a laboratory dedicated to research on slurry flow or similar facility,

(*b*) as an equipment package, accompanying a team of specialists who would temporarily install and use the system in some industrial plant, to support Startup or calibrate other, on-line flowmeters.

II Detailed Operation of System

The arrangement of components on the duct is illustrated schematically in Fig. 1. As already mentioned, shielding and collimation are used for both the neutron source and gamma detector, so that the source irradiates only a relatively short slice of the duct and the gamma detector similarly only "sees" a short slice. Since typical burst generators produce pulses of less than 100 microseconds duration, motion of the medium during the burst is negligible at flow speeds less than 10 m/s. Thus the tag is deposited within a well-defined region, from which it moves downstream and eventually reaches the gamma detector in a pattern that is characteristic of the flow regime.

The data acquisition system receives logic pulses, of 1-2 microsecond length, whenever the gamma detector has sensed a photon. These pulses are accumulated for a certain dwelltime in one channel of a Multiscaler, whereupon the next channel is accessed; the Multiscaler recycles when the last of, say, 200 channels is reached. Normally, the first few channels are used to register background (always present in gamma detectors); then, the neutron burst is triggered, causing a certain number of counts in that time channel as the neutron generation process releases concomitant gamma radiation, some of which will penetrate the gamma detector shield. The resultant sharp spike is a convenient time marker. Immediately afterwards, the background count resumes while the tag moves towards the gamma detector "window". What follows is a "signature" countrate peak, of which Fig. 2 illustrates typical turbulent flow, Fig. 3 laminar-Newtonian, Fig. 4 laminar-Bingham and Fig. 5 laminar-Ostwald (pseudoplastic) flow. These figures already convey direct, though qualitative information regarding the flow regime, available through an on-line display. We shall now show how tag dispersion and flow modelling can be used to extract quantitative information, specifically, the duct-averaged tag velocity $\bar{v}$.

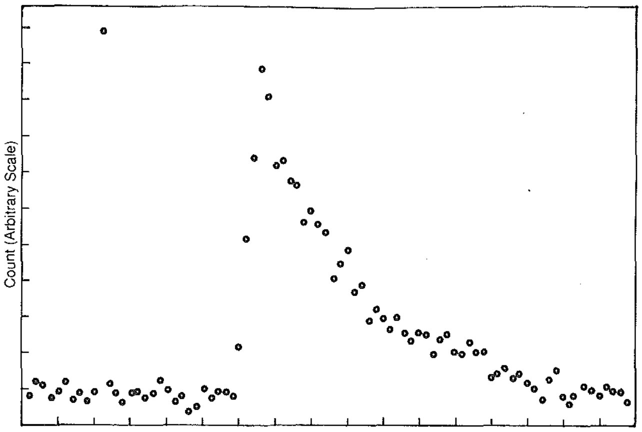

Fig. 5 Laminar/Ostwald PNA profile

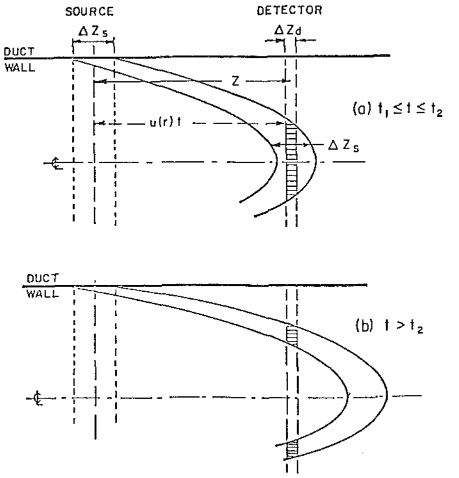

Fig. 6 Schematic geometry, laminar transport of tagged medium "slice"; tag "frozen" into the moving medium. Injection of tag is quasi-instantaneous; uniformly activited slice is carried downstream with negligible diffusion/dispersion.

III Flow Modelling and Data Processing

Considering, firstly, turbulent flow, Taylor [5, 6] and Aris [7, 8] have derived an equation for tag displacement in that regime, where radial dispersion is much faster than axial translation. According to that equation, the tag concentration at time t from the burst, and at a distance Z downstream, comes to

$$F(z,t)=A\,(2\pi Ht)^{-1/2}\exp-(Z-\bar{v}t)^2/2Ht \qquad (1)$$

in terms of the dispersion parameter $H(t)$ (m^2/sec) and a scaling constant A. Through direct integration, it can be shown that the identity

$$\bar{v}=\int_0^\infty (Z/t)F(Z,t)dt\int_0^\infty F(Z,t)dt \qquad (2)$$

holds; other moments yield the dispersion parameter. Equation (2) provides a simple means of extracting $\bar{v}$ from the data, which first have to be corrected for background and decay: let

$$S_i = (C_i - \bar{B})e^{i\lambda\tau} \qquad (3)$$

where λ = radioactive decay constant, τ = dwelltime, i = channel number starting from the neutron burst and $\bar{B}$ = gamma channel background count, averaged over the regions on both sides of the burst, then

$$\bar{v} = (Z/\tau)\Sigma(S_i/i)/\Sigma S_j. \qquad (4)$$

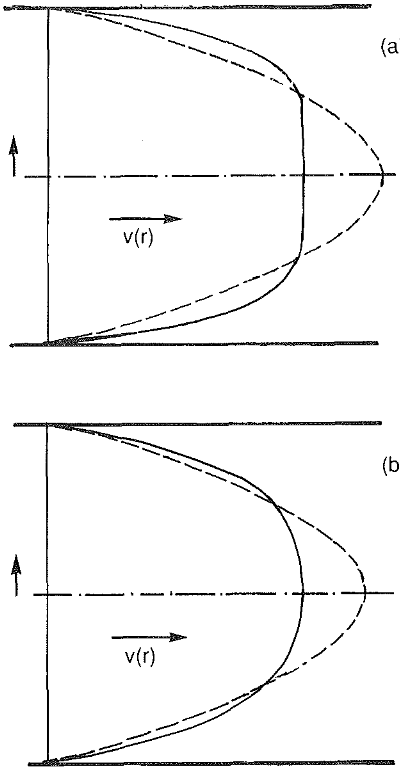

Fig. 7 Non-Newtonian velocity profiles. (*a*) Bingham, (*b*) Ostwald

This equation was extensively tested with water flowing at different velocities, and for different detector locations Z, by comparing PNA-computed results with measurement provided by a timed full-flow diversion scheme [26]. This series of measurements was found to agree within about 0.2 percent, the reproducibility of the timed diverter.

Turning now to laminar flow, one must develop a different model here, based on the opposite assumption that dispersion is now slow compared to axial translation. This leads to the tag behavior that is illustrated schemically in Fig. 6: the disk that initially contains the tag is gradually deformed into a sack; when the tip of that sack enters the detector, the count rate rises abruptly; as the tip passes, the count rate declines as $1/t$.

Figure 7 shows the difference between Newtonian, Bingham and Ostwald flow, for which the well-known radial velocity distributions

$$v(x) = v_c(1-x^2), \qquad \text{(Newton)} \qquad (5)$$

$$v(x) = v_c[1-(x-a)^2/(1-a)^2] \qquad \text{(Bingham)} \qquad (6)$$

$$v(x) = v_c[1-x^{2/(1-s)}], \qquad \text{(Ostwald)} \qquad (7)$$

obtain. In these equations, $x=r/R$, R = duct radius, v_c = centerflow velocity, a = yield to wall shear stress ratio. The parameter s, ranging from zero (Newtonian limit) to unity (paste flow limit), is related to the Metzner flow behavior index n through

$$s=(1-n)/(1+n). \qquad (8)$$

The duct-averaged and centerflow velocities v and v are related through

$$\bar{v}=v_c/2, \qquad \text{(Newton)} \qquad (9)$$

$$\bar{v}=(v_c/2)[1+a(2-a)/3], \qquad \text{(Bingham)} \qquad (10)$$

$$\bar{v}=v_c/(2-s), \qquad \text{(Ostwald)} \qquad (11)$$

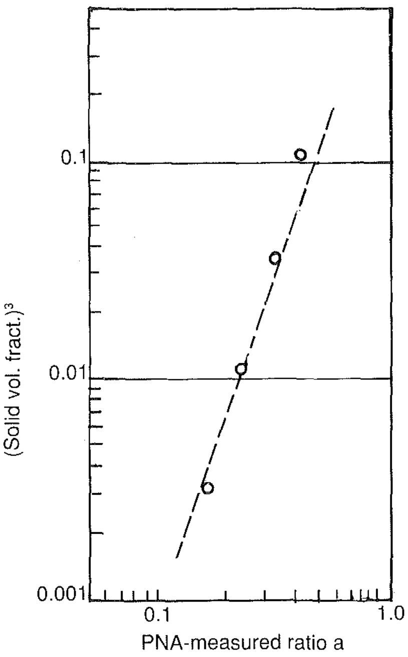

Fig. 8 "Thomas" plot for Bingham ratio

The count rate profiles predicted by these radial velocity distributions can be expressed in terms of the onset of the peak and its upper turning point,

$$t_1 = (Z - \Delta z/2)/v_c \qquad (12a)$$

$$t_2 = (Z + \Delta z/2)/v_c \qquad (12b)$$

where Δz = detector window width, noting that

$$(t_1 + t_2)/2 = Z/v_c. \qquad (13)$$

Recasting equations (5) to (7), this yields

$$\begin{aligned} S(t) &= K(1 - t_1/t), \quad t_1 < t < t_2, \\ &= K(t_2 - t_7)/t, \quad t_2 < t \end{aligned}$$

$$\text{(Newton)} \qquad (14)$$

$$\begin{aligned} S(t) &= K[a + (1-a)(1 - t_1/t)^{1/2}]^2, \quad t_1 < t < t_2, \\ &= K(1-a)\{(1-a)(t_2 - t_1)/t \\ &\quad + 2a[(1 - t_1/t)^{1/2} - (1 - t_2/t)^{1/2}]\}, \quad t_2 < t \end{aligned}$$

$$\text{(Bingham)} \qquad (15)$$

$$\begin{aligned} S(t) &= K(1 - t_1/t)^{1-s}, \quad t_1 < t < t_2 \\ &= K[(1 - t_1/t)^{1-s} - (1 - t_2/t)^{1-s}], \quad t_2 < t \end{aligned}$$

$$\text{(Ostwald)} \qquad (16)$$

in terms of a scaling constant K that includes source strength and detection efficiency.

On physical grounds, one further finds that for laminar flow, the second to first moment ratio (rather than the first to zeroth moment ratio that is appropriate for turbulent flow) yields the duct-averaged velocity:

$$\bar{v} = (Z/\tau) \sum (S_i/i^2) / \sum (S_j/j) \qquad (17)$$

One further complication, inherent in laminar flow, must be dealt with: as a result of rapid decay and extremely slow movement of the peripheral tag, the latter eludes measurement; to complete the moment integrals, corrections must be applied. In those corrections, it is expedient to use estimates of the parameters a and s, obtained from equations (10) and (11), respectively; the first estimate of $\bar{v}$ is then improved through iteration. In this process, values of the rheometry parameters a or s are also produced. The software needed for this task is extensive and takes considerable time to run; a hard disk and coprocessor are minimum requirements if a PC is used.

The rheological constants that could thus be extracted from the on-line PNA data were compared to results of spindle-viscometer laboratory measurements on grab-samples, and found to agree fairly well except for the highest solid fractions (up to 60 percent by volume), again for coal-oil and coal-water slurries. On the whole, the on-line data appeared somewhat more reliable; a number of problems arise in the use of spindle viscometers with slurries that become increasingly difficult to cope with as the solid concentration increases.

As observed by others, coal-water slurries tended to produce a Bingham profile, unmistakeable through the strong spike that announces the arrival of the central plug at the detector, cf. Fig. 4; oil-coal slurries in contrast yielded Ostwald flow profiles that showed a broaded peak, cf. Fig. 5. Confirming the Bingham shear stress measurements, a Thomas plot [27], i.e., a plot of the relation

$$a = \text{const.} f^3, \qquad (18)$$

f = solid concentration, is reproduced in Fig. 8; the data appear to agree with equation (18) within the experimental error. To completely characterize the flow mode, the pressure drop along the Test Section may be measured together with the PNA profile.

IV Summary and Conclusion

The PNA scheme, though costly and demanding, offers an intrinsic capability for measurement accuracy:

(*a*) In comparison to other, conventional flow-tagging schemes, flow is not disturbed by tag injection; the latter can be repeated without difficulty for an arbitrary number of bursts until statistics are adequate; burst duration is very short, hence, no corrections are needed for tag displacement during the burst.

(*b*) Measured count rate profiles provide, on one hand, a visual, straightforward recognition of the flow regime and furnish, on the other hand, a means of absolute velocity calculation from the data, as a ratio of weighted integrals or moments.

(*c*) Rheometric parameters that can be extracted from the data tend to be more reliable than measurements on grab-samples, inasmuch as the on-line readings are made at the exact temperature, composition etc. of the flowing medium.

(*d*) In comparison to certain other techniques, accuracy is unimpaired by high temperatures and pressures.

For potential use in an industrial environment, the clamp-on nature of the equipment allows measurements at sites that defeat almost any other scheme; for example, on coal conversion reactor slurry feedlines. This potential has, thus far, found little practical use. Further laboratory studies are indicated to refine especially the treatment of data in laminar non-Newtonian flow, and to characterize the behavior of two-phase media that are potential candidates for industrial solids conveyance. Finally, it remains to be explored to what extent PNA measurements could become useful for separated phases, where, although tag dispersion modelling becomes moot, selective tagging of either phase (available if only one phase contains a neutron acceptor) offers the prospect of additional information—another unique feature of the PNA scheme.

References

1 Boswell, C. R., and Pierce, T. B., "Flow Rate Determination by Neutron Activation," Modern Dev. in Flowmeas., Conf Publ 10, 1971, p. 264.

2 Larson, H. A., Price, C. C., Curran, R. N., and Sackett, J. I., "Flow Measurement in Sodium and Water Using Pulsed Neutron Activation: Part I, Theory," *Nucl. Tech.*, Vol. 57, 1982, p. 272.

3 Price, C. C., Larson, H. A., Curran, R. N., and Sackett, J. I., "Flow Measurement in Sodium and Water Using Pulsat Neutron Activation: Part II, Experiment," *Nucl. Tech.*, Vol. 57, 1982, p. 272.

4 Santee, G. E., Price, C. C., and Wilson, A. E., "Asymmetry Effects in Flow Measurements Using PNA," *Trans. ANS*, Vol. 27, 1977, p. 217.

5 Taylor, G. I., "The Dispersion of Matter in Turbulent Flow Through a Pipe," *Proc. Roy. Soc. Lond.*, Series A, Vol. 223, 1954, p. 446.

6 Taylor, G. I., "Dispersion of Soluble Matter In Solvent Flowing Slowly Through a Tube," *Proc. Roy. Soc. Lond.*, Series A, Vol. 219, 1953, p. 186.

7 Aris, R., "On the Dispersion of Solute in Fluids Flowing Through Tubes," *Proc. Roy. Soc. Lond.*, Series A, Vol. 237, 1956, p. 67.

8 Aris, R., "On the Dispersion of a Solute Through Diffusion, Convection and Exchange Betweeen Phases," *Proc. Roy. Soc. Lond.*, Series A, Vol. 252, 1959, p. 538.

9 Kehler, P., "Two-Phase Flow Measurement by Pulsed Neutron Activation Techniques," ASME Publ. H00121, Dec. 1978.

10 Kehler, P., "Two-Phase Flow Measurement by PNA," ANL Rept. ANL/NUREG/CT-78-17, 1977.

11 Kehler, P., *IEEE Trans. Nucl. Sci. NS-26*, 1977, p. 1627.

12 Kehler, P., "Measurement of Slow Flow Velocities by PNA," *Proc. USNRC Rev. Gp. Conf. NUREG CP-0015*, USNRC, 1980.

13 Perez-Griffo, M. L., "Analysis of the PNA Technique," Ph.D. thesis, R.P.I. Troy, NY 1981.

14 Perez-Griffo, M. L., Block, R. C., and Lahey, R. T., "Measurement of Flow in Large Pipes by the Pulsed Neutron Activation Method," *Nuc Sci. Eng.*, Vol. 82, 1982, p. 19.

15 Perez-Griffo, M. L., Block, R. C., and Lahey, R. T., Trans ANS 27, 682 1977, Trans ANS 30, 500, 1978, Trans ANS 32, 984, 1979.

16 Taylor D. J., Hartwell, J. K., et al., "The LOFT PNA System of Flow Measurement," EG&G Idaho Report L087-81-165, 1982.

17 Achard, J. L., and Delhaye, J. M., "Modelling Aspects of the PNA Method of Flowrate Measurement," *Proc II Annual Mtg on Nuclear Thermohydraulics*, Santa Barbara, CA, Jan. 1983.

18 Achard, J. L., and Delhaye, J. M., "Theorie de la mesure du debit d'un ecoulement monophasique par marquage radioisotopique induit par activation neutronique," CEA-R/15, 1983.

19 Gaul, H., "Measurement of the Mass Flow in the Down-Comer of the PKL Test Facility by Pulsed Neutron Activation," KWU Report R 513/2/81, Jan. 1981.

20 Gozani, T., Esterl, J., Bernatovicz, H., and Goodman, J., "Neutronic Mass Flowmeter for Continuous Mass Flowrate Measurement," SAI-315-82-PA, 1982.

21 Gozani, T., Esterl, J., Goodman, J., and Bernatovicz, H., "Development of Neutronic Mass Flowmeter," *Proc. 1982 Sympos. on Instr. and Control for Fossil Energy Proc.*, ANL 82-62/CONF-820612, 1982.

22 Porges, K., Cox, S. A., Kampschoer, C., and Herzenberg, C., "Calibration of Flowmeters by Pulsed Neutron Activation," ANL-80-62/CONF-800602, 1980.

23 Porges, K., Cox, S. A., Kampschoer, C., Cohn, C., Groh, E., Lewandowski, E., and Hacker, D., "The Argonne Slurry Loop Test Facility (SLTF)," ANL-18-62/CONF 810607, 1981.

24 Porges K. G. A., "Flow Characterization and Calibration of Slurries by Pulsed Neutron Activation," ANL/FE-84-16, 1984.

25 Porges, K. G., "Online Mass Flow Measurement by Nonintrusive, Nuclear Techniques," *Trans ANS*, Vol. 45, 1982, p. 762.

26 Porges, K. G., Cox, S. A., Brewer, W. E., and Hacker, D. S., "System Description of the ANL Slurry Loop Testing Facility (SLTF)," ANL/FE-84-20, 1986.

27 Thomas, D. G., "Non-Newtonian Suspensions," Ind. and Eng. Chem. 55, 27, 1963.

H. E. Snyder
Graduate Student.

D. W. Senser
Assistant Professor.

A. H. Lefebvre
Reilly Professor of Combustion Engineering.

Thermal Science and Propulsion Center,
School of Mechanical Engineering,
Purdue University, W. Lafayette, IN 47907

Mean Drop Sizes From Fan Spray Atomizers

The drop size distributions produced by two geometrically similar fan spray nozzles were measured over an injection pressure range from 1.38 to 10.34 MPa (200 to 1500 psi). The fluids employed were water, water/glycerine mixtures, silicone oils, paint, and paint solvent. These liquids were selected to provide wide ranges in liquid viscosity and surface tension. A nonintrusive Malvern 2600 particle sizer, based on the forward scattering of a 5 mW He-Ne laser beam, was used to yield line-of-sight and cross-sectional drop size distributions. The atomizer was traversed across the laser beam and drop size profiles as a function of distance from the centerline were developed. Analysis of the experimental data showed that the effects of injection pressure and liquid properties on atomization quality are described with good accuracy by the following dimensionally - correct equation.

$$\frac{\mathrm{SMD}}{d_h} = 2.83\left[\frac{\sigma\mu_L^2}{\rho_A d_h^3 \Delta P_L^2}\right]^{0.25} + 0.26\left[\frac{\sigma\rho_L}{\rho_A d_h \Delta P_L}\right]^{0.25}$$

Introduction

Fan spray atomizers are used in the coating industry, in some small annular gas turbine combustors, and in other special applications where a narrow elliptical spray pattern is more appropriate than the normal circular pattern. The elliptically shaped spray is usually formed by using high injection pressures to drive the liquid through an orifice whose projection is elliptical. The liquid streamlines within the nozzle are divergent in the direction of the slit and convergent at right angles to it. At low injection pressures, a sheet of liquid is formed at the nozzle exit. Instabilities within this sheet grow until at a critical amplitude the sheet breaks down into ligaments which rapidly collapse to form spray droplets of various sizes (Dombrowski and Johns, 1963). At higher pressures, instabilities generated within the nozzle preclude sheet formation. Ligaments form immediately downstream of the nozzle and rapidly collapse into droplets of various sizes (Janna and John, 1979).

In comparison with other forms of pressure atomizers, such as plain-orifice and pressure-swirl designs, the fan-spray atomizer has not been subjected to the same systematic study. In consequence, comparatively little is known about the drop-size distributions produced by fan-spray atomizers, and how these distributions are affected by variations in operating conditions and liquid properties. This lack of detailed information on the spray characteristics of fan spray atomizers provided the incentive for the present investigation.

Previous Work

One of the earliest experimental studies on the drop sizes produced by fan-spray atomizers was carried out by Dorman (1952). The liquids employed were dyed water and kerosine, and drop sizes were estimated by measuring the stain diameters produced on absorbent paper. This method is considered inaccurate for drop sizes less than 100 μm because the stains produced are small and difficult to measure. Furthermore, the stains from small drops are not always round, due to dye running along the fibers of the paper. For nozzle pressure differentials of 310 to 724 kPa (45 to 105 psi), Dorman's measured drop sizes ranged from 120 to 300 μm. His analysis of the experimental data led to the following dimensionally - correct equation for mean drop size

$$\mathrm{SMD}\ \alpha\ (Q\sigma\rho_L^{0.5}/\theta)^{1/3}\ \Delta P_L^{-1/2} \tag{1}$$

This equation may be rewritten in a more useful form as

$$\mathrm{SMD}\ \alpha\ \left(\frac{FN\sigma}{\theta\Delta P_L}\right)^{1/3} \tag{2}$$

Equation (2) illustrates the effect of surface tension, nozzle dimensions, and nozzle operating conditions on spray quality. It shows that, for liquids of low viscosity, the mean drop size is increased by increasing liquid surface tension and nozzle flow number, yet is reduced by increasing liquid injection pressure.

Yeo (1959) also used dimensional analysis to derive an expression for relating his measured values of mean drop size to the properties of the sprayed liquid. His expression for SMD may be written as

$$\mathrm{SMD}\ \alpha\ \frac{(Q\sigma/\rho_L)^{1/3}}{U_E} f\left(\frac{U_E}{U_R}\right) \tag{3}$$

By making appropriate substitutions, equation (3) can be expressed as

$$\mathrm{SMD} = \left(\frac{FN\sigma}{\Delta P_L}\right)^{1/3} f\left(\frac{U_E}{U_R}\right) \tag{4}$$

Contributed by the Fluids Engineering Division and presented at the Winter Annual Meeting, Chicago, Ill. November 27-December 1, 1988 of THE AMERICAN SOCIETY OF MECHANICAL ENGINEERS. Manuscript received by the Fluids Engineering Division January 4, 1989.

This equation is clearly very similar to Dorman's expression, equation (2), with an additional term to take into account the velocity of air flow past the nozzle.

It should be noted that in their dimensional analyses neither Dorman nor Yeo considered the effect of viscosity on drop size. Thus the practical application of equations (2) and (4) is limited to low viscosity liquids, such as water and light distillate fuels.

Fraser et al. (1962) extended the theories of Hagerty and Shea (1955) and Squire (1955) to derive the following expression for the drop sizes produced by the breakup of a low-viscosity, fan-spray sheet

$$D \alpha \left[\frac{\rho_L}{\rho_A}\right]^{1/6} \left[\frac{k\sigma}{\rho_L U_L^2}\right]^{1/3} \tag{5}$$

The dimensions of k in this equation are m^2, and from the description of k provided by Fraser it would appear to be proportional to the nozzle flow number. By making this substitution, and substituting also for $\Delta P_L = 0.5\rho_L U_L^2$, equation (5) becomes

$$D \alpha \left[\frac{\rho_A}{\rho_A}\right]^{1/6} \left[\frac{FN\sigma}{\Delta P_L}\right]^{1/3} \tag{6}$$

This equation is virtually identical to equations (2) and (4), as derived previously by Dorman (1952) and Yeo (1959), but it also indicates that drop sizes decrease with increase in ambient air density. This result was confirmed by Fraser et al.'s measurements of the drop sizes produced by the disintegration of water sheets at subatmospheric pressures.

Equation (6) applies solely to flow situations where the liquid viscosity is negligibly small. Dombrowski and Johns (1963) and Hasson and Mizrahi (1961) have examined the more realistic case where the liquid has finite viscosity and where the thickness of the sheet diminishes as it moves away from the orifice. The latter workers were able to correlate their measurements of Sauter mean diameter for a fan-spray nozzle by utilizing the following equation which was developed theoretically for inviscid flow and empirically correlated for viscosity,

$$\text{SMD} = 0.071 \left[\frac{t_s \, x \, \sigma \, \mu_L^{0.5}}{\rho_L^{0.5} \, U_L^2}\right]^{1/3} \text{cm} \tag{7}$$

where t_s is the sheet thickness at breakup, x is the distance downstream from the nozzle at which the sheet breaks apart; c.g.s. units are employed.

This equation was found to provide a satisfactory correlation of the experimental data over a range of viscosities from 0.003 to 0.025 Ns/m^2. However, the practical utility is seriously impaired by its dependence on t_s, the sheet thickness at breakup, which is normally unknown.

The photographic studies of Dombrowski et al. (1954, 1963) identified two main mechanisms for the disintegration of spray sheets into drops. The first mechanism is manifested as perforations which appear in the sheet and expand under the influence of surface tension forces to form a network of ligaments which break up into drops. The second mechanism is initiated by waves which are formed in the sheet and increase in amplitude with increasing distance from nozzle until they become large enough to split into ribbons of liquid parallel to the leading edge of the sheet which then disintegrate into drops. Which of these two mechanisms predominates depends upon liquid properties, nozzle design features, and nozzle operating conditions. According to Fraser et al. (1962) the production of drops by wave formation is more prevalent, and gives finer atomization than the perforated sheet mechanism.

Ford and Furmidge's (1967) photographic studies of fan-jet atomization confirmed wave formation as the main contributor to sheet disintegration, but they also observed that ligaments were formed at the edges of the sheet which broke up into chains of large drops independently of the rest of the sheet. Tests carried out on liquids of different viscosities revealed that an increase in viscosity caused a larger proportion of the total liquid in the spray to be contained in these ligaments until, at the highest viscosity examined, they were the dominant factor in the breakup of the liquid. Thus, according to Ford and Furmidge (1967), in any examination of the breakup of sprays of liquids from fan-jet nozzles it is necessary to treat the central sheet of liquid separately from the ligaments which are formed at the edges of the sheet.

Snyder et al. (1987) have also noted the presence of large drops at the edges of the sheet, with SMD values up to four times larger than at the center of the sheet. They attribute this Ignore drop size distribution in part to the migration of smaller drops to the spray centerline due to their smaller initial momentum.

Ford and Furmidge (1967) derived the following expression for the mean drop sizes produced by wavy sheet disintegration.

$$(\text{MMD})\, U_E \, \alpha \left(\frac{Q\,\sigma^2}{r\,\theta\,\rho_L^2\,U_E^2}\right)^{1/3} \tag{8}$$

For comparison with equations (2) and (4), the above equation may be rewritten as

$$\text{MMD} \, \alpha \left(\frac{FN\,\sigma^2}{r\,\theta\,\Delta P_L^2}\right)^{1/3} \tag{9}$$

This expression is of similar form to those derived previously by Dorman (1952) and Yeo (1959), with a stronger dependence of mean drop size on surface tension and injection pressure. An obvious drawback to equation (9) is its inclusion of a term to denote the length of the liquid sheet from the nozzle to the point of breakup, which is usually unknown.

For drop formation by ligament breakup at the edges of the sheet, Ford and Furmidge used Weber's (1931) expression for the wavelength of an oscillating liquid column to derive the following equation for mean drop size

Nomenclature

A,B = constants in equation (15)
D = drop diameter, m
d_h = hydraulic mean diameter of nozzle orifice, m
d_L = diameter of ligaments, m
FN = nozzle flow number, m^2
MMD = mass median diameter, m
ΔP_L = nozzle injection pressure differential, Pa
Oh = Ohnesorge number, $(\mu_L^2/\sigma\rho_L d_h)^{0.5}$
Q = nozzle flow, rate, liters/s
Re = Reynolds number, $(U_L\rho_L d_h/\mu_L)$
r = length of liquid sheet to point of breakup, m
SMD = Sauter mean diameter, m
U = velocity, m/s
We = Weber number, $(\rho_A U_A^2 d_h/\sigma)$
σ = surface tension, N/m
ρ = density, kg/m^3
μ = absolute viscosity, Ns/m^2
ν = kinematic viscosity, m^2/s
τ = wall shear stress, Pa
θ = spray angle, radians

Subscripts

A = air
E = exit value
L = liquid
R = relative value

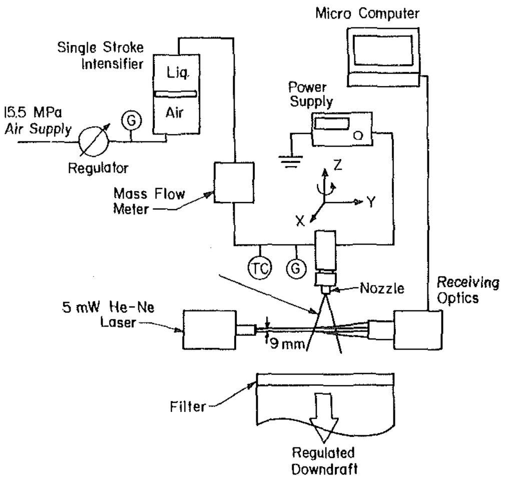

Fig. 1 Schematic of test facility

$$\mathrm{MMD} = d_L \left(\frac{3\pi}{\sqrt{2}}\right)^{1/3} \left(1 + \frac{3\mu_L}{(d_L \sigma \rho_L)^{0.5}}\right)^{1/6} \qquad (10)$$

For liquids of high viscosity this becomes

$$\frac{\mathrm{MMD}}{d_L} \propto \left(\frac{\mu_L}{(d_L \sigma \rho_L)^{0.5}}\right)^{1/6} \qquad (11)$$

or,

$$\frac{\mathrm{MMD}}{d_L} \propto \mathrm{Oh}^{1/6} \qquad (12)$$

It is of interest to note in equation (10) that mean drop size is independent of nozzle injection pressure. Also noteworthy in both equations (9) and (10) is the absence of any term to denote an effect of air density on mean drop size. Thus an important conclusion from the experimental and analytical studies of Ford and Furmidge is that the mean drop sizes produced by fan-jet atomizers are independent of air density, regardless of whether the drops are produced from the central sheet or from the ligaments formed at the edges of the sheet.

A significant feature of Ford and Furmidge's experimental study is that it was confined to relatively low injection pressures [<0.38 MPa (40 psi)]. Photographs taken by Janna and John (1979) of water sprays injected at much higher pressures [17.3 MPa (2,500 psi)] show ligament formation occurring at the nozzle exit with ligaments breaking down into drops of various sizes further downstream. Of special interest and importance is the absence of sheet formation in this high pressure case. According to Janna and John, the liquid is deformed into ligaments by the wall shear stresses within the nozzle, with the wall shear stress being a maximum at the nozzle exit. These ligaments then disintegrate into drops of various sizes under the action of viscous and surface tension forces outside the nozzle. Any further breakdown of drops is caused by air friction.

Janna and John collected drops of water and water-glycerine mixtures on soot-coated slides and measured the flattened particle sizes with an optical microscope. Their results were correlated satisfactorily by the expression

$$\frac{\mathrm{MMD}}{d_0} = 8.5183 - 1.1113 \log\,(\tau \rho_L Q / \mu_L \sigma) \qquad (13)$$

Experimental

The apparatus employed is shown schematically in Fig. 1. A single stroke intensifier is used to pressurize the liquid, thereby eliminating the potential complexities associated with pressure pulses in commercial pumps. Driver air and liquid are separated by an aluminum piston in order to prevent gasification of the liquid. Liquid mass flow rate, temperature, and pressure measurements are made just upstream of the nozzle. Liquid delivery pressure is controlled by regulating the air driver pressure.

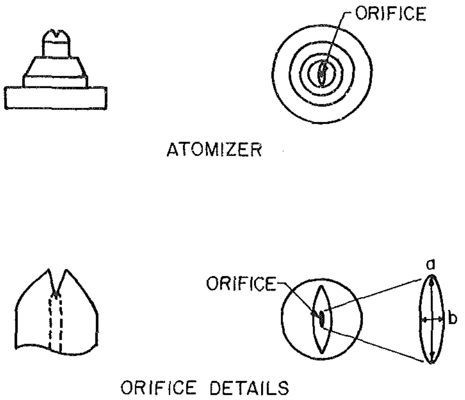

Fig. 2 Geometrical details of fan-spray nozzle

Table 1 Fluid property data

Fluid	Density kg/m^3	Viscosity m^2/s $\times 10^{-6}$	Surface Tension N/m
Water	1000	1.0	0.073
Glycerine/Water	1150	10	0.068
Glycerine/Water	1220	100	0.065
LS 150	900	1.33	0.028
Paint	990	17	0.030
Silicone oil	940	10	0.020
Silicone oil	970	100	0.021

The nozzle is mounted on a translator directly above a rectangular 152 cm × 102 cm draft vent. The nozzle and resulting spray are translated both vertically and horizontally relative to the optical diagnostics which remain stationary. Paper filters are placed over the vent inlet to act as a diffuser and liquid trap. The downward flow removes solvent vapors and entrains any overspray, preventing accumulation on lenses and surrounding equipment. Average air velocities at the filter surface are approximately 3 m/s.

A general drawing of the nozzles employed in this study is shown in Fig. 2. The two nozzle flow areas were measured from projections of negatives provided by a scanning electron microscope with a built-in length scale. The flow areas were determined to be 0.0320 mm^2 and 0.0579 mm^2 which compared favorably with the calculated values of 0.0343 mm^2 and 0.0582 mm^2 assuming an elliptical orifice shape. The corresponding hydraulic diameters, using measured flow areas, were 0.1570 mm and 0.2143 mm, respectively.

The liquids employed in this study exhibit wide variations in viscosity and surface tension. They were selected to allow the effects of these two properties on drop size distribution to be investigated separately. Their properties of relevance to atomization are listed in Table 1. The water/glycerine mixtures allowed viscosity to be varied by a factor of one hundred while maintaining surface tension constant at around 0.070 N/m. Silicone oils were also used to provide a tenfold variation in viscosity at a much lower level of surface tension, namely 0.021 N/m. The other two liquids listed in Table 1 are a commercial enamel paint and a paint solvent (LS 150). These two liquids were selected to provide a large variation in viscosity for a constant value of surface tension - circa 0.029 N/m, which is representative of practical hydrocarbon liquid fuels.

Drop size measurements were made with a Malvern 2600 Particle Sizer. This instrument is based on the Fraunhoffer diffraction theory of a collimated laser beam scattered by drops. The principle of operation of the Malvern has been reviewed by Swithenbank et al. (1977), while its accuracy and limitations have been discussed by Hirleman et al. (1984) and Dodge and Cerwin (1984). All measurements were made with a 300 mm lens, yielding percent volume fractions for the 16 bin sizes listed in Table 2. Data reductions performed with both Rosin-Rammler and model independent options showed little change in log error. The data presented are based on the Rosin-Rammler procedure.

The Malvern is a spatial, line-of-sight instrument. It provides measurements of drop size distribution in terms of mass fractions (m_i), mass fraction of spray contained within its 9 mm diameter laser beam due to droplets in the range of diameters of bin i, and sample percent volume concentration (SPVC), the percentage of the laser probe volume occupied by droplets. Determination of actual SPVC requires user input of the illuminated sample length (ISL) from which the volume of the laser probe is calculated. As shown in Fig. 3, the ISL varies along the major axis. By translating the atomizer at right angles to the major axis of the nozzle, line-of-sight drop size measurements are made as a function of radial distance from the centerline, X, at a constant distance downstream of the nozzle, Z. These measurements indicate the variation in drop size from the centerline to the edge of the spray, as well as the degree of spray symmetry.

Table 2 Malvern 2600 Bin Sizes (300 mm lens)

Bin	Particle diameter (μm)	
	Lower	Upper
1	1.5	5.8
2	5.8	7.2
3	7.2	9.1
4	9.1	11.4
5	11.4	14.5
6	14.5	18.5
7	18.5	23.7
8	23.7	30.3
9	30.3	39.0
10	39.0	50.2
11	50.2	64.6
12	64.6	84.3
13	84.3	113.
14	113.	160.
15	160.	262.
16	262.	564.

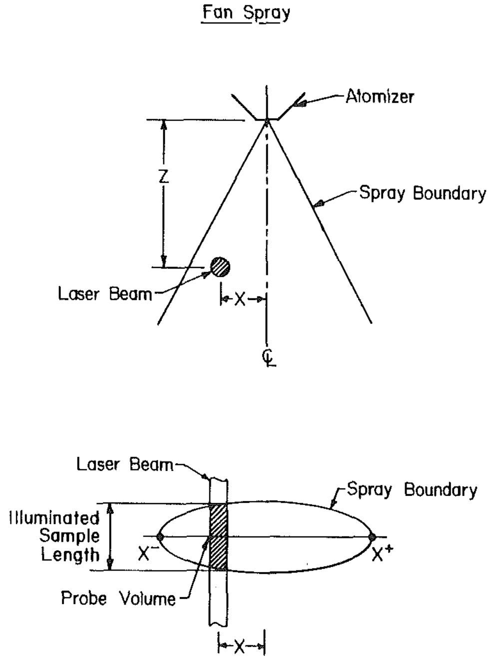

Fig. 3 Fan spray boundary

The results presented in Figs. 4 to 8 were obtained by traversing the atomizer slowly across the laser beam at a constant rate. The translational speed of the atomizer was adjusted to allow some two thousand five hundred separate measurements to be taken as the laser beam moved from one outside edge of the spray to the other outside edge. Thus the SMD values shown in Figs. 4 to 8 represent the compilation of a very large number of separate measurements carried out in all regions of the spray.

Results

Measurements of mean drop size were carried out at liquid injection pressures ranging from 1.38 to 10.34 MPa (200 to 1500 psi), with the liquid discharging from the nozzle into air at normal atmospheric pressure and temperature. All measurements were made at a distance of 15 cm downstream from the nozzle. The results obtained with water/glycerine mixtures are shown in Fig. 4. In common with all previous measurements on pressure atomizers, they show that mean drop sizes increase with an increase in viscosity and diminish

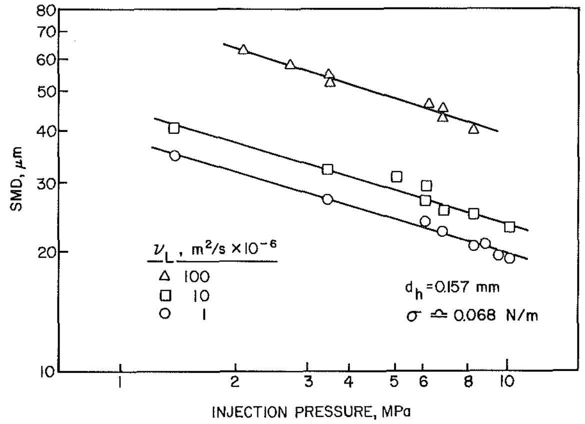

Fig. 4 Influence of viscosity on mean drop size for liquids of high surface tension

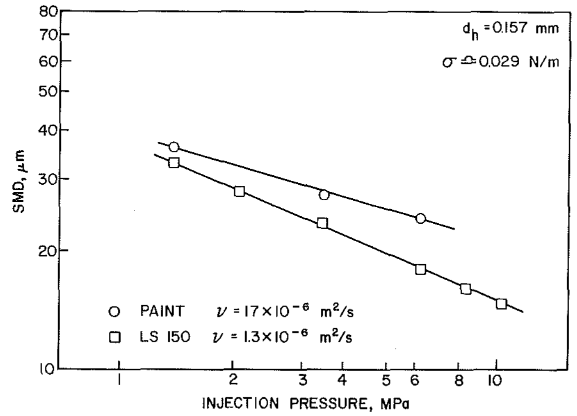

Fig. 5 Influence of viscosity on mean drop size for liquids of medium surface tension

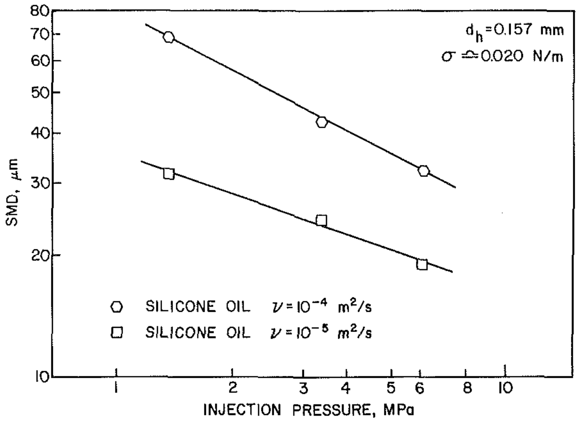

Fig. 6 Influence of viscosity on mean drop size for liquids of low surface tension

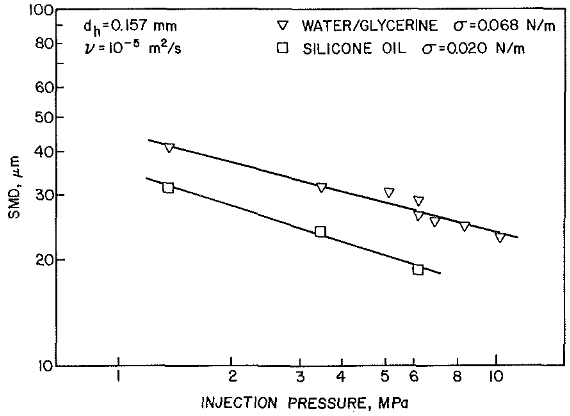

Fig. 7 Graphs illustrating the influence of surface tension on mean drop size

with an increase in liquid injection pressure. Figures 5 and 6 show similar data to illustrate the effects of viscosity and injection pressure on mean drop size. The results shown in Fig. 5 were obtained using a paint and a paint solvent. For these two liquids the surface tension values are 0.030 and 0.028 N/m, respectively. Similar data for liquids of lower surface tension (≃ 0.020 N/m) were obtained using silicone oils, as shown in Fig. 6. The effect of surface tension on mean drop size may be assessed by comparing the results contained in Figs. 4-6, but it is demonstrated more directly in Fig. 7. This figure compares measured values of SMD obtained with silicone oil and a glycerine water mixture. Both these liquids have the same viscosity, so the results shown in Fig. 7 illustrate the effect of increase in surface tension on mean drop size.

The influence of nozzle dimensions on mean drop size was investigated by carrying out measurements on two geometrically - similar nozzles of different size. For the data shown in Figs. 4-7, the hydraulic mean diameter of the nozzle discharge orifice was 0.157 mm. The results presented in Fig. 8 were obtained using a geometrically similar nozzle for which the corresponding hydraulic mean diameter was 0.214 mm. The influence of atomizer dimensions on mean drop size can be judged by comparing Figs. 4 and 8. These two figures contain experimental data on SMD that were acquired with the same liquids at the same nozzle operating conditions. The only difference between these two figures lies in the size of the nozzle employed, so that comparison of the two sets of SMD data shows directly the influence of nozzle dimension on mean drop size.

While specific size distribution functions can be assumed as part of the data processing of the Malvern spray analyzer, for the present experiments the Rosin-Rammler (1933) drop-size distribution parameter was selected. It may be expressed in the form:

$$1-\nu=\exp(-bx)^{q} \qquad (14)$$

where ν is the fraction of the total volume contained in drops of diameter less that x, and b and q are constants. The exponent q provides a measure of the spread of drop sizes. The higher the value of q, the more uniform is the spray. If q is infinite, the drops in the spray are all the same size. For most practical pressure atomizers, the values of q usually lie between 1.5 and 4. For the two fan-spray nozzles employed in the present research, the values of q ranged from around 2 to around 4. The lowest values of q were found in the central portion of the spray and the highest values in the two "edges" of the spray where drop sizes are appreciably larger than in the central spray core.

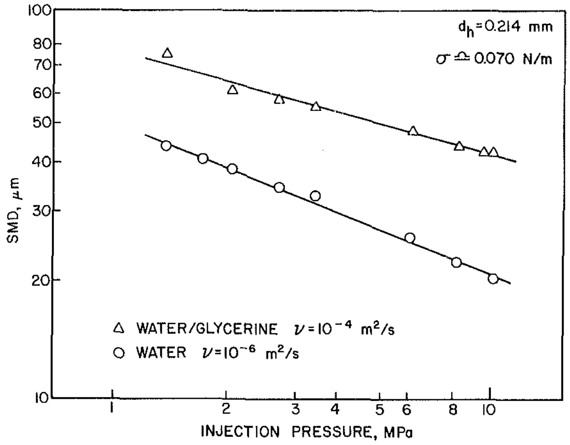

Fig. 8 Influence of viscosity on mean drop size for a nozzle of larger flow number

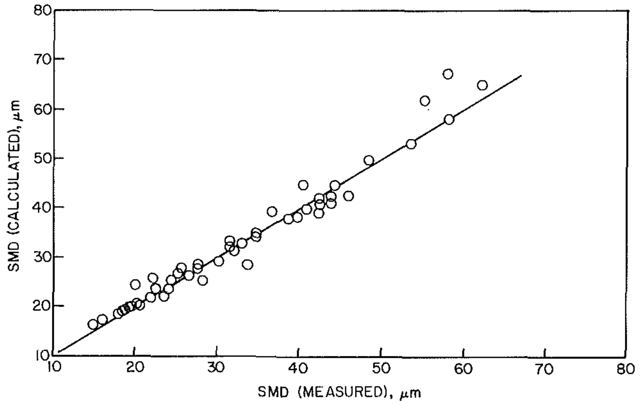

Fig. 9 Comparison of measured values of mean drop size with predicted values based on equation (16)

Correlation of the experimental data was attempted using equations (2), (4) and (6), but the best correlation was provided by a parameter recently-developed by Lefebvre (1987) and Wang and Lefebvre (1987) for pressure-swirl atomizers. This dimensionally correct parameter has the form

$$\frac{\mathrm{SMD}}{d_h}=A\left(\frac{\sigma\mu_L^2}{\rho_A d_h^3\Delta P_L^2}\right)^{0.25}+B\left(\frac{\sigma\rho_L}{\rho_A d_h\Delta P_L}\right)^{0.25} \qquad (15)$$

Analysis of the experimental data yielded optimum values for A and B of 2.83 and 0.26, respectively. Equation (15) thus becomes

$$\frac{\mathrm{SMD}}{d_h}=2.83\left(\frac{\sigma\mu_L^2}{\rho_A d_h^3\Delta P_L^2}\right)^{0.25}+0.26\left(\frac{\sigma\rho_L}{\rho_A d_h\Delta P_L}\right)^{0.25} \qquad (16)$$

The ability of equation (16) to predict values of SMD over wide ranges of liquid viscosity, surface tension, and injection pressure is demonstrated in Fig. 9. In general, the accuracy of prediction obtained is very satisfactory, almost all of the predicted values of SMD lying within 5 percent of the experimental values. Only for liquids which combine high surface tension with very high viscosity (10^{-4}m^2/s or 100 cst) does the prediction accuracy fall off. There the calculated values exceed the measured values by about 10 percent. During the test program it was noted that when spraying these liquids, a coherent liquid sheet persisted for some distance before disintegrating into drops, whereas with liquids of comparatively low viscosity and/or surface tension the sheet disintegration process commenced closer to the nozzle. Thus the observed discrepancy between measured and predicted values of SMD for these special liquids is attributed to a change in the mechanism of atomization which results when liquid viscosity and surface tension are both relatively high.

Conclusions

Over the following range of conditions:

Liquid viscosity	10^{-6} to 10^{-4} m^2/s
Liquid surface tension	0.020 to 0.073 N/m
Liquid density	900 to 1220 kg/m^3
Nozzle injection pressure	1.38 to 10.34 MPa
Hydraulic mean diameter of nozzle discharge orifice	0.157-0.214 mm

mean drop sizes for fan-spray atomizers are predicted with good accuracy by the equation:

$$\frac{\mathrm{SMD}}{d_h} = 2.83\left(\frac{\sigma\mu_L^2}{\rho_A d_h^3 \Delta P_L^2}\right)^{0.25} + 0.26\left(\frac{\sigma\rho_L}{\rho_A d_h \Delta P_L}\right)^{0.25}$$

This equation is unsuitable for liquids which combine high surface tension with very high viscosity (100×10^{-6}m^2/s, or 100 cst). For such liquids the predicted values tend to be higher than the corresponding measured values by as much as 10 percent. This discrepancy is attributed to a change in the mode of sheet disintegration into drops which occurs when high surface tension is accompanied by an abnormally high viscosity. This phenomenon is currently the subject of further investigation.

References

Dodge, L. A., and Cerwin, S. A., 1984, "Extending the Applicability of Diffraction-Based Drop Sizing Instruments," *Liquid Particle Size Measurement Techniques*, ASTM STP 848, ed. J. M. Tishkoff, R. D. Ingebo and J. B. Kennedy.

Dombrowski, N., and Fraser, R. P., 1954, "A Photographic Investigation into the Disintegration of Liquid Sheets," *Phil. Trans. Roy. Soc.*, London, Series A, *Maths. and Phys. Sci.*, Vol. 247, No. 924, pp. 101-130.

Dombrowski, N., and Johns, W. R., 1963 "The Aerodynamic Instability and Disintegration of Viscous Liquid Sheets," *Chemical Engineering Science*, Vol. 18, pp. 203-214.

Dorman, R. G., 1952, "The Atomization of Liquid in a Flat Spray," *British Journal of Applied Physics*, Vol. 3, pp. 189-192.

Ford, R. E. and Furmidge, C. G. L., 1967, "The Formation of Drops from Viscous Newtonian Liquids Sprayed through Fan-Jet Nozzles," *British Journal of Applied Physics*, Vol. 18, pp. 335-349.

Fraser, R. P., Eisenklam, P., Dombrowski, N., and Hasson, D., 1962, "Drop Formation from Rapidly Moving Sheets," *A.I.Ch.E. Journal*, Vol. 8, No. 5, pp. 672-680.

Hagerty, W. W., and Shea, J. F., 1955, "A Study of the Stability of Plane Fluid Sheets," ASME *Journal of Applied Mechanics*, Vol. 22, No. 4, pp. 509-514.

Hasson, D., and Mizrahi, J., 1961, "The Drop Size of Fan Spray Nozzle, Measurements by the Solidifying Wax Method Compared with Those Obtained by Other Sizing Techniques," *Trans. Inst. Chem. Engrgs.*, Vol. 39, No. 6, pp. 415-422.

Hirleman, E. D., Oeschsle, V., and Chigier, N. A., 1984, "Response Characteristics of Laser Diffraction Particle Size Analyzers: Optical Sample Volume Extent and Lens Effects," *Optical Engineering*, Vol. 23, No. 5, pp. 610-619.

Janna, W. S., and John, J. E. A., 1979, "Drop-Size Distributions of Newtonian Liquid Sprays Produced by Fan-Jet Pressure Nozzles," ASME *Journal of Engineering for Industry*, Vol. 101, pp. 171-177.

Lefebvre, A. H., 1987, "Prediction of Sauter Mean Diameter for Simplex Pressure-Swirl Atomizers," *International Journal of Atomization and Spray Technology*, Vol. 3, pp. 37-51.

Rosin, P., and Rammler, E., 1933, "The Laws Governing the Fineness of Powdered Coal," *J. Inst. Fuel*, Vol. 7, No. 31, pp. 29-6.

Snyder, H. E., Senser, D. W., Lefebvre, A. H., and Coutinho, R. S., 1987, "Drop Size Measurements in Electrostatic Paint Sprays," paper presented at the IEE/Industry Applications Society Meeting in Atlanta, Ga.

Squire, H. B., 1953, "Investigation of the Instability of a Moving Liquid Film," *British Journal of Applied Physics*, Vol. 4, pp. 167-169.

Swithenbank, J., Beer, J. M., Taylor, D. S., Abbot, D. and McCreath, G. C., 1977, "Experimental Diagnostics in Gas Phase Combustion Engines," *Prog. Aeronaut. Astronaut.*, B. T. Zinn (Ed.), AIAA, Vol. 53, p. 421.

Yeo, D., 1959, "Droplet Size Distributions from Flat Spray Nozzles Fitted to Aircraft," *Journal of Agricultural Engineering Research*, Vol. 4, pp. 93-99.

Wang, X. F., and Lefebvre, A. H., 1987, "Mean Drop Sizes from Pressure-Swirl Nozzles," *AIAA Journal of Propulsion and Power*, Vol. 3, No. 1, pp. 11-18.

Weber, C., 1983, "Disintegration of Liquid Jets," *Z. agnew Math. and Mech. (German)*, Vol. 11, No. 2, pp. 136-159.

D. A. Nelson
Assoc. Member ASME

L. W. Evers
ME-EM Department,
Michigan Technological University,
Houghton, MI 49931

D. M. O'Donnell
Science Applications International
Corporation,
San Diego, CA 92121

E. J. Morgan
Mercury Marine Division,
Brunswick Corporation,
Fond du Lac, WI 54935

Determination of Surface Pressure Distributions for Axisymmetric Bluff Bodies

The conditions governing liquid droplet breakup are particularly important to the process of fuel atomization for spark-ignition engines. A proper mathematical description of the problem requires knowledge of the pressure distributions about the droplet surface. This work presents the results of measurements of pressure distributions about the surfaces of certain bluff, axi-symmetric bodies in airflows at $Re_D = 3 \times 10^4$ *and* $Re_D = 10^5$. *The results of measurements from a sphere, disk, and two ellipsoids are used to develop a general method for estimating surface pressures. These estimates are compared with the results of pressure measurements about the surfaces of a concave and a nonellipsoidal convex body and with results obtained from a numerical study by other authors.*

Introduction

The production of liquid sprays or mists with desired droplet sizes is essential to a variety of processes. These include direct delivery of medicines to the respiratory system [1], pneumatic fuel injection in gas turbines [2], and in spark-ignited engines [3]. The process by which liquid droplets deform and ultimately may break up has a primary role in determining the resultant droplet size distribution.

Some mathematical models developed to predict equilibrium shapes of liquid droplets tend to be highly sensitive to the assumed pressure distribution about the droplet surface. This requires a method for predicting *a priori* the pressure about the surface of a droplet of unknown shape.

This work develops a method for predicting surface pressure distributions for axisymmetric bluff bodies, based only on the local geometry. This pressure estimation method has been used in conjunction with a marching technique to predict equilibrium droplet shapes [4].

The objectives of this research were: (1) measure pressures about the surfaces of a family of oblate ellipsoids in airflow at $\mathrm{Re}_D = 3 \times 10^4$ and $\mathrm{Re}_D = 10^5$; (2) correlate surface pressure with location and geometry to enable prediction of pressure distributions for other ellipsoidal bodies; and (3) predict surface pressure distributions for selected nonellipsoidal, axisymmetric bluff bodies and compare predictions with measurements. The results have significant implications for the prediction of conditions conducive to atomization and liquid droplet breakup.

The process by which liquid droplets break up is fundamental to the pneumatic atomization process. The ultimate droplet size distribution in sprays from pneumatic atomizers is strongly affected by the droplet breakup process [3]. Currently, there is particular interest in development of pneumatic fuel atomization systems for spark-ignited engines. Improved atomizers offer the potential for improved combustion efficiency and engine performance. A better understanding of the conditions governing droplet breakup is essential to prediction of size distributions in sprays and optimization of atomizer performance.

Background

The situation of interest is that of a liquid droplet in air. The air has a nominal, constant velocity U_∞ relative to the droplet. The internal circulation of the droplet is negligible. A simple force balance on the droplet yields:

$$p_g - p_L = \sigma\left(\frac{1}{r_1} + \frac{1}{r_2}\right). \tag{1}$$

The quantity σ is the surface tension for the air-liquid interface and r_1 and r_2 are the principal radii of curvature at a point on the droplet surface. The quantities p_g and p_L are gas and liquid pressures at the air-liquid interface. Equation (1) is recast in dimensionless form as:

$$\Delta p^* = \frac{4}{\mathrm{We}}\left(\frac{1}{r_1^*} + \frac{1}{r_2^*}\right) \tag{2}$$

where $\Delta p^* = 2(p_g - p_L)/\rho\, U_\infty{}^2$, $r_1^* = r_1^*/r_{\max}$, $r_2^* = r_2/r_{\max}$ and $r_{\max}$ is the maximum droplet radius in a plane normal to the direction of motion. The quantity We, the Weber number, is defined by $\mathrm{We} = (2\,\rho\, U_\infty{}^2\, r_{\max})/\sigma$ and represents the ratio of inertial to surface tension forces. Equation (2) demonstrates that the curvature of the droplet surface at any point depends solely on the pressure difference Δp^* and the Weber number. Thus, given the value of the Weber number and the pressure difference everywhere on the droplet surface, the surface curvature at every point is specified. This allows an equilibrium shape for a droplet to be determined from the Weber number and the surface pressure difference. However, since the pressure distribution is shape-dependent, a *priori*

Contributed by the Fluids Engineering Division for publication in the JOURNAL OF FLUIDS ENGINEERING. Manuscript received by the Fluids Engineering Division September 17, 1987.

knowledge of Δp^* is unavailable. Savic [5] and Pruppacher and Pitter [6] attempted to predict the shapes of falling droplets using a form of equation (2), but discovered the pressure distributions around "droplet-shaped" (i.e., axisymmetric, bluff) bodies were unavailable.

Krzeczkowski [7] and Hinze [8] propose a critical Weber number, $\mathrm{We}_{\mathrm{cr}}$, above which a droplet unconditionally breaks into smaller droplets. The value of $\mathrm{We}_{\mathrm{cr}}$ has been placed between 5 and 15 by various experimental investigations [7, 8, 9].

Equation (2) suggests a technique for predicting $\mathrm{We}_{\mathrm{cr}}$. This method consists of selecting an appropriate starting point (e.g., the rear stagnation point) and determining the principal radii of curvature at that point from equation (2), based on the Weber number and Δp^*. The surface is then projected incrementally and the calculation repeated. This iterative procedure can be used to predict the shape of a droplet under stated conditions of Weber number and surface pressure differential. This approach was employed by Ruman [4] to predict equilibrium shapes of liquid droplets in gas streams.

If the procedure does not yield a closed curve, it is inferred that the droplet must break into smaller droplets under the stated conditions. Note that this does not address the issue of stability of the droplet. It may be possible to satisfy the equilibrium force balance for a droplet which is unstable and will break up. However, conditions under which equation (2) cannot be satisfied must lead to droplet breakup. Thus, this technique may yield a sufficient, though not necessary, condition for droplet break-up.

Efforts to determine a value for $\mathrm{We}_{\mathrm{cr}}$ using this method have shown results which are highly sensitive to the assumed pressure distribution. However, pressure data for axisymmetric, bluff bodies (other than spheres) generally are not available in the literature.

The goal of this work is to measure the surface pressures around oblate ellipsoids in an airflow. A correlative method for estimating the surface pressure from the local surface curvature is then developed and tested against data obtained in this and other investigations [10].

Experimental Methods

Six highly polished, aluminum models were tested in a suction type, open-circuit wind-tunnel at Reynolds numbers (based on maximum model diameter) of 3×10^4 and 1×10^5. (Unless stated otherwise, the term "model" will refer to physical models.)

Consider the case of a spherical water droplet, 1000 μm in diameter, in air at We = 10. This translates to a Reynolds number of approximately 1.6×10^3. Reynolds numbers (based on model diameter) this low were not sustainable in the wind tunnel, given that model diameters of less than a few centimeters were not practical. However, Schlichting [11] demonstrates the drag coefficient for a sphere varies little over the range $10^3 < \mathrm{Re} < 2 \times 10^5$. Thus it was initially assumed that, for all models, the form of the pressure distribution was consistent with the drag coefficient and varied little over that Reynolds number range. This allowed measurements to be performed at $\mathrm{Re} >> 10^3$ without losing applicability to the problem of interest. The results tend to verify the assumption of pressure distribution similarity over the range $10^3 < \mathrm{Re} < 10^5$.

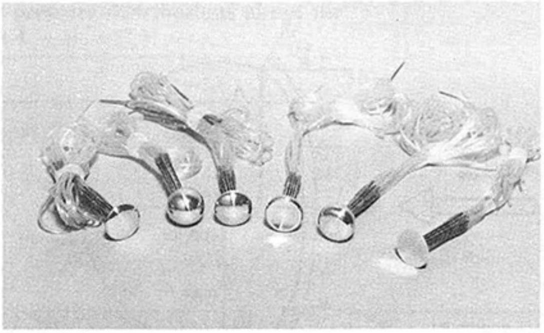

Fig. 1 The six models tested in the study are shown, left to right. A 4:1 ellipsoid, a sphere, a 2:1 ellipsoid, a concave model, a convex model and a disk.

The six models tested, shown in Fig. 1, were: a sphere, two ellipsoids (major to minor axis ratios of 2:1 and 4:1), a disk, a nonellipsoidal convex body and a concave, or dimpled, body. Each model had a maximum diameter in a plane normal to the flow of 4.0 cm. Twelve pressure taps (0.5 mm diameter) were drilled in each model in a helical pattern about the model axis. Each tap connected via an internal passage to a separate, stainless steel tube. The tubes were arranged in a 10-mm-diameter circle about the support sting at the rear of the model. Each tube connected to an inclined manometer filled with Merian red oil (specific gravity = .826). This system was capable of resolving pressure differences of 2.0 Pascals or greater.

The tubes at the rear of the models may affect boundary layer separation. For this reason, no attempts were made to estimate the separation points. Rather, the correlative expres-

Nomenclature

A_n = nth Fourier cosine coefficient for pressure at sphere surface
B_n = nth Fourier cosine coefficient for pressure at disk surface
C_n = $A_n - B_n$
C_p = pressure coefficient at model surface, $2(p-p_\infty)/\rho U_\infty{}^2$
$C_{p_{dsk}}$ = pressure coefficient at disk model surface
$C_{p_{est}}$ = estimated surface pressure coefficient
$C_{p_{E2}}$ = pressure coefficient at 2:1 ellipsoid model surface
$C_{p_{E5}}$ = pressure coefficient at 5:1 ellipsoid model surface
$C_{p_{sph}}$ = pressure coefficient at spherical model surface
D = maximum diameter normal to flow
p = pressure at model surface
p_g = gas pressure at interface
p_L = liquid pressure at interface
p_∞ = free-stream pressure
r = radial distance from model axis
$r_{\max}$ = maximum radial distance from model axis to surface; $r_{\max} = D/2$
r^* = dimensionless radial distance from model axis
r_1 = first principal radius of curvature
r_1^* = dimensionless first principal radius of curvature
r_2 = second principal radius of curvature
r_2^* = dimensionless second principal radius of curvature
Re_D = Reynolds number; $\mathrm{Re}_D = \rho U_\infty D/\mu$
s = arc distance from forward stagnation point
s^* = dimensionless arc distance from forward stagnation point
$s_{\max}$ = arc distance to point at which $r = r_{\max}$
U_∞ = freestream velocity
We = Weber number; We = 2 $\rho U_\infty^2 r_{\max}/\sigma$
$\mathrm{We}_{\mathrm{cr}}$ = critical Weber number
Δp^* = $2(p_g - p_L)/\rho U_\infty^2$
μ = fluid viscosity
θ = angle of surface normal with respect to model axis
ρ = mass density
Σ = summation symbol
σ = surface tension

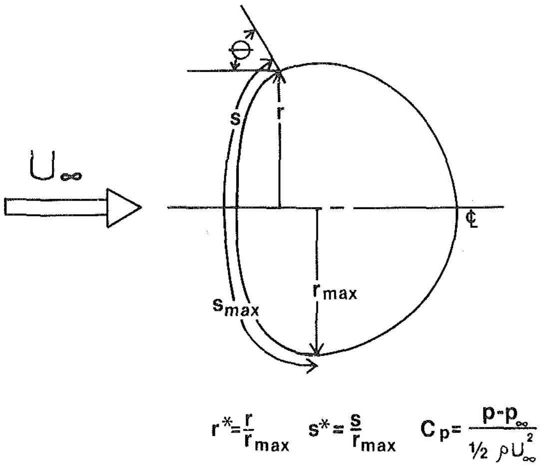

Fig. 2 The geometric variables employed are defined

sion developed was applied only to the forward-facing portion of the model surfaces. A constant value was used for the pressure coefficients over the rear-facing portions of the model surfaces, consistent with observations. However, the pressure distributions in these regions in the absence of the protruding tubes may differ from the observations reported here.

Experimental Error. Pressure measurements were performed repetitively, with a minimum of twelve values obtained at each pressure tap at $\mathrm{Re}_D = 3 \times 10^4$ and at least four values obtained at each tap for $\mathrm{Re}_D = 10^5$. Each model was rotated 90 degrees about its axis of symmetry between measurements. This was done to minimize any effects which may be attributable to misalignment of the model or nonuniformity of flow in the wind tunnel.

Pressure data are reported in the form of the dimensionless pressure coefficient, $C_p = 2(p - p_\infty)/\rho U_\infty^2$. The quantity p is the pressure measured at the model surface and p_∞ is the stagnation pressure. Values of C_p presented are the mean values of the pressure coefficients calculated from measurements at a given location on a model surface and at a particular Reynolds number. The standard deviations of the C_p measurements are generally 0.02 or less, with a maximum standard deviation of .06. (Note the values are dimensionless; C_p is of order one or less). It should be noted that these values represent the standard deviations of the dimensionless difference between the model surface pressure and the stagnation pressure, not the standard deviations of the surface pressure alone.

Results

The pressure on the surface of a body is assumed a function of location on the surface and surface curvature. This implies the pressure coefficient may be described by an equation of the general form

$$C_p = f(r^*, \theta/s^*) \tag{3}$$

where C_p is the dimensionless pressure at the model surface, r^* and s^* are the dimensionless radius from the model axis and the dimensionless arc distance from the forward stagnation point, respectively. (See Fig. 2.) The variable θ is the angle of the surface normal with respect to the model axis.

Results for the sphere, flat plate, 2:1 ellipsoid and 4:1 ellipsoid are presented in Fig. 3 for $\mathrm{Re}_D = 3 \times 10^4$ and $\mathrm{Re}_D = 10^5$. (Note the sphere and flat plate may be considered ellipsoids with major-to-major axis ratios of unity and infinity, respectively.)

The pressure data for the flat plate and the sphere are used to develop an expression for pressure as a function of location and local surface curvature. The values predicted by the resulting expression are compared with measured pressures about the surfaces of the 2:1 and 4:1 ellipsoids, the concave and the convex axisymmetric bluff bodies.

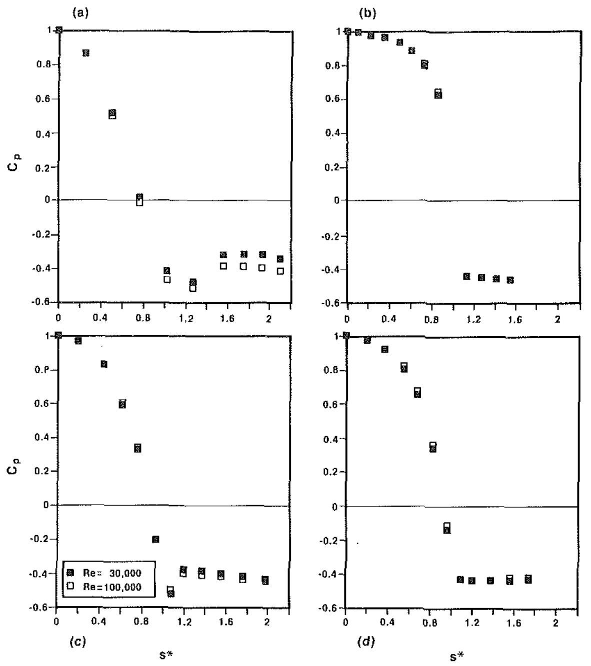

Fig. 3 Pressure is shown as a function of distance from the forward stagnation point for: (*a*) the sphere; (*b*) the disk; (c) the 2:1 ellipsoid; (*d*) the 4:1 ellipsoid

Estimation of Surface Pressures. The quantity θ/s^* is equal to unity everywhere on the surface of a sphere and is zero on the forward-facing surface of a disk. For those two shapes, equation (3) implies the surface pressure is a function solely of r^*, the dimensionless radial distance from the model axis. For the remaining, intermediate ellipsoids studied (axis ratios of 2:1 and 4:1), the pressure coefficient was observed to be approximately linear in the variable θ/s^* with r^* held constant. While it may be argued that a higher-order expression for $C_p(r^*, \theta/s^*)$ would be more accurate, the results will demonstrate a linear expression in θ/s^* results in generally good agreement between observed and predicted pressure coefficients for a variety of shapes.

For any of the four ellipsoids, the pressure at a point on the surface may be estimated from

$$C_{p_{\mathrm{est}}}(r^*, \theta/s^*) = (C_{p_{\mathrm{sph}}}(r^*) - C_{p_{\mathrm{dsk}}}(r^*))\theta/s^* + C_{p_{\mathrm{dsk}}}(r^*) \tag{4}$$

The pressure coefficients for the sphere and disk are denoted by $C_{p_{\mathrm{sph}}}(r^*)$ and $C_{p_{dsk}}(r^*)$, respectively.

Application of equation (4) to estimation of the pressure on an ellipsoidal surface is illustrated by Fig. 4, which shows a family of lines of constant r^* connecting pressure values on the forward-facing disk surface (the line $\theta/s^* = 0$) and the sphere surface (the line $\theta/s^* = 1$). The pressure at a point on an ellipsoid surface can be estimated by fixing the point in terms of θ/s^* and r^*, which specifies both the location and the local curvature. The estimate of C_p $(r^*, \theta/s^*)$ is read directly from Fig. 4.

It should be noted that equation (4) is but one example of a linear expression for estimation of the surface pressures. Other equations could be developed which are based on pressure data from surfaces other than the disk and sphere. However, use of $C_{p_{\mathrm{sph}}}(r^*)$ and $C_{p_{\mathrm{dsk}}}(r^*)$ is particularly convenient since θ/s^* is constant over the entire surface for those two shapes.

Estimating the pressure at a given point on the surface of an

Table 1 Fourier cosine coefficients for the pressure distributions about the sphere (A_n), the disk (B_n) and the difference ($A_n - B_n = C_n$)

	$\text{Re}_D = 3 \times 10^4$			$\text{Re}_D = 10^5$		
	A_n	B_n	C_n	A_n	B_n	C_n
$n=0$	.130	.626	−.496	.103	.630	−.527
1	.760	.552	.208	.790	.549	.241
2	.168	−.280	.448	.172	−.283	.377
3	−.090	.153	−.243	−.093	.157	−.250
4	−.030	−.075	.105	.020	−.076	.096
5	−.001	.026	−.027	.007	.024	−.017

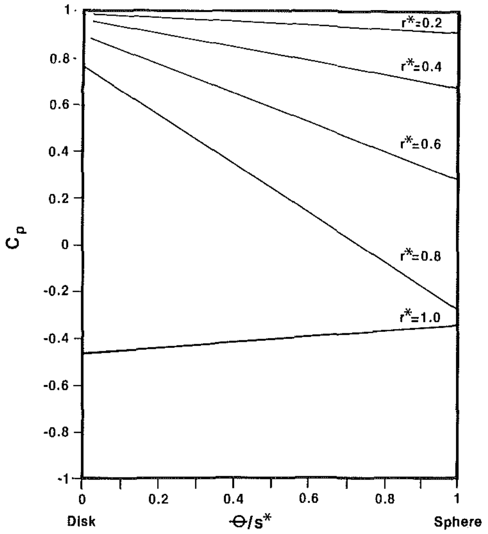

Fig. 4 The linear interpolation estimation method is illustrated. Lines connect pressure on the disk surface ($\theta/s^* = 0$) with pressures at the same r^* values on the sphere surface ($\theta/s^* = 1$). Pressures are estimated from a six-term Fourier cosine series.

ellipsoid according to equation (4) requires the pressure at the corresponding r^* on the surface of the sphere and disk. The values of $C_{p_{sph}}(r^*)$ and $C_{p_{dsk}}(r^*)$ may be estimated from a Fourier cosine series fit to the data for the sphere and disk; i.e.,

$$C_{p_{sph}}(r^*) = \sum_{n=0}^{\infty} A_n \cos(2n \arcsin r^*) \qquad (5)$$

and

$$C_{p_{dsk}}(r^*) = \sum_{n=0}^{\infty} B_n \cos(2n \arcsin r^*) \qquad (6)$$

The first six coefficients are sufficient to accurately reproduce the experimental results for the sphere and flat disk. These coefficients are given as Table 1. Table 1(*c*) lists the results of a term-by-term subtraction of the coefficients in 1(*b*) from those in 1(*a*), corresponding to the first six Fourier coefficients of the estimate of the function $C_{p_{sph}}(r^*) - C_{p_{dsk}}(r^*)$. Equation (4) can thus be written as:

$$C_{p_{est}}(r^*, \theta/s^*) = \sum_{n=0}^{5} C_n \cos(2n \arcsin r^*)\, \theta/s^* + \sum_{n=0}^{5} B_n \cos(2n \arcsin r^*) \qquad (7)$$

Equation (7) can be used to estimate the pressure on the surface of ellipsoidal bodies, up to the point where $r^* = 1$; i.e., for all points such that $s^* \leq s_{\max}/r_{\max}$. This corresponds to the forward-facing portion of the model. For $s^* > s_{\max}/r_{\max}$, the observed value of C_p varies only weakly with location. The pressure coefficient in this region also varies little between models. Thus, it is reasonable to approximate the pressure coefficient by a constant in the region $s^* > s_{\max}/r_{\max}$. The values employed here, −.40 for $\text{Re}_D = 3 \times 10^4$ and −.43 for $\text{Re}_D = 10^5$, are the medians of all C_p values obtained in this region at the respective Reynolds numbers.

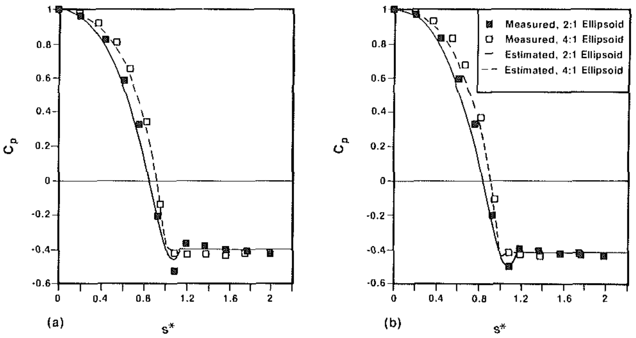

Fig. 5 Comparison of dimensionless pressure C_p, as determined from the data and estimated from linear interpolation. (*a*) $\text{Re}_D = 3 \times 10^4$; (*b*) $\text{Re}_D = 1 \times 10^5$.

Comparisons of Estimates and Data

Figure 5 shows the estimated pressures about the ellipsoids, presented with the measured values. The estimates were obtained by applying equation (7) up to the point where $r^* = 1$ and using the constant value $C_p = -.40$, over the remainder of the surface. The estimates closely agree with the observed values for the two ellipsoids at both $\text{Re}_D = 3 \times 10^4$ and $\text{Re}_D = 1 \times 10^5$. This suggests equation (7) may represent a valid technique for estimating pressure distributions about the surfaces of ellipsoids of various axis ratios.

Comparisons With Prior Work. Estimates of the pressure distributions about the surfaces of certain oblate ellipsoids at $\text{Re}_D \leq 100$ were obtained by Masliyah and Epstein [10]. They applied a finite-difference technique to the two-dimensional, incompressible equations of motion to obtain results for a sphere and for ellipsoids with axis ratios of 2:1 and 5:1. As their work does not include results for a disk, their results cannot be compared directly to the results obtained from equation (7). The sphere and disk results are needed to evaluate the parameters $C_{p_{sph}}(r^*)$ and $C_{p_{dsk}}(r^*)$ in equation (4). However, a linear equation can be written which is similar to equation (4), but employs the pressure data from a sphere and 5:1 ellipsoid. This results in an expression of the form:

$$C_{p_{E2}}(r^*, \theta/s^*) \approx (C_{p_{sph}}(r^*) - C_{p_{E5}}(r^*))[(\theta/s^* - \theta/s^*_{E5})/(1 - \theta/s^*_{E5})] + C_{p_{E5}}(r^*, \theta/s^*) \qquad (8)$$

where $C_{p_{E2}}(r^*)$ and $C_{p_{E5}}(r^*)$ are the dimensionless pressures at the surfaces of the 2:1 and 5:1 ellipsoids, respectively. The quantity θ/s^*_{E5} is the value of $\theta/s^*(r^*)$ on the 5:1 ellipsoid. In general, $\theta/s^*_{E5} << 1$ and is neglected to simplify computation.

The pressure coefficients of $C_{p_{sph}}(r^*)$ and $C_{p_{E5}}(r^*)$, are estimated from the data of [10]. The pressure about the forward-facing portion of the 2:1 ellipsoid surface, $C_{p_{E2}}(r^*)$, is estimated according to equation (8). The results are presented in Fig. 6. No attempt is made to estimate the

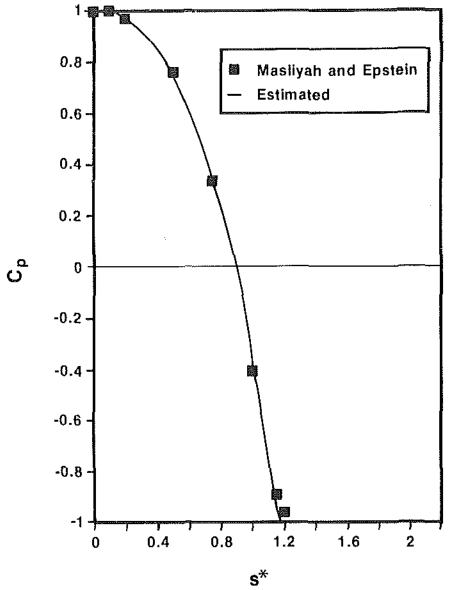

Fig. 6 Data for a 2:1 ellipsoid at Re_D = 100 from [10] are compared with linear interpolation estimates

pressure coefficients about the rear-facing portion of the ellipsoid surface.

Convex and Concave Models. This work is motivated by a need for pressure distributions about axisymmetric bluff bodies of arbitrary profile. Thus, it is worthwhile to consider using equation (7) for predicting pressure distributions about bluff, *non-ellipsoidal bodies.*

The dimensionless pressures about the surfaces of the nonellipsoidal convex and concave models have been estimated using equation (7). The estimates and the measured pressures for these two models are shown as Fig. 7. Results for the concave model are obtained under the condition that θ be set to zero in the concave portion of the model. This produces a discontinuity near $C_p = 0.7$ for the curves corresponding to the concave model in Fig. 7. As with the other models, equation (7) is applied only in the region from the forward stagnation point to the point where $r^* = 1$. The dimensionless pressure at the model surface is assumed constant rearward from that point. The agreement between measured and estimated values appears quite good for the convex model. The results are somewhat less favorable for the concave shape.

Summary

The objectives set forth for this work were to provide fundamental data on the surface pressures for selected axisymmetric, bluff bodies in an airflow and to provide a method for estimating pressures about the surfaces of axisymmetric, bluff bodies of arbitrary profile. Results of pressure measurements have been presented for $Re_D = 3 \times 10^4$ and $Re_D = 10^5$ for each of six rigid models: a disk, a 2:1 and a 4:1 ellipsoid, a sphere, a convex and a concave body.

A method has been described which enables estimation of pressures at the surface of bodies of arbitrary profile. This method assumes the pressure is a function of two geometric variables which specify location and surface geometry. Employment of this estimation method in the general case requires independent knowledge of the pressure distributions for a flat disk and a sphere (or two other appropriate geometries) under the desired conditions.

The pressure estimation technique described in this work has been used successfully by Ruman [4] to predict equilibrium droplet shapes via the marching technique discussed previously.

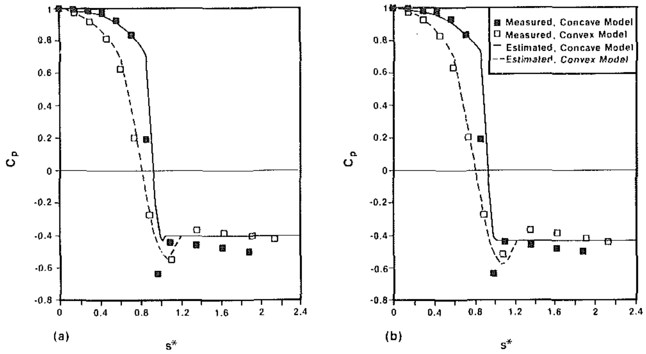

Fig. 7 Comparison of the data and estimates for the concave and convex models. (*a*) $Re_D = 3 \times 10^4$; (*b*) $Re_D = 1 \times 10^5$.

Estimates of the pressure distributions for the 2:1 and 4:1 ellipsoidal models are in close agreement with the measured pressures at both $Re_D = 3 \times 10^4$ and $Re_D = 10^5$. Estimates also closely agree with pressure data for the convex model. The pressure estimates for the concave droplet are somewhat less accurate. Whether or not this is a general consequence for concave, axisymmetric bodies is unknown and will form a basis for further investigation.

The method described is a very promising technique for estimating pressure distributions for certain axisymmetric bodies (chiefly, oblate ellipsoids) in airflows at Reynolds numbers on the order of 10^4 to 10^5. Schlichting [11] has shown that the drag coefficient for a sphere is virtually constant over the range $Re_D = 10^3$ to $Re_D = 3 \times 10^5$. Thus, it is reasonable to speculate that the pressure-estimating technique might be valid over a similar range of Reynolds numbers.

Future efforts will be devoted to examination of other geometries and applications of the results to predictions of the conditions leading to liquid droplet breakup.

Acknowledgments

This work was sponsored by the Mercury Marine Division, Brunswick Corporation. Their financial support and active participation is gratefully acknowledged.

References

1 Bryan, C. D., and Taylor, J. P., *Manual of Respiratory Therapy*, C. V. Moshy, St. Louis, 1973.

2 Lefebvre, A. H., *Gas Turbine Combustion*, McGraw-Hill, New York, 1983.

3 Miller, D. B. and Evers, L. W., "Pneumatic Atomization in an Annular Flow Nozzle," SAE Technical Paper Series No. 870611, 1987.

4 Ruman, M. A., "A Computational Model for the Prediction of Droplet Shapes and the Onset of Droplet Breakup," M.S. thesis, Michigan Technological University, 1988.

5 Savic, P., "Circulation and Distortion of Liquid Drops Falling Through A Viscous Medium," National Research Council of Canada, Report No. MT-22, 1953.

6 Pruppacher, H. R., and Pitter, R. L., "A Semi-Empirical Determination of the Shape of Cloud and Rain Drops," *Journal of the Atmospheric Sciences*, Vol. 28, 1971, pp. 86-94.

7 Krzeczkowski, S. A., "Measurement of Liquid Droplet Disintegration Mechanisms," *International Journal of Multiphase Flow*, Vol. 6, 1980, pp. 227-239.

8 Hinze, J. O., "Critical Speeds and Sizes of Liquid Globules," *Applied Scientific Research*, Vol. A1, No. 4, 1949, pp. 273-288.

9 Hanson, A. R., Domich, E. G., and Adams, H. S., "Shock Tube Investigations of the Breakup of Drops by Air Blasts," *Physics of Fluids*, Vol. 6, 1963, pp. 1070-1080.

10 Masliyah, J. H., and Epstein, N., "Numerical Study of Steady Flow Past Spheroids," *Journal of Fluid Mechanics*, Vol. 44, 1970, pp. 493-512.

11 Schlichting, H., *Boundary Layer Theory*, 7th ed., New York, McGraw-Hill, 1979, p. 17.

Journal of Fluids Engineering
Technical Briefs

The Use of a Photoelastic Method to Study the Effects of Bubble Collapse on Surfaces

E. Nienaltowska[1]

A photoelastic technique using two laser beams and high acquisition rate (20 MHz) has been used to investigate the dynamics of a single bubble in a fluid at rest. The bubbles are spark-generated in the vicinity of a photoelastic wall. The influence of liquid pressure, proximity of the wall and the bubble life-time on the collapse intensity is examined. The results obtained are compared qualitatively with the measurements of pressure obtained by Shima and Tomita for the liquid at atmospheric pressure.

Introduction

In early work Naude and Ellis [1] showed the possibility of obtaining fringe pictures of photoelastic material near collapsing vapour bubbles. Because of the small time scale of the experiments, they used a very high speed camera (1 million frames per second) to obtain sufficient detail of fringes. More recently Fujikawa and Arkamatsu [2] and Shima and Tomita [3, 4] also used a photoelastic technique and a high speed recording system for visualization of bubble collapse. The most interesting result seems to be the localization of impact [4] on the wall surface.

All these contributions [1–4] do not quantify the stress level due to the bubble collapse nor they do not give an estimation of optical parameters (phase shift) resulting from these stresses. In order to obtain the pictures with a large number of photoelastic fringes the photoelastic coefficient of the material must be as high as possible. Usually, it implies that the material is also nonelastic and the fringe number may not be representative of the bubble collapse intensity if the dynamic behavior of material is not known. Consequently the previous investigations are only qualitative.

In our experiments local measurements were performed: two laser beams were focused on a given point of photoelastic material and transmitted light was collected on the surfaces of two photodiodes. The output signals were recorded, permitting the evaluation of bubble life-times and variation of phase-shifts during the bubble collapse. In order to obtain the corresponding stress variations it was necessary to calibrate the photoelastic material. This was performed with small steel spheres: the maximum phase shift for each impact was measured and the corresponding stress values were calculated using the model of Hertz model of contact loading.

Two points should be emphasized. The material we used is nearly elastic and the signal sampling speed is very high (above 20 MHz). This permitted us to obtain new information about material behavior during bubble collapse. From our previous studies [5] it is clear that the material can inhibit high-frequency stresses. Thus the results presented in this paper must be understood with respect to the particular material which was employed.

Experimental Facilities

The bubbles were generated inside a 2 liter reservoir filled with water. This stainless steel reservoir can support pressures from 0.01 to 0.8 MPa. A schematic diagram, Fig. 1, shows the windows, the electrodes and the location of the photoelastic sample. The path of the laser beam is also shown.

The separation between tungsten electrodes and the wall was adjusted from 0 to 15 mm with 0.05 mm precision using a precision displacement system mounted on the electrode holder. The distance between each electrode could also be changed, but it was necessary to remove the holder from the reservoir. In the spark producing device, three 0.047 μF capacitors were mounted in parallel and the charged voltage could be adjusted up to 10 kV. In this manner the discharged energy was controlled.

The photoelastic material was a 6.4 mm thick sheet of

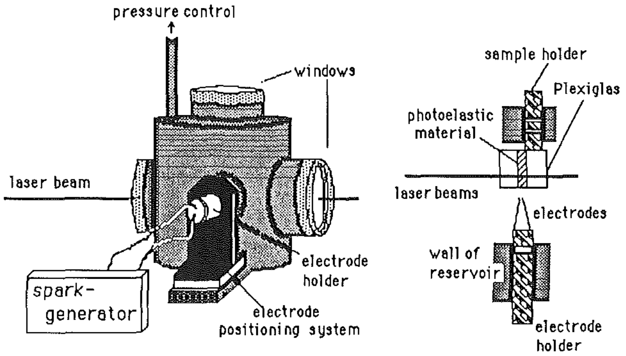

Reservoir a) - general view b) -details of interior: top view

Fig. 1 Reservoir (*a*) general view, (*b*) details of interior top view

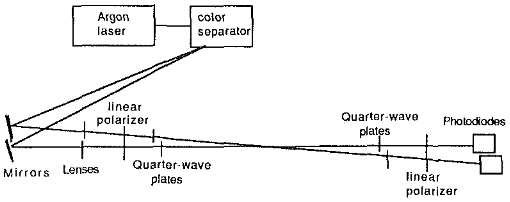

Fig. 2 Diagram of optical system. The photoelastic sample was placed in beam intersection

---

[1] Ecole Nationale Supérieure de Techniques Advancées, 75014 Paris, France.

Contributed by the Fluids Engineering Division of THE AMERICAN SOCIETY OF MECHANICAL ENGINEERS. Manuscript received by the Fluids Engineering Division April 19, 1988.

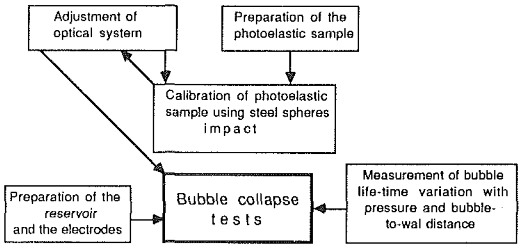

Fig. 3 Diagram of experimental procedure

polycarbonate ref. PSM1 glued between two Plexiglas blocks using liquid photoelastic resin. Young's modulus and the Poisson coefficient of the photoelastic material were about 2600 MPa and 0.38 respectively, the same parameters for Plexiglas being about 3000 MPa and 0.3.

The optical system, Fig. 2, consisted of a 100 mW Argon laser (Spectra-Physics model 162-A), color separator, two mirrors, two lenses, two linear polarizers and four quarter-wave plates (two for each wavelength), and two photodiodes. Only two wavelengths were selected and these beams were circularly polarized before entering the test section. The diameter of each beam inside the photoelastic material was about 0.25 mm and the distance between mirrors and photodiodes was approximately 3m.

The photodiode outputs were stored in a Gould 4074 digital memory using 1008 acquisition points per channel. A post-trigger mode was used with a time delay of approximately 90 percent of the presumed bubble life-time. The oscilloscope was linked with an HP 85 computer permitting the transfer of data blocs to the computer memory.

Experimental Procedure

A diagram of the experimental procedure is shown in Fig. 3. The details of dynamic calibration, by impact of two steel spheres (22 and 112.3g) on the photoelastic sample, are given in [6]. The velocity at the instant when they touched the wall was between 0.37 and 1.83 m/s for the smaller sphere and between 0.16 and 1.55 m/s for the other one, so kinetic energy was between 1.5 and 135 mJ. The measurements of phase shift were performed at the distances z_f from the surface: $6\text{mm} < z_f < 12\text{mm}$.

It should be noted that the photoelastic sample was first calibrated before any contact with liquid media. From our previous studies it is known that optical properties of certain resins change after contact with water for a few days. The polycarbonate optical properties do not change, but the glue layer may probably absorb water if immerged. So the calibration experiments were repeated after bubble collapse tests and it was concluded that results did not differ from the previous calibration.

During the bubble collapse tests a liquid pressure p_l and the electrode-to-wall distance d were measured. The bubble life-time t_b and the maximum phase shift ϕ_{max} were determined from the photoelastic signals. The maximum bubble radius R_{max} was calculated using

(i) t_b, p_l, and d values

(ii) nondimensional relationship giving the variation of t_b with respect to its value at infinity t_b^* as a function of d/R_{max} (cf Fig. 5(*b*))

(iii) the Rayleigh relation between $t_b^*/2$ and R_{max}:

$$t_b^*/2 = 0.915\, R_{max}\sqrt{\frac{\rho}{p_l - p_v}}$$

The relationship mentioned in (ii) was experimentally established as a result of a very large number of t_b measurements[3] (for different values of p_l, d and discharged energy)

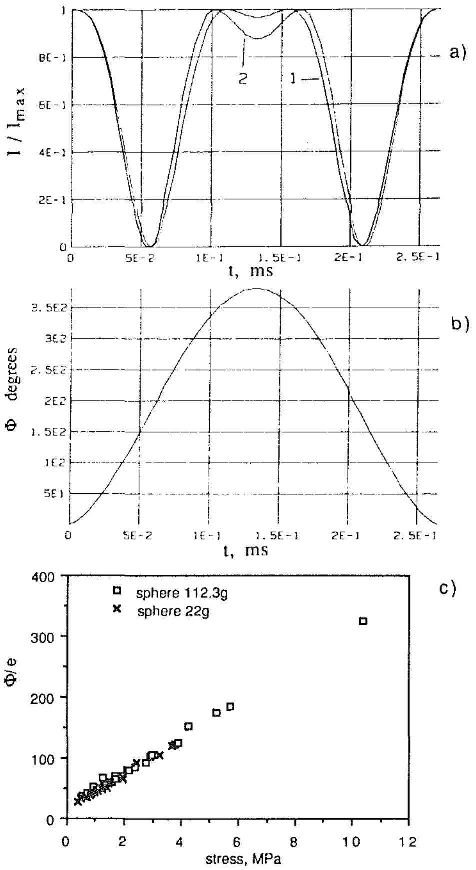

Fig. 4 *Calibration Results:* (*a*) Intensities of green beam (1) and blue beam (2) during a steel sphere impact signals stored, respectively, with 0.01 ms and 5 percent uncertainty in time and amplitude scales have been fitted; *b*) Phase shift (green beam) calculated using the data of (*a*); c) The maximum phase shift over a thickness of photoelastic sheet (measured with 10 deg/mm maximum uncertainty) as a function of stress calculated using Hertz model.

$$t_b = f(p_l, d, R_{max}, t_b^*)$$

which may be presented in the dimensionless form as follows

$$t_b/t_b^* = f(d/R_{max})$$

For several bubbles it was also verified (using high-speed cinematography visualizations) that R_{max} calculated and measured directly (as an equivalent radius for ellipsoidal shapes) were the same.

Results and Discussion

The results of the calibration are summarized in Fig. 4. Figure 4(*a*) is an example of the intensity signal. Figure 4(*b*) shows the corresponding phase shift as a function of time. Note the symmetrical character of the signals with respect to the point of a maximum shift (Fig. 4(*a*)). In Fig. 4(*c*) the maximum values of the phase-shifts are plotted as a function of corresponding local stresses.

The slope of this curve will be used to calculate the stress values, in the case of bubble collapse, in spite of the different time scales in the two phenomena, namely, 0.2-0.5 ms for the impact of steel spheres and 0.01 and 0.04 ms for the collapse.

In Fig. 5 are shown dimensionless values of bubble life-time

---

[2] Photoelastic Division of Measurements Group, Inc., Rayleigh, NC

[3] In this case the bubble life-time was measured using an additional optical arrangement in which laser beams passed though water near the extremity of the electrodes. The value t_b was defined as the time interval starting with the spark generation and ending when the shock wave crossed the laser beams.

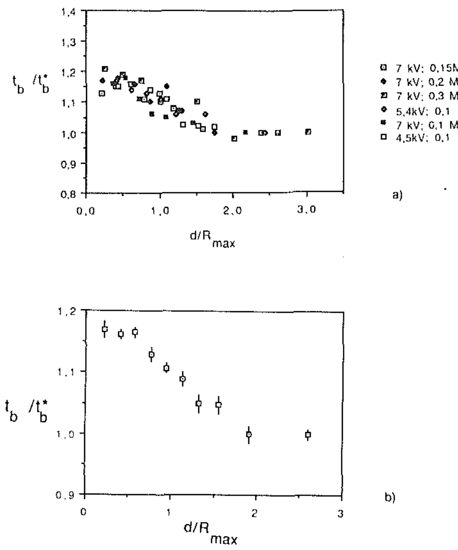

Fig. 5 Bubble life-time increase with the wall proximity: (*a*) different measurements, (*b*) mean values

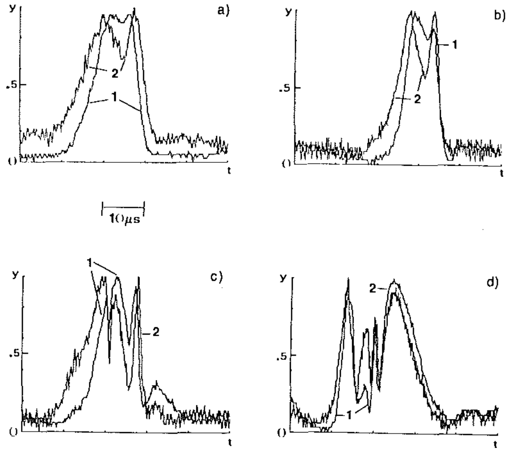

Fig. 6 Variations of beam intensities (5 percent uncertainty) during the final stage of collapse at z_f-8mm from the surface as a function of time (0.2μs uncertainty) for different bubbles conditions:
(*a*) $d/R_{max} = 0.65$, $R_{max} = 4.6$mm, $p = 0.1$ MPa; (*b*) $d/R_{max} = 0.62$, $R_{max} = 3.2$mm, $p = 0.1$ MPa; (*c*) $d/R_{max} = 1.03$, $R_{max} = 2.8$mm, $p = 0.1$ MPa; (*d*) $d/R_{max} = 0.89$, $R_{max} = 2.8$mm, $p = 0.2$ MPa

as a function of dimensionless bubble-to-wall distance. Each point in Fig. 5(*a*) was obtained as a mean value of 3 to 5 measurements. The capacitor supply voltages and the liquid pressures are specified in the figure. For $d/R_{max} < 0.2$ the scatter of $t_b/t_b{}^*$ values was greater than 5 percent of their mean value. Consequently they were not considered.

Some "photoelastic" signals obtained during the first collapse[4] of the bubbles are shown in Fig. 6(*a-d*). The intensities of each signal were normalized using the corresponding maximum values. The time scale of all these signals is the same. Each passage of the signal near zero corresponds to the "dark fringe" of classical photoelasticity. The signal before the impact of the collapsing bubble is relatively flat; small fluctuations of amplitude are due to the laser fluctuations. When the phase-shift is increasing the variation of intensity of the blue beam precedes that of the green beam. The contrary occurs if the phase-shift is decreasing.

Therefore, one can follow the phase shift increase and decrease as a function of time. During the bubble collapse we observed the "simple" shocks which mean that the phase shift increases, reaches its maximum and decreases. But sometimes "double shocks" occurred and the phase shift had to maxima. The maxima of phase shift were calculated (only one par signal) and using the calibration results the corresponding stresses were obtained.

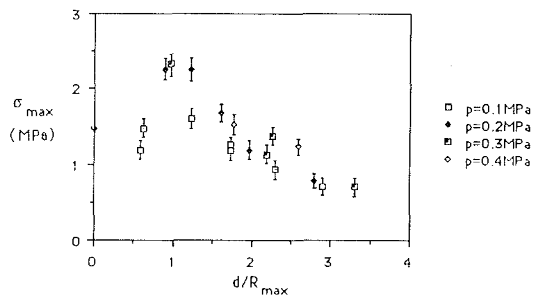

Fig. 7 Maximum stresses as a function of proximity parameter for different values of liquid pressure

Table 1

d/R_{max}	R_{max} (mm)	P (MPa)	$e^{-1}d\Phi/dt$ deg mm$^{-1}\mu s^{-1}$
0.42	4.8	0.1	5.7
0.59	3.4	0.28	25
0.61	2.4	0.3	14.2
0.62	3.2	0.1	8.0
0.89	2.8	0.2	10.2
1.22	2.9	0.2	27.5
1.22	3.3	0.1	21.2
1.6	2.8	0.2	29
1.7	3.5	0.1	17.2
2.84	2.8	0.2	42.5

In Fig. 7 we present the maximum stresses as a function of d/R_{max} parameter for 4 pressure values and $z_f = 8$mm. The bubble radii we comprised between 2.6 and 3.2 mm. It should be noted that if we consider the interval $d/R_{max} \geq 0.5$ the maximum stresses were obtained for d/R_{max} approaching 1, independent of liquid pressure. At constant d/R_{max} the increase of liquid pressure from 0.1 to 0.2 MPa implies the increase of stresses inside the wall. Nevertheless, the further increase of pressure, up to 0.4 MPa, did not produce a significant increase of maximum stress.

From the shape of the intensity curves (cf Fig. 6) it can be observed that the deformation history of photoelastic material depends on the bubble proximity and on the bubble maximum radius. For a given distance z_f from the photoelastic surface, the slope of the intensity evolution can indicate the rate of change of phase shift. But one must measure a slope for points where the intensity approaches half of its maximum value. In fact, if $\Phi(t)$ is the shift value at instant t, the dimensionless intensity $y = I/I_{max}$ is given by

$$y = (1 \pm \cos \Phi(t))/2$$

and the sign before $\cos \Phi(t)$ depends on the relative orientation of the axis of the quarter-wave plates. Thus the derivative of it is

$$dy/dt = \pm \sin\Phi(t) d\Phi/dt$$

and it is clear that if $y = 1/2$ then

$$dy/dt = \pm d\Phi/dt$$

In Table 1 are shown some values of $d\Phi(t)/dt$ divided by photoelastic material thickness,[5] e, for different bubble radii and pressure values.

---

[4] Some acquisitions during the second collapse were also obtained but their analysis was not completed because the bubble localization is unknown.

[5] In the case of steel spheres impact, the photoelastic material thickness and z_f were chosen in order to obtain the *mean value* of phase shift, Φ/e, close to its *local value*. For the bubble collapse the mean and local values are not necessarily the same.

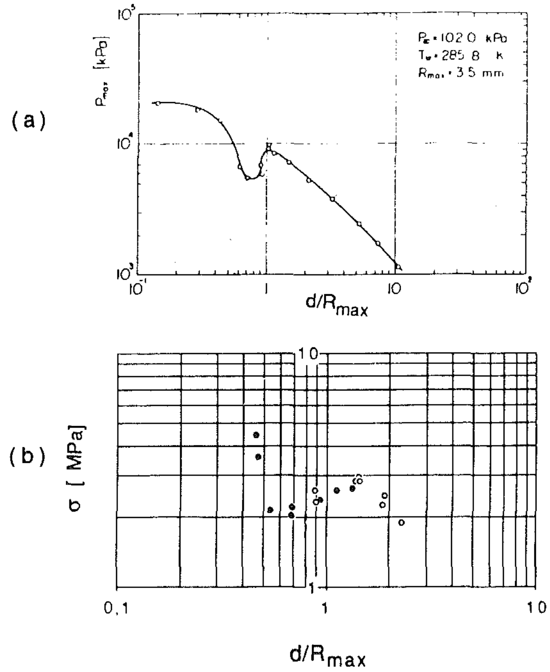

Fig. 8 Collapse effect as a function of wall proximity: (*a*) Shima measurements of pressure exerted on the wall surface, (*b*) our results: stresses inside the wall (for $z = 7$mm)

We did not mention the time of the deformation of photoelastic material during bubble collapse. In fact, when a solid-solid impact is considered it is easy to define the contact time (or time of deformation). In the bubble "impact" on the photoelastic sample the maximum value of phase shift does not coincide with a half-deformation time. Nevertheless, it was observed that the total duration of deformation, for the 3mm radius bubbles, can vary from 20 to 30 μs.

For a very few signals we calculated the phase shift evolution as a function of time during the end of collapse. Two different types of behavior were observed.

(i) the existence of only one local maximum ("simple shock") if $d/R_{max} > 1$

(ii) the occurrence of two local maxima ("double shock") in the other case.

The effect of the bubble size on the collapse intensity has been also investigated. Preliminary results indicate that if the ratio d/R_{max} is constant the maximum stress is nearly independent of bubble size (for R_{max} between 2.8 and 4.4 mm) but the deformation duration increases.

Another point which merits attention is the comparison of pressure and photoelastic measurements. Shima and Tomita presented the variation of pressure exerted on a wall surface as a function of d/R_{max} for bubbles generated in water at atmospheric pressure (Fig. 8(*a*)). They observed a local maximum of pressure for d/R_{max} close to one and a local minimum in the interval $0.6 < d/R_{max} < 0.8$. It can be seen that the stress values which we obtained follow the same tendency (Fig. 8(*b*)).

Conclusions

It was shown that photoelastic measurements can be employed to study bubble dynamics and some quantitative results have been presented. The importance of wall proximity on the collapse intensity (maximum stress) was shown. The local maximum collapse intensity was obtained for d/R_{max} close to 1. The pressure increase implies the increase of maximum stress. If, for fixed d/R_{max} the bubble size increases, the deformation duration increases; but the maximum stress is constant.

The shape of photoelastic signal varies with the bubble-to-wall proximity. The "simple shock" (for the bubble collapsing far from the wall) and "double shock" deformation can be distinguished.

References

1 Naude, C. F., and Ellis, A. T., 1961, "On the Mechanism of Cavitation Damage by Nonspherical Cavities Collapsing in Contact With a Solid Boundary," ASME *Journal of Basic Engineering*, Vol. 93.

2 Fujikawa, S., and Akamatsu, T., 1980, "Effects of the Non-Equilibrium Condensation of Vapour on the Pressure Wave Produced by the Collapse of a Bubble in a Liquid," *J. Fluid Mech.*, Vol. 97, Part 3, pp. 481-512.

3 Shima, A. Takayama, K., and Tomita, Y., 1984, "Mechanism of the Bubble Collapse Near a Solid Wall and Induced Impact Pressure Generation," *Rep. Inst. High Speed Mech.*, Vol. 48, No. 367, Tohoku University, Sendai, Japan.

4 Tomita, Y., and Shima, A., 1986, "Mechanism of Impulsive Pressure Generation and Damage Pit Formation by Bubble Collapse," *J. Fluid Mech.*, Vol. 169, pp. 535-564.

5 Nienaltowska, A. E., 1984, "Etude de chocs au moyen d'un ellipsomètre à deux faisceaux laser," *Rapport de recherche ENSTA*, Paris, France.

6 Dorey, J. M., and Nienaltowska, E., "The Erosion Pits Due to Collapsing Bubbles," presented at *ASME Cavitation and Multiphase Flow Forum* 88.

A Modified Form of the Betz' Wind Turbine Theory Including Losses

A. Dyment[1]

The aim of this brief paper is to present a variant of the classical Betz' theory concerning the flow through a wind turbine. The new model includes losses and gives more realistic maximum values of the characteristic nondimensional coefficients of the machine.

1 Introduction

The Froude's theory of the propeller was extended by Betz to the wind turbine about sixty years ago. The basic idea of this theory is to replace the machine by a disk—the so called actuator disk—through which the pressure is discontinuous. The flow inside the stream tube T that feeds the machine is considered as almost one dimensional. As the pressure far upstream and downstream has the same value p_∞, and as the fluid crossing the machine loses or gains some energy, the velocity inside the tube T is everywhere different from the upstream velocity U_∞. That means the border of the tube behaves as a shear layer. Consequently, eddies are formed which are located rather on the side where the flow is slowed, that is outside the central tube T for a propeller, and inside for a wind turbine. Thus Bernoulli equation can be used in the central tube only in the case of a propeller. This remark implies that the Betz approach must be reconsidered.

2 The Modified Theory

In order to avoid complicated calculations we shall use artificial means. We start with a wind turbine encased in a coaxial cylindrical duct. The symbols are those indicated in Fig. 1.

From conservation of mass one obtains:

$$aS = cS_1, \tag{1}$$

$$b\sigma = dS_2, \tag{2}$$

$$(1-a)S = (1-b)\sigma. \tag{3}$$

---

[1] Professor, Department of Mechanics, Université des Sciences et Techniques de Lille, 59655 Villeneuve d'Ascq, France.

Contributed by the Fluids Engineering Division of The American Society of Mechanical Engineers. Manuscript received by the Fluids Engineering Division May 12, 1988.

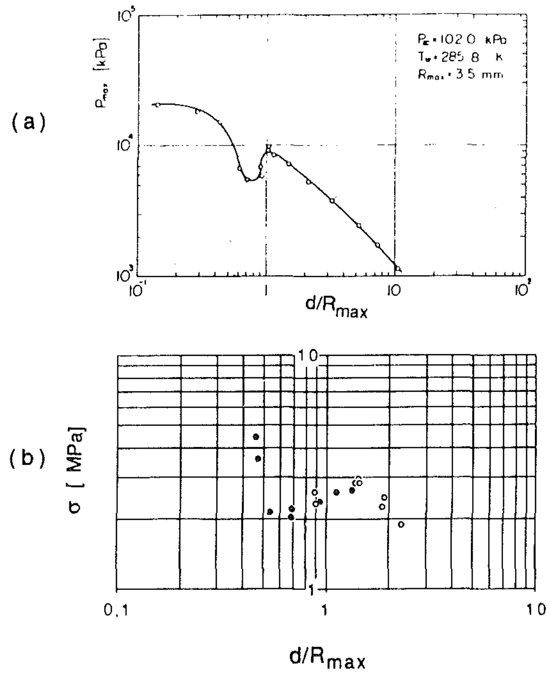

Fig. 8 Collapse effect as a function of wall proximity: (*a*) Shima measurements of pressure exerted on the wall surface, (*b*) our results: stresses inside the wall (for $z = 7$mm)

We did not mention the time of the deformation of photoelastic material during bubble collapse. In fact, when a solid-solid impact is considered it is easy to define the contact time (or time of deformation). In the bubble "impact" on the photoelastic sample the maximum value of phase shift does not coincide with a half-deformation time. Nevertheless, it was observed that the total duration of deformation, for the 3mm radius bubbles, can vary from 20 to 30 μs.

For a very few signals we calculated the phase shift evolution as a function of time during the end of collapse. Two different types of behavior were observed.

(i) the existence of only one local maximum ("simple shock") if $d/R_{\max} > 1$

(ii) the occurrence of two local maxima ("double shock") in the other case.

The effect of the bubble size on the collapse intensity has been also investigated. Preliminary results indicate that if the ratio $d/R_{\max}$ is constant the maximum stress is nearly independent of bubble size (for $R_{\max}$ between 2.8 and 4.4 mm) but the deformation duration increases.

Another point which merits attention is the comparison of pressure and photoelastic measurements. Shima and Tomita presented the variation of pressure exerted on a wall surface as a function of $d/R_{\max}$ for bubbles generated in water at atmospheric pressure (Fig. 8(*a*)). They observed a local maximum of pressure for $d/R_{\max}$ close to one and a local minimum in the interval $0.6 < d/R_{\max} < 0.8$. It can be seen that the stress values which we obtained follow the same tendency (Fig. 8(*b*)).

Conclusions

It was shown that photoelastic measurements can be employed to study bubble dynamics and some quantitative results have been presented. The importance of wall proximity on the collapse intensity (maximum stress) was shown. The local maximum collapse intensity was obtained for $d/R_{\max}$ close to 1. The pressure increase implies the increase of maximum stress. If, for fixed $d/R_{\max}$ the bubble size increases, the deformation duration increases; but the maximum stress is constant.

The shape of photoelastic signal varies with the bubble-to-wall proximity. The "simple shock" (for the bubble collapsing far from the wall) and "double shock" deformation can be distinguished.

References

1 Naude, C. F., and Ellis, A. T., 1961, "On the Mechanism of Cavitation Damage by Nonspherical Cavities Collapsing in Contact With a Solid Boundary," ASME *Journal of Basic Engineering*, Vol. 93.

2 Fujikawa, S., and Akamatsu, T., 1980, "Effects of the Non-Equilibrium Condensation of Vapour on the Pressure Wave Produced by the Collapse of a Bubble in a Liquid," *J. Fluid Mech.*, Vol. 97, Part 3, pp. 481-512.

3 Shima, A. Takayama, K., and Tomita, Y., 1984, "Mechanism of the Bubble Collapse Near a Solid Wall and Induced Impact Pressure Generation," *Rep. Inst. High Speed Mech.*, Vol. 48, No. 367, Tohoku University, Sendai, Japan.

4 Tomita, Y., and Shima, A., 1986, "Mechanism of Impulsive Pressure Generation and Damage Pit Formation by Bubble Collapse," *J. Fluid Mech.*, Vol. 169, pp. 535-564.

5 Nienaltowska, A. E., 1984, "Etude de chocs au moyen d'un ellipsomètre à deux faisceaux laser," *Rapport de recherche ENSTA*, Paris, France.

6 Dorey, J. M., and Nienaltowska, E., "The Erosion Pits Due to Collapsing Bubbles," presented at *ASME Cavitation and Multiphase Flow Forum* 88.

A Modified Form of the Betz' Wind Turbine Theory Including Losses

A. Dyment[1]

The aim of this brief paper is to present a variant of the classical Betz' theory concerning the flow through a wind turbine. The new model includes losses and gives more realistic maximum values of the characteristic nondimensional coefficients of the machine.

1 Introduction

The Froude's theory of the propeller was extended by Betz to the wind turbine about sixty years ago. The basic idea of this theory is to replace the machine by a disk—the so called actuator disk—through which the pressure is discontinuous. The flow inside the stream tube T that feeds the machine is considered as almost one dimensional. As the pressure far upstream and downstream has the same value p_∞, and as the fluid crossing the machine loses or gains some energy, the velocity inside the tube T is everywhere different from the upstream velocity U_∞. That means the border of the tube behaves as a shear layer. Consequently, eddies are formed which are located rather on the side where the flow is slowed, that is outside the central tube T for a propeller, and inside for a wind turbine. Thus Bernoulli equation can be used in the central tube only in the case of a propeller. This remark implies that the Betz approach must be reconsidered.

2 The Modified Theory

In order to avoid complicated calculations we shall use artificial means. We start with a wind turbine encased in a coaxial cylindrical duct. The symbols are those indicated in Fig. 1.

From conservation of mass one obtains:

$$aS = cS_1, \tag{1}$$

$$b\sigma = dS_2, \tag{2}$$

$$(1-a)S = (1-b)\sigma. \tag{3}$$

---

[1] Professor, Department of Mechanics, Université des Sciences et Techniques de Lille, 59655 Villeneuve d'Ascq, France.

Contributed by the Fluids Engineering Division of THE AMERICAN SOCIETY OF MECHANICAL ENGINEERS. Manuscript received by the Fluids Engineering Division May 12, 1988.

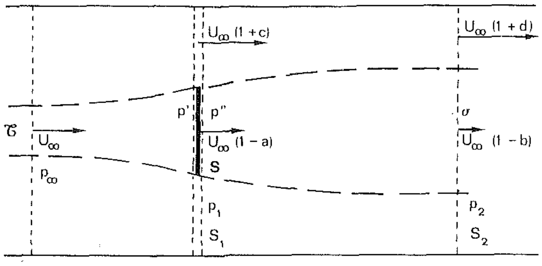

Fig. 1

The Bernoulli equation is applied only to the external stream which forms a converging passage with downstream increasing velocity:

$$p_\infty+\rho\frac{U_\infty^2}{2}=p_1+\rho\frac{U_\infty^2}{2}(1+c)^2=p_2+\rho\frac{U_\infty^2}{2}(1+d)^2. \quad (4)$$

Let us write now the momentum equation for the two cylindrical domains indicated by dotted lines, the first situated upstream the rotor and the second downstream:

$$-\rho\, U_\infty^2(S+S_1)+\rho\, U_\infty^2(1-a)^2S+\rho\, U_\infty^2(1+c)^2S_1$$
$$-p_\infty(S+S_1)+p'\, S+p_1S_1=0,$$
$$-\rho\, U_\infty^2(1-a)^2S-\rho\, U_\infty^2(1+c)^2S_1+\rho\, U_\infty^2(1-b)^2\sigma$$
$$+\rho\, U^2(1+d)^2S_2-p''S-p_1\, S_1+p_2(\sigma+S_2)=0.$$

By use of (1), (2), (3), and (4) one obtains:

$$p'-p_\infty=\rho\, U_\infty^2 a\left(1-a-\frac{c}{2}\right), \quad (5)$$

$$p''-p_\infty=\rho\, U_\infty^2\left[a\left(1-a-\frac{c}{2}\right)\right.$$
$$\left.+\left(b^2-b-d-\frac{d^2}{2}+\frac{bd}{2}\right)\frac{1-a}{1-b}\right]. \quad (6)$$

Let us calculate now the losses in the successive diverging parts of the tube T, on both sides of the turbine.

Upstream the losses are:

$$\zeta'=\left(p_\infty+\rho\frac{U_\infty^2}{2}\right)-\left[p'+\rho\frac{U_\infty^2}{2}(1-a)^2\right]$$
$$=\rho\frac{U_\infty^2}{2}a(a-c). \quad (7)$$

Downstream we have:

$$\zeta''=\left[p''+\rho\frac{U_\infty^2}{2}(1-a)^2\right]$$
$$-\left[p_2+\rho\frac{U_\infty^2}{2}(1-b)^2\right] \quad (8)$$
$$=\rho\frac{U_\infty^2}{2}\left[2a-2a^2-ac-(2b-2b^2+2d\right.$$
$$\left.+d^2-bd)\frac{1-a}{1-b}+2d+d^2+2b-2a+a^2-b^2\right].$$

Now we put S_1, $S_2\to\infty$, so that (1) and (2) imply: c, $d\to 0$. Then, according to (4), (5) and (6) we obtain:

$$p_1=p_2=p_\infty,$$
$$p'-p_\infty=\rho\, U_\infty^2 a(1-a), \quad (9)$$
$$p''-p_\infty=\rho\, U_\infty^2(1-a)(a-b). \quad (10)$$

Upstream, according to (7) the losses become

$$\zeta'=\rho\frac{U_\infty^2}{2}a^2. \quad (11)$$

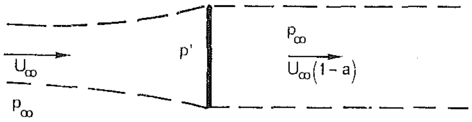

Fig. 2

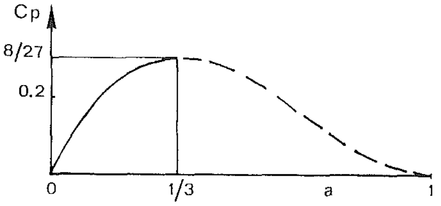

Fig. 3

That is the same result as for a sudden enlargment in a pipe. As for the losses downstream, we obtain from (8):

$$\zeta''=-\rho\frac{U_\infty^2}{2}(a-b)^2. \quad (12)$$

This result has no significance unless $b=a$. As a consequence we obtain the flow sketched in Fig. 2, with a cylindrical wake behind the turbine: $\sigma=S$. For this flow the total losses occur upstream of the turbine and they are equal to $\rho\, U_\infty^2/2$ a^2.

Let $1/2\,\rho\, U_\infty^3 S\, C_L$ be the power delivered by the fluid passing in the slipstream, $1/2\,\rho\, U_\infty^3 S\, C_p$ the power output and $1/2\,\rho\, U_\infty^3 C_w$ the power wasted. These quantities are defined by

$$\frac{1}{2}\rho\, U^3\, S\, C_L=\frac{1}{2}[U_\infty^2-U_\infty^2(1-b)^2]q$$
$$\frac{1}{2}\rho\, U^3\, S\, C_p=(p'-p'')q$$
$$C_w=C_L-C_p,$$

where q is the discharge through the turbine: $q=\rho\, U_\infty\,(1-\mathrm{a})$ S. Taking into account previous results one can easily obtain:

$$C_L=a(1-a)(2-a), \quad (13)$$
$$C_p=2a(1-a)^2, \quad (14)$$
$$C_w=a^2(1-a). \quad (15)$$

The efficiency, defined by $\eta=C_{P/C_L}$, is:

$$\eta=\frac{1-a}{1-a_{/2}}. \quad (16)$$

Let $1/2\,\rho\, U_\infty^2 S\, C_D$ be the force applied to the turbine. We have:

$$C_D=2a(1-a). \quad (17)$$

The maximum of C_p is reached for $a=1/3$: $C_{p\max}=8/27$. The corresponding values of C_L, η and C_D are 10/27, 4/5, and 4/9.

Formula (14) shows that for a given value of the power output there are two possible values of a (Fig. 3). It is well known in physics that when various solutions are theoretically obtained the one which actually occurs corresponds to the minimum of dissipation. Here, as the losses are proportional to a^2, the actual solution is that for which $a\le 1/3$. So, all formulas (13), (14), (15), (16), and (17) are valid only for $a\le 1/3$.

3 Further Comments

As it has been recalled in the introduction Betz has considered that Bernoulli equation holds in the stream tube T. As a consequence $b=2a$, so that $\sigma=(1-a)/(1-2a)\ S$ which is unrealistic for $a\ge 1/2$. No inconsistency of this kind appears in the new theory.

Besides, the values obtained by Betz for C_p and C_D are exactly twice those given by formulas (14) and (17). As it is well known [2], the largest values of C_p obtained in experiments are 50 percent lower than Betz' maximal value 16/27, so that they are closer to the present theory. However, some performing wind turbines overstep our prescribed highest value 8/27. That means the calculated losses are somewhat overestimated. In this sense, the new theory is pessimistic. The reality is somewhere between the two theories, probably closer to the new one. The main weakness of both theories lies in the rough representation of the machine. But that is the price we must pay for simplicity!

In order to obtain better results the rotary effects should be taken into account. Besides, the present model of actuator disk should be improved by introducing momentum flux and kinetic energy correction factors. Unfortunately, these factors cannot be calculated in a global approach.

References

1 De Vries, O., "On the Theory of the Horizontal Axis Wind Turbine," *Ann. Rev. Fl. Mech.*, Vol. 15, 1983, pp. 77–96.

2 Hunter, U., "Optimum Wind-Energy Conversion Systems," *Ann. Rev. Fl. Mech.*, Vol. 9, 1977, pp. 399–419.